

Numerical Simulation of Complex Viscoelastic Flows using Discontinuous Galerkin Spectral/hp Element Methods

by

Susanne Claus

Supervised by Prof. T. N. Phillips



SCHOOL OF MATHEMATICS,
CARDIFF UNIVERSITY

A THESIS SUBMITTED FOR THE DEGREE OF DOCTOR OF
PHILOSOPHY OF CARDIFF UNIVERSITY

May 1, 2013

Declaration

This work has not been submitted in substance for any other degree or award at this or any other university or place of learning, nor is being submitted concurrently in candidature for any degree or other award.

Signature _____
(candidate)
Date May 1, 2013

Statement 1

This thesis is being submitted in partial fulfillment of the requirements for the degree of PhD.

Signature _____
(candidate)
Date May 1, 2013

Statement 2

This thesis is the result of my own independent work/investigation, except where otherwise stated. Other sources are acknowledged by explicit references. The views expressed are my own.

Signature _____
(candidate)
Date May 1, 2013

Statement 3

I hereby give consent for my thesis, if accepted, to be available for photocopying and for inter-library loan, and for the title and summary to be made available to outside organisations.

Signature _____
(candidate)
Date May 1, 2013

Acknowledgements

First and foremost I would like to thank my supervisor Prof. Tim Phillips, for valuable guidance and advice. During the course of this thesis, you have always been there for me and without your guidance this thesis would not have been possible. I am deeply grateful for all you have done for me.

I would also like to thank my examiners, Dr. Xue-feng Yuan and Prof. Russell Davies for their constructive feedback.

Additionally, I am very grateful to Prof. Robert Owens for his detailed and inspiring feedback on my thesis.

I gratefully acknowledge the funding I received from the Engineering and Physical Sciences Research Council of the United Kingdom (tuition fees) and Cardiff University (stipend).

I would like to thank Prof. Spencer Sherwin, Chris Cantwell and Alessandro Bolis for their support and advice concerning questions about the implementation in Nektar++ and for always quickly and constructively responding to my questions.

I would like to express my gratitude to Prof. Evan Mitsoulis for generously providing detailed results for the extrudate swell.

I would also like to thank all the friends I made during my time in Cardiff. Their support meant everything to me and they made living in Cardiff such a pleasure for me.

Special thanks to Prof. Stephane Bordas for his encouragement and Dr. Karl Schmidt for numerous enriching discussions.

Last but not least, I would like to express my deepest gratitude to Ursula Claus, who has always supported and inspired me and Dr. Pierre Kerfriden for his support, patience and advice.

Summary

Viscoelastic flows are characterised by fast spatial and temporal variations in the solution featuring thin stress boundary near walls and stress concentrations in the vicinity of geometrical singularities. Resolving these fast variations of the fields in space and time is important for two reasons: (i) they affect the quantity of interest of the computation (e.g. drag force); and (ii) they are commonly believed to be associated with the numerical breakdown of the computation. Traditional discretisation methods such as finite differences or low-order finite elements require a large number of degrees of freedom to resolve these variations. Spectral methods enable this issue to be resolved by defining spatial expansions that are able to represent such variations with a smaller number of degrees of freedom. However, such methods are limited in terms of geometric flexibility. Recently, the spectral/hp element method (Karniadakis and Sherwin, 2005) has been developed in order to guarantee both spectral convergence, and geometric flexibility by allowing the use of quadrilateral and triangular elements. Our work is the first attempt to apply this method to viscoelastic free surface flows in arbitrary complex geometries.

The conservation equations are solved in combination with the Oldroyd-B or Giesekus constitutive equation using the DEVSS-G/DG formulation. The combination of this formulation with a spectral element method is novel. A continuous approximation is employed for the velocity and discontinuous approximations for pressure, velocity gradient and polymeric stress. The conservation equations are discretised using the Galerkin method and the constitutive equation using a discontinuous Galerkin method to increase the stability of the approximation. The viscoelastic free surface is traced using an arbitrary Lagrangian Eulerian method.

The performance of our scheme is demonstrated on the time-dependent Poiseuille flow in a channel, the flow around a cylinder and the die-swell problem. The comparison of the scheme to the analytical solution in the transient Oldroyd-B Poiseuille flow shows that the DEVSS-G stabilisation increases the critical Weissenberg number from $Wi = 3.3$ to $Wi = 9.8$ and converges to the steady state solution with machine precision. For the flow around the cylinder of an Oldroyd-B fluid, we find a transient flow regime for $Wi > 0.6$ for finer meshes. We identify the tendency of a velocity inflection on top of the cylinder as a possible cause for the onset of this transient flow regime. Furthermore, we give detailed results for the flow around a cylinder for the Giesekus model and investigate the influence of the mobility parameter on the flow. For Newtonian extrudate swell, we investigate the impact of inertia and slip along the die wall on the swelling ratio and give detailed results about the behaviour of the dependent variables at the flow singularity. We find excellent agreement between our results and those in the literature. Additionally, we give detailed results for Oldroyd-B and Giesekus fluids including no-slip and slip along the die wall in plane extrudate swell and investigate the behaviour of the pressure and polymeric stress components at the flow singularity.

Contents

1. Introduction	1
1.1. Viscoelastic Phenomena	1
1.2. Challenges in the Numerical Solution of Viscoelastic Flows	2
1.3. About this Thesis	6
1.3.1. Numerical Method	7
1.3.2. Validation and Results	7
1.3.3. Outline	9
2. Mathematical Description of Viscoelastic Flows	11
2.1. Kinematic Description of the Flow in Different Reference Frames	11
2.1.1. Eulerian and Lagrangian Flow Descriptions	11
2.1.2. Arbitrary Lagrangian-Eulerian Flow Description	12
2.2. Conservation Laws	15
2.3. Transport Theorems	15
2.3.1. Conservation of Mass	17
2.3.2. Conservation of Linear Momentum	17
2.4. Constitutive Equations	20
2.4.1. The Newtonian Fluid	20
2.4.2. The Generalised Newtonian Fluid	21
2.4.3. Viscoelastic Models for Dilute Polymer Solutions	23
2.5. Simple Flows, Viscosities and Stress Differences	29
2.5.1. Steady Shear Flow and Viscometric Functions	29
2.5.2. Steady Uniaxial Extensional Flow and Elongational Viscosity	30
2.5.3. Viscometric Functions for Newtonian Fluids	32
2.5.4. Viscometric Functions for Oldroyd-B Fluid	32
2.5.5. Viscometric Functions for Giesekus Fluid	34
2.6. Governing Equations	37
2.6.1. Boundary and Initial Conditions	37
2.6.2. Weak Formulation	42
2.7. Non-Dimensionalisation	43
3. Spectral/hp element methods	47
3.1. Discretisation	47
3.1.1. Discretisation of the Solution Space	47
3.1.2. Discretisation of the Domain	48
3.2. Numerical Methods	50
3.2.1. Finite element method	50
3.2.2. Spectral Method	51
3.2.3. Spectral/hp element method	52

3.3.	Integration and Differentiation on the Standard Element	58
3.3.1.	Integration	58
3.3.2.	Differentiation	59
3.4.	Geometrical Mapping	59
3.5.	Integration and Differentiation for Generally Shaped Elements	62
3.5.1.	Integration	62
3.5.2.	Differentiation	63
3.6.	Matrix notation	63
3.6.1.	Integration	65
3.6.2.	Differentiation	65
3.6.3.	Backward transformation	66
3.6.4.	Forward transformation	66
3.7.	Coupling between Elements	67
3.7.1.	Continuous Galerkin Method	68
3.7.2.	Discontinuous Galerkin Method	73
3.8.	Example: One-Dimensional Projection and Advection	77
3.8.1.	Galerkin Projection	79
3.8.2.	Advection	81
4.	Temporal and Spatial Approximation for Viscoelastic Flows	91
4.1.	Stabilisation Techniques	92
4.1.1.	Upwinding Techniques for the Constitutive Equations	92
4.1.2.	DEVSS-G Formulation	93
4.2.	Spatial Approximation of Velocity, Pressure and Polymeric Stress	96
4.3.	Temporal schemes	99
4.4.	DEVSS/DG Algorithm in a Fixed Domain	99
4.4.1.	Solving the Coupled System of Velocity and Pressure	101
4.4.2.	Solving the Constitutive Equation	105
5.	Numerical Results for Fixed Meshes	109
5.1.	Unsteady Poiseuille Flow of an Oldroyd-B Fluid	109
5.1.1.	Analytical Solution	109
5.1.2.	Transient Numerical Solution	112
5.2.	Flow around a Confined Cylinder	117
5.2.1.	Benchmark Geometry	120
5.2.2.	Oldroyd-B Model	124
5.2.3.	Oldroyd-B Model for higher Reynolds numbers	137
5.2.4.	Giesekus Model	141
6.	DEVSS/DG Algorithm for Viscoelastic Free Surface Flows	155
6.1.	Weak DEVSS/DG Formulation in the ALE framework	155
6.2.	Domain Movement	159
6.3.	Free Surface Representation	161
6.4.	Spatial discretisation	163
6.5.	Mesh Movement	168
6.6.	Solving the Coupled System of Velocity, Pressure and \mathbf{G}	169

6.7. Solving the Constitutive Equation	173
7. Die Swell Simulations	177
7.1. Computational Domain and Quantities of Interest	183
7.2. Newtonian Die Swell	186
7.3. Viscoelastic Die Swell	204
7.3.1. Swelling Ratio and Exit Pressure Correction Factor	206
7.3.2. Spline Profiles and Contour Plots	214
7.3.3. Mesh Refinement and Stress Components in the Vicinity of the Singularity	218
8. Conclusions	225
A. Jacobi Polynomials	229
B. Free Surface Governing Equations in Components	233
B.1. Semi-Discretised Weak Formulation in Components	233
B.2. Matrix Notation in Components	237

List of Figures

1.1.	Viscoelastic flow phenomena which differ vastly from Newtonian flow behaviour.	1
1.2.	Schematic diagram of the molecular deformation in the die swell experiment which causes the significant swell of the liquid jet. In a shear layer, near the wall inside the die, the molecules get stretched significantly. As soon as they approach the die exit and the shear free surface of the free liquid jet, they start to relax and recoil. This elastic recoil process causes a tension along the streamlines and the significant swelling of the liquid jet (MacMinn and McKinley, 2004).	2
2.1.	Reference frames and transformations.	13
2.2.	Stress and body force definition.	18
2.3.	Notation used for the stress tensor.	19
2.4.	Dumbbell model to describe dilute polymer solutions.	23
2.5.	Simple shear flow configuration.	29
2.6.	Steady Uniaxial Extensional Flow Configuration.	31
2.7.	Elongational viscosity predicted by Oldroyd-B model with unphysical singularity at $\dot{\epsilon} = \frac{1}{2\lambda}$	34
2.8.	Viscometric functions for the Giesekus model for a range of different α with $\lambda = 1$, $\eta_p = 0.5$ and $\eta_0 = 1$	36
2.9.	Free Surface Boundary Conditions	41
3.1.	Domain decomposition and mapping onto standard element.	49
3.2.	One-dimensional finite element expansion.	50
3.3.	Expansion sets for (a) the classical spectral element method and (b) the spectral/hp element method.	56
3.4.	Spectral/hp expansion set for $P = 3$ on a two dimensional quadrilateral element. The expansion modes can be decomposed into vertex, edge and interior modes and are formed by the tensor product of the one-dimensional expansion functions illustrated in Figure 3.3(b).	57
3.5.	Mapping between an element in physical space Ω_e and the standard element Ω_{st}	60
3.6.	Illustration of the integration over a generally shaped element.	63
3.7.	(a) Construction of globally continuous global modes Φ_g from elemental modes ϕ_{pq} by matching of corresponding boundary modes and (b) integration in the global region is the sum of the integration in the local regions (see Karniadakis and Sherwin (2005)).	69
3.8.	Schematic structure of the global matrix (see Karniadakis and Sherwin (2005) for further details).	70

3.9. Coupling of element Ω_e with neighbouring element Ω_{e_l} through upwind flux.	73
3.10. One dimensional advection of square wave on domain $\Omega = [0, 10]$ subdivided into 10 equally-sized elements.	77
3.11. Comparison of Galerkin projection for the Gaussian function of ((a), (b)) spectral/hp element method and ((c), (d)) linear finite element method for $DOF = 90$ and the corresponding L^2 and L^∞ error for increasing DOF ((e), (f)).	85
3.12. Comparison of Galerkin projection for the hat function of ((a), (b)) spectral/hp element method and ((c), (d)) linear finite element method for $DOF = 90$ and the corresponding L^2 and L^∞ error for increasing DOF ((e), (f)).	86
3.13. Comparison of Galerkin projection for the square wave function of ((a), (b)) spectral/hp element method and ((c), (d)) linear finite element method for $DOF = 90$ and the corresponding L^2 and L^∞ error for increasing DOF ((e), (f)).	87
3.14. Comparison of the numerical results for the advection equation after 30000 timesteps with $\Delta t = 10^{-4}$ using the continuous Galerkin method and the discontinuous Galerkin method for the spectral/hp element method for $P = 8, N_{el} = 10$ ((a), (b)) and the linear finite element method, i.e. $P = 1$, for $N_{el} = 45$ ((c), (d)) for the smooth Gaussian function and the L^2 and L^∞ error for increasing DOF ((e), (f)).	88
3.15. Comparison of the numerical results for the advection equation after 30000 timesteps with $\Delta t = 10^{-4}$ using the continuous Galerkin method and the discontinuous Galerkin method for the spectral/hp element method for $P = 8, N_{el} = 10$ ((a), (b)) and the linear finite element method, i.e. $P = 1$, for $N_{el} = 45$ ((c), (d)) for the hat function and the L^2 and L^∞ error for increasing DOF ((e), (f)).	89
3.16. Comparison of the numerical results for the advection equation after 30000 timesteps with $\Delta t = 10^{-4}$ using the continuous Galerkin method and the discontinuous Galerkin method for the spectral/hp element method for $P = 8, N_{el} = 10$ ((a), (b)) and the linear finite element method, i.e. $P = 1$, for $N_{el} = 45$ ((c), (d)) for the hat function and the L^2 and L^∞ error for increasing DOF ((e), (f)).	90
5.1. Schematics (a) and mesh configuration (b) for Poiseuille channel flow. . .	112
5.2. Comparison of numerical and analytical solution for $Wi = 1.0$ for increasing stabilisation parameter θ at point P_1 (a), (b) and point P_2 (c).	115
5.3. Comparison of analytical and numerical solution for a range of Weissenberg numbers.	116
5.4. Schematic diagram of flow around a cylinder.	120
5.5. Mesh for $N_{el} = 20$, (a) complete computational domain, (b) zoom of region around the cylinder.	122
5.6. Comparison of the dependence of the drag coefficient on Wi computed using the spectral/hp element method with results in the literature. Oldroyd-B fluid with $\beta = 0.59$	126

5.7.	Dependence of the evolution of the drag coefficient on P for (a) $Wi = 0.5$, (b) $Wi = 0.6$, (c) $Wi = 0.7$	127
5.8.	Profiles of τ_{xx} along centreline and cylinder surface for increasing Wi for $P = 14$	129
5.9.	Convergence of the profiles of τ_{xx} along the centreline and around the cylinder with P for (a) $Wi = 0.5$, (b) $Wi = 0.6$, and (c) $Wi = 0.7$	130
5.10.	Dependence of (a) u and (b) $u - u_N$ (the velocity shift with respect to the Newtonian velocity profile), on Wi along the downstream centreline. . . .	131
5.11.	Dependence of the pressure profiles on top of the cylinder on Wi . In the boundary layer near the cylinder the ratio of energy gradients, K , can be expressed as the ratio of the pressure gradient in the transverse and streamwise direction, which is given the inverse tangent of the angle γ depicted above. As this angle increases with increasing Wi , K increases with increasing Wi and therefore the tendency of the flow to develop an instability increases.	132
5.12.	Dependence of horizontal velocity u on top of the cylinder on Wi	133
5.13.	Dependence of (a) $u - u_N$ and (b) v on Wi along the shortest path from the top of the cylinder to the channel wall.	133
5.14.	Contour plots of pressure p (left) and velocity component u in x -direction (right) for $P = 18$ for an Oldroyd-B fluid.	135
5.15.	Contour plots of polymeric stress component τ_{xx} (left) and flow dependent normal stress S_2 (right) for an Oldroyd-B fluid.	136
5.16.	Contour plots of flow dependent shear stress S_1 (left) and flow dependent principal stress T for an Oldroyd-B fluid.	136
5.17.	Dependence of the drag coefficient on Wi and Re for $P = 14$	138
5.18.	Dependence on Re of the profiles of (a) τ_{xx} along the centreline and cylinder surface, (b) u along the downstream centreline,(c) $u - u_N$ along the downstream centreline for $P = 14$	139
5.19.	Dependence of (a) $u - u_N$ and (b) v on Re along the shortest path from the top of the cylinder to the channel wall for $Wi = 0.7$	140
5.20.	Dependence of transient viscometric functions on parameter α for a shear rate of $\dot{\gamma} = 10$ and $\dot{\gamma} = 5$ and an elongation rate of $\dot{\epsilon} = 1$ for $\beta = 0.59$ and $Wi = 0.7$	142
5.21.	Dependence of the drag coefficient on Wi and α for Giesekus fluid for $P = 14$	144
5.22.	Profile of τ_{xx} along symmetry line and cylinder surface for $Wi = 0.7$, $P = 14$ and increasing α	146
5.23.	Dependence of (a) u and (b) $u - u_N$ (the velocity shift with respect to the Newtonian velocity profile), on Wi along the downstream centreline. . . .	146
5.24.	Dependence of u on top of the cylinder on α for $Wi = 0.7$	147
5.25.	Dependence of (a) $u - u_N$ and (b) v on α along the shortest path from the top of the cylinder to the channel wall for $Wi = 0.7$	147
5.26.	Dependence of the pressure profile on top of the cylinder on α for $Wi = 0.7$. The pressure derivative in cross stream direction decreases with increasing α . This means for higher α , the flow field is more stable.	148

5.27. Dependence of the profiles of τ_{xx} along the centreline and around the cylinder on P for $Wi = 0.7$ for (a) $\alpha = 0.001$, (b) $\alpha = 0.01$ and (c) $\alpha = 0.1$	149
5.28. Contour plots for Giesekus fluid for different values of α : pressure p (left) and horizontal velocity component u (right) for $Wi = 0.7$ and $P = 18$	151
5.29. Contour plots for Giesekus fluid for different values of α : polymeric stress component τ_{xx} (left) and flow dependent normal stress S_2 (right) for $Wi = 0.7$, $P = 18$	152
5.30. Contour plots for Giesekus fluid for different values of α : flow dependent shear stress S_1 (left) and flow dependent principal stress T (right) for $Wi = 0.7$, $P = 18$	153
6.1. Cubic spline free surface representation.	161
7.1. Extrudate or die swell phenomenon for a Newtonian (a) and a viscoelastic fluid (b).	177
7.2. Schematic diagrams of (a) the re-entrant corner singularity between two walls, (b) the stick-slip problem and (c) the separation point between wall and free surface, which yield stress singularities.	178
7.3. Dependency of the smallest Newtonian eigenvalue on the angle θ of a corner singularity between no-slip/no-slip, no-slip/shear-free and slip/shear-free boundaries.	182
7.4. Schematics of the die swell flow configuration including boundary conditions.	183
7.5. Mesh configuration used for the Newtonian die swell computation.	186
7.6. Swell ratios for Newtonian fluid for $P = 10$ in comparison with Mitsoulis et al. (2012)	188
7.7. Free surface spline profiles for Newtonian extrudate swell for $P = 10$ for a range of Reynolds numbers.	194
7.8. Contour plots of horizontal velocity component u for $P = 10$ for a range of Reynolds numbers.	195
7.9. Contour plots of vertical velocity component v for $P = 10$ for a range of Reynolds numbers.	196
7.10. Dependency of velocity components along (a) the symmetry line and (b)- (c) along the free surface on the Reynolds number.	197
7.11. Velocity components in cross stream wise direction at inflow ($x = -10$), near the die exit ($x = -0.2$, $x = -0.2$), further downstream in the free jet region $x = 1$ and at outflow $x = 10$	198
7.12. Contour plots of pressure p for $P = 10$ for a range of Reynolds numbers.	199
7.13. Plots of pressure p along (a) the centreline and (b) the wall and the free surface.	200
7.14. Influence of P -mesh refinement on (a) the velocity components u , (b) v and (c) pressure p along the free surface and the increase of maximum and minimum values of the pressure at the singularity with increasing polynomial order (d).	201

7.15. Dependence of (a) velocity components u , (c) v and (e) pressure on the slip parameter for $P = 10$ and on mesh refinement for $B_{sl} = 0.01$ ((b),(d),(f))	202
7.16. Free surface spline profile for increasing slip parameter.	203
7.17. Computational meshes employed for the viscoelastic extrudate swell computations.	204
7.18. Comparison of geometries employed by (a) Crochet and Keunings (1982), (b) Tomé et al. (2002), (c) Russo and Phillips (2011) and (d) our computational domain.	210
7.19. Swelling Ratio (a) and exit pressure correction factor (b) for Oldroyd-B fluid in comparison with literature.	211
7.20. Comparison of (a) swelling ratio for Oldroyd-B, Oldroyd-B with slip along the wall and the Giesekus model and (b) values of recoverable shear, S_R , at the upstream wall determined from simple shear flow.	212
7.21. Dependency of exit pressure correction factor on the Weissenberg number for the Giesekus model (a) and plot of pressure values along the symmetry line for $P = 3$ for the Giesekus model (b) and the Oldroyd-B model (c).	213
7.22. Free surface spline profiles for the Oldroyd-B (a) and Giesekus model (b) for increasing Weissenberg number.	215
7.23. Contour plots of velocity components u (a)-(d) and v (e)-(f) for Oldroyd-B model for a range of Weissenberg numbers.	216
7.24. Contour plots of pressure p (a)-(b) and flow dependent shear stress S_1 (c)-(d), normal stress S_2 (e)-(f) for Oldroyd-B model for $Wi = 0.25, 0.5$	217
7.25. Dependence of pressure ((a), (c)) and polymeric stress τ_{xx} ((b),(d)) in the vicinity of the singularity on the polynomial order for $Wi = 0.1$ for the no-slip and slip boundary condition and the increase in magnitude of τ_{xx} with polynomial order (e).	220
7.26. Dependence of polymeric stress components τ_{xy} ((a), (c)) and τ_{yy} ((b),(d)) in the vicinity of the singularity on the polynomial order for $Wi = 0.1$ for the no-slip and slip boundary condition and their increase in magnitude with polynomial order (e),(f).	221
7.27. Numerical breakdown for (a) Mesh M1 for $P = 6$ at $Wi = 0.2$ and (b) Mesh M2 for $P = 3$ at $Wi = 0.35$	222
7.28. Dependency of the profiles of velocity component u , pressure p and the polymeric stress components on the Weissenberg number with slip along the wall and the increase of magnitude with increasing Weissenberg number for the polymeric stress components for no-slip and partial slip along the die wall.	223

List of Tables

5.1.	Dependence of maximum relative error at each overshoot and undershoot in percent on the stabilisation parameter θ	114
5.2.	Dependence of critical Weissenberg number yielding numerical breakdown on stabilisation parameter θ within the time interval $t \in [0, 100]$. . .	114
5.3.	Parameters for flow around a confined cylinder.	120
5.4.	Number of degrees of freedom for dependent variables and the distance of the closest quadrature point to the cylinder surface, h_q , on a mesh consisting of 20 elements for increasing polynomial order.	123
5.5.	Comparison of computed values of the drag coefficient for an Oldroyd-B fluid ($\beta = 0.59$) with results in the literature. (D) means computations diverge after an apparent converged drag value is reached.	125
5.6.	Computed values of the drag coefficient for an Oldroyd-B fluid for $0 \leq Wi \leq 1$ and $Re = 0.01, 0.1, 1$	138
5.7.	Minimum and maximum values for dependent variables for $P = 18$ and $Wi = 0.7$ for $Re = \{0.01, 0.1, 1\}$	138
5.8.	Comparison of drag coefficients for the Giesekus fluid for different values of α	143
5.9.	Minimum and maximum values of the polymeric stress components for the Giesekus model for $P = 18, Wi = 0.7$	145
7.1.	Newtonian swelling ratios for $Re = 0$	187
7.2.	Comparison of Newtonian die swell ratio for increasing Reynolds number with Mitsoulis et al. (2012).	189
7.3.	Comparison of swell ratios and exit pressure corrections for increasing number of degrees for freedom (DOF) between our algorithm and that of Taliadorou et al. (2007).	192
7.4.	Dependence of the swelling ratio on P for $B_{sl} = 0.1$ and $B_{sl} = 0.01$. . .	193
7.5.	Dependency of swelling ratio on mesh refinement for the Oldroyd-B model.	219
7.6.	Dependency of swelling ratio on mesh refinement in mesh M1 for the Oldroyd-B model with slip along the wall $B_{sl} = 0.1$	222

Chapter 1

Introduction

1.1. Viscoelastic Phenomena



(a) Weissenberg effect (McKinley, 2008). (b) Die swell in Newtonian and polymeric liquids (YouTube, Psidot (2007)).

Figure 1.1.: Viscoelastic flow phenomena which differ vastly from Newtonian flow behaviour.

Viscoelastic fluids exhibit both viscous and elastic characteristics when undergoing deformations. Figure 1.1 shows two of the most fascinating macroscopic phenomena observed for viscoelastic fluids: the Weissenberg effect and the die-swell effect. The Weissenberg effect (Figure 1.1(a)) can be observed when a rotating rod is inserted into a beaker filled with a viscoelastic liquid. In a Newtonian fluid, the rotating motion generates a centrifugal force which pushes the liquid outward and the free surface dips near the rod. In contrast, in viscoelastic fluids, the free surface rises and the fluid climbs up the rod. The die-swell effect can be observed when a fluid is forced out of a die. The jet of exiting liquid expands radially to a diameter greater than that of the orifice. For Newtonian fluids, we observe a small increase in diameter while for viscoelastic liquids, the exiting jet can swell up to a radius of two times the die radius (Figure 1.1(b)). Such viscoelastic effects originate from the deformation of large molecular chains within the fluid. A schematic diagram of the deformation of the molecular chains and their impact on the macroscopic flow in the die

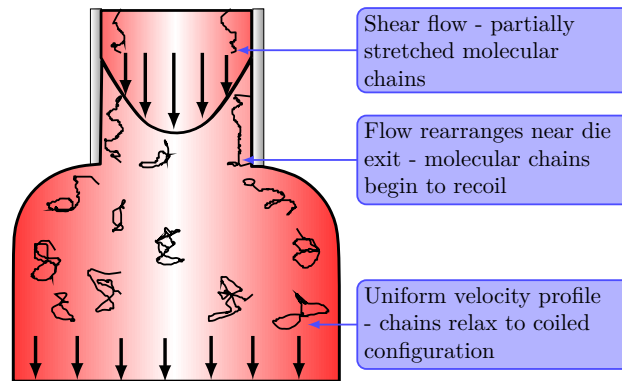


Figure 1.2.: Schematic diagram of the molecular deformation in the die swell experiment which causes the significant swell of the liquid jet. In a shear layer, near the wall inside the die, the molecules get stretched significantly. As soon as they approach the die exit and the shear free surface of the free liquid jet, they start to relax and recoil. This elastic recoil process causes a tension along the streamlines and the significant swelling of the liquid jet (MacMinn and McKinley, 2004).

swell experiment is shown in Figure 1.2.

In fact, viscoelastic effects can be observed in any flow involving fluids with complex microstructures. In industrial processes, many fluids such as engine oils, gels and paints exhibit these properties. Being able to adequately understand and model viscoelasticity is therefore of prime interest for the optimisation of these processes.

1.2. Challenges in the Numerical Solution of Viscoelastic Flows

The flow of a viscoelastic fluid can be described mathematically using the conservation of mass and momentum and a relationship between the stress and rate-of-deformation. This relationship is called the constitutive equation and it is used to differentiate one material from another. As the molecular structure of each complex liquid differs vastly from one material to the other, there is no general constitutive equation to describe all viscoelastic materials. Therefore, a large number of models have been developed over the last few decades to understand and predict the behaviour of viscoelastic liquids (for an overview see e.g. Bird et al. (1987a,b)). These models are either phenomenological, meaning that they assume the local stress/deformation relationship from macroscopic observations of simple flows, or based on homogenisation principles, whereby the stress/deformation law is obtained from statistical averaging of the microscopic behaviour of the molecular chains or a combination of both approaches.

Choosing, identifying and validating a mathematical model for a specific viscoelastic material is still an open issue. In general, the mathematical models are fitted to experimental data obtained for a viscoelastic fluid undergoing pure shear or elongational deformations (see e.g. Tanner (2002), Macosko (1994)). Additionally, these so-called viscometric flows have the advantage of having some analytical results available. However, the main bottleneck in rheology is the extension of this identification and validation to complex flows, for which no analytical results are available. Numerical methods can help tackle this issue, by providing the missing link between model and macroscopic prediction for complex flows. The first challenge in the numerical simulation of viscoelastic flows is to choose the right numerical techniques in order to solve the system of equations describing viscoelastic flows, which are of mixed type: the conservation of mass and momentum are of elliptic/parabolic type and the constitutive equation is hyperbolic (Gerritsma (1996); Owens and Phillips (2005)). This choice includes the implementation of appropriate stabilisation techniques. The two main categories of stabilisation techniques for this system of equations are: (i) stabilisation techniques that enhance the elliptic operator in the momentum equation and (ii) upwinding techniques for the solution of the hyperbolic constitutive equation.

The success of techniques that enhance the ellipticity in the momentum equation arises from the explicit form of the viscous operator in the momentum equation, which results in solving an elliptic saddle point problem. For viscoelastic liquids this viscous term is scaled with the ratio of Newtonian to total viscosity. As we are often interested in flow configurations with dominant viscoelastic effects, the ratio of Newtonian to total viscosity is chosen to be small. In these cases the elastic stress contribution can dominate the viscous term and this can lead to instabilities. The more dominant the viscous term is in the equation, relative to the elastic stress contribution, the better the performance of the method. The idea of introducing ellipticity through a change of variables was first employed in the elastic viscous split stress (EVSS) formulation, introduced by Perera and Walters (1977), Mendelson et al. (1982) for second order fluids and extended to viscoelastic liquids by Beris et al. (1984). In the EVSS scheme, we perform a change of variables to the stress variable. Later, Sun et al. (1996) introduced the adaptive viscoelastic stress split (AVSS) scheme, in which the viscosity in the change of variables is adapted according to the flow configuration. Brown et al. (1993) used the velocity gradient tensor as an additional unknown, instead of using the rate of deformation tensor. leading to what is known as the EVSS-G method. However, the change of variables performed in EVSS-type methods introduces the upper-convected derivative of the rate of deformation tensor, which includes second order derivatives of the velocity and therefore poses challenges in the implementation of C^0 continuous approximation spaces. Therefore, Guénette and Fortin (1995) introduced the discrete EVSS (DEVSS) method, in which no change of vari-

ables is required and the viscous term is introduced into the momentum equation only in an approximate sense using the numerical approximations. The discrete splitting method essentially adds and subtracts two different approximations of the same viscous contribution to increase the viscous contribution in the momentum equation that comes from the Newtonian viscosity. In the limit where these approximations are exact, the added terms cancel, giving the original equation. In analogy to the EVSS-G method, the DEVSS-G method (Liu et al. (1998)) may be defined, where a projection of the velocity gradient tensor is made instead of the rate of deformation tensor Sun et al. (1999) introduced the DAVSS-G formulation in analogy to the AVSS formulation employing an adaptive stabilisation viscosity that differs from element to element depending on the flow properties in an element. An overview over these methods can be found in Baaijens (1998) and Owens and Phillips (2005).

Choosing suitable upwinding techniques such as streamline upwind/ Petrov-Galerkin (SUPG, Brooks and Hughes (1982)) or discontinuous Galerkin methods (Lesaint and Raviart (1974)) to discretise the hyperbolic constitutive equation can enhance the stability of the computations significantly. The SUPG method, first applied to viscoelastic flows by Marchal and Crochet (1987), is applied to the constitutive equation by replacing the test functions ϕ with $\phi + \gamma \nabla \phi$. Here, γ is an upwind factor dependent on the characteristic length-scale of an element and a characteristic velocity of the flow. However, the SUPG method may produce oscillatory stress fields at steep stress boundary layers or near singularities. Another possibility to account for the hyperbolic nature of the constitutive equation is the discontinuous Galerkin method which was first applied to viscoelastic flows by Fortin and Fortin (1989). An overview over these stabilisation techniques and their appropriate combination can be found in Baaijens (1998) and Owens and Phillips (2005).

Even though these stabilisation techniques improve the stability of the numerical solution, all numerical algorithms which solve viscoelastic flows face one big outstanding issue: the so-called high Weissenberg number problem (HWNP). To date, all numerical schemes breakdown above a certain value of the Weissenberg number, which is a non-dimensional measure for the elasticity of the fluid. This critical Weissenberg number depends on a number of factors: the geometrical complexity of the flow; the chosen viscoelastic model; other characteristic numbers of the flow such as the Reynolds number and on the computational mesh.

Indeed, the attainable Weissenberg number is often seen to decrease with mesh refinement (see e.g. Keunings (1986)). Keiller (1992) identified a mesh-ratio dependent instability criterion in the time-dependent simulation of planar Couette flow for the upper-convected Maxwell, Oldroyd-B and FENE equations, $Wi_{\text{crit}} \sim \left(\frac{\Delta y}{\Delta x} \right)$, where Δx and Δy are the

resolution scales of the computational grid in the streamwise and cross-stream directions, respectively. Further evidence of the dependence of the critical Weissenberg number on the grid size ratio was given by Sureshkumar et al. (1999) and Smith et al. (2000), who observed the same dependence of the critical Weissenberg number on the aspect ratio $\Delta y/\Delta x$ in transient calculations of a flow around a cylinder of an Oldroyd-B fluid.

Another critical mesh dependent factor was discovered by Fattal and Kupferman (2004, 2005) who identified a stability criterion dependent on the mesh-size Δx . They demonstrated that Δx has to be chosen very small in areas of the flow where convection is weak and the deformation rate is high. Such areas include regions near stagnation points or near geometric singularities. The stability criterion arises from the fact that the combination of the rate of deformation of the fluid and convection of the fluid particles gives rise to steep exponential stress profiles which are poorly approximated by polynomial interpolation. Therefore, Fattal and Kupferman (2004, 2005) proposed to reformulate the constitutive equation in terms of the logarithm of the stress tensor. However, the logarithm of the stress tensor may not always exist as its strict positive definiteness cannot be guaranteed. Therefore, we take the logarithm of a physical quantity related to the stress tensor that preserves positive definiteness: the conformation tensor \mathbf{c} , which is a dimensionless measure for the deformation. Fattal and Kupferman (2004, 2005) called the change of variables $\boldsymbol{\psi} = \log(\mathbf{c})$ and the resulting equations the log-conformation representation.

Another factor putting severe restriction on the success of numerical simulations for higher Weissenberg numbers is the difficulty of resolving thin stress boundary layers near solid boundaries and near corner singularities which feature steep stress gradients (Renardy, 2000). For example, for no-slip boundaries, the velocity and all its tangential derivatives vanish at the wall and therefore the convective terms disappear at the wall. However, these terms enter the force balance at a very short distance from the wall. This transition from viscometric shear flow behaviour near the wall boundary to a convection dominated region away from the wall yields a substantially different stress behaviour in a thin layer near the wall. Renardy (2000) demonstrated that the thickness of this boundary layer decreases with increasing Weissenberg number. For the upper convected Maxwell model the boundary layer thickness is of order Wi^{-1} , for the Phan-Thien Tanner model (PTT), it is of order $Wi^{-1/3}$, and for the Giesekus model, it is of order $Wi^{-1/2}$. This means the boundary layer for the PTT and the Giesekus models sharpen much less rapidly with increasing Weissenberg number than the upper convected Maxwell model. In fact, numerical simulations using the PTT and the Giesekus models seem indeed to achieve stable results for much higher Weissenberg numbers than the ones using the upper convected Maxwell model.

In addition to the thin stress boundary layers, the numerical solution of viscoelastic flows in domains involving corner singularities is very challenging. At corner singularities the

stress values become infinite yielding high approximation errors at the singularity. This discretisation error can then be propagated downstream due to the hyperbolic nature of the constitutive equations (Owens and Phillips, 2005). This propagated error can grow downstream causing large scale oscillations in the solution. Fontelos and Friedman (2000) observed a downstream growth of the error for the Oldroyd-B model for a no-slip re-entrant corner singularity. However, for the PTT model, Renardy (1997) did not observe any downstream growth of errors. The reason for this might be that the boundary layers in the PTT model have a different scaling and are much broader than in the Oldroyd-B model. As a result, for particles which enter the boundary layer, the stress relaxation takes over before the downstream instability has had a chance to fully manifest itself.

1.3. About this Thesis

In this thesis, we propose a numerical technique that allows us to capture local effects such as the thin stress boundary layers near walls or the stress concentrations in the vicinity of geometrical singularities mentioned above. Resolving these fast variations of the fields in space and time is important for two reasons (i) they affect the quantity of interest of the computation (e.g. the drag force around an object in a channel, or the swelling ratio in the die swell experiment) and (ii) they are commonly believed to be associated with the numerical breakdown of the computation (see explanations above). Additionally, we want to apply this numerical technique to viscoelastic flows in arbitrary geometries including viscoelastic flows with free surfaces.

In the literature, the vast majority of numerical investigations concerning complex viscoelastic flows rely on the finite element method, finite differences and finite volume methods (Owens and Phillips, 2005). These low-order methods have the advantage of being easy to implement, well-understood, geometrically flexible and, in the case of viscoelasticity, to have a filtering effect which tends to stabilise the problem. However, if steep boundary layers have to be resolved, the associated numerical costs can become tremendous.

On the other end of the spectrum, spectral methods propose the use of higher-order polynomial expansions, which allows for high resolution and accuracy of limited numerical cost, at least for smooth problems. The main drawback is their relative lack of geometrical flexibility and their challenging implementation. Recently, the spectral/hp element method (Karniadakis and Sherwin, 2005) has been developed in order to guarantee both spectral convergence, and geometric flexibility by allowing the use of quadrilateral and triangular elements.

1.3.1. Numerical Method

In order to resolve the boundary regions without prohibitive numerical cost, we will adapt the spectral/hp method (Karniadakis and Sherwin, 2005) to the computation of complex viscoelastic flows. Our numerical scheme is based on the popular decoupled approach to split the formulation into the solution of the conservation equations for velocity-pressure and the computation of the constitutive equation for the polymeric stress. The method is stabilised using a discontinuous Galerkin method for the constitutive equation in space in combination with the DEVSS-G (Liu et al., 1998) method to enhance the ellipticity of the moment equation. A continuous approximation is employed for the velocity and discontinuous approximations for pressure, velocity gradient and polymeric stress. This is the first time such coupling between a spectral element method and the DEVSS-G/DG method is proposed for the accurate and robust prediction of complex viscoelastic free surface flows. The free surface is traced using an arbitrary Lagrangian Eulerian technique (ALE).

1.3.2. Validation and Results

We first demonstrate the capabilities and limitations of the spectral/hp element method in comparison to the finite element method by investigating the approximation error for different functions using Galerkin projection and one-dimensional constant linear advection. We examine three functions with decreasing smoothness and demonstrate the advantages of the discontinuous Galerkin discretisation over the continuous Galerkin discretisation for the one dimensional advection.

Then, we validate our DEVSS/DG algorithm on the transient Poiseuille channel flow of an Oldroyd-B fluid, for which we know the analytical solution. This simple time-dependent flow does not exhibit the previously mentioned steep boundary layers, but features fast variations in time, which will help us demonstrate the efficiency and robustness of the proposed method and the impact of the stabilisation measures on the accuracy of the method. Furthermore, we test the method on two complex flow examples. The flow around the cylinder of Oldroyd-B and Giesekus fluids and the extrudate swell of Newtonian, Oldroyd-B and Giesekus fluids including no-slip and slip boundary conditions inside the die.

The flow around a cylinder features the formation of thin boundary layers with steep stress gradients around the cylinder and the formation of a thin birefringent strand in the wake behind the cylinder. We explore the influence of Wi on the drag coefficient and the flow profiles along the centreline, around the cylinder and in the gap between the cylinder surface and the channel walls for the Oldroyd-B model for $Re = \{0, 0.01, 0.1, 1\}$ and for the Giesekus model for $\alpha = \{0.001, 0.01, 0.1\}$. We observe oscillations in the convergence of the drag coefficient for $Wi \geq 0.6$ on finer meshes for the Oldroyd-B model. To find

a possible explanation for the onset of this instability, we interpret the results by means of the theory of Dou and Phan-Thien (2007). In this theory the onset of the instability is explained in terms of a velocity inflection on top of the cylinder which leads to oscillations in the shear layer which are then transported downstream into the cylinder wake. We demonstrate that the velocity and pressure profiles in the gap between the top of the cylinder and the channel wall show a clear tendency for the formation of a velocity inflection with increasing Wi when particles leave the shear layer near the cylinder. In summary, we identify three distinct regimes. In the first regime ($Wi \leq 0.6$), the flow is stable and convergent values of the drag coefficient are obtained. Excellent agreement is obtained across a wide range of numerical schemes. In the second regime ($Wi \in [0.6, 1]$), there is a transition to an oscillatory flow near the rear stagnation point. Steady state values of the drag can be determined provided the mesh is not too fine. For a given mesh, a convergent steady state approximation is obtained. However, there is a lack of convergence with mesh refinement. In the third regime ($Wi > 1$), the flow becomes unstable and numerical schemes fail to converge. The evidence that such a transient regime can be predicted by numerical simulations becomes more and more apparent with the enhancement of numerical algorithms and the use of high-resolution meshes. Oliveira and Miranda (2005) find a time-dependent regime featuring a recirculation zone at the rear of the cylinder for a FENE-CR fluid for $Wi \approx 1.3$ for an extensibility parameter of $L^2 = 144$ with their finite volume method on highly refined meshes. We discover a qualitatively similar behaviour for the Oldroyd-B model for $Wi \gtrsim 0.62$. However, the numerical cost of our scheme to reveal this transient regime is significantly lower than the cost for the finite volume and finite element schemes, which require the use of high performance computers.

Last, we will try to extend this success to the die swell problem. This example requires the development of a free surface algorithm, which needs to be developed consistently with the spectral/hp method. The extrudate swell problem features a stress singularity at the die exit and boundary layers at the wall near the die exit and near the free surface boundary. The validity and efficiency of the free surface algorithm will be shown in the Newtonian case. In the case of viscoelastic die-swell however, unstable modes originating from the corner singularity prevent us from obtaining the accurate and stable results that would have been expected. We will however provide some partial results, which conform to the literature.

In more detail, we consider the swelling ratio and the exit pressure loss for Newtonian fluids in the die swell problem and investigate the impact of inertia on the swelling ratio for Reynolds numbers ranging from 0 to 100. We obtain excellent agreement with the results in the literature for a much smaller number of degrees of freedom, which demonstrates that p -refinement is effective for the Newtonian extrudate swell even though the result is polluted by Gibbs oscillations in the pressure around the singularity. However, these

Gibbs oscillations in the pressure stay confined to elements adjacent to the singularity. We demonstrate that the Gibbs oscillations disappear when the slip condition is employed along the die wall and mesh convergence is significantly improved.

For viscoelastic flows, the simulation of the extrudate swell problem becomes very difficult. Discretisation errors originating at the singularity can be convected downstream. Indeed, we find that the extrudate swell computations could only be successfully performed for a very narrow range of parameters and success is highly dependent on the mesh configuration. However, for meshes with low polynomial order $P = 3$, we obtain swelling ratios up to 2.067 for $Wi = 0.85$. This result agrees with those in the literature. For an increase in the polynomial order, the numerical algorithm breaks down at a much lower Weissenberg number due to oscillations on the free surface boundary. These oscillations originate at the singularity and are convected downstream. We attempt to alleviate the problem associated with the singularity using the slip condition along the die wall. Even though this seems to cure the break down of the computation with mesh refinement for the tested polynomial orders, the computations breakdown at $Wi = 0.6$ even for the coarsest mesh. We explore possible reasons for the breakdown using a range of contour plots and plots of the dependent variables in the vicinity of the singularity.

1.3.3. Outline

This thesis is outlined as follows

Chapter 2 We present the equations which describe the motion of viscoelastic fluids. First, we introduce the description of a fluid flow in different reference frames including the Eulerian, Lagrangian and arbitrary Lagrangian-Eulerian frames. Second, we derive the equations for the conservation of mass and momentum in these different reference frames. Then, we introduce a range of constitutive equations relating the stress tensor to the rate of deformation including the Oldroyd-B and Giesekus models. Furthermore, we investigate the Oldroyd-B and Giesekus model in steady shear flow and in steady uniaxial extensional flow. Subsequently, to complete the description of the governing equations, we give a detailed overview of different boundary conditions. Finally, we present the weak formulation of the governing equations in their dimensionless form.

Chapter 3 We review several numerical methods for solving partial differential equations including the finite element method, spectral methods and spectral/hp element methods. Then, we present details about the spectral/hp element method employed in this thesis. We introduce integration and differentiation on general shaped elements including the isoparametric geometrical mapping and we give their corresponding matrix notations. In this work, we employ the spectral/hp element method to solve the equations describing viscoelastic flow. Then, we discuss the continuous Galerkin and the discontinuous Galerkin

methods to couple the spectral elements. Finally, we demonstrate the capabilities and the limitations of the spectral/hp element method in comparison to the finite element method for one-dimensional constant linear advection for three functions with decreasing smoothness.

Chapter 4 We present the spatial and temporal approximations used in this thesis to solve the weak formulation of the governing equations for viscoelastic flow. We review upwinding stabilisation techniques for hyperbolic problems and elastic viscous split stress techniques to enhance the ellipticity of the momentum equation. We use a continuous approximation space for the velocity field and discontinuous approximation spaces for the stress tensor, velocity gradient projection tensor and pressure. We introduce the first order explicit Euler and second order BDF2/EX2 time integration schemes and we detail the DEVSS-G/DG algorithm used to solve the governing equations for fixed computational meshes. Finally, we describe the solution procedure employed to solve the discrete coupled system of velocity and pressure using the multi-static condensation technique and the discontinuous Galerkin method used to compute the polymeric stress.

Chapter 5 We demonstrate the performance and accuracy of our algorithm for the unsteady Poiseuille flow of an Oldroyd-B fluid, for which an analytical solution exists, and the flow around a cylinder for the Oldroyd-B model for $Re = \{0, 0.01, 0.1, 1\}$ and for the Giesekus model for $\alpha = \{0.001, 0.01, 0.1\}$.

Chapter 6 We introduce the DEVSS-G/DG formulation in the ALE framework. Then, we discuss the details of the algorithm used to move the mesh in order to trace the free surface boundary movement. We employ a cubic spline representation of the free surface boundary in order to guarantee the smoothness of the free surface to obtain continuous normals and curvature across several spectral elements. Then, we discuss the algorithm used to solve the discrete coupled system for the velocity, pressure and velocity gradient projection tensor and the discretised constitutive equation.

Chapter 7 We investigate the performance of the ALE-algorithm in simulating the extrudate swell phenomenon for Newtonian fluids including the impact of inertia and slip along the die wall and for Oldroyd-B and Giesekus fluids including no-slip and slip along the die wall.

Chapter 8 We draw some conclusions from our investigations and propose further developments of the algorithm.

Chapter 2

Mathematical Description of Viscoelastic Flows

In this Chapter, we present the equations which describe the motion of viscoelastic fluids. First, we introduce the description of a fluid flow in different reference frames including the Eulerian, Lagrangian and arbitrary Lagrangian-Eulerian frames. Second, we derive the equations for the conservation of mass and momentum in these different reference frames. Then, we introduce a range of constitutive equations relating the stress tensor to the rate of deformation including the Oldroyd-B and Giesekus models. Furthermore, we investigate the Oldroyd-B and Giesekus models in steady shear flow and in steady uniaxial extensional flow. Subsequently, to complete the description of the governing equations, we give a detailed overview of different boundary conditions. Finally, we present the weak formulation of the governing equations in their dimensionless form. This Chapter is based on Claus (2008), Owens and Phillips (2005), Donea et al. (2004), Scovazzi and Hughes (2007) and Pena (2009).

2.1. Kinematic Description of the Flow in Different Reference Frames

2.1.1. Eulerian and Lagrangian Flow Descriptions

In fluid dynamics, the flow of a liquid is usually described either by a fixed observer, who observes the flow in terms of the flow velocity $\mathbf{u}(\mathbf{x}, t)$ in a spatial domain with spatial points \mathbf{x} over time t , which is called the Eulerian description; or by an observer, who follows a fluid particle \mathbf{X} through time. We call reference frames that follow material particles the *material or Lagrangian reference frame*.

The two reference frames can be related as follows. Consider a domain Ω_{t_0} at time $t = t_0$ filled with fluid particles at positions \mathbf{X} . To describe the trajectory of the particles, we

consider a family of mappings

$$\begin{aligned}\mathcal{L}_t : \Omega_{t_0} &\rightarrow \Omega_t, \quad \forall t \geq 0, \\ \mathbf{X} &\mapsto \mathbf{x}(\mathbf{X}, t) = \mathcal{L}_t(\mathbf{X}), \quad \forall \mathbf{X} \in \Omega_{t_0}.\end{aligned}\quad (2.1)$$

Here, \mathbf{x} represents the current position of an infinitesimal material particle originally at \mathbf{X} . The domain Ω_t and Ω_{t_0} are referred to as the *current* and the *original* or *reference* configuration, respectively. Note that, \mathcal{L}_t is a Lagrangian to Eulerian map. The velocity of a material particle identified by the Lagrangian coordinate \mathbf{X} , or *material velocity*, is defined as the increment in position per unit time

$$\mathbf{u}(\mathbf{x}, t) = \left. \frac{\partial \mathbf{x}(\mathbf{X}, t)}{\partial t} \right|_{\mathbf{X}} = \left. \frac{\partial \mathcal{L}_t(\mathbf{X})}{\partial t} \right|_{\mathbf{X}}. \quad (2.2)$$

The *deformation gradient tensor*, \mathbf{F} and the *Jacobian determinant*, J , are defined as

$$\mathbf{F} = \nabla_{\mathbf{X}} \mathcal{L}_t(\mathbf{X}) = \frac{\partial \mathbf{x}}{\partial \mathbf{X}}, \quad (2.3)$$

$$J = \det(\mathbf{F}). \quad (2.4)$$

Consider a scalar function $f : \Omega_t \times [t_0, T] \rightarrow \mathbb{R}$ defined in the Eulerian frame. Then, the Lagrangian or *material time derivative* of this function in the Eulerian frame is given by

$$\frac{Df(\mathbf{x}, t)}{Dt} := \left. \frac{\partial f(\mathbf{x}, t)}{\partial t} \right|_{\mathbf{x}} = \left. \frac{\partial f(\mathbf{x}(\mathbf{X}, t), t)}{\partial t} \right|_{\mathbf{X}} = \left. \frac{\partial f}{\partial t} \right|_{\mathbf{x}} + \left. \frac{\partial \mathcal{L}_t(\mathbf{X})}{\partial t} \right|_{\mathbf{X}} \cdot \nabla_{\mathbf{x}} f = \left. \frac{\partial f}{\partial t} \right|_{\mathbf{x}} + \mathbf{u} \cdot \nabla_{\mathbf{x}} f \quad (2.5)$$

Here, we used the chain rule. Therefore, the *acceleration* of a material particle in the Eulerian frame is given by

$$\mathbf{a}(\mathbf{x}, t) = \left. \frac{\partial \mathbf{u}(\mathbf{x}, t)}{\partial t} \right|_{\mathbf{x}} = \left. \frac{\partial \mathbf{u}}{\partial t} \right|_{\mathbf{x}} + \mathbf{u} \cdot \nabla_{\mathbf{x}} \mathbf{u}. \quad (2.6)$$

2.1.2. Arbitrary Lagrangian-Eulerian Flow Description

In computational methods, we can distinguish between Lagrangian algorithms in which the computational mesh nodes follow the associated material parameter during motion and Eulerian algorithms in which the mesh is fixed and the fluid moves with respect to the grid. Lagrangian algorithms allow one to track the movement of interfaces and free surfaces between different materials very easily and accurately. However, the computational mesh becomes very distorted for large deformations and frequent remeshing becomes necessary in order to guarantee the accuracy and stability of the algorithm. Eulerian algorithms on the other hand can cope with large material deformations but interfaces and small flow details

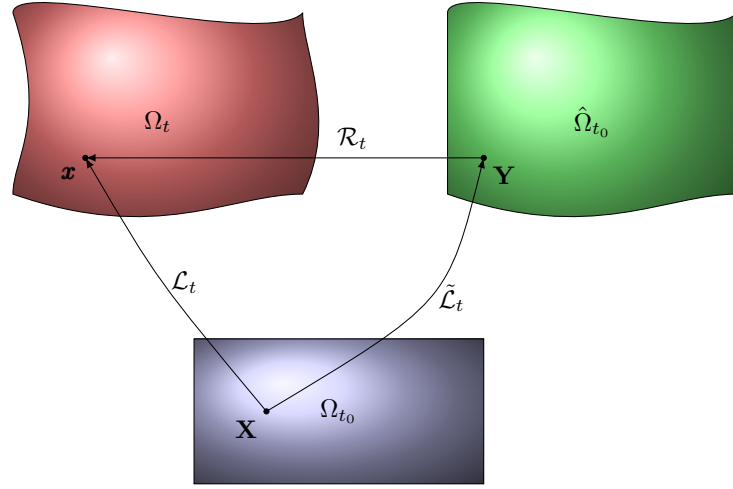


Figure 2.1.: Reference frames and transformations.

cannot be captured very precisely. In order to overcome some of these shortcomings and to incorporate the strengths of both descriptions, we can employ computational methods in which the mesh follows the flow in an arbitrary fashion using reference frames which are neither fixed in space nor attached to the material. These computational algorithms are called *arbitrary Lagrangian-Eulerian (ALE)* algorithms. This description gives rise to a third reference frame associated to the mesh motion, which we term the *referential frame*. The referential frame can be related to the Eulerian and the Lagrangian frame through the following mappings. First, we consider the parametrized family of diffeomorphisms relating the referential frame to the Eulerian frame:

$$\begin{aligned} \mathcal{R}_t : \hat{\Omega}_{t_0} &\rightarrow \Omega_t, \quad \forall t \geq 0, \\ \mathbf{Y} &\mapsto \mathbf{x}(\mathbf{Y}, t) = \mathcal{R}_t(\mathbf{Y}), \quad \forall \mathbf{Y} \in \hat{\Omega}_{t_0}. \end{aligned} \quad (2.7)$$

Here, the points \mathbf{Y} are usually associated with the positions of the nodes of the computational mesh. The mapping \mathcal{R}_t is called the *ALE map*. Now, we can define the velocity of the mesh (or *mesh-velocity*) in the Eulerian frame as

$$\mathbf{w} := \left. \frac{\partial \mathbf{x}(\mathbf{Y}, t)}{\partial t} \right|_{\mathbf{Y}} = \left. \frac{\partial \mathcal{R}_t(\mathbf{Y})}{\partial t} \right|_{\mathbf{Y}}. \quad (2.8)$$

This gives the velocity of the "mesh particles" in the Eulerian frame. In addition, the *mesh deformation gradient tensor* and the *mesh Jacobian determinant* are defined as

$$\hat{\mathbf{F}} = \nabla_{\mathbf{Y}} \mathcal{R}_t(\mathbf{Y}) = \frac{\partial \mathbf{x}}{\partial \mathbf{Y}}, \quad (2.9)$$

$$\hat{J} = \det(\hat{\mathbf{F}}). \quad (2.10)$$

Considering a scalar function $f : \Omega_t \times [t_0, T] \rightarrow \mathbb{R}$ defined in the Eulerian frame, the *referential time derivative* of this function in the Eulerian frame is given by

$$\left. \frac{\partial f(\mathbf{x}, t)}{\partial t} \right|_{\mathbf{Y}} = \left. \frac{\partial f(\mathbf{x}(\mathbf{Y}, t), t)}{\partial t} \right|_{\mathbf{Y}} = \left. \frac{\partial f}{\partial t} \right|_{\mathbf{x}} + \left. \frac{\partial \mathcal{R}_t(\mathbf{Y})}{\partial t} \right|_{\mathbf{Y}} \cdot \nabla_{\mathbf{x}} f = \left. \frac{\partial f}{\partial t} \right|_{\mathbf{x}} + \mathbf{w} \cdot \nabla_{\mathbf{x}} f \quad (2.11)$$

Finally, it is also important to consider the Lagrangian-to-referential transformation, which tracks the motion of the referential frame, observed from the Lagrangian reference frame,

$$\begin{aligned} \tilde{\mathcal{L}}_t : \Omega_{t_0} &\rightarrow \hat{\Omega}_{t_0}, \quad \forall t \geq 0, \\ \mathbf{X} &\mapsto \mathbf{Y}(\mathbf{X}, t) = \tilde{\mathcal{L}}_t(\mathbf{X}), \quad \forall \mathbf{X} \in \hat{\Omega}_{t_0}. \end{aligned} \quad (2.12)$$

The previous map has to be interpreted as the following composition:

$$\tilde{\mathcal{L}}_t = \mathcal{R}_t^{-1} \circ \mathcal{L}_t. \quad (2.13)$$

The velocity of the referential frame observed from the Lagrangian frame (i.e. the velocity of a material particle relative to the moving mesh "particles") is

$$\tilde{\mathbf{v}} := \left. \frac{\partial \mathbf{Y}(\mathbf{X}, t)}{\partial t} \right|_{\mathbf{X}} = \left. \frac{\partial \tilde{\mathcal{L}}_t(\mathbf{X})}{\partial t} \right|_{\mathbf{X}}. \quad (2.14)$$

Now, consider a scalar function $f : \hat{\Omega}_{t_0} \times [t_0, T] \rightarrow \mathbb{R}$ defined in the referential frame. Using the chain rule, we obtain

$$\left. \frac{\partial f(\mathbf{Y}, t)}{\partial t} \right|_{\mathbf{X}} = \left. \frac{\partial f(\mathbf{Y}(\mathbf{X}, t), t)}{\partial t} \right|_{\mathbf{X}} = \left. \frac{\partial f}{\partial t} \right|_{\mathbf{Y}} + \left. \frac{\partial \tilde{\mathcal{L}}_t(\mathbf{X})}{\partial t} \right|_{\mathbf{X}} \cdot \nabla_{\mathbf{Y}} f = \left. \frac{\partial f}{\partial t} \right|_{\mathbf{Y}} + \tilde{\mathbf{v}} \cdot \nabla_{\mathbf{Y}} f. \quad (2.15)$$

Applying this relationship to $\mathbf{x}(\mathbf{Y}, t) = \mathcal{R}_t(\mathbf{Y})$ yields

$$\mathbf{u} = \mathbf{w} + \hat{\mathbf{F}} \tilde{\mathbf{v}}, \quad (2.16)$$

which can be recast as

$$\mathbf{c} := \hat{\mathbf{F}} \tilde{\mathbf{v}} = \mathbf{u} - \mathbf{w}, \quad (2.17)$$

where \mathbf{c} is termed *convective velocity*, the difference between material and mesh velocity. We can obtain an alternative expression for the material time derivative by combining (2.5) and (2.11)

$$\frac{Df(\mathbf{x}, t)}{Dt} = \left. \frac{\partial f(\mathbf{x}, t)}{\partial t} \right|_{\mathbf{X}} \quad (2.18)$$

$$\stackrel{(2.5)}{=} \left. \frac{\partial f}{\partial t} \right|_{\mathbf{x}} + \mathbf{u} \cdot \nabla_{\mathbf{x}} f \quad (2.19)$$

$$\stackrel{(2.11)}{=} \left. \frac{\partial f}{\partial t} \right|_{\mathbf{Y}} - \mathbf{w} \cdot \nabla_{\mathbf{x}} f + \mathbf{u} \cdot \nabla_{\mathbf{x}} f. \quad (2.20)$$

This means the acceleration of a fluid particle can be expressed as

$$\mathbf{a}(\mathbf{x}, t) = \left. \frac{\partial \mathbf{u}(\mathbf{x}, t)}{\partial t} \right|_{\mathbf{X}} = \left. \frac{\partial \mathbf{u}}{\partial t} \right|_{\mathbf{Y}} + (\mathbf{u} - \mathbf{w}) \cdot \nabla_{\mathbf{x}} \mathbf{u}. \quad (2.21)$$

2.2. Conservation Laws

The motion of every fluid is governed by the conservation of mass and momentum, and if thermal effects are important, the balance of energy. In this thesis, we will be only concerned with purely mechanical problems, where we assume a constant temperature. We will also assume that the fluids are **incompressible**, i.e. $\frac{D\rho}{Dt} = 0$.

2.3. Transport Theorems

In order to compute the rate of change of volume integrals, we need to introduce transport theorems, which express the rate of change in time of some integral quantity using the properties of maps between reference frames. Each of the mappings in the previous Section corresponds to an appropriate transport theorem

Theorem 2.1 (Reynolds transport theorem for \mathcal{L}_t). *Let Ω_t be a region filled with a fluid which deforms according to the diffeomorphism (2.1) $\mathcal{L}_t : \Omega_{t_0} \rightarrow \Omega_t$ with velocity \mathbf{u} . Let $\partial\Omega_t$ be the boundary of Ω_t with outward normal \mathbf{n} and let $f(\mathbf{x}, t)$ be a scalar or vector*

function defined over Ω_t . Then

$$\begin{aligned}
\frac{d}{dt} \int_{\Omega_t = \mathcal{L}_t(\Omega_{t_0})} f \, d\Omega &= \int_{\Omega_t} \left[\left. \frac{\partial f}{\partial t} \right|_{\mathbf{x}} + \nabla_{\mathbf{x}} \cdot (f \mathbf{u}) \right] d\Omega \\
&= \int_{\Omega_t} \left[\left. \frac{\partial f}{\partial t} \right|_{\mathbf{x}} + \mathbf{u} \cdot \nabla_{\mathbf{x}} f + f (\nabla_{\mathbf{x}} \cdot \mathbf{u}) \right] d\Omega \\
&= \int_{\Omega_t} \left[\frac{Df}{Dt} + f (\nabla_{\mathbf{x}} \cdot \mathbf{u}) \right] d\Omega. \tag{2.22}
\end{aligned}$$

Theorem 2.2 (Leibnitz transport theorem for \mathcal{R}_t). Let $\hat{\Omega}_{t_0}$ be an arbitrary control volume which deforms according to the diffeomorphism (2.7) $\mathcal{R}_t : \hat{\Omega}_{t_0} \rightarrow \Omega_t$ with velocity \mathbf{w} . Let $f(\mathbf{x}, t)$ be a scalar or vector function defined over Ω_t . Then

$$\frac{d}{dt} \int_{\Omega_t = \mathcal{R}_t(\hat{\Omega}_{t_0})} f \, d\Omega = \int_{\Omega_t} \left[\left. \frac{\partial f}{\partial t} \right|_{\mathbf{x}} + \nabla_{\mathbf{x}} \cdot (f \mathbf{w}) \right] d\Omega. \tag{2.23}$$

Theorem 2.3 (Generalised Reynolds transport theorem for $\tilde{\mathcal{L}}_t$). Let Ω_t be a region filled with a fluid which deforms according to the diffeomorphism (2.1) $\mathcal{L}_t : \Omega_{t_0} \rightarrow \Omega_t$ with velocity \mathbf{u} . Furthermore, let $\hat{\Omega}_{t_0}$ be the inverse image of Ω_t through the diffeomorphism $\mathcal{R}_t : \hat{\Omega}_{t_0} \rightarrow \Omega_t$, that is $\Omega_t = \mathcal{R}_t(\hat{\Omega}_{t_0})$. Let $\partial \hat{\Omega}_{t_0}$ be the boundary of $\hat{\Omega}_{t_0}$ with outward normal $\hat{\mathbf{n}}$. Also, let Ω_{t_0} be the inverse image of $\hat{\Omega}_{t_0}$ through the diffeomorphic map (2.12) $\tilde{\mathcal{L}}_t : \Omega_{t_0} \rightarrow \hat{\Omega}_{t_0}$ with velocity $\tilde{\mathbf{v}}$. That is, $\hat{\Omega}_{t_0} = \tilde{\mathcal{L}}_t(\Omega_{t_0})$ with $\mathcal{L}_t = \mathcal{R}_t \circ \tilde{\mathcal{L}}_t$. Let $f(\mathbf{x}, t)$ be a scalar or vector function defined over Ω_t . Then

$$\frac{d}{dt} \int_{\Omega_t = \mathcal{L}_t(\Omega_{t_0})} f \, d\Omega = \int_{\hat{\Omega}_{t_0}} \left[\left. \frac{\partial(\hat{J}f)}{\partial t} \right|_{\mathbf{Y}} + \nabla \cdot (\hat{J}\tilde{\mathbf{v}}) \right] d\Omega = \frac{d}{dt} \int_{\Omega_t = \mathcal{R}_t(\hat{\Omega}_{t_0})} f \, d\Omega + \int_{\partial \Omega_t} (f \mathbf{c}) \cdot \mathbf{n} \, d\Gamma, \tag{2.24}$$

where \mathbf{c} is the convective velocity defined in Equation (2.17).

The detailed proofs of the transport theorems can be found in Scovazzi and Hughes (2007). With (2.11), we obtain an alternative version of the Reynolds transport theorem in terms of the referential time derivative

$$\frac{d}{dt} \int_{\Omega_t = \mathcal{L}_t(\Omega_{t_0})} f \, d\Omega = \int_{\Omega_t} \left[\left. \frac{\partial f}{\partial t} \right|_{\mathbf{Y}} + (\mathbf{u} - \mathbf{w}) \cdot \nabla_{\mathbf{x}} f + f (\nabla_{\mathbf{x}} \cdot \mathbf{u}) \right] d\Omega. \tag{2.25}$$

2.3.1. Conservation of Mass

The mass in the volume Ω_t is conserved at all time, i.e.

$$\frac{d}{dt} \int_{\Omega_t} \rho d\Omega = 0, \quad (2.26)$$

where $\rho(\mathbf{x}, t)$ is the density field at time t . Using the Reynolds transport theorem (2.25), we obtain

$$\int_{\Omega_t} \left(\frac{D\rho}{Dt} + \rho(\nabla_{\mathbf{x}} \cdot \mathbf{u}) \right) d\Omega = 0, \quad (2.27)$$

where

$$\begin{aligned} \frac{D\rho}{Dt} &= \left. \frac{\partial \rho}{\partial t} \right|_{\mathbf{x}} + \mathbf{u} \cdot \nabla_{\mathbf{x}} \rho && \text{for a fixed mesh,} \\ \frac{D\rho}{Dt} &= \left. \frac{\partial \rho}{\partial t} \right|_{\mathbf{Y}} + (\mathbf{u} - \mathbf{w}) \cdot \nabla_{\mathbf{x}} \rho && \text{for a deforming mesh.} \end{aligned} \quad (2.28)$$

Since the volume Ω_t is arbitrary and the integrand continuous, we deduce that

$$\frac{D\rho}{Dt} + \rho(\nabla_{\mathbf{x}} \cdot \mathbf{u}) = 0. \quad (2.29)$$

For incompressible fluids (i.e. $\frac{D\rho}{Dt} = 0$), we obtain

$$\nabla_{\mathbf{x}} \cdot \mathbf{u} = 0. \quad (2.30)$$

2.3.2. Conservation of Linear Momentum

We recognise two types of force acting on an infinitesimal fluid element, which occupies a volume Ω_t at some time t (see Figure 2.2). One, due to the action-at-a-distance type of force such as gravitation and electromagnetic forces, can be expressed as a force per unit mass, and is called the **body force**; the other, due to the direct action across the boundary surface S , is called the **surface force**. To describe the body force, we assume that the fluid element has a well-defined **mass density** ρ . The mass of the fluid element with volume Ω_t is then given by

$$m = \int_{\Omega_t} \rho d\Omega, \quad (2.31)$$

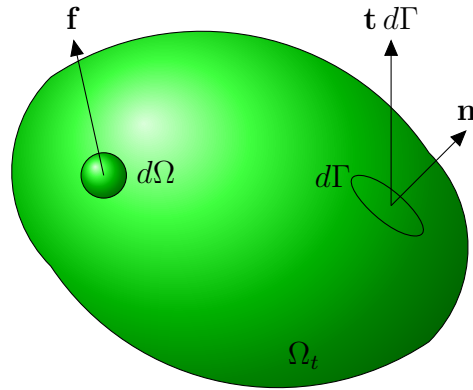


Figure 2.2.: Stress and body force definition.

such that the total body force acting on the volume V is given by

$$\mathbf{F}_b = \int_{\Omega_t} \rho \mathbf{b} d\Omega, \quad (2.32)$$

where \mathbf{b} is the body force per unit mass.

To describe the surface force, let us consider a small surface element of area $d\Gamma$ with an outward pointing unit normal vector \mathbf{n} . Then the total surface force acting on Γ is given by

$$\mathbf{F}_t = \int_{\Gamma} \mathbf{t} d\Gamma, \quad (2.33)$$

where \mathbf{t} is the force per unit area acting on the surface and is called the **stress vector**. The clear isolation of surface forces in a continuum is usually attributed to Cauchy.

Then the total force experienced by the fluid occupying Ω_t , given by Newton's second law (mass \times acceleration), is

$$m \mathbf{a} = \int_{\Omega_t} \rho \mathbf{b} d\Omega + \int_{\Gamma} \mathbf{t} d\Gamma. \quad (2.34)$$

Here,

$$\mathbf{a} = \frac{\frac{d}{dt} \int_{\Omega_t} \rho \mathbf{u} d\Omega}{\int_{\Omega_t} \rho d\Omega} \quad (2.35)$$

is an average acceleration.

Theorem 2.4 (Existence and Symmetry of the Stress Tensor). *Let $\Omega \subset \mathbb{R}^d$, $d = 2, 3$, be some bounded region and let \mathbf{t} be the stress vector defined above. Then there exists a second-order stress tensor $\boldsymbol{\sigma}$ such that throughout Ω*

(i)

$$\mathbf{t} = \boldsymbol{\sigma} \cdot \mathbf{n}, \quad (2.36)$$

i.e. the stress tensor $\boldsymbol{\sigma}$ can be seen as a linear mapping of the unit normal vector \mathbf{n} into the stress vector \mathbf{t} .

(ii)

$$\boldsymbol{\sigma} \text{ is symmetric.} \quad (2.37)$$

$\boldsymbol{\sigma}$ is called the **Cauchy stress tensor**.

Proof. See e.g. Owens and Phillips (2005), p. 361ff. □

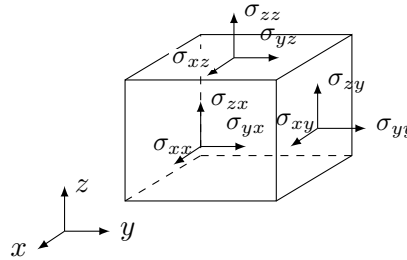


Figure 2.3.: Notation used for the stress tensor.

Notation:. The components of the stress tensor are usually denoted as seen in Figure 2.3 by

$$\boldsymbol{\sigma} = \begin{bmatrix} \sigma_{xx} & \sigma_{xy} & \sigma_{xz} \\ \sigma_{yx} & \sigma_{yy} & \sigma_{yz} \\ \sigma_{zx} & \sigma_{zy} & \sigma_{zz} \end{bmatrix}, \quad (2.38)$$

where the $\sigma_{xx}, \sigma_{yy}, \sigma_{zz}$ components are called **normal stresses** and $\sigma_{xy} = \sigma_{yx}, \sigma_{xz} = \sigma_{zx}, \sigma_{yz} = \sigma_{zy}$ are called **shear stresses**.

Definition 2.5 (deviatoric stress/extra-stress tensor). For fluids, we decompose the Cauchy stress tensor into contributions from the rate of deformation independent spherically-symmetrical pressure and the **deviatoric stress** or more generally **extra-stress tensor** \mathbf{T} , i.e.

$$\boldsymbol{\sigma} = -p\mathbf{I} + \mathbf{T}. \quad (2.39)$$

By (2.33) the total force acting on a volume element is given by

$$m\mathbf{a} = \int_{\Omega_t} \rho \mathbf{b} d\Omega + \int_{\Gamma} \mathbf{t} d\Gamma. \quad (2.40)$$

By (2.36) and the divergence theorem (DT), we are led to

$$\int_{\Omega_t} \rho \frac{D\mathbf{u}}{Dt} d\Omega = \int_{\Omega_t} \rho \mathbf{b} d\Omega + \int_{\Gamma} \boldsymbol{\sigma} \cdot \mathbf{n} d\Gamma \stackrel{\text{DT}}{=} \int_{\Omega_t} \rho \mathbf{b} d\Omega + \int_{\Omega_t} \nabla_{\mathbf{x}} \cdot \boldsymbol{\sigma} d\Omega. \quad (2.41)$$

With Equation (2.39), we obtain

$$\int_{\Omega_t} \rho \frac{D\mathbf{u}}{Dt} d\Omega = \int_{\Omega_t} \rho \mathbf{b} d\Omega - \int_{\Omega_t} \nabla_{\mathbf{x}} p d\Omega + \int_{\Omega_t} \nabla_{\mathbf{x}} \cdot \mathbf{T} d\Omega. \quad (2.42)$$

Since the integrand is continuous in an arbitrary region Ω_t , the conservation of linear momentum becomes

$$\rho \frac{D\mathbf{u}}{Dt} = -\nabla_{\mathbf{x}} p + \nabla_{\mathbf{x}} \cdot \mathbf{T} + \rho \mathbf{b}. \quad (2.43)$$

where

$$\begin{aligned} \frac{D\mathbf{u}}{Dt} &= \left. \frac{\partial \mathbf{u}}{\partial t} \right|_{\mathbf{x}} + \mathbf{u} \cdot \nabla_{\mathbf{x}} \mathbf{u} && \text{in Eulerian frame,} \\ \frac{D\mathbf{u}}{Dt} &= \left. \frac{\partial \mathbf{u}}{\partial t} \right|_{\mathbf{Y}} + (\mathbf{u} - \mathbf{w}) \cdot \nabla_{\mathbf{x}} \mathbf{u} && \text{in ALE frame.} \end{aligned} \quad (2.44)$$

For the following Sections, we will drop the \mathbf{x} notation for the sake of simplicity, until we discuss the discretisation of the equations in the ALE framework.

2.4. Constitutive Equations

To complete the mathematical formulation, we need to relate the extra-stress tensor \mathbf{T} to the motion. These supplementary relations, which are called the **constitutive equations** or the **rheological equations of state**, differentiate one material from another. This Chapter is based on the books of Tanner (2002), Böhme (2000), Bird et al. (1987a,b), Renardy (2000), Owens and Phillips (2005) and on Claus (2008).

2.4.1. The Newtonian Fluid

For a **Newtonian fluid**, we assume that

1. the stress is independent of any previous history of distortion, i.e. it depends only on the deformation state at the present time (**present time**),
2. the stress depends only on the local kinematic state of the immediate neighbourhood (**local action**),

3. the stress depends linearly on the rate of deformation (**linearity**),
4. the material is considered to be isotropic, that means its physical properties are independent of direction (**isotropy**).

Taking these four considerations into account, the constitutive law for a **Newtonian fluid** is given by

$$\mathbf{T} = 2\eta_0\mathbf{D}. \quad (2.45)$$

Here, \mathbf{D} is the *rate of deformation tensor* and $\nabla\mathbf{u}$ is the *velocity gradient tensor*. For example, in two space dimensions, \mathbf{D} is defined by

$$\mathbf{D} := \frac{1}{2}(\nabla\mathbf{u} + \nabla\mathbf{u}^T) = \begin{pmatrix} \frac{\partial u}{\partial x} & \frac{1}{2}\left(\frac{\partial u}{\partial y} + \frac{\partial v}{\partial x}\right) \\ \frac{1}{2}\left(\frac{\partial u}{\partial y} + \frac{\partial v}{\partial x}\right) & \frac{\partial v}{\partial y} \end{pmatrix}, \quad (2.46)$$

and $\nabla\mathbf{u}$ is given by

$$\nabla\mathbf{u} = \begin{pmatrix} \frac{\partial u}{\partial x} & \frac{\partial u}{\partial y} \\ \frac{\partial v}{\partial x} & \frac{\partial v}{\partial y} \end{pmatrix}. \quad (2.47)$$

The rate of deformation tensor contains information about the deformation rate at the present time at a local point. It is symmetric, which means it is suitable for the description of isotropic materials. In the relation (2.45), we assume that the extra stress \mathbf{T} depends linearly on the rate of deformation \mathbf{D} . The proportionality coefficient η_0 is called the **viscosity**. This law shows that the viscosity, i.e. the friction of particles at the molecular level, is uniquely responsible for the existence of extra stresses.

Substituting Equation (2.45) into the momentum equation (2.43) leads in the case of incompressible flow to the **Navier-Stokes equations**

$$\begin{cases} \rho \frac{D\mathbf{u}}{Dt} = -\nabla p + \eta_0 \Delta \mathbf{u} + \rho \mathbf{b}, \\ \nabla \cdot \mathbf{u} = 0. \end{cases} \quad (2.48)$$

2.4.2. The Generalised Newtonian Fluid

As a first step towards deriving constitutive relations for non-Newtonian fluids, we lift the linearity assumption and allow for non-linear dependency of the stress on the rate of deformation. To derive a model, which is independent of the coordinate system, we write the viscosity η as a function of the invariants of \mathbf{D} . We use the symmetry of the

rate of deformation tensor by noticing that every symmetric second order tensor can be diagonalized and its eigenvalues are guaranteed to be real, i.e.

$$\mathbf{D} = \begin{pmatrix} \lambda_1 & 0 & 0 \\ 0 & \lambda_2 & 0 \\ 0 & 0 & \lambda_3 \end{pmatrix}, \quad (2.49)$$

$$\det(\mathbf{D} - \lambda\mathbf{I}) = -\lambda^3 + I_D\lambda^2 - II_D\lambda + III_D = 0, \quad (2.50)$$

where

$$I_D = D_{xx} + D_{yy} + D_{zz} = \text{tr } \mathbf{D}, \quad (2.51)$$

$$II_D = D_{xx}D_{yy} + D_{yy}D_{zz} + D_{zz}D_{xx} - D_{xy}^2 - D_{xz}^2 - D_{yz}^2 = \frac{1}{2}[(\text{tr } \mathbf{D})^2 - \text{tr } \mathbf{D}^2], \quad (2.52)$$

$$III_D = \det \mathbf{D} \quad (2.53)$$

are called the **principal invariants** of \mathbf{D} and they are independent of the coordinate system. Hence, we obtain the following relation between the extra stress tensor and the rate of deformation tensor

$$\mathbf{T} = 2\eta_0(I_D, II_D, III_D)\mathbf{D}. \quad (2.54)$$

- $I_D = 0$ for incompressible fluids. Then $II_D \leq 0$, $|III_D| \leq \frac{2}{3\sqrt{3}}(-II_D)^{\frac{3}{2}}$.
- $III_D = 0$ for simple shear flow.

This model is only suitable for the description of flows, where elastic effects are negligible and the shear-thinning effect has a strong influence on the flow behaviour. Its principal usefulness is for calculating flow rates and shearing forces in steady-state simple shear flow such as tube flow. The most widely used form of the general viscous constitutive relation is the **power law model**

$$\mathbf{T} = 2K|II_D|^{\frac{(n-1)}{2}}\mathbf{D}, \quad (2.55)$$

where K and n are positive material parameters. Details on models of this kind can be found in Macosko (1994), Bird et al. (1987a), Böhme (2000) and Owens and Phillips (2005). Like the Newtonian fluid, the generalised Newtonian fluid has zero first and second normal stress differences, but it shows shear-thinning for $n < 1$ and shear-thickening for $n > 1$.

2.4.3. Viscoelastic Models for Dilute Polymer Solutions

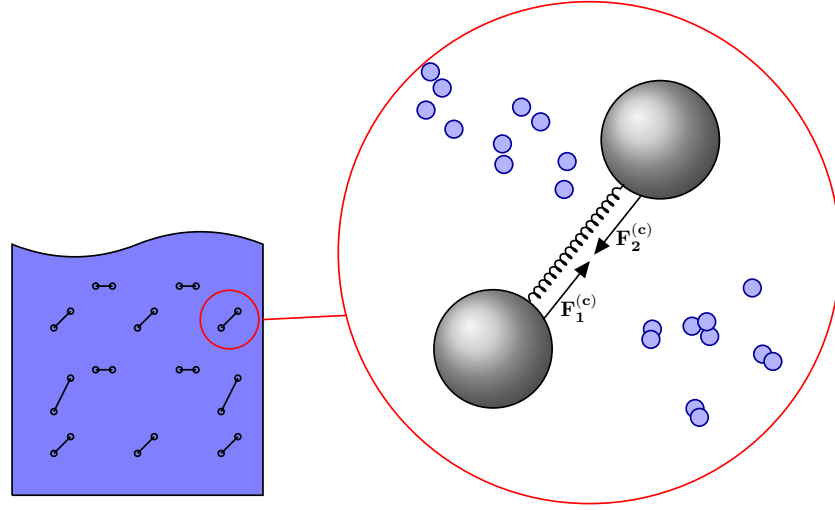


Figure 2.4.: Dumbbell model to describe dilute polymer solutions.

To describe viscoelastic behaviour in complex flow configurations, we need to take the molecular structure of the fluid material into account in the mathematical modelling. The variety of viscoelastic models to describe the stress response to the presence of molecules and molecular networks in a fluid is almost as large as the variety of fluid materials. In principle, we assume that the total stress $\boldsymbol{\sigma}$ (as defined in (2.36)) in a polymer solution is the sum of a contribution from the Newtonian solvent $\boldsymbol{\sigma}_N$ and the polymeric stress contribution $\boldsymbol{\sigma}_P$, resulting from the presence of the polymer molecules, i.e.

$$\boldsymbol{\sigma} = \boldsymbol{\sigma}_S + \boldsymbol{\sigma}_P \quad (2.56)$$

$$= (-p_S \mathbf{I} + \mathbf{T}_S) + (-p_P \mathbf{I} + \boldsymbol{\tau}) \quad (2.57)$$

$$= -p \mathbf{I} + \mathbf{T}, \quad (2.58)$$

where $p = p_S + p_P$, $\mathbf{T} = \mathbf{T}_S + \boldsymbol{\tau} = 2\eta_N \mathbf{D} + \boldsymbol{\tau}$ and η_N is the solvent viscosity. The stress tensor \mathbf{T} is zero at equilibrium.

In this thesis, we will concentrate on models based on the notion that the molecules, which are dispersed in a Newtonian fluid, can be modelled by so-called elastic dumbbells. These dumbbells have a strong impact on the stress response of the fluid to deformations.

We model the elastic dumbbells as two identical beads and a massless inter-connecting elastic spring. Each of the two beads has mass m with position vectors \mathbf{r}_1 and \mathbf{r}_2 relative to some fixed coordinate frame. Let $\mathbf{Q} = \mathbf{r}_2 - \mathbf{r}_1$ denote the end-to-end vector of the dumbbell.

Furthermore, we constitute an equation of motion for each bead of the elastic dumbbell,

assuming that there are three significant forces acting on each bead:

1. **Friction force** $\mathbf{F}_i^{(f)}$

This is the force of resistance experienced by a bead as it moves through the solution. This friction force is for spherical beads assumed to be given by Stokes' Law:

$$\mathbf{F}_i^{(f)} = 6\pi\eta_N a \left(\frac{d\mathbf{r}_i}{dt} - \mathbf{u}(\mathbf{r}_i) \right) = \zeta \left(\frac{d\mathbf{r}_i}{dt} - \mathbf{u}(\mathbf{r}_i) \right). \quad (2.59)$$

Here, η_N is the solvent viscosity, a is the radius of the bead and $u(\mathbf{r}_i)$ is the velocity of the surrounding fluid at the point with position vector \mathbf{r}_i . Hence, $\left(\frac{d\mathbf{r}_i}{dt} - \mathbf{u}(\mathbf{r}_i) \right)$ is the velocity of the i -th bead relative to the surrounding fluid. We shall write ζ for $6\pi\eta_N a$. This constant ζ is the so-called **friction coefficient**.

Note that we have neglected any effect which one bead may have on the velocity of the solvent in the neighbourhood of the other bead. That means, we assume that the concentration of dumbbells in the Newtonian solvent is very low and therefore that the dumbbells don't interact with each other. This restricts our model to extremely dilute polymer solutions.

2. **Spring force** $\mathbf{F}_i^{(c)}$

The spring connecting the beads exerts a spring force $\mathbf{F}_i^{(c)}$ on the i -th bead. We assume this spring force to be given by Hooke's law:

$$\mathbf{F}_1^{(c)} = -H(\mathbf{r}_1 - \mathbf{r}_2) = H\mathbf{Q}, \quad (2.60)$$

$$\mathbf{F}_2^{(c)} = -H(\mathbf{r}_2 - \mathbf{r}_1) = -H\mathbf{Q}, \quad (2.61)$$

where H is the spring constant.

3. **Brownian forces** $\mathbf{F}_i^{(b)}$

Brownian forces are the cumulative effect of the exceedingly frequent collisions between a large particle, called a Brownian particle, and the many surrounding much smaller fluid particles, which are in perpetual thermal motion. The mathematical model to describe these random movements is the so called Wiener process $\mathbf{W}_i = \mathbf{W}_i(t)$ ($i = 1, 2$), which is a Gaussian stochastic process and is therefore completely characterized by the mean and autocorrelation of its components $W_{i,j}$:

$$\langle W_{i,j}(t) \rangle = 0, \quad \langle W_{i,j}(t) W_{i,j}(t') \rangle = \min(t', t). \quad (2.62)$$

We assume that a bead is large compared to the solvent molecules. This assumption justifies the continuum description of the solvent. With the Wiener process we may write the Brownian force $\mathbf{F}_i^{(b)}$ acting on the i -th bead in the form

$$\mathbf{F}_i^{(b)} dt = \sqrt{2kT\zeta} d\mathbf{W}_i, \quad (2.63)$$

where k is the Boltzmann constant, T is the absolute temperature and ζ is the friction coefficient. The coefficient $\sqrt{2kT\zeta}$ may be derived from the principle of equipartition of energy from kinetic gas theory, which states that in equilibrium

$$E_{kin} = \frac{1}{2} \langle \mathbf{V}(t)^2 \rangle = \frac{kT}{2}, \quad (2.64)$$

where $\mathbf{V}(t)$ is the velocity of the Brownian particle, which is the solution of the stochastic differential equation describing the motion of a Brownian particle

$$m \frac{d\mathbf{V}(t)}{dt} = -\zeta \mathbf{V}(t) + \mathbf{F}_i^{(b)}. \quad (\text{Langevin equation}) \quad (2.65)$$

A detailed derivation may be found in Phan-Thien (2002) or Öttinger (1996).

We assume that inertial forces at the molecular level can be neglected. Additionally, we neglect external forces such as gravity on a bead. This yields the following equation of motion for the beads

$$\mathbf{F}_i^{(f)} + \mathbf{F}_i^{(c)} + \mathbf{F}_i^{(b)} = 0, \quad i=1,2 \quad (2.66)$$

Inserting all the expressions for the forces above yields

$$-\zeta \left(\frac{d\mathbf{r}_1}{dt} - \mathbf{u}(\mathbf{r}_1, t) \right) + H\mathbf{Q} + \sqrt{2kT\zeta} \frac{d\mathbf{W}_1}{dt} = 0, \quad (2.67)$$

$$-\zeta \left(\frac{d\mathbf{r}_2}{dt} - \mathbf{u}(\mathbf{r}_2, t) \right) - H\mathbf{Q} + \sqrt{2kT\zeta} \frac{d\mathbf{W}_2}{dt} = 0. \quad (2.68)$$

Subtracting the two equations from each other and assuming a homogeneous solvent flow field, i.e.

$$\mathbf{u}(\mathbf{r}_2, t) = \mathbf{u}(\mathbf{r}_1, t) + (\nabla \mathbf{u})(\mathbf{r}_2 - \mathbf{r}_1). \quad (2.69)$$

yields the following equation of change for the end-to-end vector of the dumbbell

$$\frac{d\mathbf{Q}}{dt} = \nabla \mathbf{u} \cdot \mathbf{Q} - \frac{2H}{\zeta} \mathbf{Q} - \sqrt{\frac{4kT}{\zeta}} d\mathbf{W}(t), \quad (2.70)$$

where we set $\mathbf{W}(t) := (\mathbf{W}_2(t) - \mathbf{W}_1(t))/\sqrt{2}$. The Equation (2.70) is a stochastic differential equation and $\mathbf{Q}(t)$ is a stochastic process. Using methods in stochastic differential

equations we can convert the stochastic differential equation (2.70) to the corresponding **Fokker-Planck** or **diffusion equation**

$$\frac{\partial}{\partial t} p(\mathbf{Q}, t) = -\frac{\partial}{\partial \mathbf{Q}} \cdot \left[\left(\nabla \mathbf{u} \cdot \mathbf{Q} - \frac{2H}{\zeta} \mathbf{Q} \right) p(\mathbf{Q}, t) - \frac{2kT}{\zeta} \frac{\partial}{\partial \mathbf{Q}} p(\mathbf{Q}, t) \right], \quad (2.71)$$

where $p(\mathbf{Q}, t)$ is the probability density function which means that $p(\mathbf{Q}, t)d\mathbf{Q}$ gives the probability that a dumbbell has an orientation in the range \mathbf{Q} to $\mathbf{Q} + d\mathbf{Q}$. It can also be used to determine the expectation of a given function $g(\mathbf{Q})$

$$\langle g(\mathbf{Q}) \rangle = \int g(\mathbf{Q}) p(\mathbf{Q}, t) d\mathbf{Q}. \quad (2.72)$$

In order to determine an expression for the macroscopic polymeric stress contribution σ_P , we follow Bird et al. (1987b), Kramers (1946) and Deville and Gatski (2012). The elastic dumbbells will contribute to the stress in the suspension in two principal ways: through the spring force and through the momentum of the beads. The average force contribution through the momentum of the beads is given by

$$\sigma_P^{(b)} = 2nkT\mathbf{I}, \quad (2.73)$$

if we assume that the velocity distribution of the beads is given by the Maxwell-Boltzmann distribution from kinetic gas theory. This means we assume that the velocity distribution of the flow system (here consisting of the dumbbells swimming in the Newtonian solvent) is the same as that in a solution at equilibrium. This isotropic tensor part will be merged into the pressure term.

The averaged contribution of the spring connecting the beads to the stress is given by

$$\sigma_P^{(c)} = n \int (\mathbf{Q} \otimes \mathbf{F}^{(c)}) p(\mathbf{Q}, t) d\mathbf{Q} = n \langle \mathbf{Q} \otimes \mathbf{F}^{(c)} \rangle = nH \langle \mathbf{Q} \otimes \mathbf{Q} \rangle. \quad (2.74)$$

Here, n is the number of dumbbells per unit volume and \otimes denotes the tensor product of two vectors. The total polymeric stress is given by

$$\sigma_P = -p_P \mathbf{I} + \boldsymbol{\tau} = nH \langle \mathbf{Q} \otimes \mathbf{Q} \rangle + 2nkT\mathbf{I}. \quad (2.75)$$

The tensor

$$\mathbf{c} = \langle \mathbf{Q} \otimes \mathbf{Q} \rangle \quad (2.76)$$

is called the *conformation tensor*. To obtain an expression in terms of the conformation tensor \mathbf{c} from the Fokker-Planck equation (2.71), we multiply it by $\mathbf{Q} \otimes \mathbf{Q}$ and integrate

over the whole configuration space \mathbb{R}^3 to obtain

$$\frac{D\mathbf{c}}{Dt} - \nabla\mathbf{u} \cdot \mathbf{c} - \mathbf{c} \cdot \nabla\mathbf{u}^T = \frac{4kT}{\zeta}\mathbf{I} - \frac{4H}{\zeta}\mathbf{c}. \quad (2.77)$$

The left hand side of (2.77) is called the *upper-convected derivative* of \mathbf{c} denoted by $\overset{\nabla}{\mathbf{c}}$

$$\overset{\nabla}{\mathbf{c}} := \frac{D\mathbf{c}}{Dt} - \nabla\mathbf{u} \cdot \mathbf{c} - \mathbf{c} \cdot \nabla\mathbf{u}^T. \quad (2.78)$$

Finally we note that, in a system at equilibrium (that is, $\nabla\mathbf{u} = \mathbf{0}$, $\frac{D\mathbf{c}}{Dt} = \mathbf{0}$), Eq. (2.77) gives

$$\mathbf{c}_{eq} = \frac{kT}{H}\mathbf{I}. \quad (2.79)$$

The corresponding equation at equilibrium (i.e. $\boldsymbol{\tau} = \mathbf{0}$) gives us the polymeric contribution to the pressure

$$p_P\mathbf{I} = -nH\mathbf{c}_{eq} - 2nkT\mathbf{I} \stackrel{(2.79)}{=} -3nkT\mathbf{I}. \quad (2.80)$$

Finally, we get the **Kramers expression** for the extra stress tensor

$$\mathbf{T} = \mathbf{T}_S + \boldsymbol{\tau} = 2\eta_N\mathbf{D} + nH\mathbf{c} - nkT\mathbf{I}. \quad (2.81)$$

If we normalise the conformation tensor (in order to give $\mathbf{c}_{eq} = \mathbf{I}$), then with

$$\mathbf{c}^* = \frac{H}{kT}\mathbf{c} \quad (2.82)$$

we obtain

$$\overset{\nabla}{\mathbf{c}}^* = -\frac{4H}{\zeta}(\mathbf{c}^* - \mathbf{I}). \quad (2.83)$$

and

$$\mathbf{T} = \mathbf{T}_S + \boldsymbol{\tau} = 2\eta_N\mathbf{D} + nkT(\mathbf{c}^* - \mathbf{I}). \quad (2.84)$$

We define the *relaxation time* λ (time constant for the Hookean elastic dumbbells) and the *polymeric viscosity* η_P in terms of the parameters appearing in (2.83) and (2.84) by

$$\lambda = \frac{\zeta}{4H} \quad \text{and} \quad \eta_P = \frac{nkT\zeta}{4H} = nkT\lambda. \quad (2.85)$$

This results in the so-called **Oldroyd-B model in terms of the conformation tensor**

$$\begin{cases} \overset{\nabla}{\mathbf{c}}^* = -\frac{1}{\lambda}(\mathbf{c}^* - \mathbf{I}), \\ \mathbf{T} = \mathbf{T}_S + \boldsymbol{\tau} = 2\eta_N \mathbf{D} + \frac{\eta_p}{\lambda}(\mathbf{c}^* - \mathbf{I}). \end{cases} \quad (2.86)$$

We can use the expression for the polymeric stress contribution $\boldsymbol{\tau} = \frac{\eta_p}{\lambda}(\mathbf{c}^* - \mathbf{I})$ to obtain the **Oldroyd-B model**

$$\begin{cases} \mathbf{T} = 2\eta_N \mathbf{D} + \boldsymbol{\tau}, \\ \boldsymbol{\tau} + \lambda \overset{\nabla}{\boldsymbol{\tau}} = 2\eta_p \mathbf{D}. \end{cases} \quad (2.87)$$

where we used

$$\overset{\nabla}{\mathbf{I}} = -\nabla \mathbf{u} - (\nabla \mathbf{u})^T = -2\mathbf{D}. \quad (2.88)$$

Giesekus (1966) dropped the assumption of an isotropic influence of neighboring dumbbells on the dumbbell at hand, and proposed that the environment of the adjacent dumbbells induces an anisotropic drag that is dependent on the orientation. To take this effect into account, we replace the friction coefficient $\frac{1}{\zeta}$ in the relaxation time λ with an anisotropic mobility tensor \mathbf{B} such that

$$\overset{\nabla}{\mathbf{c}} + 4H [\mathbf{B}(\mathbf{c} - \mathbf{I})] = \mathbf{0}. \quad (2.89)$$

Since at equilibrium the stress is isotropic, this would imply that $\mathbf{B} = \mathbf{I}$ with $\mathbf{c} = \mathbf{I}$. The simplest representation for the anisotropy would be obtained by choosing \mathbf{B} proportional to $\mathbf{c} - \mathbf{I}$,

$$\mathbf{B} = \frac{1}{\zeta} (\mathbf{I} + \alpha(\mathbf{c} - \mathbf{I})), \quad (2.90)$$

where α is the proportionality constant, which we will call the *anisotropy parameter*. This yields the **Giesekus model in terms of the conformation tensor**

$$\overset{\nabla}{\mathbf{c}} + \frac{1}{\lambda} [(\mathbf{c} - \mathbf{I}) + \alpha(\mathbf{c} - \mathbf{I})^2] = \mathbf{0}. \quad (2.91)$$

Alternatively, expressed in terms of the polymeric stress contribution the **Giesekus model**

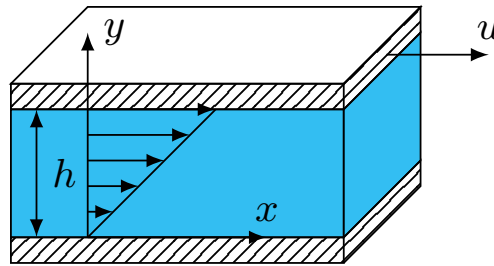
becomes

$$\boldsymbol{\tau} + \lambda \overset{\nabla}{\boldsymbol{\tau}} + \alpha \frac{\lambda}{\eta_p} \boldsymbol{\tau}^2 = 2\eta_p \mathbf{D}. \quad (2.92)$$

2.5. Simple Flows, Viscosities and Stress Differences

The first step in evaluating constitutive models is to consider their predictions in a number of simple flows. We will look at two simple types of flows: steady shear flow and uniaxial extensional flow. This will lead us to the definition of shear-dependent viscosity, normal stress differences and elongational viscosity.

2.5.1. Steady Shear Flow and Viscometric Functions



$$\dot{\gamma} = \frac{\partial u}{\partial y} \text{ shear rate}$$

Figure 2.5.: Simple shear flow configuration.

Consider a fluid between two infinite parallel plates separated by a distance h as shown in Figure 2.5. Now, suppose that the top plate moves with a constant velocity u in the x -direction. This flow is called **steady shear flow** or **viscometric flow**. The velocity field is given by

$$\mathbf{u} = (u(y), 0, 0).$$

Consequently, the velocity gradient and the rate of deformation tensor are given by

$$\nabla \mathbf{u} = \begin{pmatrix} 0 & \frac{\partial u}{\partial y} & 0 \\ 0 & 0 & 0 \\ 0 & 0 & 0 \end{pmatrix}; \quad 2\mathbf{D} = \begin{pmatrix} 0 & \frac{\partial u}{\partial y} & 0 \\ \frac{\partial u}{\partial y} & 0 & 0 \\ 0 & 0 & 0 \end{pmatrix}. \quad (2.93)$$

The quantity

$$\dot{\gamma} := \frac{\partial u(y)}{\partial y}, \quad (2.94)$$

is known as the **shear rate**. If we consider an isotropic material, the zx - and zy -components of stress must be zero and the stress tensor reduces to

$$\boldsymbol{\sigma} = \begin{bmatrix} \sigma_{xx} & \sigma_{xy} & 0 \\ \sigma_{xy} & \sigma_{yy} & 0 \\ 0 & 0 & \sigma_{zz} \end{bmatrix}. \quad (2.95)$$

When a viscoelastic liquid is brought from rest into a state of steady shearing motion, a time-dependent shear stress is built up. However, if the shearing motion continues at a constant rate, the shear stress approaches a steady-state value that depends only on the shear rate.

Definition 2.6 (Viscometric Functions). *The ratio of the shear stress σ_{xy} to the shear rate is a function*

$$\eta(\dot{\gamma}) = \frac{\sigma_{xy}}{\dot{\gamma}} \quad (2.96)$$

called the (**shear-rate dependent**) **viscosity**. The shear viscosity η is typically a monotonically decreasing function of shear rate that tends to some limit η_∞ for very high-shear rates. Such fluids are termed **shear-thinning**. At low shear rates, the viscosity approaches a constant value

$$\eta_0 = \lim_{\dot{\gamma} \rightarrow 0} \eta(\dot{\gamma}),$$

which is called the **zero-shear-rate-viscosity**.

The two independent differences

$$N_1(\dot{\gamma}) := \sigma_{xx} - \sigma_{yy}, \quad (2.97)$$

$$N_2(\dot{\gamma}) := \sigma_{yy} - \sigma_{zz}, \quad (2.98)$$

are called the **first** and **second normal stress differences**, respectively. Polymeric fluids usually have non-zero normal stress differences, where the first normal stress difference is positive, the second normal stress difference is negative and its absolute value is much smaller than that of N_1 .

2.5.2. Steady Uniaxial Extensional Flow and Elongational Viscosity

Suppose that a rod of material is being extended homogeneously along its x -axis, so that each part of the rod is stressed uniformly as shown in Figure 2.6. We suppose that the constant rate of elongation $\partial u / \partial x (\equiv \dot{\epsilon})$ is independent of x . For an incompressible fluid,

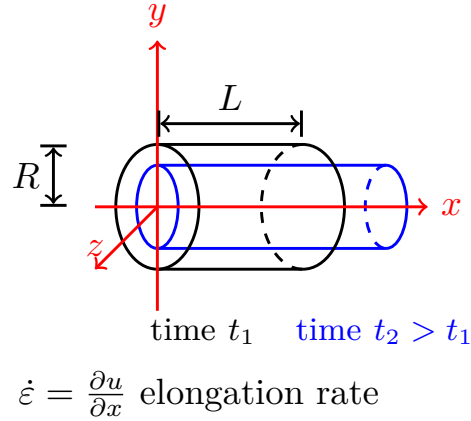


Figure 2.6.: Steady Uniaxial Extensional Flow Configuration.

mass conservation and axial symmetry then demand that $\partial v/\partial y = \partial w/\partial z = -\dot{\epsilon}/2$. Thus, the velocity in a steady elongational flow is given by

$$\mathbf{u} = \left(\dot{\epsilon}x, -\frac{\dot{\epsilon}}{2}y, -\frac{\dot{\epsilon}}{2}z \right). \quad (2.99)$$

Consequently, the velocity gradient tensor and the rate of deformation tensor are equal and

$$\nabla \mathbf{u} = \mathbf{D} = \begin{pmatrix} \dot{\epsilon} & 0 & 0 \\ 0 & -\frac{\dot{\epsilon}}{2} & 0 \\ 0 & 0 & -\frac{\dot{\epsilon}}{2} \end{pmatrix}. \quad (2.100)$$

All shear stress components are zero and $\sigma_{yy} = \sigma_{zz}$ by symmetry. The presence of non-zero shear stress would lead to an angle change in volume elements. Therefore, the stress tensor becomes

$$\boldsymbol{\sigma} = \begin{bmatrix} \sigma_{xx} & 0 & 0 \\ 0 & \sigma_{yy} & 0 \\ 0 & 0 & \sigma_{yy} \end{bmatrix}. \quad (2.101)$$

The stress response is then completely defined by the dependence of $\sigma_{xx} - \sigma_{yy}$ on the constant rate of extension $\dot{\epsilon}$.

Definition 2.7 (Elongational Viscosity). *The ratio of the stress difference $\sigma_{xx} - \sigma_{yy}$ to the elongation rate $\dot{\epsilon}$*

$$\eta_E(\dot{\epsilon}) = \frac{\sigma_{xx} - \sigma_{yy}}{\dot{\epsilon}}, \quad (2.102)$$

*is called the **elongational** or **extensional viscosity**. For polymeric fluids, the elongational viscosity is usually seen to increase as the elongation rate is increased. This behaviour is termed **extensional-thickening**. The ratio between the extensional viscosity and the*

zero-shear-rate viscosity is called the **Trouton ratio**

$$\text{Trouton ratio} = \frac{\eta_E(\dot{\epsilon})}{\eta_0}. \quad (2.103)$$

The strain accumulated by a fluid element in elongational flows is called the **Hencky strain** and is given by

$$\varepsilon(t) := \int_0^t \dot{\epsilon}(t') dt' \quad (2.104)$$

2.5.3. Viscometric Functions for Newtonian Fluids

For steady simple shear flow (see Section 2.5.1), the stress tensor for a Newtonian fluid becomes

$$\boldsymbol{\sigma} = \begin{bmatrix} -p & \eta_0 \dot{\gamma} & 0 \\ \eta_0 \dot{\gamma} & -p & 0 \\ 0 & 0 & -p \end{bmatrix}. \quad (2.105)$$

Therefore, a Newtonian fluid has a constant shear viscosity η_0 , i.e. it is not shear-thinning and it has zero first and second normal stress differences. For steady uniaxial elongation (see Section 2.5.2), we obtain

$$\boldsymbol{\sigma} = \begin{bmatrix} -p + 2\eta\dot{\epsilon} & 0 & 0 \\ 0 & -p - \eta\dot{\epsilon} & 0 \\ 0 & 0 & -p - \eta\dot{\epsilon} \end{bmatrix}. \quad (2.106)$$

Therefore, the elongational viscosity

$$\eta_E(\dot{\epsilon}) = 3\eta_0, \quad (2.107)$$

is three times larger than the shear viscosity, i.e. the Trouton ratio is $\eta_E(\dot{\epsilon})/\eta_0 = 3$.

2.5.4. Viscometric Functions for Oldroyd-B Fluid

For steady simple shear flow, i.e. $\frac{D\boldsymbol{\tau}}{Dt} = \mathbf{0}$, the Oldroyd-B constitutive equation becomes

$$\begin{aligned} & \begin{pmatrix} \tau_{xx} & \tau_{xy} & 0 \\ \tau_{xy} & \tau_{yy} & 0 \\ 0 & 0 & \tau_{zz} \end{pmatrix} - \lambda \left\{ \begin{pmatrix} 0 & \dot{\gamma} & 0 \\ 0 & 0 & 0 \\ 0 & 0 & 0 \end{pmatrix} \begin{pmatrix} \tau_{xx} & \tau_{xy} & 0 \\ \tau_{xy} & \tau_{yy} & 0 \\ 0 & 0 & \tau_{zz} \end{pmatrix} \right\} \\ & - \lambda \left\{ \begin{pmatrix} \tau_{xx} & \tau_{xy} & 0 \\ \tau_{xy} & \tau_{yy} & 0 \\ 0 & 0 & \tau_{zz} \end{pmatrix} \begin{pmatrix} 0 & 0 & 0 \\ \dot{\gamma} & 0 & 0 \\ 0 & 0 & 0 \end{pmatrix} \right\} = \eta_p \begin{pmatrix} 0 & \dot{\gamma} & 0 \\ \dot{\gamma} & 0 & 0 \\ 0 & 0 & 0 \end{pmatrix}, \end{aligned}$$

so that solving this system yields

$$\tau_{xy} = \eta_p \dot{\gamma}, \quad \tau_{xx} = 2\eta_p \lambda \dot{\gamma}^2, \quad \tau_{yy} = \tau_{zz} = 0. \quad (2.108)$$

Therefore, the viscometric functions are given by

$$\eta(\dot{\gamma}) = \frac{\sigma_{xy}}{\dot{\gamma}} = \eta_0, \quad N_1(\dot{\gamma}) = \sigma_{xx} - \sigma_{yy} = 2\lambda\eta_0\dot{\gamma}^2, \quad N_2(\dot{\gamma}) = \sigma_{yy} - \sigma_{zz} = 0, \quad (2.109)$$

where $\eta_0 = \eta_N + \eta_p$ is the total viscosity. Hence, we see that the Oldroyd-B model predicts a constant shear-rate viscosity, a quadratic first normal stress difference and a zero second normal stress difference. For steady elongational flow, the equations

$$\begin{aligned} & \begin{pmatrix} \tau_{xx} & 0 & 0 \\ 0 & \tau_{yy} & 0 \\ 0 & 0 & \tau_{zz} \end{pmatrix} - \lambda \left\{ \begin{pmatrix} \dot{\epsilon} & 0 & 0 \\ 0 & -\frac{\dot{\epsilon}}{2} & 0 \\ 0 & 0 & -\frac{\dot{\epsilon}}{2} \end{pmatrix} \begin{pmatrix} \tau_{xx} & 0 & 0 \\ 0 & \tau_{yy} & 0 \\ 0 & 0 & \tau_{zz} \end{pmatrix} \right\} \\ & - \lambda \left\{ \begin{pmatrix} \tau_{xx} & 0 & 0 \\ 0 & \tau_{yy} & 0 \\ 0 & 0 & \tau_{zz} \end{pmatrix} \begin{pmatrix} \dot{\epsilon} & 0 & 0 \\ 0 & -\frac{\dot{\epsilon}}{2} & 0 \\ 0 & 0 & -\frac{\dot{\epsilon}}{2} \end{pmatrix} \right\} = 2\eta_p \begin{pmatrix} \dot{\epsilon} & 0 & 0 \\ 0 & -\frac{\dot{\epsilon}}{2} & 0 \\ 0 & 0 & -\frac{\dot{\epsilon}}{2} \end{pmatrix} \end{aligned}$$

yield

$$\tau_{xx} = \frac{2\eta_p \dot{\epsilon}}{1 - 2\lambda\dot{\epsilon}}, \quad \tau_{yy} = \tau_{zz} = -\frac{\eta_p \dot{\epsilon}}{1 + \lambda\dot{\epsilon}}. \quad (2.110)$$

Thus, the elongational viscosity is given by

$$\eta_E(\dot{\epsilon}) = \frac{3\eta_0}{(1 - 2\lambda\dot{\epsilon})(1 + \lambda\dot{\epsilon})}. \quad (2.111)$$

As shown in Figure 2.7 the elongational viscosity becomes infinitely large at the finite elongation rate $\dot{\epsilon} = \frac{1}{2\lambda}$. This is one of the severest disadvantages of the Oldroyd-B model.

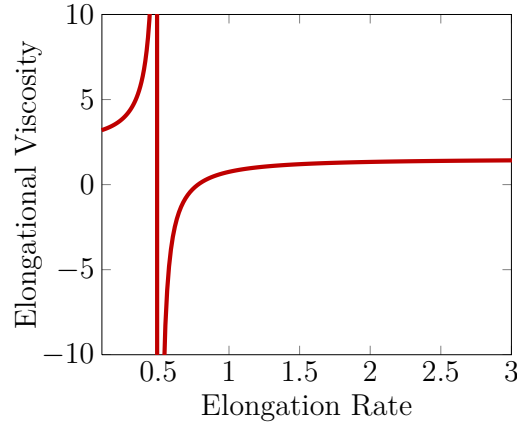


Figure 2.7.: Elongational viscosity predicted by Oldroyd-B model with unphysical singularity at $\dot{\epsilon} = \frac{1}{2\lambda}$.

2.5.5. Viscometric Functions for Giesekus Fluid

For steady simple shear flow, the Giesekus model reduces to the system of equations

$$\tau_{xx} - 2\lambda\tau_{xy}\dot{\gamma} + \frac{\alpha\lambda}{\eta_p} (\tau_{xx}^2 + \tau_{xy}^2) = 0, \quad (2.112)$$

$$\tau_{xy} - \lambda\tau_{yy}\dot{\gamma} + \frac{\alpha\lambda}{\eta_p} (\tau_{xy}(\tau_{xx} + \tau_{yy})) = \eta_p\dot{\gamma}, \quad (2.113)$$

$$\tau_{yy} + \frac{\alpha\lambda}{\eta_p} (\tau_{xy}^2 + \tau_{yy}^2) = 0, \quad (2.114)$$

$$\tau_{zz} + \frac{\alpha\lambda}{\eta_p} \tau_{zz}^2 = 0. \quad (2.115)$$

We investigate the equations following Renardy (2000). First, the physical relevant solution for τ_{zz} is

$$\tau_{zz} = 0, \quad (2.116)$$

as the first and second normal stress differences should approach zero for small shear rates.

Next, we can eliminate τ_{xx} and τ_{yy} from the system of equations to obtain a quadratic equation relating the shear rate $\dot{\gamma}$ to a given shear stress τ_{xy} , which yields

$$\begin{aligned} & \dot{\gamma}^2 \left(\frac{\eta_p}{\lambda^2} - \frac{\eta_p\alpha}{\lambda^2} - \frac{\eta_p}{\lambda^2} \tau_{xy}^2 \right)^2 + \dot{\gamma} \tau_{xy} \left(\frac{\eta_p}{\lambda^4} + \frac{\eta_p\alpha}{\lambda^4} - \frac{\alpha}{\eta_p\lambda^2} \tau_{xy} + \frac{8\alpha^2}{\lambda^2\eta_p} \tau_{xy}^2 - \frac{8\alpha^3}{\lambda^2\eta_p} \tau_{xy}^2 \right) \\ & + \frac{\alpha}{\eta_p} \tau_{xy}^2 \left(\frac{\eta_p}{\lambda^4} - \frac{\alpha}{\lambda^3} + \frac{\alpha}{\lambda^2\eta_p} \tau_{xy} - \frac{4\alpha}{\eta_p\lambda^2} \tau_{xy}^2 + \frac{4\alpha^3}{\lambda^2\eta_p} \tau_{xy}^2 \right) = 0. \end{aligned} \quad (2.117)$$

Investigating the solution of this quadratic equation in the limits of low and high shear rates yields

$$\dot{\gamma} \rightarrow \infty : \tau_{xy} = \frac{\eta_p}{\lambda} \sqrt{(1-\alpha)/\alpha} \quad (2.118)$$

$$\dot{\gamma} \rightarrow 0 : \begin{cases} \tau_{xy} = \eta_p \dot{\gamma} & \text{physical} \\ \tau_{xy} = \eta_p \dot{\gamma} \frac{(1-\alpha)}{\alpha} & \text{unphysical} \end{cases} \quad (2.119)$$

In the solution for high shear rates, we observe that we need to choose $\alpha < 1$ in order to obtain a solution in \mathbb{R} . For low shear rates, we obtain two solutions for the shear stress, which coincide for $\alpha = 0.5$. The solution $\tau_{xy} = \eta_p \dot{\gamma} \frac{1}{\alpha} (1-\alpha)$ can be ruled out as unphysical as it leads to nonzero normal stress differences in the limit of zero shear rate. The viscometric functions for the Giesekus model are given by

$$\eta(\dot{\gamma}) = \frac{\eta_N \dot{\gamma} + \tau_{xy}}{\dot{\gamma}}, \quad (2.120)$$

$$N_1(\dot{\gamma}) = \tau_{xx} - \tau_{yy}, \quad (2.121)$$

$$N_2(\dot{\gamma}) = \tau_{yy} - \tau_{zz}, \quad (2.122)$$

which in the limits of large and small shear rates yields

$$\dot{\gamma} \rightarrow 0 : \eta(\dot{\gamma}) = \eta_0, \quad N_1(\dot{\gamma}) \rightarrow 0, \quad N_2(\dot{\gamma}) \rightarrow 0 \quad (2.123)$$

$$\begin{aligned} \dot{\gamma} \rightarrow \infty : \eta(\dot{\gamma}) &= \eta_N, \quad N_1(\dot{\gamma}) \sim \sqrt{\dot{\gamma}}, \\ N_2(\dot{\gamma}) &= -\frac{\eta_p}{2\alpha\lambda} \left(1 - \sqrt{1 - 4\alpha(1-\alpha)} \right). \end{aligned} \quad (2.124)$$

The impact of the mobility parameter α on the viscometric functions is illustrated in Figure 2.8 (a) - (c) for $\alpha = 0, 0.1, 0.25, 0.5$. We see that the Giesekus model becomes increasingly shear thinning with increasing α and that the first and second normal stress differences decrease with increasing α . For uniaxial steady elongational flow, the Giesekus equations reduce to

$$(1 - 2\lambda\dot{\epsilon}) \tau_{xx} + \frac{\alpha\lambda}{\eta_p} \tau_{xx}^2 = 2\eta_p \dot{\epsilon}, \quad (2.125)$$

$$(1 + \lambda\dot{\epsilon}) \tau_{yy} + \frac{\alpha\lambda}{\eta_p} \tau_{yy}^2 = -\eta_p \dot{\epsilon}. \quad (2.126)$$

The physically relevant solutions have $\tau_{xx} > 0$ and $-\frac{\eta_p}{\lambda} < \tau_{yy} < 0$. This determines a unique value of τ_{xx} and τ_{yy} . The elongational viscosity is given by

$$\eta_E(\dot{\epsilon}) = 3\eta_N + \frac{\tau_{xx} - \tau_{yy}}{\dot{\epsilon}}. \quad (2.127)$$

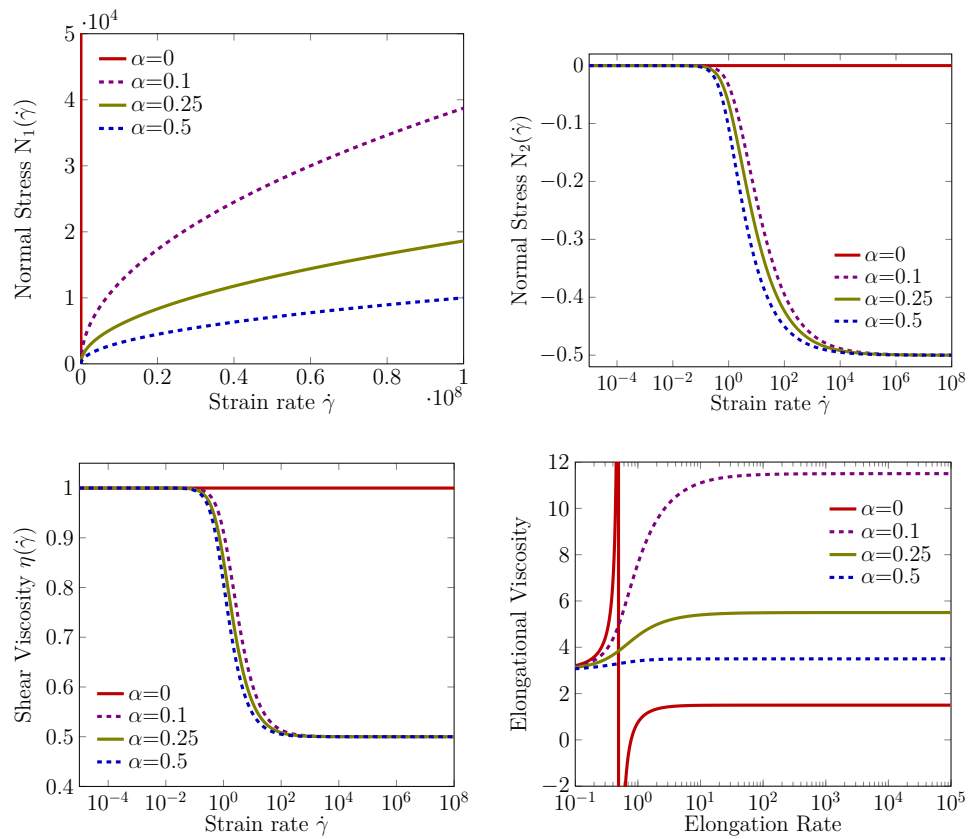


Figure 2.8.: Viscometric functions for the Giesekus model for a range of different α with $\lambda = 1$, $\eta_p = 0.5$ and $\eta_0 = 1$.

The elongational viscosity is finite for all elongation rates. It is an increasing function of the elongation rate as can be seen in Figure 2.8(d) and reaches a constant value for high elongation rates given by

$$\eta_E(\dot{\epsilon}) = 3\eta_N + 2\frac{\eta_p}{\alpha}. \quad (2.128)$$

That means the elongational viscosity decreases with increasing α .

2.6. Governing Equations

In summary, we have the following equations describing an incompressible viscoelastic fluid in a domain Ω_t with boundary Γ over a time interval $[0, T]$

$$\begin{cases} \rho \frac{D\mathbf{u}}{Dt} = \rho \mathbf{g} - \nabla p + \eta_N \nabla \cdot \mathbf{D} + \nabla \cdot \boldsymbol{\tau}, & \text{Momentum Equation} \\ \nabla \cdot \mathbf{u} = 0, & \text{Continuity Equation} \\ \boldsymbol{\tau} + \lambda \overset{\nabla}{\boldsymbol{\tau}} + \frac{\alpha \lambda}{\eta_p} \boldsymbol{\tau}^2 = 2\eta_p \mathbf{D}. & \text{Constitutive Equation} \end{cases} \quad (2.129)$$

The constitutive equation describing the viscoelastic response of the fluid to deformations contains the following models

$$\begin{cases} \text{Oldroyd-B:} & \alpha = 0; \\ \text{Giesekus:} & 0 \leq \alpha < 1. \end{cases} \quad (2.130)$$

The system of partial differential equations (2.129) is of mixed type and portrays traits of elliptic, parabolic and hyperbolic character (Gerritsma (1996); Owens and Phillips (2005)). The constitutive equations for the extra stress tensor contain the hyperbolic part, i.e. the components of the extra stress tensor are convected along the streamlines, while the conservation laws contain the elliptic/ parabolic part. To ensure the well-posedness of the equation system, we need to prescribe appropriate boundary and initial conditions as described in the following Section.

2.6.1. Boundary and Initial Conditions

In this Section, we describe suitable boundary and initial conditions in order to complete the equation system (2.129). For the conservation equations, we can distinguish between two boundary condition types: essential boundary conditions (Dirichlet boundary condi-

tions), for which we prescribe the velocity and natural boundary conditions, for which we prescribe the traction (Neumann boundary condition). That means, for the Dirichlet part of the boundary, denoted by Γ_D , we impose

$$\mathbf{u} = \mathbf{g}_u, \quad (2.131)$$

and for the Neumann part of the boundary, denoted by Γ_N , we impose

$$\boldsymbol{\sigma} \cdot \mathbf{n} = \mathbf{h}. \quad (2.132)$$

The constitutive equation is a hyperbolic equation that needs prescribed values at inflow

$$\boldsymbol{\tau} = \mathbf{g}_\tau. \quad (2.133)$$

We employed the following boundary and initial conditions.

Initial Conditions

At the initial time $t = t_0$, we need to prescribe the velocity \mathbf{u} and the polymeric stress $\boldsymbol{\tau}$

$$\mathbf{u}(\mathbf{x}, t_0) = \mathbf{u}_0 \quad \text{and} \quad \boldsymbol{\tau}(\mathbf{x}, t_0) = \boldsymbol{\tau}_0. \quad (2.134)$$

Typically, we either prescribe zero initial conditions for the velocity and the polymeric stress; or we set the initial values of velocity and polymeric stress equal to a previous solution in the same geometry with a different set of parameters.

No-Slip Boundary Conditions

At wall and obstacle boundaries, Γ_w , we prescribe no-slip and no-penetration boundary conditions for the velocity $\mathbf{u} = (u, v)$, i.e.

$$u = 0, v = 0 \quad \text{on } \Gamma_w. \quad (2.135)$$

The elastic stress is obtained from the constitutive equation using the velocity.

Slip Boundary Conditions

The slip boundary condition, Γ_{sl} , is a combination of Dirichlet and Neumann conditions

$$\mathbf{u} \cdot \mathbf{n} = 0 \quad \text{on } \Gamma_{sl}, \quad (2.136)$$

$$\mathbf{t} \cdot \boldsymbol{\sigma} \cdot \mathbf{n} = 0 \quad \text{on } \Gamma_{sl}. \quad (2.137)$$

Alternatively, we can employ Navier's slip condition in order to account for wall friction

$$\mathbf{u} \cdot \mathbf{n} = 0 \quad \text{on } \Gamma_{sl}, \quad (2.138)$$

$$\mathbf{t} \cdot \boldsymbol{\sigma} \cdot \mathbf{n} = \frac{1}{\beta_{sl}} \mathbf{u} \cdot \mathbf{t} \quad \text{on } \Gamma_{sl}, \quad (2.139)$$

where β_{sl} is an empirical slip length with the dimension of length. This condition expresses a linear dependency of the tangential velocity component to the shear rate at the boundary. For pure shear flow, the parameter β_{sl} can be interpreted as the fictitious distance below the boundary, where the no slip condition would be satisfied. The condition $\mathbf{u} \cdot \mathbf{n} = 0$ ensures that mass cannot penetrate the boundary.

Symmetry Boundary Conditions

Similar to the slip boundary condition, the symmetry condition, Γ_{sym} , is a combination of Dirichlet and Neumann conditions given by

$$\mathbf{u} \cdot \mathbf{n} = 0 \quad \text{on } \Gamma_{sym}, \quad (2.140)$$

$$\mathbf{t} \cdot \boldsymbol{\sigma} \cdot \mathbf{n} = 0 \quad \text{on } \Gamma_{sym}, \quad (2.141)$$

which means fluid cannot penetrate the boundary and the shear stress is zero.

Inflow Boundary Conditions

At the inflow boundary Γ_{in} of the domain, we prescribe the velocity field of the flow. For viscoelastic fluids, the values for the polymeric stress components are also required at inflow, because they represent the information carried with the fluid from its previous deformation states. Therefore, we set Dirichlet boundary conditions for the velocity field and the polymeric stress tensor at inflow

$$\mathbf{u} = \mathbf{u}_{in} \quad \text{on } \Gamma_{in}, \quad (2.142)$$

$$\boldsymbol{\tau} = \boldsymbol{\tau}_{in} \quad \text{on } \Gamma_{in}. \quad (2.143)$$

We have to be aware that it is not possible to simply prescribe arbitrary stress values at inflow, because they have to be consistent with the constitutive equations. If we don't know the stress response to the prescribed velocity field, we assume that the polymeric stress is zero at inflow, i.e.

$$\boldsymbol{\tau} = \mathbf{0} \quad \text{on } \Gamma_{in}. \quad (2.144)$$

Renardy (1988) showed that, while for the Oldroyd-B model all elastic stress components must be prescribed, for the UCM model prescribing all stress components leads to an over-

determined system, which can lead to errors. However, we will not use the UCM model and therefore we always set Dirichlet conditions for the polymeric stress tensor at inflow.

Outflow Boundary Conditions

At the outflow boundary Γ_{out} , we impose one of the following boundary conditions

1. a combination of Dirichlet and Neumann boundary conditions

$$\mathbf{u} \cdot \mathbf{t} = 0, \quad (2.145)$$

$$\mathbf{t} \cdot \boldsymbol{\sigma} \cdot \mathbf{n} = 0, \quad \mathbf{n} \cdot \boldsymbol{\sigma} \cdot \mathbf{n} = -p_\infty. \quad (2.146)$$

where $\boldsymbol{\sigma}$ is the Cauchy stress tensor, \mathbf{t} is the unit tangential vector to the boundary and p_∞ is a prescribed pressure. The prescribed pressure is usually set to zero.

2. imposed pressure $p = p_\infty$ through the boundary integral
3. for fully developed unidirectional flow fields at outflow, we impose

$$\nabla u \cdot \mathbf{n} = \nabla v \cdot \mathbf{n} = 0 \quad \text{on } \Gamma_{out}, \quad (2.147)$$

through the boundary integral in conjunction with imposing a pressure value at outflow.

Free Surface Boundary Conditions

At a free surface boundary, Γ_f , we have a combination of Dirichlet and Neumann boundary conditions

$$\mathbf{u} \cdot \mathbf{n} = \mathbf{w} \cdot \mathbf{n} \quad \text{on } \Gamma_f \quad (\text{kinematic boundary condition}) \quad (2.148)$$

$$[\boldsymbol{\sigma}] \cdot \mathbf{n} = \sigma \kappa \mathbf{n} \quad \text{on } \Gamma_f \quad (\text{dynamic boundary condition}) \quad (2.149)$$

where \mathbf{w} is the velocity of the free surface, σ is the surface tension coefficient, κ is the curvature of the free surface, \mathbf{n} is the unit outward normal on the free surface and $[\boldsymbol{\sigma}]$ denotes the jump in the Cauchy stress tensor across the free surface. We will describe a few further details considering the boundary conditions.

Dynamic Boundary Condition Assume the free surface is an interface between a liquid and a gas. The dynamic boundary condition sets the sum of the contact forces given by the traction exerted from the fluid to the gas and the traction exerted by the gas to the

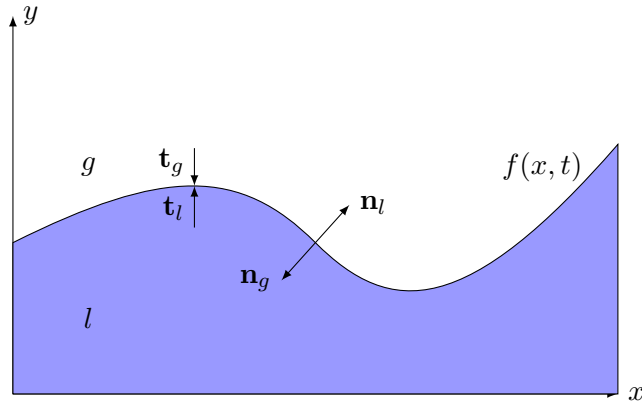


Figure 2.9.: Free Surface Boundary Conditions

fluid equal to the surface tension

$$\mathbf{t}_l + \mathbf{t}_g = \boldsymbol{\sigma}_l \cdot \mathbf{n}_l + \boldsymbol{\sigma}_g \cdot \mathbf{n}_g = (\boldsymbol{\sigma}_l - \boldsymbol{\sigma}_g) \cdot \mathbf{n}_l = \sigma \kappa \mathbf{n}_l \quad (2.150)$$

where $\boldsymbol{\sigma}_g$ is the Cauchy stress tensor of the gas phase and $\boldsymbol{\sigma}_l$ is the Cauchy stress tensor of the liquid phase and we define the jump

$$[\boldsymbol{\sigma}] := \boldsymbol{\sigma}_l - \boldsymbol{\sigma}_g. \quad (2.151)$$

If we assume that the gas is inviscid, then the Cauchy stress tensor of the gas is given by

$$\boldsymbol{\sigma}_g = -p_g \mathbf{I}, \quad (2.152)$$

and the dynamic boundary condition becomes

$$\boldsymbol{\sigma}_l \cdot \mathbf{n}_l = \sigma \kappa \mathbf{n}_l - p_g \mathbf{n}_l \quad (2.153)$$

which can be expressed in terms of a condition on the tangential and normal stress as

$$\mathbf{n}_l \cdot \boldsymbol{\sigma}_l \cdot \mathbf{n}_l = \sigma \kappa - p_g, \quad (2.154)$$

$$\mathbf{s}_l \cdot \boldsymbol{\sigma}_l \cdot \mathbf{n}_l = 0, \quad (2.155)$$

where \mathbf{s}_l is the unit tangent vector on the free surface.

Kinematic Boundary Condition The kinematic boundary condition ensures that no particle crosses the interface. Note that, we can describe the free surface as a function

$$f(x, t) = y. \quad (2.156)$$

This function can then be used to determine the unit outward normals \mathbf{n} and the curvature κ of the free surface using

$$\mathbf{n}(t) = \frac{1}{\sqrt{\frac{\partial f(x,t)^2}{\partial x} + 1}} \begin{pmatrix} -\frac{\partial f(x,t)}{\partial x} \\ 1 \end{pmatrix}, \quad (2.157)$$

$$\kappa(t) = \frac{|\frac{\partial^2 f(x,t)}{\partial x^2}|}{(1 + \frac{\partial f(x,t)^2}{\partial x})^{3/2}}. \quad (2.158)$$

The kinematic boundary condition just gives a constraint on the normal velocity. However there is no condition on the tangential velocity. In this work, we use the ALE scheme to trace the free surface movement. In these schemes, we move the mesh with the normal fluid velocity at the free surface and choose the tangential mesh velocity such that the distortion of the mesh is minimal. For problems that can be expressed as a function $f(x, t) = y$, setting $w_x = 0$ usually prevents the mesh from distorting. The kinematic boundary condition can then be expressed with $w_y = \frac{\partial y}{\partial t} = \frac{\partial f(x, t)}{\partial t}$ and $\frac{n_y}{n_x} = -\frac{\partial f(x, t)}{\partial x}$ as

$$\frac{\partial f(x, t)}{\partial t} + u \frac{\partial f(x, t)}{\partial x} = v. \quad (2.159)$$

Alternatively, we can express the free surface using the zero level set value of a function

$$F(x, y, t) \equiv f(x, t) - y = 0 \quad (2.160)$$

and solve

$$\frac{DF(x, y, t)}{Dt} = 0. \quad (2.161)$$

2.6.2. Weak Formulation

In the finite element method and in spectral methods, the equations are solved in their weak form. To obtain the weak form of the equations, we multiply them by test functions and integrate the equations. We need to choose appropriate spaces for the dependent variables \mathbf{u} , p and $\boldsymbol{\tau}$ and for their test functions. For the velocity \mathbf{u} , we choose

$$[H_D^1(\Omega)]^d := \{\mathbf{u} \in [H^1(\Omega)]^d : \mathbf{u} = \mathbf{u}_D \text{ on } \Gamma_D\}, \quad (2.162)$$

where Γ_D is the part of Γ on which Dirichlet conditions are imposed and $d = 2, 3$ is the space dimension. The corresponding test functions $\phi_{\mathbf{u}}$ are chosen to be in

$$[H_0^1(\Omega)]^d := \{\phi_{\mathbf{u}} \in [H^1(\Omega)]^d : \phi_{\mathbf{u}} = \mathbf{0} \text{ on } \Gamma_D\}. \quad (2.163)$$

For the pressure p and the corresponding test functions ψ , we choose

$$L_0^2(\Omega) := \{q \in L^2(\Omega) : \int_{\Omega_t} q \, d\Omega = 0\}. \quad (2.164)$$

The polymeric stress $\boldsymbol{\tau}$ and corresponding test functions $\phi_{\boldsymbol{\tau}}$ are chosen to be in $[L^2(\Omega)]_s^{d^2}$, where s denotes the space of symmetric tensors. The weak formulation reads

Problem 2.8. Find $(\mathbf{u}, p, \boldsymbol{\tau}) \in [H_D^1(\Omega)]^2 \times [L_0^2(\Omega)] \times [L^2(\Omega)]_s^{d^2}$ such that, for all $(\phi_{\mathbf{u}}, \psi, \phi_{\boldsymbol{\tau}}) \in [H_0^1(\Omega)]^d \times [L_0^2(\Omega)] \times [L^2(\Omega)]_s^{d^2}$

$$\begin{aligned} & \rho \int_{\Omega_t} \frac{D\mathbf{u}}{Dt} \cdot \phi_{\mathbf{u}} \, d\Omega + 2\eta_N \int_{\Omega_t} \mathbf{D} : \nabla \phi_{\mathbf{u}} \, d\Omega - \int_{\Omega_t} p (\nabla \cdot \phi_{\mathbf{u}}) \, d\Omega + \int_{\Omega_t} \boldsymbol{\tau} : \nabla \phi_{\mathbf{u}} \, d\Omega, \\ & - \int_{\Gamma_N} (\boldsymbol{\sigma} \cdot \mathbf{n}) \cdot \phi_{\mathbf{u}} \, d\Gamma = 0, \\ & \int_{\Omega_t} (\nabla \cdot \mathbf{u}) \psi \, d\Omega = 0, \end{aligned} \quad (2.165)$$

$$\begin{aligned} & \lambda \int_{\Omega_t} \left(\frac{D\boldsymbol{\tau}}{Dt} - \nabla \mathbf{u} \cdot \boldsymbol{\tau} - \boldsymbol{\tau} \cdot \nabla \mathbf{u}^T \right) : \phi_{\boldsymbol{\tau}} \, d\Omega + \int_{\Omega_t} \boldsymbol{\tau} : \phi_{\boldsymbol{\tau}} \, d\Omega + \frac{\alpha\lambda}{\eta_p} \int_{\Omega_t} \boldsymbol{\tau}^2 : \phi_{\boldsymbol{\tau}} \, d\Omega \\ & = 2\eta_p \int_{\Omega_t} \mathbf{D} : \phi_{\boldsymbol{\tau}} \, d\Omega, \end{aligned} \quad (2.166)$$

where Γ_N is the Neumann boundary.

Here, we integrated the momentum equation by parts. The Neumann boundary condition can be decomposed into the outflow boundary part, the symmetry boundary part, the slip boundary part and the free surface boundary part. That means the boundary integral is given by

$$\begin{aligned} \int_{\Gamma_N} (\boldsymbol{\sigma} \cdot \mathbf{n}) \cdot \phi_{\mathbf{u}} \, d\Gamma &= \int_{\Gamma_{out}} (\boldsymbol{\sigma} \cdot \mathbf{n}) \cdot \phi_{\mathbf{u}} \, d\Gamma + \int_{\Gamma_{sym}} (\boldsymbol{\sigma} \cdot \mathbf{n}) \cdot \phi_{\mathbf{u}} \, d\Gamma \\ &+ \int_{\Gamma_{sl}} (\boldsymbol{\sigma} \cdot \mathbf{n}) \cdot \phi_{\mathbf{u}} \, d\Gamma + \int_{\Gamma_f} (\boldsymbol{\sigma} \boldsymbol{\kappa} \cdot \mathbf{n}) \cdot \phi_{\mathbf{u}} \, d\Gamma. \end{aligned} \quad (2.167)$$

2.7. Non-Dimensionalisation

We employ the following non-dimensionalisation

$$x^* = \frac{x}{L}, \quad \mathbf{u}^* = \frac{\mathbf{u}}{U}, \quad t^* = \frac{U}{L} t, \quad \rho^* = \frac{\rho}{\rho_{ref}}, \quad p^* = \frac{L}{\eta_0 U} p, \quad \boldsymbol{\tau}^* = \frac{L}{\eta_0 U} \boldsymbol{\tau},$$

where L, U, ρ_{ref} denote the characteristic length, velocity and density scales for the flow respectively. This leads to the following system of dimensionless equations

$$\begin{cases} \text{Re} \frac{D\mathbf{u}^*}{Dt} = -\nabla p^* + 2\beta \nabla \cdot \mathbf{D}^* + \nabla \cdot \boldsymbol{\tau}^*, \\ \boldsymbol{\tau}^* + \text{Wi} \overset{\nabla}{\boldsymbol{\tau}^*} + \frac{\alpha \text{Wi}}{(1-\beta)} (\boldsymbol{\tau}^*)^2 = 2(1-\beta) \mathbf{D}^*, \\ \nabla \cdot \mathbf{u}^* = 0. \end{cases} \quad (2.168)$$

We recall the upper convected derivative

$$\overset{\nabla}{\boldsymbol{\tau}^*} = \frac{\partial \boldsymbol{\tau}^*}{\partial t} + \mathbf{u} \cdot \nabla \boldsymbol{\tau}^* - \nabla \mathbf{u}^* \cdot \boldsymbol{\tau}^* - \boldsymbol{\tau}^* \cdot \nabla \mathbf{u}^{*T}. \quad (2.169)$$

The dimensionless numbers in (2.168) describe the nature of the flow and are defined as follows:

Definition 2.9 (Dimensionless Numbers).

$$\text{Re} = \frac{UL\rho_{ref}}{\eta_0} = \frac{\text{inertial forces}}{\text{viscous forces}} \quad (2.170)$$

is the ratio of inertial forces to viscous forces and is called the **Reynolds number**.

$$\text{Wi} = \lambda \frac{U}{L} = \frac{\lambda}{T} = \frac{\text{relaxation time}}{\text{characteristic time}} \quad (2.171)$$

is the ratio of the relaxation time to the characteristic time scale of the fluid process and is called the **Weissenberg number**. It can be regarded as a measure of the elasticity of the fluid in the flow. For high Weissenberg numbers, the fluid behaves like an elastic solid and for low Weissenberg numbers, it behaves like a Newtonian fluid. Another useful dimensionless number describing the importance of elasticity relative to inertial forces is the so-called **elasticity number**, which we define as

$$\text{El} = \frac{\text{Wi}}{\text{Re}}. \quad (2.172)$$

Furthermore, we define

$$\beta = \frac{\eta_N}{\eta_0} \quad (2.173)$$

which is measuring the percentage of the solvent Newtonian viscosity η_N to the total viscosity $\eta_0 = \eta_N + \eta_p$, i.e. $0 \leq \beta \leq 1$. Here, η_p denotes the polymeric viscosity.

In addition, we have dimensionless numbers arising from the non-dimensionalisation of

the boundary conditions.

Definition 2.10 (Dimensionless Numbers - Boundary Conditions). *For the slip boundary condition, we have*

$$B_{sl} (\mathbf{t} \cdot \boldsymbol{\sigma}^* \cdot \mathbf{n}) = \mathbf{u}^* \cdot \mathbf{t} \quad \text{on } \Gamma_{sl}, \quad (2.174)$$

where the slip coefficient

$$B_{sl} = \frac{\beta_{sl} \eta_0}{L} \quad (2.175)$$

measures the fluid slip at the wall. For $B_{sl} = 0$, we recover the no-slip boundary condition. For the free surface boundary condition, we have

$$\boldsymbol{\sigma}^* \cdot \mathbf{n} = \frac{\kappa^*}{Ca} \mathbf{n} \quad (2.176)$$

where the capillary number

$$Ca = \frac{U \eta_0}{\sigma} \quad (2.177)$$

measures viscous forces over surface tension effects. For high capillary numbers, viscous forces dominate and for low capillary numbers, surface tension dominates.

In the following, we will drop the star notation for the sake of simplicity. The non-dimensionalised weak form reads

Problem 2.11. Find $(\mathbf{u}, p, \boldsymbol{\tau}) \in [H_D^1(\Omega)]^2 \times [L_0^2(\Omega)] \times [L^2(\Omega)]_s^{d^2}$ such that, for all $(\phi_{\mathbf{u}}, \psi, \phi_{\boldsymbol{\tau}}) \in [H_0^1(\Omega)]^d \times [L_0^2(\Omega)] \times [L^2(\Omega)]_s^{d^2}$

$$\left\{ \begin{array}{l} Re \int_{\Omega_t} \frac{D\mathbf{u}}{Dt} \cdot \phi_{\mathbf{u}} d\Omega + 2\beta \int_{\Omega_t} \mathbf{D} : \nabla \phi_{\mathbf{u}} d\Omega - \int_{\Omega_t} p (\nabla \cdot \phi_{\mathbf{u}}) d\Omega \\ + \int_{\Omega_t} \boldsymbol{\tau} : \nabla \phi_{\mathbf{u}} d\Omega - \int_{\Gamma_N \setminus \Gamma_f} (\boldsymbol{\sigma} \cdot \mathbf{n}) \cdot \phi_{\mathbf{u}} d\Gamma - \frac{1}{Ca} \int_{\Gamma_f} \kappa \mathbf{n} \cdot \phi_{\mathbf{u}} d\Gamma = 0, \\ \int_{\Omega_t} (\nabla \cdot \mathbf{u}) \psi d\Omega = 0, \\ Wi \int_{\Omega_t} \left(\frac{D\boldsymbol{\tau}}{Dt} - \nabla \mathbf{u} \cdot \boldsymbol{\tau} - \boldsymbol{\tau} \cdot \nabla \mathbf{u}^T \right) : \phi_{\boldsymbol{\tau}} d\Omega + \int_{\Omega_t} \boldsymbol{\tau} : \phi_{\boldsymbol{\tau}} d\Omega \\ + \frac{\alpha Wi}{(1-\beta)} \int_{\Omega_t} \boldsymbol{\tau}^2 : \phi_{\boldsymbol{\tau}} d\Omega = 2(1-\beta) \int_{\Omega_t} \mathbf{D} : \phi_{\boldsymbol{\tau}} d\Omega, \end{array} \right.$$

where Γ_N is the Neumann boundary and Γ_f is the free surface boundary.

Chapter 3

Spectral/hp element methods

In this Chapter, we review several numerical methods for solving partial differential equations including the finite element method, spectral methods and spectral/hp element methods. Then, we present details about the spectral/hp element method employed in this thesis. We introduce the integration and differentiation on general shaped elements including the iso-parametric geometrical mapping and we give their corresponding matrix notations. In this work, we employ the spectral/hp element method to solve the equations describing viscoelastic flow. Then, we discuss the continuous Galerkin and the discontinuous Galerkin methods to couple the spectral elements. Finally, we demonstrate the capabilities and the limitations of the spectral/hp element method in comparison to the finite element method for a one-dimensional constant linear advection equation for three functions with decreasing smoothness. The explanations given in this Chapter draw on the monographs by Karniadakis and Sherwin (2005), Kopriva (2009), Trefethen (2000) and Canuto et al. (2006) and the thesis of Vos (2011).

3.1. Discretisation

3.1.1. Discretisation of the Solution Space

The issue of how to approximate the solution of a differential equation in a discrete space can be illustrated using the so-called *method of weighted residuals*. Consider a linear differential equation for the unknown function u defined in some domain Ω given by

$$\mathcal{L}(u) = f, \quad (3.1)$$

subject to appropriate initial and boundary conditions. Further, assume an appropriate space for the unknown function u is given by \mathcal{V} . Then, the solution $u(x)$ can be approximated by the truncated series $u^\delta(x)$

$$u^\delta(x) = \sum_{i=0}^{N_{dof}-1} \hat{u}_i \phi_i(x), \quad (3.2)$$

where \hat{u}_i are called *expansion coefficients* and ϕ_i are called *trial or expansion functions*. This approximation of the unknown means we are no longer determining the exact solution in \mathcal{V} but an approximate solution in a discrete subspace \mathcal{V}^δ which, in general, yields a non zero residual

$$R(u^\delta) = L(u^\delta) - f \neq 0. \quad (3.3)$$

To obtain the unknown coefficients, the aim of the method of weighted residuals is to force the residual to zero in some average sense over the domain by forming the inner product of the residual R with so-called *weight or test functions* $v_j(x)$ in the test function space \mathcal{W}^δ , that is,

$$\int_{\Omega} R(u^\delta, x) v_j(x) dx = 0, \quad j = 1, \dots, N_{dof}. \quad (3.4)$$

These N_{dof} conditions form a system of ordinary differential equations in $\hat{u}_i(t)$. As $N_{dof} \rightarrow \infty$, the residual tends to zero since the approximate solution approaches the exact solution.

The choice of the expansion functions $\phi_i(x)$ and the test functions v_j determines the numerical scheme. The most popular choices are

- *Collocation method*: The test functions are chosen to be the Dirac delta functions, i.e. $v_j = \delta(x - x_j)$, which yields

$$R(u^\delta, x_j) = 0, \quad j = 1, \dots, N_{dof}. \quad (3.5)$$

Here, x_j denotes a set of given distinct collocation points. In the context of spectral methods the use of collocation projection is called *pseudo-spectral method*.

- *Galerkin method*: The test functions are chosen to be the same as the trial or expansion functions $v_j = \phi_j$.
- *Petrov-Galerkin method*: The test functions are chosen such that $v_j \neq \phi_j$ but typically they are based upon a perturbation of the trial functions, e.g. to impose an upwind condition.

3.1.2. Discretisation of the Domain

To approximate the solution of a differential equation in a complex geometry Ω , we subdivide the domain into non-overlapping subdomains Ω_e , i.e.

$$\Omega = \bigcup_{e=1}^{N_{el}} \Omega_e, \quad \Omega_{e_1} \cap \Omega_{e_2} = \emptyset \text{ for } e_1 \neq e_2. \quad (3.6)$$

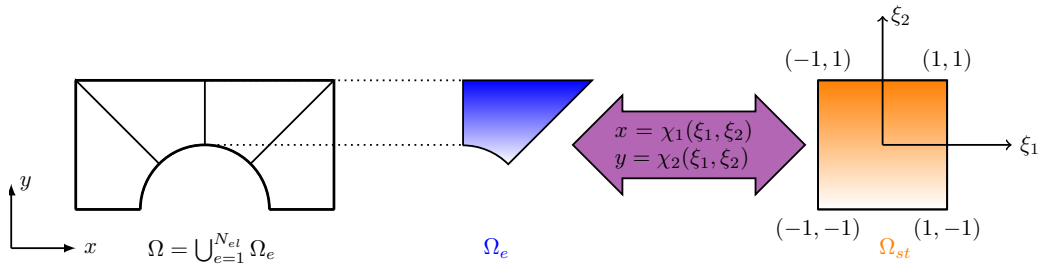


Figure 3.1.: Domain decomposition and mapping onto standard element.

where N_{el} is the number of subdomains or elements. Each of these subdomains, Ω_e , is then mapped onto a standard element Ω_{st} using a transformation χ^e . This transformation maps the physical coordinates \mathbf{x} onto the standard coordinates $\boldsymbol{\xi}$. For quadrilateral subdomains in two space dimensions, the standard element is given by

$$\Omega_{st} = \{(\xi_1, \xi_2) \mid -1 \leq \xi_i \leq 1, i = 1, 2\}. \quad (3.7)$$

Usually, we construct the mapping by expressing the physical coordinates x and y in terms of the same expansion functions as the ones that we use to represent the dependent variables. These type of same-order mappings for the geometry are called *isoparametric*. Details on the isoparametric mappings for the different discretisation techniques are given in Section 3.4.

To obtain a global solution from the elemental solutions, we need to introduce some form of coupling between adjacent elements. This coupling of the elements is achieved either by enforcing continuity of the approximation in some sense (weak or strong) (*continuous Galerkin*) or by considering fluxes across element boundaries (*discontinuous Galerkin*). Details about these methods can be found in Section 3.3.1.

3.2. Numerical Methods

3.2.1. Finite element method

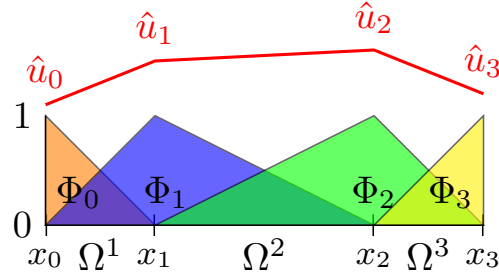


Figure 3.2.: One-dimensional finite element expansion.

The classical finite element method uses a decomposition of the domain and builds up the solution from the local elemental contributions. In each element the solution is approximated by piecewise polynomial expansion functions. For example in 1D, the linear basis functions are given by

$$\phi_0(\xi) = \begin{cases} \frac{1-\xi}{2}, & \xi \in \Omega_{st} \\ 0, & \xi \notin \Omega_{st} \end{cases}, \quad \phi_1(\xi) = \begin{cases} \frac{1+\xi}{2}, & \xi \in \Omega_{st} \\ 0, & \xi \notin \Omega_{st} \end{cases} \quad (3.8)$$

where $\Omega_{st} = \{\xi \mid -1 \leq \xi \leq 1\}$ and the standard coordinate ξ is related to the physical coordinate x by the mapping

$$x = \chi^e(\xi) = \phi_0(\xi)x_{e-1} + \phi_1(\xi)x_e \quad (3.9)$$

where $\Omega_e = \{x \mid x_{e-1} < x < x_e\}$. In the example shown in Figure 3.2, the global solution u^δ is then obtained in terms of the global expansion modes Φ_i , which are constructed from the local expansion modes, e.g.

$$\begin{aligned} \Phi_0 &= \begin{cases} \phi_0(\xi) = \phi_0([\chi^1]^{-1}(x)), & x \in \Omega^1, \\ 0, & x \notin \Omega^1, \end{cases} \\ \Phi_1 &= \begin{cases} \phi_1(\xi) = \phi_1([\chi^1]^{-1}(x)), & x \in \Omega^1, \\ \phi_0(\xi) = \phi_0([\chi^2]^{-1}(x)), & x \in \Omega^2, \\ 0, & \text{otherwise.} \end{cases} \end{aligned} \quad (3.10)$$

The approximated solution then becomes (see Figure 3.2)

$$u^\delta(x, t) = \sum_{i=0}^{N_{dof}-1} \hat{u}_i \Phi_i(x) = \sum_{e=1}^{N_{el}} (\hat{u}_0^e \phi_0^e(\xi) + \hat{u}_1^e \phi_1^e(\xi)). \quad (3.11)$$

If we are seeking a continuous solution, we can determine the global expansion coefficients from the local expansion coefficients by enforcing continuity in the local expansion coefficient, e.g.

$$\hat{u}_0 = \hat{u}_0^1, \quad (3.12)$$

$$\hat{u}_1 = \hat{u}_1^1 = \hat{u}_0^2 \quad \text{etc.} \quad (3.13)$$

We can express these relations in terms of a sparse matrix that scatters the global degrees of freedom onto the local degrees of freedom

$$\hat{\mathbf{u}}_l = \mathcal{A} \hat{\mathbf{u}}_g, \quad (3.14)$$

where

$$\hat{\mathbf{u}}_g = [\hat{u}_0, \dots, \hat{u}_{N_{dof}-1}]^T, \quad (3.15)$$

$$\hat{\mathbf{u}}_l = [\hat{u}_0^1, \hat{u}_1^1, \dots, \hat{u}_0^{N_{el}}, \hat{u}_1^{N_{el}}]^T. \quad (3.16)$$

3.2.2. Spectral Method

In contrast to the finite element method, which is based on the computation of local solutions, spectral methods, first presented by Gottlieb and Orszag (1977), represent a function u in the entire domain via a truncated series expansion of high order polynomials

$$u^\delta(x, t) = \sum_{p=0}^P \hat{u}_p(t) \phi_p(x). \quad (3.17)$$

For classical global spectral methods, these basis functions are typically given by Fourier basis functions

$$\phi_p(x) = e^{ipx} \quad (3.18)$$

which are subject to periodic boundary conditions, or orthogonal polynomials which are a member of the family of Jacobi polynomials $P_p^{(\alpha, \beta)}$ (see Appendix A for details), such

as Legendre polynomials

$$\phi_p(x) = L_p(x) = P_p^{(0,0)}(x) \quad (3.19)$$

or Chebyshev polynomials

$$\phi_p(x) = T_p(x) = \frac{2^{2n}(n!)^2}{(2n)!} P_p^{(-1/2,-1/2)}(x). \quad (3.20)$$

Jacobi polynomials are not subject to periodic boundary conditions and maintain the approximation property of exponentially decaying coefficients \hat{u}_n for smooth functions $u \in C^\infty$ of the Fourier series. This property of exponentially decaying coefficients yields *spectral or exponential convergence* to the exact solution in the approximation of a smooth function with a truncated series.

In the spectral method, these series expansions are then used in the context of the method of weighted residuals. That means the solution to a differential equation can be computed using collocation methods (pseudo-spectral method), Galerkin methods or other methods as explained in Section 3.1.1.

3.2.3. Spectral/hp element method

As global spectral methods are restricted to simple geometries due to difficulties that we encounter if we try to combine these expansions with h -type elemental decompositions, modifications to the classical spectral method were made in order to extend the method to complex geometries while maintaining their excellent approximation properties. The difficulty with a basis formed by orthogonal polynomials such as Legendre polynomials is that if we want to couple the elements by imposing C^0 continuity across element boundaries, we need to prescribe an interface matching condition of the form

$$\sum_{p=0}^P \hat{u}_p^e \phi_p^e(1) = \sum_{p=0}^P \hat{u}_p^{e+1} \phi_p^{e+1}(-1), \quad (3.21)$$

where the superscripts e and $e+1$ denote contributions from two adjacent domains. Such a condition couples all of the degrees of freedom in one element with the modes in the adjacent element. This is more difficult to implement and it destroys the sparsity of the global matrix structure. Therefore, we seek expansions for which only a few expansion modes have a non-zero contribution at an elemental boundary and which we can decompose into boundary and interior modes. Boundary modes only have non-zero contributions at one

of the elemental boundaries and are zero on all other boundaries and interior modes have non-zero contributions in the interior of the element.

In general, spectral methods can be classified into two categories: modal methods, where the unknowns are coefficients or modes and nodal methods, where we represent the solution in terms of grid points values and the coefficients are associated with these grid point values.

Modal expansion bases are built up hierarchically, which means the expansion set of order $P - 1$ is contained within the expansion set of order P . This property does not hold for the nodal basis - the expansion sets of orders $P - 1$ and P do not have common members. Note that, we can formulate any modal expansion basis in terms of a Lagrangian interpolant through the grid points by

$$h_j(x) = \frac{g(x)}{g'(x)(x - x_j)}. \quad (3.22)$$

where $g(x)$ is the polynomial of order $P + 1$ with zeros at the $P + 1$ nodal points x_j . We will introduce two examples for possible spectral element bases, which have a boundary-interior decomposition: one modal expansion, which builds the basis for a method we will call the *spectral/hp method* due to Karniadakis and Sherwin (2005); and one nodal expansion, which builds the basis for a method that has become known as *the spectral element method* due to Patera (1984).

Nodal spectral element method

The nodal expansion basis due to Patera (1984) is constructed using Legendre polynomials, defined in (3.19), in the construction of Lagrange polynomials through the Gauss-Lobatto-Legendre (GLL) points ξ_p

$$\phi_p(\xi) = h_p(\xi) = \frac{(\xi - 1)(\xi + 1)L'_P(\xi)}{P(P + 1)L_P(\xi_p)(\xi_p - \xi)}. \quad (3.23)$$

The Gauss-Lobatto-Legendre points are the zeroes of $g(\xi) = (1 - \xi)(1 + \xi)L'_P(\xi)$. Note that, all modes are polynomials of order P with $h_p(\xi_q) = \delta_{pq}$. The Gauss-Lobatto Legendre points contain the boundary points of the element -1 and 1 and therefore these modes are decomposed into interior and boundary modes. The resulting polynomials of this Lagrange basis are displayed in Figure 3.3(a).

In addition to the convenient boundary interior decomposition, this Lagrange basis has several other advantages: firstly, the quadrature weights for Gaussian quadrature in the numerical evaluation of integrals are unity and secondly the construction of the Lagrange

basis through the GLL points avoids a problem that can be encountered in the construction of Lagrange polynomials: the Runge phenomenon. The Runge phenomenon manifests itself in terms of violent oscillations near the end points $x = -1$ and $x = 1$ for Lagrange polynomials which are constructed through equidistant points. These oscillations can be prevented using interpolation points distributed with a spacing of $O(N^{-2})$ near $x = \pm 1$ and $O(N^{-1})$ spacing in the interior (see Trefethen (2000) for a further explanation), which is fulfilled by the GLL points.

Modal spectral element method

The modal expansion basis based on Dubiner (1991) and extended by Karniadakis and Sherwin (2005) is another choice for a high order expansion basis which is applicable to h -type domain decomposition due to its boundary interior decomposition. This modal (hierarchical) expansion basis is constructed by adding second and higher-order polynomials to the linear finite element expansion. Note that in contrast to classical spectral methods this expansion is a set of polynomials of increasing order with maximal order P . The boundary interior decomposition is ensured as follows: the linear finite element expansion functions give us the elemental boundary modes and since only polynomials of second and higher order are added, it is possible to ensure that they are zero at the elemental boundaries, thereby meeting the requirements for interior modes. In addition, we choose the higher order modes such that the mass and Laplacian elemental matrices have a minimal bandwidth. The expansion basis fulfilling these requirements is given by

$$\phi_p(\xi) = \begin{cases} \frac{1-\xi}{2}, & p = 0, \\ \left(\frac{1-\xi}{2}\right) \left(\frac{1+\xi}{2}\right) P_{p-1}^{(1,1)}(\xi), & 0 < p < P \\ \frac{1+\xi}{2}, & p = P, \end{cases} \quad (3.24)$$

where ϕ_0 and ϕ_P are the linear finite element basis functions and

$$\phi_1(\xi) = \left(\frac{1-\xi}{2}\right) \left(\frac{1+\xi}{2}\right)$$

is the usual quadratic hierarchical expansion mode for quadratic elements. Here, P denotes the highest polynomial order of the hierarchical expansion and $P_p^{(\alpha,\beta)}(\xi)$ denotes the p th-order Jacobi polynomial. Figure 3.3(b) shows plots of the expansion modes ϕ_p for $0 \leq p \leq 5$. For the two dimensional standard quadrilateral, we obtain the expansion set using the tensor product of the modal expansion basis functions ϕ_p , such that the

approximation of a two dimensional function in the e -th element becomes

$$u(\mathbf{x}, t) = \sum_{p=0}^P \sum_{q=0}^P \hat{u}_{pq} \phi_p(\xi_1) \phi_q(\xi_2), \quad (3.25)$$

where P is the highest polynomial order of the expansion and

$$\xi_1 = [\chi_1^e]^{-1}(x, y), \quad \xi_2 = [\chi_2^e]^{-1}(x, y), \quad (3.26)$$

which are given by the inverse of the transformation χ . The two dimensional tensor product expansion set for polynomial order $P = 3$ is displayed in Figure 3.4. The two dimensional expansion modes can be decomposed into vertex, edge and interior modes. This decomposition makes an efficient coupling of neighbouring elements possible.

This expansion basis was extended to a wide range of element shapes in 2D (Dubiner (1991)) and 3D (Karniadakis and Sherwin (2005)), which gives methods based on these expansion functions huge geometric flexibility. In 2D, it can be modified to be applied to quadrilateral and triangular elements and in 3D to hexahedrons, prisms, pyramids and tetrahedrons. We call numerical methods based on this expansion basis *spectral/hp element methods*. We use this expansion basis in this thesis. However, in this work, we only use the expansion functions for quadrilaterals, which is given by the tensor product of the expansion functions ϕ_p defined by (3.24).

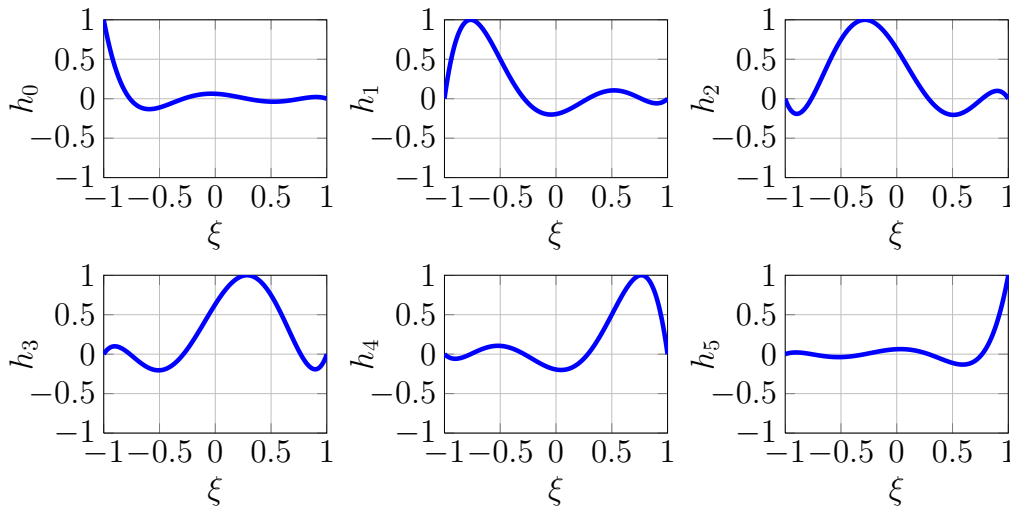
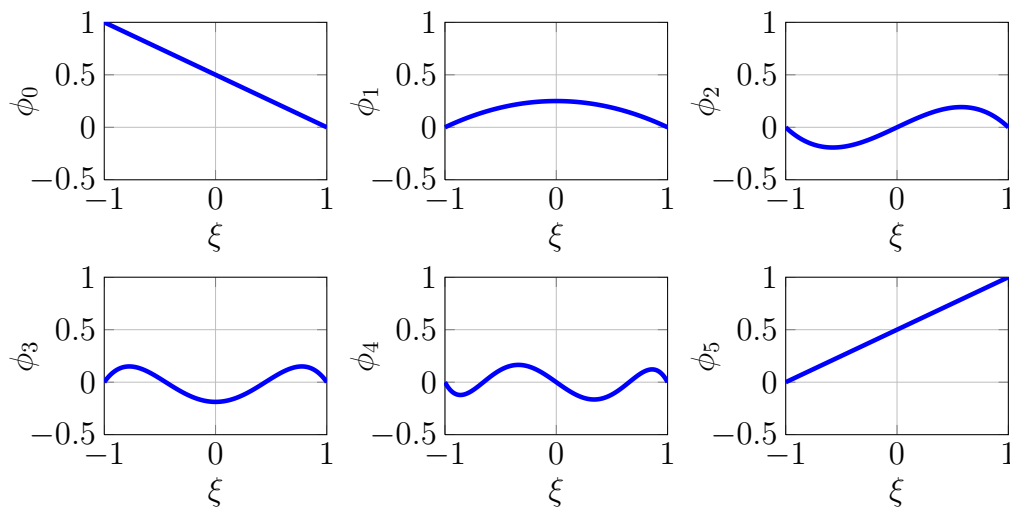
(a) Nodal P-type expansion set $\{h_i : P = 5, 0 \leq i \leq P\}$.(b) Modal P-type expansion set $\{\phi_p : 0 \leq p \leq 5\}$.

Figure 3.3.: Expansion sets for (a) the classical spectral element method and (b) the spectral/hp element method.

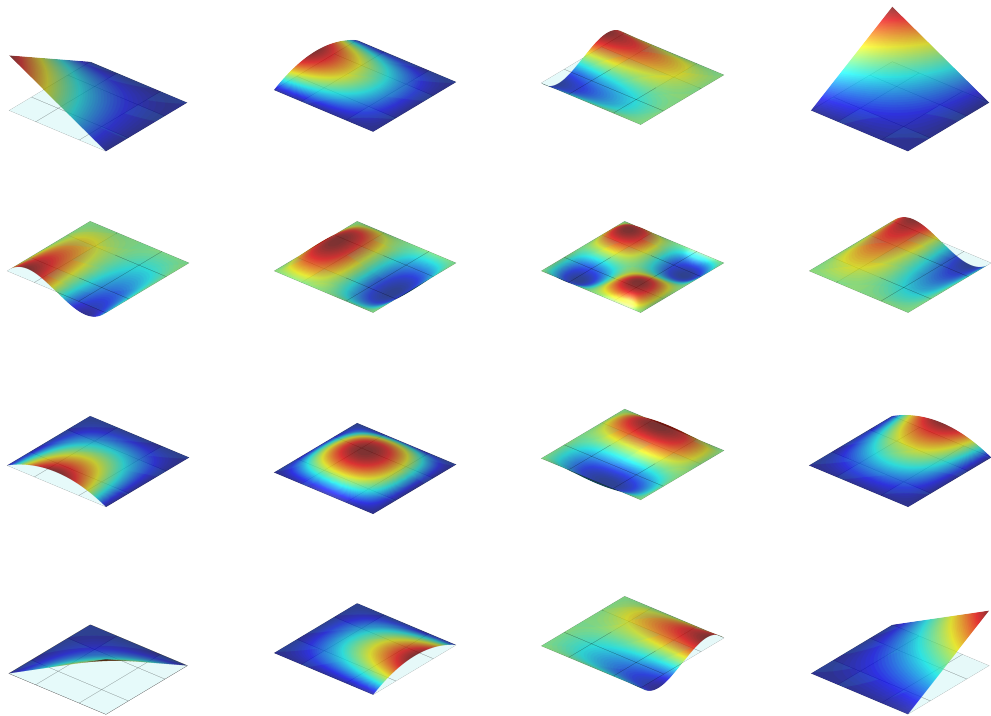


Figure 3.4.: Spectral/hp expansion set for $P = 3$ on a two dimensional quadrilateral element. The expansion modes can be decomposed into vertex, edge and interior modes and are formed by the tensor product of the one-dimensional expansion functions illustrated in Figure 3.3(b).

3.3. Integration and Differentiation on the Standard Element

3.3.1. Integration

Solving a differential equations using Galerkin or Petrov-Galerkin methods involves the evaluation of integrals. We want to find a way to discretely evaluate integrals that retains orthogonality and spectral accuracy. This means the quadrature rule on the one-dimensional standard region $[-1, 1]$ should satisfy

$$\sum_{j=0}^{Q-1} u(\xi_j) \phi_p(\xi_j) w_j = \int_{-1}^1 u(\xi) \phi_p(\xi) dx, \quad (3.27)$$

where w_j are the quadrature weights and ξ_j are the abscissas of the Q quadrature points. Such an exact integration is possible using Gauss rules. In this work, we use the Gauss-Legendre-Lobatto quadrature rule, which evaluates integrals exactly for polynomials of degree $2Q - 3$ or less. The Gauss-Legendre-Lobatto quadrature rule is given by

$$\xi_j = -1, \text{ zeros of } L'_{Q-1}(\xi), +1, \quad (3.28)$$

$$w_j = \frac{2}{Q(Q-1)} \frac{1}{L_{Q-1}(\xi_j)^2}. \quad (3.29)$$

Note that, the zeroes of $L'_{Q-1}(\xi)$ are identical to the zeroes of $P_{Q-2}^{(1,1)}(\xi)$. We choose the quadrature order $Q = P + 2$ (i.e. exact integration for polynomials of order $2P + 1$) in order to guarantee that all discrete inner products involving the spectral/hp element expansion functions such as

$$(\phi_p, \phi_q)^\delta := \sum_{j=0}^{Q-1} \phi_p(\xi_j) \phi_q(\xi_j) w_j = \int_{-1}^1 \phi_p \phi_q dx \quad (3.30)$$

are evaluated exactly, as the highest order of the polynomials in the inner product for the spectral/hp element method is $2P$. We can trivially extend the quadrature rule to two dimensional standard regions

$$\int_{-1}^1 \int_{-1}^1 u(\xi_1, \xi_2) \phi_{pq}(\xi_1, \xi_2) d\xi_1 d\xi_2 \approx \sum_{i=0}^{Q-1} w_i \left\{ \sum_{j=0}^{Q-1} w_j u(\xi_{1_i}, \xi_{2_j}) \phi_{pq}(\xi_{1_i}, \xi_{2_j}) \right\} \quad (3.31)$$

with $\phi_{pq}(\xi_1, \xi_2) = \phi_p(\xi_1) \phi_q(\xi_2)$.

3.3.2. Differentiation

Let us assume that we have the approximation of the function $u^\delta(\xi)$ in terms of polynomials, such that $u^\delta(\xi)$ is a polynomial of order P or less in $[-1, 1]$. To calculate the derivative of such a function on the standard element, we employ the so-called collocation differentiation technique. In this technique, we first express the function $u^\delta(\xi)$ in terms of Lagrange polynomials $h_i(\xi)$ through a set of Q nodal points ξ_i

$$u(\xi) \approx \sum_{j=0}^{Q-1} h_j(\xi) u(\xi_j), \quad (3.32)$$

where

$$h_j(\xi) = \frac{\prod_{i=0, i \neq j}^{Q-1} (\xi - \xi_i)}{\prod_{i=0, i \neq j}^{Q-1} (\xi_j - \xi_i)}. \quad (3.33)$$

This gives an exact representation of the function $u^\delta(\xi) \in \mathcal{P}_P([-1, 1])$ for $Q \geq P + 1$. Here, $\mathcal{P}_P([-1, 1])$ is the space of all polynomials of degree P defined on the standard element $\Omega_{st} = \{\xi \mid -1 \leq \xi \leq 1\}$. The derivative of $u^\delta(\xi)$ can then be evaluated as

$$\frac{du(\xi_i)}{d\xi} \approx \sum_{j=0}^{Q-1} \frac{dh_j(\xi_i)}{d\xi} u(\xi_j). \quad (3.34)$$

If we choose the Q quadrature points (we use $Q = P + 2$, see previous Section), this allows us to compute the derivative of a function at the quadrature points based on the function values at the quadrature points. For two dimensions, the collocation differentiation becomes

$$\frac{\partial u(\xi_{1_r}, \xi_{2_s})}{\partial \xi_1} \approx \sum_{i=0}^{Q-1} \sum_{j=0}^{Q-1} \frac{dh_i(\xi_{1_r})}{d\xi_1} h_j(\xi_{2_s}) u(\xi_{1_i}, \xi_{2_j}). \quad (3.35)$$

3.4. Geometrical Mapping

As described in Section 3.1.2, in order to describe complex geometries we decompose the domain into elements. Each element is then mapped onto a standard element on which all computations are performed. In this Section, we will describe how this one-to-one mapping $\mathbf{x} = (x, y) = \chi^e(\xi_1, \xi_2)$ between the physical coordinates (x, y) and the local or computational coordinates (ξ_1, ξ_2) is constructed in the spectral/hp element method. The geometry is approximated with the same expansion functions that we use in order to

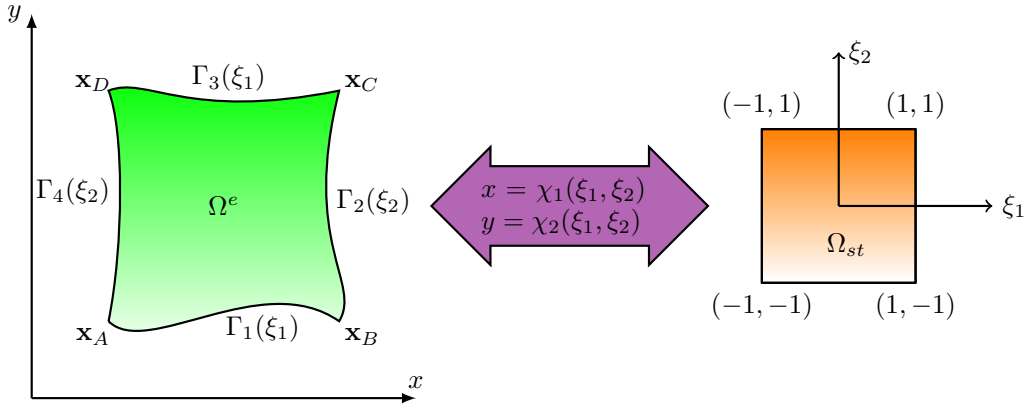


Figure 3.5.: Mapping between an element in physical space Ω_e and the standard element Ω_{st} .

approximate the dependent variables, i.e. we express the coordinates as

$$\mathbf{x} = \boldsymbol{\chi}^e(\xi_1, \xi_2) = \sum_{p=0}^P \sum_{q=0}^P \hat{\mathbf{x}}_{pq} \phi_p(\xi_1) \phi_q(\xi_2). \quad (3.36)$$

For a straight-sided element, the linear finite element functions are sufficient to describe the geometry, so that the mapping can be constructed using these vertex modes and the coordinates of the vertices of the element $(\mathbf{x}_A, \mathbf{x}_B, \mathbf{x}_C, \mathbf{x}_D)$

$$\begin{aligned} \mathbf{x} = \boldsymbol{\chi}^e(\xi_1, \xi_2) = & \mathbf{x}_A \left(\frac{1 - \xi_1}{2} \right) \left(\frac{1 - \xi_2}{2} \right) + \mathbf{x}_B \left(\frac{1 + \xi_1}{2} \right) \left(\frac{1 - \xi_2}{2} \right) \\ & + \mathbf{x}_C \left(\frac{1 + \xi_1}{2} \right) \left(\frac{1 + \xi_2}{2} \right) + \mathbf{x}_D \left(\frac{1 - \xi_1}{2} \right) \left(\frac{1 + \xi_2}{2} \right), \end{aligned} \quad (3.37)$$

where

$$\hat{\mathbf{x}}_{00} = \mathbf{x}_A, \quad \hat{\mathbf{x}}_{P0} = \mathbf{x}_B, \quad \hat{\mathbf{x}}_{PP} = \mathbf{x}_C, \quad \hat{\mathbf{x}}_{0P} = \mathbf{x}_D \quad (3.38)$$

and all the other coefficients are zero. For elements with a curved boundary, we use the expansion with the same polynomial order as for the dependent variables to approximate each edge of the element and then blend between these polynomial curves into the interior of the element using the vertex modes. In detail, this works as follows.

First, given coordinates of N points along the i th edge, we parametrise the edge according to arc length or a reasonable approximation thereto and map this parameter to $s \in [-1, 1]$ to obtain the curves $\Gamma_i : [-1, 1] \rightarrow \mathbb{R}^2$. Then we construct Lagrange polynomials through the N given points s_k in order to determine the interpolation of the given curve values onto the values along the curve, which are the image of the Q Gauss-Lobatto-Legendre

points ξ_j

$$\begin{aligned}\Gamma_1(\xi_{1j}) &\approx \sum_{k=0}^N \Gamma_1(s_k) h_k(\xi_{1j}), \quad j = 0, \dots, Q-1, \\ \Gamma_2(\xi_{2j}) &\approx \sum_{k=0}^N \Gamma_2(s_k) h_k(\xi_{2j}), \quad j = 0, \dots, Q-1, \\ \Gamma_3(\xi_{1j}) &\approx \sum_{k=0}^N \Gamma_3(s_k) h_k(\xi_{1j}), \quad j = 0, \dots, Q-1, \\ \Gamma_4(\xi_{2j}) &\approx \sum_{k=0}^N \Gamma_4(s_k) h_k(\xi_{2j}), \quad j = 0, \dots, Q-1,\end{aligned}\quad (3.39)$$

where

$$h_k(\xi_{i_j}) = \prod_{m=0, m \neq k}^N \frac{\xi_{i_j} - s_m}{s_k - s_m}, \quad i = 1, 2 \quad (3.40)$$

and

$$\Gamma_i(s_k) = (x_k, y_k), \quad i = 1, 2, 3, 4. \quad (3.41)$$

where (x_k, y_k) are the given points along the curves in the physical domain. To obtain the unknown coefficients for the coordinate expansion (3.36), we use the Q values of each edge $\Gamma_i(\xi_j)$ from Equation (3.39) and determine the unknown coefficients edge-by-edge through a Galerkin projection or a collocation projection. For example, for the first edge described by $\Gamma_1(\xi_1)$ this means, we solve

$$\sum_{p=0}^P \left(\int_{-1}^1 \phi_p \phi_q d\xi \right) \hat{\mathbf{x}}_{p0} \approx \sum_{j=0}^{Q-1} w_j \phi_q(\xi_{1j}) \Gamma_1(\xi_{1j}), \quad q = 0, \dots, P. \quad (3.42)$$

Here, w_j are the quadrature weights of the Gauss-Lobatto-Legendre quadrature introduced in Section 3.3.1. The projection for the other edges can be performed analogously. Details on Galerkin projections are given in the following Section. Performing the projection for each edge, gives us the approximation of the curves in terms of the modal spectral/hp

expansion functions, i.e.

$$\Gamma_1(\xi_1) = \sum_{p=0}^P \hat{\mathbf{x}}_{p0} \phi_p(\xi_1), \quad (3.43)$$

$$\Gamma_2(\xi_2) = \sum_{q=0}^P \hat{\mathbf{x}}_{Pq} \phi_q(\xi_2), \quad (3.44)$$

$$\Gamma_3(\xi_1) = \sum_{p=0}^P \hat{\mathbf{x}}_{pP} \phi_p(\xi_1), \quad (3.45)$$

$$\Gamma_4(\xi_2) = \sum_{q=0}^P \hat{\mathbf{x}}_{0P} \phi_q(\xi_2). \quad (3.46)$$

The remaining coefficients in the expansions (3.36) are zero. Therefore, the expansion can be expressed as

$$\begin{aligned} \mathbf{x} = \boldsymbol{\chi}^e(\xi_1, \xi_2) &= \Gamma_1(\xi_1)\phi_0(\xi_2) - \Gamma_1(-1)\phi_0(\xi_1)\phi_0(\xi_2) - \Gamma_1(1)\phi_P(\xi_1)\phi_0(\xi_2) \\ &+ \Gamma_2(\xi_2)\phi_P(\xi_1) \\ &+ \Gamma_3(\xi_1)\phi_P(\xi_2) - \Gamma_3(-1)\phi_0(\xi_1)\phi_P(\xi_2) - \Gamma_3(1)\phi_P(\xi_1)\phi_P(\xi_2) \\ &+ \Gamma_4(\xi_2)\phi_0(\xi_1). \end{aligned} \quad (3.47)$$

Note that, the vertex values are subtracted once to avoid multiplicity, since they are contained in two terms in (3.47). This expression is equivalent to using linear blending functions as originally proposed by Gordon and Hall (1973).

3.5. Integration and Differentiation for Generally Shaped Elements

3.5.1. Integration

In practice, we use the mapping introduced in the previous Section to transform integrals or derivatives over generally shaped elements to the standard element. In a generally shaped element Ω_e , the inner products arising from the Galerkin method are typically given by

$$\int_{\Omega_e} \phi_{pq}(x, y) u(x, y) dx dy, \quad \forall p, q \in [0, P], \quad (3.48)$$

which can be transformed into an integral over the standard element

$$\int_{\Omega_e = \boldsymbol{\chi}^e(\Omega_{st})} \phi_{pq}(x, y) u(x, y) dx dy = \int_{\Omega_{st}} \phi_{pq}(\xi_1, \xi_2) u(\xi_1, \xi_2) |J| d\xi_1 d\xi_2 \quad (3.49)$$

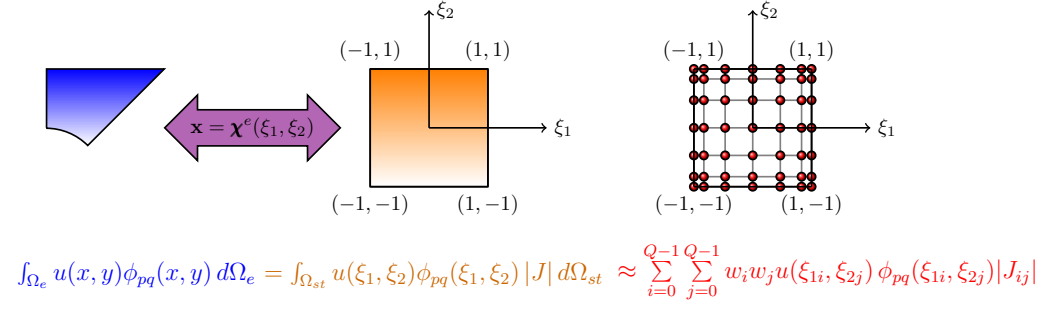


Figure 3.6.: Illustration of the integration over a generally shaped element.

using the mapping χ^e and its Jacobian

$$J = \frac{\partial x}{\partial \xi_1} \frac{\partial y}{\partial \xi_2} - \frac{\partial y}{\partial \xi_1} \frac{\partial x}{\partial \xi_2}. \quad (3.50)$$

Finally, we use Gaussian quadrature to evaluate the integral over the standard element

$$(\phi_{pq}, u)_{\Omega_e}^\delta := \sum_{i=0}^{Q-1} \sum_{j=0}^{Q-1} w_i w_j |J_{ij}| \phi_{pq}(\xi_{1i}, \xi_{2j}) u(\xi_{1i}, \xi_{2j}), \quad (3.51)$$

where

$$J_{ij} = \frac{\partial x_i}{\partial \xi_{1i}} \frac{\partial y_j}{\partial \xi_{2j}} - \frac{\partial y_j}{\partial \xi_{1i}} \frac{\partial x_i}{\partial \xi_{2j}}. \quad (3.52)$$

3.5.2. Differentiation

For the differentiation of a function within a generally shaped element, we apply the chain rule and obtain

$$\begin{bmatrix} \frac{\partial u}{\partial x} \\ \frac{\partial u}{\partial y} \end{bmatrix} = \begin{bmatrix} \frac{\partial \xi_1}{\partial x} & \frac{\partial \xi_2}{\partial x} \\ \frac{\partial \xi_1}{\partial y} & \frac{\partial \xi_2}{\partial y} \end{bmatrix} \begin{bmatrix} \frac{\partial u}{\partial \xi_1} \\ \frac{\partial u}{\partial \xi_2} \end{bmatrix} = \frac{1}{J} \begin{bmatrix} \frac{\partial y}{\partial \xi_2} & -\frac{\partial y}{\partial \xi_1} \\ -\frac{\partial x}{\partial \xi_2} & \frac{\partial x}{\partial \xi_1} \end{bmatrix} \begin{bmatrix} \frac{\partial u}{\partial \xi_1} \\ \frac{\partial u}{\partial \xi_2} \end{bmatrix}. \quad (3.53)$$

The values in the last expression can then all be evaluated using the collocation differentiation technique over the standard element as explained in Section 3.3.2.

3.6. Matrix notation

Before we continue by demonstrating the spectral/hp method on a one-dimensional example, we introduce the notation for the elemental vectors and matrices based on the thesis of Vos (2011) and the monograph of Karniadakis and Sherwin (2005). For every element

Ω_e of general shape, we form the *vector of physical values*, \mathbf{u}^e , which contains the values of the unknown function at the image of the quadrature points. In two-dimensions, for the spectral/hp tensor-product expansion, these quadrature point values are ordered according to a lexicographical ordering along the ξ_1 direction given by the index $m(ij)$ which runs consecutively from 0 to $Q^2 - 1$ with

$$m(ij) = i + jQ, \quad 0 \leq i < Q, \quad 0 \leq j < Q. \quad (3.54)$$

The entries of the vector of physical values are then given by

$$\mathbf{u}^e[m(ij)] := u^e(\xi_{1_i}, \xi_{2_j}), \quad (3.55)$$

$$\mathbf{u}^e = \left[u(\xi_{1_0}, \xi_{2_0}), \dots, u(\xi_{1_{Q-1}}, \xi_{2_0}), u(\xi_{1_0}, \xi_{2_1}), \dots, u(\xi_{1_{Q-1}}, \xi_{2_{Q-1}}) \right]^T. \quad (3.56)$$

The corresponding vector of unknown expansion coefficients for the element e , is denoted by $\hat{\mathbf{u}}^e$, and is ordered using a lexicographical numbering convention defined by

$$n(pq) = q + p(P + 1), \quad 0 \leq p \leq P, \quad 0 \leq q \leq P. \quad (3.57)$$

Note that, we order the expansion coefficients such that the coefficients for vertex modes are listed first followed by edges and finally the interior modes. This means, the vector of expansion coefficients in the element Ω_e is defined as

$$\hat{\mathbf{u}}^e[n(pq)] := \hat{u}_{pq}, \quad 0 \leq p \leq P, \quad 0 \leq q \leq P, \quad (3.58)$$

$$\hat{\mathbf{u}}^e = [\hat{u}_{00}, \dots, \hat{u}_{0P}, \hat{u}_{10}, \dots, \hat{u}_{PP}]^T. \quad (3.59)$$

Furthermore, we define *the elemental basis matrix* \mathbf{B}^e , which stores the discrete representation of the basis functions. Every column of \mathbf{B}^e is defined as the evaluation of a fixed expansion function $\phi_{pq}(\xi_{1_i}, \xi_{2_j}) = \phi_p(\xi_{1_i})\phi_q(\xi_{2_j})$ at all the quadrature points, that is,

$$\mathbf{B}^e[m(ij)][n(pq)] := \phi_{pq}(\xi_{1_i}, \xi_{2_j}). \quad (3.60)$$

Note that both the expansion functions (the columns) and the quadrature points (the rows) within the matrix \mathbf{B}^e are ordered in a consistent fashion to the vectors $\hat{\mathbf{u}}$ and \mathbf{u} respectively. In the following Subsections, we will introduce the matrix notation for the integration, differentiation and forward and backward transformations on an arbitrarily shaped

element.

3.6.1. Integration

The integration of an unknown function u on an arbitrarily shaped element Ω_e given by

$$(\phi_{pq}, u)_{\Omega_e}^\delta := \sum_{i=0}^{Q-1} \sum_{j=0}^{Q-1} w_i w_j |J_{ij}| \phi_{pq}(\xi_{1_i}, \xi_{2_j}) u(\xi_{1_i}, \xi_{2_j}), \quad (3.61)$$

as explained in Section 3.5.1 can be expressed as

$$(\phi_{pq}, u)_{\Omega_e}^\delta = [\mathbf{B}^e]^T \mathbf{W}^e \mathbf{u}^e. \quad (3.62)$$

in terms of the elemental basis matrix \mathbf{B}^e and the *weight matrix* \mathbf{W}^e . The weight matrix \mathbf{W}^e is a diagonal matrix containing the Gaussian quadrature weights multiplied by the Jacobian at the quadrature points, such that

$$\mathbf{W}^e[m(ij)][n(rs)] := w_i w_j |J_{ij}| \delta_{mn}. \quad (3.63)$$

The weight matrix \mathbf{W} is ordered in a consistent fashion with the vector \mathbf{u} .

3.6.2. Differentiation

To express the derivative of an unknown function u in an arbitrarily shaped element Ω_e as explained in Section 3.5.2 in terms of elemental matrices, we first define the *differentiation matrices* $\mathbf{D}_{\xi_1}^e$ and $\mathbf{D}_{\xi_2}^e$ acting on \mathbf{u}^e evaluated at the quadrature points

$$\mathbf{D}_{\xi_1}^e \mathbf{u}^e := \frac{\partial u(\xi_{1_i}, \xi_{2_j})}{\partial \xi_1} = \sum_{r=0}^{Q-1} \sum_{s=0}^{Q-1} \frac{dh_r(\xi_{1_i})}{d\xi_1} h_s(\xi_{2_j}) u(\xi_{1_r}, \xi_{2_s}), \quad (3.64)$$

$$\mathbf{D}_{\xi_1}^e[m(ij)][n(rs)] = \frac{dh_r(\xi_{1_i})}{d\xi_1} h_s(\xi_{2_j}). \quad (3.65)$$

Then, within a general shaped element, we define the differentiation matrices \mathbf{D}_x^e and \mathbf{D}_y^e as

$$\mathbf{D}_x^e := \Xi_1^1 \mathbf{D}_{\xi_1}^e + \Xi_1^2 \mathbf{D}_{\xi_2}^e, \quad (3.66)$$

$$\mathbf{D}_y^e := \Xi_2^1 \mathbf{D}_{\xi_1} + \Xi_2^2 \mathbf{D}_{\xi_2}, \quad (3.67)$$

where Ξ_l^k are the diagonal matrices containing the derivative metrics evaluated at the quadrature points, i.e.

$$\Xi_1^k[m(ij)][n(rs)] = \frac{\partial \xi_{k_i}}{\partial x_j} \delta_{mn}, \quad \Xi_2^k[m(ij)][n(rs)] = \frac{\partial \xi_{k_i}}{\partial y_j} \delta_{mn}. \quad (3.68)$$

3.6.3. Backward transformation

When using modal expansion bases, it is often necessary to transform the coefficients of an expansion to the value of the spectral/hp expansion at the quadrature points. This is the case for example when applying the collocation differentiation technique to a spectral/hp expansion. This backward transformation from coefficient space to physical space is simply defined as

$$u^e(\xi_{1_i}, \xi_{2_j}) = \sum_{p=0}^P \sum_{q=0}^P \phi_{pq}(\xi_{1_i}, \xi_{2_j}) \hat{u}_{pq}^e, \quad (3.69)$$

that is, the backward transformation is merely the evaluation of the spectral/hp element expansion at the quadrature points. In matrix notation this can be represented as

$$\mathbf{u}^e = \mathbf{B}^e \hat{\mathbf{u}}^e. \quad (3.70)$$

3.6.4. Forward transformation

For the inverse transformation of obtaining the coefficients of an expansion from the physical values at the quadrature points, we employ the method of weighted residuals

$$\left(\sum_{p=0}^P \sum_{q=0}^P \hat{u}_{pq}^e \phi_{pq}(\boldsymbol{\xi}), \phi_{rs}(\boldsymbol{\xi}) \right)_{\Omega_e}^\delta - (u^e, \phi_{rs}(\boldsymbol{\xi}))_{\Omega_e}^\delta = R(u) \stackrel{!}{=} 0, \quad \forall r, s \in [0, P] \quad (3.71)$$

$$\sum_{p=0}^P \sum_{q=0}^P (\phi_{pq}(\boldsymbol{\xi}), \phi_{rs}(\boldsymbol{\xi}))_{\Omega_e}^\delta \hat{u}_{pq}^e = (u^e, \phi_{rs}(\boldsymbol{\xi}))_{\Omega_e}^\delta, \quad \forall r, s \in [0, P] \quad (3.72)$$

which yields in matrix notation

$$[\mathbf{B}^e]^T \mathbf{W}^e \mathbf{B}^e \hat{\mathbf{u}}^e = [\mathbf{B}^e]^T \mathbf{W}^e \mathbf{u}^e. \quad (3.73)$$

Here, $\boldsymbol{\xi} = (\xi_1, \xi_2)$ are the coordinates of the standard element. We define the *elemental mass matrix*

$$\mathbf{M}^e[n(pq)][n'(rs)] := [\mathbf{B}^e]^T \mathbf{W}^e \mathbf{B}^e = (\phi_{pq}, \phi_{rs})_{\Omega_e}^{\delta}, \quad (3.74)$$

where n' and n are integers following the lexicographical numbering convention defined in Equation (3.57). To obtain the vector of expansion coefficients from the vector of physical values, we perform

$$\hat{\mathbf{u}}^e = [\mathbf{M}^e]^{-1} [\mathbf{B}^e]^T \mathbf{W}^e \mathbf{u}^e. \quad (3.75)$$

This is called discrete *forward transformation*.

3.7. Coupling between Elements

In the previous Section, we described how to perform integration and differentiation on each element Ω_e in the domain. However, in order to obtain a global solution over the whole domain Ω , we need to introduce some appropriate form of coupling between the elements. There are different choices dependent on the type of the underlying partial differential equations. In this Section, we will introduce the continuous Galerkin method, where we couple the elements by imposing continuity and this is achieved by making the approximation globally continuous. We also consider the discontinuous Galerkin method, in which elements are coupled using fluxes across element boundary. Before we go into the details of each of these methods, let us introduce the following notation for the concatenation of all elemental vectors and matrices:

1. *vector of all local degrees of freedom*

$$\hat{\mathbf{u}}_l := [\hat{\mathbf{u}}^1, \hat{\mathbf{u}}^2, \dots, \hat{\mathbf{u}}^{N_{el}}]. \quad (3.76)$$

2. *vector of all local physical values*

$$\mathbf{u}_l := [\mathbf{u}^1, \mathbf{u}^2, \dots, \mathbf{u}^{N_{el}}]. \quad (3.77)$$

3. global element-by-element matrix

$$\underline{\mathbf{M}}^e := \begin{bmatrix} \mathbf{M}^1 & 0 & 0 & 0 \\ 0 & \mathbf{M}^2 & 0 & 0 \\ 0 & 0 & \ddots & 0 \\ 0 & 0 & 0 & \mathbf{M}^{N_{el}} \end{bmatrix}. \quad (3.78)$$

Define the local expansion modes $\phi_{pq}^e(x, y)$ within our global solution domain Ω by

$$\phi_{pq}^e(x, y) = \begin{cases} \phi_{pq}(\xi_1, \xi_2), & (x, y) \in \Omega^e, \\ 0, & \text{otherwise,} \end{cases} \quad (3.79)$$

where

$$\xi_1 = [\chi_1^e]^{-1}(x, y), \quad \xi_2 = [\chi_2^e]^{-1}(x, y) \quad (3.80)$$

and χ_i^e is the iso-parametric mapping introduced in Section 3.4.

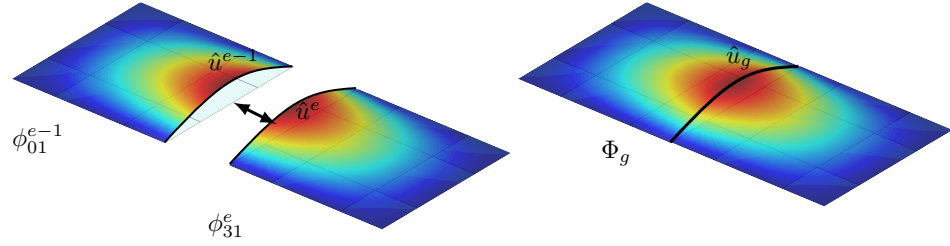
3.7.1. Continuous Galerkin Method

If we choose to couple the elements by enforcing continuity in the approximation of the solution, we are looking for a solution in the following discrete space within the spectral/hp element framework

$$\mathcal{V}_\delta(\Omega) := \left\{ v \in C^0(\Omega) : v|_{\Omega_e} \in \mathcal{P}_P(\Omega_e), \forall \Omega_e \right\}. \quad (3.81)$$

Here, $\mathcal{P}_P(\Omega_e)$ is the space of polynomials of order P defined in the element Ω_e . This discrete space is spanned by globally continuous expansion modes, Φ_g . To construct this globally continuous expansion from elemental or local contributions, we need to introduce a local to global assembly process, often referred to as *direct stiffness summation* or *global assembly*. To construct a system of globally continuous expansion modes Φ_g out of the globally defined local expansion modes ϕ_{pq}^e defined by (3.79), we match corresponding boundary and vertex modes as depicted in Figure 3.7(a). We only need to match boundary and vertex modes, as all interior modes can be taken directly as global modes as they are already C^0 continuous over the whole domain, when we use definition (3.79). Constructing global modes in this manner yields the global C^0 continuous spectral/hp approximation

$$u(x, y) = \sum_{n=0}^{N_{dof}-1} \Phi_n(x, y) \hat{u}_n^g = \sum_{e=1}^{N_{el}} \sum_{p=0}^P \sum_{q=0}^P \phi_{pq}^e(x, y) \hat{u}_{pq}^e, \quad (3.82)$$

(a) Construction of global mode Φ_g .

$$\int_{\Omega} \Phi_g u(x, y) \, dx \, dy = \int_{\Omega_{01}^{e-1}} \phi_{01}^{e-1} u(x, y) \, dx \, dy + \int_{\Omega_{31}^e} \phi_{31}^e u(x, y) \, dx \, dy$$

(b) Global evaluation of inner product.

Figure 3.7.: (a) Construction of globally continuous global modes Φ_g from elemental modes ϕ_{pq} by matching of corresponding boundary modes and (b) integration in the global region is the sum of the integration in the local regions (see Karniadakis and Sherwin (2005)).

where \hat{u}_n^g are the global degrees of freedom corresponding to the global expansion basis Φ_n . The $N_{el} \times (P+1)^2$ elemental degrees of freedom \hat{u}_{pq}^e can be related to the N_{dof} global degrees of freedom \hat{u}_n^g through the local-to-global mapping, which can be represented by a matrix operation \mathcal{A} ,

$$\hat{\mathbf{u}}_l = \mathcal{A} \hat{\mathbf{u}}_g. \quad (3.83)$$

The *scatter matrix* \mathcal{A} is sparse and contains typically one entry of 1 on any given row. It distributes the vector of global coefficients $\hat{\mathbf{u}}_g$ upon the vector of local coefficients $\hat{\mathbf{u}}_l$. We can now define the assembly process from local to global degrees of freedom in terms of the global assembly matrix \mathcal{A}^T . Considering the global inner product of a function $u(x, y)$ with respect to the global basis Φ_n

$$\hat{\mathbf{I}}_g[n] = \int_{\Omega} u(x, y) \Phi_n(x, y) \, dx \, dy \quad (3.84)$$

and the elemental integral

$$\hat{\mathbf{I}}^e[m] = \int_{\Omega_e} u(x, y) \phi_m^e(x, y) dx dy \quad (3.85)$$

we can define the *global assembly matrix* \mathcal{A}^T as the representation of a mapping which expresses the global inner product in terms of the sum of their local elemental contributions as depicted in Figure 3.7(b)

$$\hat{\mathbf{I}}_g = \mathcal{A}^T \hat{\mathbf{I}}^e. \quad (3.86)$$

Here, the underlined matrix $\hat{\mathbf{I}}^e$ is the global element-by-element matrix as defined in Equation (3.78). Using these matrix definitions, we can now formulate operations in terms of global matrices. For example, the *global forward transformation* is given by

$$\mathcal{A}^T \underline{\mathbf{M}}^e \mathcal{A} \hat{\mathbf{u}}_g = \mathcal{A}^T [\underline{\mathbf{B}}^e]^T \underline{\mathbf{W}}^e \mathbf{u}_l \quad (3.87)$$

where

$$\mathbf{M}_g := \mathcal{A}^T \underline{\mathbf{M}}^e \mathcal{A} \quad (3.88)$$

is the *global mass matrix*. The global matrix \mathbf{M}_g is usually too large to store and to invert

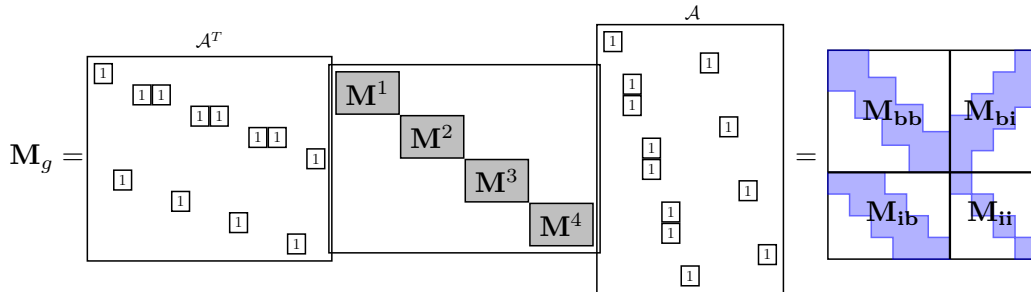


Figure 3.8.: Schematic structure of the global matrix (see Karniadakis and Sherwin (2005) for further details).

directly. However, we can reduce the global matrix into smaller components using the boundary-interior decomposition of the spectral/hp element expansion modes. The global matrix can be split into components containing boundary and interior contributions

$$\mathbf{M}_g = \begin{bmatrix} \mathbf{M}_{bb} & \mathbf{M}_{bi} \\ \mathbf{M}_{ib} & \mathbf{M}_{ii} \end{bmatrix}, \quad (3.89)$$

where the matrix \mathbf{M}_{bb} denotes the global assembly of the elemental boundary-boundary mode interactions, \mathbf{M}_{bi} and \mathbf{M}_{ib} correspond to the global assembly of the elemental boundary-interior coupling and \mathbf{M}_{ii} denotes the block-diagonal matrix of elemental interior-interior mode interactions. This matrix decomposition is called *substructuring or static condensation* and has the structure shown in Figure 3.8. Note that, \mathbf{M}_{ii} is block diagonal and therefore very inexpensive to evaluate since each block may be inverted individually. This arises from the fact that the interior modes are non-overlapping and it is the structure of \mathbf{M}_{ii} which makes the substructuring so effective. The global "submatrices" \mathbf{M}_{bb} , \mathbf{M}_{ib} , \mathbf{M}_{bi} and \mathbf{M}_{ii} are constructed from the elemental matrices by

$$\mathbf{M}_{ii} = \underline{\mathbf{M}}_{ii}^e, \quad (3.90)$$

$$\mathbf{M}_{bi} = \mathcal{A}_b^T \underline{\mathbf{M}}_{bi}^e, \quad (3.91)$$

$$\mathbf{M}_{ib} = \underline{\mathbf{M}}_{ib}^e \mathcal{A}_b, \quad (3.92)$$

$$\mathbf{M}_{bb} = \mathcal{A}_b^T \underline{\mathbf{M}}_{bb}^e \mathcal{A}_b. \quad (3.93)$$

Here, \mathcal{A}_b is the boundary version of \mathcal{A} . It scatters the global boundary degrees of freedom to the local boundary degrees of freedom. Similarly, \mathcal{A}_b^T assembles the global boundary degrees of freedom from the local boundary degrees of freedom.

Now, the static condensation enables us to solve global systems effectively. Consider, for example, the continuous forward transformation (3.87). If we decompose $\hat{\mathbf{u}}_g$ and $\mathbf{f} = \mathcal{A}^T [\mathbf{B}^e]^T \mathbf{W}^e \mathbf{u}^e$ into their boundary and interior components $\hat{\mathbf{u}}_b$, $\hat{\mathbf{u}}_i$, $\mathbf{f}_b, \mathbf{f}_i$, the forward transform becomes

$$\begin{bmatrix} \mathbf{M}_{bb} & \mathbf{M}_{bi} \\ \mathbf{M}_{ib} & \mathbf{M}_{ii} \end{bmatrix} \begin{bmatrix} \hat{\mathbf{u}}_b \\ \hat{\mathbf{u}}_i \end{bmatrix} = \begin{bmatrix} \mathbf{f}_b \\ \mathbf{f}_i \end{bmatrix}. \quad (3.94)$$

Performing a block elimination, we obtain

$$\begin{bmatrix} \mathbf{S} & 0 \\ \mathbf{M}_{ib} & \mathbf{M}_{ii} \end{bmatrix} \begin{bmatrix} \hat{\mathbf{u}}_b \\ \hat{\mathbf{u}}_i \end{bmatrix} = \begin{bmatrix} \mathbf{f}_b - \mathbf{M}_{bi} [\mathbf{M}_{ii}]^{-1} \mathbf{f}_i \\ \mathbf{f}_i \end{bmatrix}, \quad (3.95)$$

where

$$\mathbf{S} = \mathbf{M}_{bb} - \mathbf{M}_{bi} \mathbf{M}_{ii}^{-1} \mathbf{M}_{ib} = \mathcal{A}_b^T \left[\underline{\mathbf{M}}_{bb}^e - \underline{\mathbf{M}}_{bi}^e \left[\underline{\mathbf{M}}_{ii}^e \right]^{-1} \underline{\mathbf{M}}_{ib}^e \right] \mathcal{A}_b \quad (3.96)$$

is the so-called *Schur complement*. The boundary unknowns can be determined by

$$\mathbf{S} \hat{\mathbf{u}}_b = \mathbf{f}_b - \mathbf{M}_{bi} [\mathbf{M}_{ii}]^{-1} \mathbf{f}_i \quad (3.97)$$

and once the boundary solution is known, we obtain the interior solution using

$$\hat{\mathbf{u}}_i = [\mathbf{M}_{ii}]^{-1} \mathbf{f}_i - [\mathbf{M}_{ii}]^{-1} \mathbf{M}_{ib} \hat{\mathbf{u}}_b. \quad (3.98)$$

To calculate the inverse of the Schur complement, we apply the so-called *multi-static condensation technique* explained in Karniadakis and Sherwin (2005) and Vos (2011). In the multi-static condensation technique, we decompose the Schur complement repeatedly into modes that couple with each other and modes that do not interact with each other to obtain a matrix structure for the Schur complement as shown in Figure 3.8. For example, in the second level of static condensation, we use the fact that, even though the boundary modes are coupled to all boundary modes within an element and the boundary modes of neighbouring elements of that element, they are not coupled within non-neighbouring elements.

Boundary Conditions

In general, we treat all boundary modes that touch the solution domain boundary as global degrees of freedom. However, boundaries with Dirichlet conditions are not part of the Galerkin test space. Therefore, we remove the Dirichlet degrees of freedom from the global degrees of freedom by lifting the solution at the Dirichlet boundary as follows. First, we decompose the solution into an unknown homogeneous solution, $u_H(x)$, and the known Dirichlet boundary values $u_D(x)$ along the Dirichlet part of the boundary Γ_D , i.e.

$$u(x) = u_H(x) + u_D(x), \quad (3.99)$$

$$u_H(\Gamma_D) = 0, \quad u(\Gamma_D) = u_D(\Gamma_D). \quad (3.100)$$

For the discrete solution, $u^\delta(x)$, this means we separate the global solution array $\hat{\mathbf{u}}$ into known Dirichlet degrees of freedom, $\hat{\mathbf{u}}^D$, corresponding to the global expansion functions $\Phi_j^D(x)$, which has support on the Dirichlet boundary and the unknown degrees of freedom, $\hat{\mathbf{u}}^H$, corresponding to the global expansion functions with zero support on the Dirichlet boundary $\Phi_j^H(x)$, that is,

$$u^\delta(x) = \sum_{j \in \mathcal{N}^H} \hat{u}_j^H \Phi_j^H(x) + \sum_{i \in \mathcal{N}^D} \hat{u}_i^D \Phi_i^D(x), \quad (3.101)$$

where $\Phi_j(x)$ are the global expansion modes, \mathcal{N}^H is the number of global homogeneous degrees of freedom and \mathcal{N}^D is the number of global degrees of freedom with contributions on the Dirichlet boundary. In order to remove the known Dirichlet degrees of freedom from the matrix system, we reorder the global degrees of freedom such that the unknown boundary degrees of freedom are ordered first, followed by the known degrees of freedom

given by the Dirichlet boundary condition.

Consider the Galerkin L^2 -projection

$$(v_j, u(x))_\Omega = (v_j, f)_\Omega \text{ in } \Omega, \quad (3.102)$$

$$u(x) = u_D \text{ on } \Gamma_D, \quad (3.103)$$

where $v_j = \Phi_j^H$ are the Galerkin test functions which are zero at the Dirichlet boundary. Using the decomposition of $u(x)$ according to Equation (3.101), i.e.

$$\mathbf{u} = \mathbf{B}^H \hat{\mathbf{u}}^H + \mathbf{B}^D \hat{\mathbf{u}}^D, \quad (3.104)$$

the Dirichlet part of the solution can be lifted out of the global matrix system by

$$\mathbf{M}^{HH} \hat{\mathbf{u}}^H = [\mathbf{B}^H]^T \mathbf{W}^H \mathbf{f} - \mathbf{M}^{HD} \hat{\mathbf{u}}^D. \quad (3.105)$$

Here,

$$\mathbf{M}^{HH}[i][j] = \int_{\Omega_t} \Phi_j^H \Phi_i^H, \quad i \in \mathcal{N}^H, j \in \mathcal{N}^H, \quad (3.106)$$

$$\mathbf{M}^{HD}[i][j] = \int_{\Omega_t} \Phi_j^H \Phi_i^D, \quad i \in \mathcal{N}^D, j \in \mathcal{N}^H. \quad (3.107)$$

The solution is then given by

$$\mathbf{u} = \mathbf{B}^H \left[(\mathbf{M}^{HH})^{-1} \left((\mathbf{B}^H)^T \mathbf{W}^H \mathbf{f} - \mathbf{M}^{HD} \hat{\mathbf{u}}^D \right) \right] + \mathbf{B}^D \hat{\mathbf{u}}^D. \quad (3.108)$$

3.7.2. Discontinuous Galerkin Method

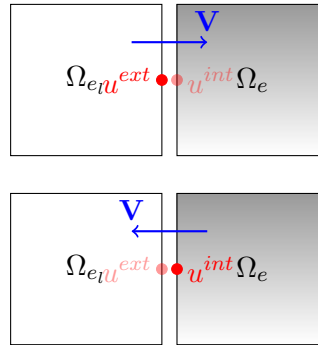


Figure 3.9.: Coupling of element Ω_e with neighbouring element Ω_{e_i} through upwind flux.

While the continuous Galerkin method is a suitable method to couple elements for the solution of a wide range of partial differential equations in a region Ω , there is a more

natural way to couple elements in equations describing transport phenomena, that can improve the stability and accuracy of a scheme. For example, the advection of a conserved quantity $u(x, t)$ in a region Ω , described by the nonlinear hyperbolic conservation law

$$\frac{\partial u}{\partial t} + \nabla \cdot \mathbf{F}(u) = 0, \quad (3.109)$$

where $\mathbf{F}(u)$ is a flux vector defining the transport of $u(x, t)$, tends to have solutions that include discontinuities, e.g. shocks. This suggests that a more appropriate choice for the discrete test and trial spaces would allow for these discontinuities to appear in the solution. The so-called discontinuous Galerkin method was first introduced by Lesaint and Raviart (1974) for the solution of the neutron transport equation. A discrete space that allows for discontinuities within spectral/hp element framework, is given by the space of piecewise continuous polynomial functions such as

$$\mathcal{V}^\delta = \left\{ v \in L^2(\Omega) : v|_{\Omega_e} \in \mathcal{P}_P(\Omega_e), \forall \Omega_e \right\}. \quad (3.110)$$

Here, $\mathcal{P}_P(\Omega_e)$ is the space of polynomials of order P defined in the element Ω_e .

Using this space as our trial and test space, we form the weak formulation of Equation (3.109) over each element Ω_e

$$\int_{\Omega_e} \phi_{pq} \frac{\partial u}{\partial t} d\Omega + \int_{\Omega_e} \phi_{pq} \nabla \cdot \mathbf{F}(u) d\Omega = 0. \quad (3.111)$$

Then, in contrast to the Galerkin method, we integrate the equation by parts and obtain

$$\int_{\Omega_e} \phi_{pq} \frac{\partial u}{\partial t} d\Omega + \int_{\partial\Omega_e} \phi_{pq} \mathbf{F}(u) \cdot \mathbf{n} d\Gamma - \int_{\Omega_e} \nabla \phi_{pq} \cdot \mathbf{F}(u) d\Omega = 0. \quad (3.112)$$

The integral term over the elemental boundary can now be used to couple the elements through the flux $\mathbf{F}(u)$. This flux $\mathbf{F}(u)$ enables information to propagate across elements and boundary conditions can be enforced through it within each element. This means that we can solve the equation element-by-element and a global assembly is no longer required. As the flux $\mathbf{F}(u)$ is computed at the boundary between adjacent elements, where the solution might be discontinuous, we have two possible values of the solution: one external to the element, $u^{ext}(x)$, and one internal to the element, $u^{int}(x)$. Therefore the flux in the boundary integral becomes a function of these two values $\tilde{\mathbf{f}}^e(u^{ext}(x), u^{int}(x))$. That means, in an implementation, we replace the flux $\mathbf{F}(u)$ in the boundary integral with the numerical flux $\tilde{\mathbf{f}}^e(u^{ext}(x), u^{int}(x))$. The numerical flux $\tilde{\mathbf{f}}^e(u^{ext}(x), u^{int}(x))$ can be chosen based on the natural propagation of the solution of the hyperbolic conservation law along the characteristics. For example, for the linear advection equation, i.e. $\mathbf{F}(u) = \mathbf{V}u$,

where \mathbf{V} is a divergence free velocity field, a choice of $\tilde{\mathbf{f}}^e(u^{ext}(x), u^{int}(x))$ using an upwinded approach generates a stable scheme (see Figure 3.9). Upwinding means that if information is transported into the element Ω_e , i.e. is entering the domain Ω_e , from a neighbouring element Ω_{e_l} , the flux at the boundary $\tilde{\mathbf{f}}^e(u^{ext}(x), u^{int}(x))$ for element Ω_e contains a higher percentage of the external value of the quantity of the neighbouring element Ω_{e_l} than of the internal value of the element. This gives an inflow condition for each element Ω_e , where information is transported into the domain. In this thesis, we employ the numerical flux $\tilde{\mathbf{f}}^e(u^{ext}(x), u^{int}(x))$ defined as follows

$$\tilde{\mathbf{f}}^e(u^{ext}(x), u^{int}(x)) = \begin{cases} \mathbf{V}(\gamma u^{ext}(x) + (1 - \gamma) u^{int}(x)), & \mathbf{V} \cdot \mathbf{n} < 0 \\ \mathbf{V}(\gamma u^{int}(x) + (1 - \gamma) u^{ext}(x)), & \mathbf{V} \cdot \mathbf{n} \geq 0 \\ \mathbf{V}u_D, & \text{at inflow boundary} \\ \mathbf{V}u^{int}, & \text{at outflow boundary} \end{cases} \quad (3.113)$$

for some $\gamma \in [0.5, 1]$. For $\gamma = 1$ we obtain a fully upwind scheme. Here, \mathbf{n} is the outward unit normal vector on $\partial\Omega_e$. However, this is just one of the many possible choices for an upwind scheme. Note that, we have used the discontinuous Galerkin formulation given in Equation (3.112) in our implementation. Solving Equation (3.112) in two space dimensions with the spectral/hp element method yields the following matrix operations for each element Ω_e

$$\frac{d\hat{\mathbf{u}}^e}{dt} = [\mathbf{M}^e]^{-1} \left[(\mathbf{D}_x^e \mathbf{B}^e)^T \mathbf{W}^e \Xi^e(f(u)) + (\mathbf{D}_y^e \mathbf{B}^e)^T \mathbf{W}^e \Xi^e(g(u)) \right] - [\mathbf{M}^e]^{-1} \mathbf{b}^e, \quad (3.114)$$

where \mathbf{b}^e is the vector corresponding to the surface integral

$$\mathbf{b}^e[n(pq)] = \int_{\partial\Omega_e} \phi_{pq} \tilde{\mathbf{f}}^e(u^{ext}(x), u^{int}(x)) \cdot \mathbf{n}^e d\Gamma, \quad (3.115)$$

$\mathbf{F}(u) = [f(u), g(u)]^T$ is the two dimensional flux and

$$\Xi^e(f(u))[m(ij)][n(rs)] = f(u)|_{(\xi_{1i}, \xi_{2j})} \delta_{mn}. \quad (3.116)$$

Note that Equation (3.114) only involves the inversion of the local elemental mass matrix, which is significantly cheaper to invert than the global mass matrix of the continuous Galerkin discretisation. This element-by-element inversion is also ideal for the purpose of parallelisation. An alternative implementation of the discontinuous Galerkin method is to

integrate by parts again and obtain

$$\int_{\Omega_e} \phi_{pq} \frac{\partial u^\delta}{\partial t} d\Omega + \int_{\partial\Omega_e} \phi_{pq} \left(\tilde{\mathbf{f}}^e(u^{ext}, u^{int}) - \mathbf{F}(u^\delta) \right) \cdot \mathbf{n} d\Gamma + \int_{\Omega_e} \phi_{pq} \nabla \cdot \mathbf{F}(u^\delta) d\Omega = 0. \quad (3.117)$$

This version does not include the derivative of the test functions and is therefore more consistent with the continuous Galerkin formulation.

Note that, in the discontinuous Galerkin method, we weakly impose the boundary conditions by enforcing them through the flux values, in contrast to the continuous Galerkin method, where we strongly enforce the Dirichlet boundary condition through lifting of the Dirichlet degrees of freedom. Details on other upwind scheme and the discontinuous Galerkin method can be found in the monographs of Karniadakis and Sherwin (2005) and Cockburn and Quarteroni (1998).

3.8. Example: One-Dimensional Projection and Advection

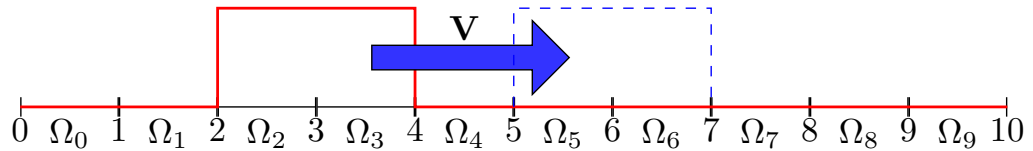


Figure 3.10.: One dimensional advection of square wave on domain $\Omega = [0, 10]$ subdivided into 10 equally-sized elements.

In order to demonstrate the capabilities and limitations of the spectral/hp element method in comparison to the finite element, we investigate the approximation error for different functions using Galerkin projection and one-dimensional constant linear advection. We examine three functions with decreasing smoothness:

- a smooth Gaussian function

$$f_0(x) = e^{-10(x-3)^2}. \quad (3.118)$$

- a hat function

$$f_0(x) = \begin{cases} x - 2, & \text{for } 2 \leq x \leq 3, \\ 1 - (x - 3), & \text{for } 3 < x \leq 4, \\ 0, & \text{otherwise.} \end{cases} \quad (3.119)$$

- a square wave function

$$f_0(x) = \begin{cases} 1, & \text{for } 2 \leq x \leq 4, \\ 0, & \text{otherwise.} \end{cases} \quad (3.120)$$

For the one-dimensional linear advection equation, we will compare the performance of the continuous Galerkin method and the discontinuous Galerkin method. And for the projection, we will perform a continuous projection and an element-by-element projection.

We consider the one dimensional domain $I = [0, 10]$ decomposed into ten elements of the same size. For the spectral/hp element method, we increase the number of degrees of freedom by increasing the polynomial order and for the finite element method we subdivide each element into equally sized smaller elements. We compare both methods for the same number of local degrees of freedom. That means we compare the behaviour of p -convergence for the spectral/hp element method and h -convergence for the linear finite

element method. Note that, we recover the linear finite element method for $P = 1$ in the spectral/hp element method.

We measure the error for each refinement level, l , in terms of the discrete normalised L^2 -error, E_2^l , and of the discrete relative L^∞ -error, E_∞^l . These errors are defined as follows

$$E_2^l = \frac{\sqrt{\sum_{e=1}^{N_{el}} (\|f_0 - f^\delta\|_2^e)^2}}{\sqrt{\sum_{e=1}^{N_{el}} (\|f_0\|_2^e)^2}}, \text{ with } \|f_0\|_2^e = \sqrt{\int_{\Omega_e} f_0^2 d\Omega}, \quad (3.121)$$

$$E_\infty^l = \frac{\max_{1 \leq e \leq N_{el}} (\|f_0 - f^\delta\|_\infty^e)}{\max_{1 \leq e \leq N_{el}} (\|f_0\|_\infty^e)}, \text{ with } \|f_0\|_\infty^e = \max_{1 \leq i, j < Q} |f_0(\xi_{1_i}, \xi_{2_j})|. \quad (3.122)$$

Here, the integrals in the norm $\|\cdot\|_2^e$ are computed using Gaussian quadrature, $|\cdot|$ denotes the absolute value and f^δ denotes the numerical solution. The rate of convergence p_l from level l to a higher refinement level $l + 1$, is determined by

$$p_l = \frac{\log\left(\frac{E^{l+1}}{E^l}\right)}{\log\left(\frac{\text{DOF}^{l+1}}{\text{DOF}^l}\right)}. \quad (3.123)$$

The rate of convergence plotted in the following graphs is computed using linear regression, i.e. we determine $y(x) = px + b$ with

$$p = \frac{\sum_{l=1}^{N_l} (x_l - \bar{x})(y_l - \bar{y})}{\sum_{l=1}^{N_l} (x_l - \bar{x})^2}, \quad (3.124)$$

where N_l is the number of levels, $x_i = \log(\text{DOF}^l)$, $y_i = \log(E^l)$ and

$$\bar{x} = \frac{1}{N_l} \sum_{l=1}^{N_l} x_l$$

is the arithmetic mean.

3.8.1. Galerkin Projection

We perform a one-dimensional Galerkin projection for the three functions $f_0(x)$ specified in (3.118), (3.119) and (3.120). We compare Galerkin projections performed element-by-element and globally C^0 . The Galerkin projection for an element is given by

$$(\mathbf{f}, \phi_q)_{\Omega_e}^\delta = (\mathbf{f}_0, \phi_q)_{\Omega_e}^\delta, \quad \forall q \in [0, P] \quad (3.125)$$

which is solved as follows

$$\hat{\mathbf{f}}^e = \left[[\mathbf{M}^e]^{-1} \left([\mathbf{B}^e]^T \mathbf{W}^e \mathbf{f}_0^e \right) \right]. \quad (3.126)$$

For the element-by-element projection, we solve Equation (3.126) for each element. For the continuous Galerkin method, we need to form the global matrix system and invert the global matrix using the multi-level static condensation technique as explained in Section 3.7.1. The global problem is given by

$$\hat{\mathbf{f}}_g = [\mathbf{M}_g]^{-1} \left(\mathcal{A}^T [\underline{\mathbf{B}}^e]^T \mathbf{W}^e \mathcal{A} \hat{\mathbf{f}}_{0,g} \right), \quad (3.127)$$

where

$$\mathbf{M}_g := \mathcal{A}^T \underline{\mathbf{M}}^e \mathcal{A}. \quad (3.128)$$

After solving Equation (3.126) or Equation (3.127), we obtain the values of the approximated solution by

$$f^{e,\delta}(\xi_i) = \sum_{p=0}^P \phi_p(\xi_i) \hat{f}_p^e, \quad \forall \xi_i, i = 1, \dots, Q, \forall \Omega_e \quad (3.129)$$

The results of the projection in comparison to the analytical functions are plotted for a total number of local degrees of freedom of 90 together with the L^2 error and the L^∞ error for an increasing number of local degrees of freedom in Figures 3.11-3.13. We compare the performance of the spectral/hp element method for $P = 8$, i.e. the number of modes per element is $N_m = 9$, and $N_{el} = 10$ with the linear finite element method, i.e. $N_m = 2$, for $N_{el} = 45$ yielding a total number of local degrees of freedom of 90 for both methods. To investigate the convergence properties of the methods, the local number of degrees of freedom is increased by increasing the polynomial order for the spectral/hp element method while keeping the element size constant and decreasing the element size for the linear finite element method.

In Figure 3.11(e) and (f), we observe that for the smooth Gaussian function the spectral/hp element method captures the function excellently and we can observe exponential conver-

gence of the computed projection to the analytical function with increasing polynomial order in terms of the L^2 and L^∞ error. In the finite element method the numerical projection suffers from numerical diffusion in contrast to the spectral/hp element method. The order of convergence with decreasing mesh size for the finite element method is around 2. Figure 3.12 (e) and (f) shows the numerical L^2 projection of the hat function. The spectral/hp element method is able to capture the hat function up to machine precision from the lowest polynomial order tested $P = 2$. The finite element method suffers again from numerical diffusion, i.e. it underpredicts the peak value. The numerical diffusion of the sharp peak value of the hat function remains dominant with decreasing mesh size and the order of convergence is 1 in terms of the L_2 error and 1.5 in terms of the L^∞ error.

In Figure 3.13, we observe the so-called Gibbs phenomenon in the numerical projection. The approximation of the jump discontinuity using the spectral/hp element method yields over- and undershoots near the jump. However, these oscillations are confined to one element. The number of over- and undershoots equals the number of degrees of freedom in the element ($P + 1$), i.e. in Figure 3.13(a) and (b) five overshoots and four undershoots for a polynomial order of $P = 8$. Even though the number of over and undershoots increases with polynomial order their magnitude decreases with increasing polynomial order and the projection slowly converges to the analytical function with a convergence order of 0.88 in terms of L^2 and 1.38 in terms of L^∞ . The magnitude of the overshoot on the element boundary of the element at the bottom of the jump discontinuity is lower for the global C^0 projection than for the element by element projection.

The numerical projection using the linear finite element method yields one over and undershoot at the bottom and the top of each jump discontinuity for the global C^0 projection and one undershoot for the element by element projection. The L^2 error for the projection almost stagnates and the L^∞ error decreases slowly with decreasing mesh size with a rate of convergence of 0.5.

3.8.2. Advection

In this Section, we consider the linear advection of the function $f(x, t)$ with constant advection velocity $V = 1$, described by the linear advection equation

$$\begin{aligned} \frac{\partial f(x, t)}{\partial t} + V \frac{\partial f(x, t)}{\partial x} &= 0 \quad \text{in } \Omega = [0, 10], \\ f(x, 0) &= f_0(x), \\ f(0, t) = f(10, t) &= 0. \end{aligned} \quad (3.130)$$

We discretise the equation in weak form, by taking the inner product of the advection equation with respect to the test function v . For the continuous Galerkin method the weak formulation is given by

$$\left(v, \frac{\partial f}{\partial t} \right)_{\Omega} + \left(v, V \frac{\partial f}{\partial x} \right)_{\Omega} = 0 \quad (3.131)$$

which, with $v = \phi_p(x)$, in matrix notation becomes

$$\mathbf{M}_g \frac{d\hat{\mathbf{f}}_g}{dt} + \mathcal{A}^T \left(\underline{[\mathbf{B}^e]^T \mathbf{W}^e \mathbf{D}^e \mathbf{B}^e} \right) \mathcal{A} \hat{\mathbf{f}}_g = 0, \quad (3.132)$$

where

$$\mathbf{D}^e = \Xi^e \mathbf{D}_{\xi}^e, \quad \Xi^e[m(ij)][n(rs)] = V \frac{\partial \xi_i}{\partial x_j} \delta_{mn}. \quad (3.133)$$

For the discontinuous Galerkin method, the weak form is given by

$$\left(v, \frac{\partial f}{\partial t} \right)_{\Omega_e} + \left[v \tilde{f}^e(f^{ext}, f^{int}) \right]_{\partial\Omega_e} - \left(\frac{\partial v}{\partial x}, V f \right)_{\Omega_e} = 0 \quad (3.134)$$

where $\langle \cdot \rangle_{\partial\Omega_e}$ denotes the boundary integral. Employing a fully upwind scheme with $\gamma = 1$ in Equation (3.113) for the numerical flux yields

$$\tilde{f}^e(f^{ext}, f^{int}) = \begin{cases} V f^{int}, & V \cdot \mathbf{n} \geq 0, \\ V f^{ext}, & V \cdot \mathbf{n} < 0. \end{cases} \quad (3.135)$$

Integrating by parts again yields

$$\left(v, \frac{\partial f}{\partial t} \right)_{\Omega_e} + \left[v \left(\tilde{f}^e(f^{ext}, f^{int}) - fV \right) \right]_{\partial\Omega_e} + \left(v, V \frac{\partial f}{\partial x} \right)_{\Omega_e} = 0. \quad (3.136)$$

In our one dimensional example the numerical flux in an element $\Omega_e = [x_L, x_R]$ with $v = \phi_p$ becomes

$$\begin{aligned} \left[\phi_p \left(\tilde{f}^e(f^{ext}, f^{int}) - fV \right) \right]_{\partial\Omega_e} &= \left[\left(\phi_p \left(\tilde{f}^e(f^{ext}, f^{int}) - fV \right) \right) \right]_{x_L}^{x_R} \\ &= \phi_p(x_R) \left(\tilde{f}^e(x_R) - f(x_R)u(x_R) \right) - \phi_p(x_L) \left(\tilde{f}^e(x_L) - f(x_L)u(x_L) \right). \end{aligned} \quad (3.137)$$

For the numerical flux, we have, for $V = 1$

$$\tilde{f}^e(x_R) = f^{int}(x_R) \quad \text{as } n_R = 1, \quad (3.138)$$

$$\tilde{f}^e(x_L) = f^{ext}(x_L) \quad \text{as } n_L = -1, \quad (3.139)$$

and as $f(x_R) = f^{int}(x_R)$ and $f(x_L) = f^{int}(x_L)$, we obtain

$$\left\langle \phi_p, \left(\tilde{f}^e(f^{ext}, f^{int}) - f \right) \cdot \mathbf{n} \right\rangle_{\partial\Omega_e} = -\phi_p(x_L) \left(f^{ext}(x_L) - f^{int}(x_L) \right). \quad (3.140)$$

Note that for our spectral/hp element basis and for the finite element basis only ϕ_0 has a contribution at the boundary vertex x_L and that contribution is one (see Figure 3.3(b)). Therefore the discontinuous Galerkin formulation with $v = \phi_p$ of Equation (3.136) becomes

$$\left(\phi_0, \frac{\partial f}{\partial t} \right)_{\Omega_e} + \left(\phi_0, \frac{\partial f}{\partial x} \right)_{\Omega_e} - \left(f^{ext}(x_L) - f^{int}(x_L) \right) = 0, \quad (3.141)$$

$$\left(\phi_p, \frac{\partial f}{\partial t} \right)_{\Omega_e} + \left(\phi_p, \frac{\partial f}{\partial x} \right)_{\Omega_e} = 0, \quad 1 \leq p \leq P. \quad (3.142)$$

The discontinuous Galerkin discretisation in matrix notation becomes

$$\mathbf{M}^e \frac{d\hat{\mathbf{f}}^e}{dt} + \left([\mathbf{B}^e]^T \mathbf{W}^e \mathbf{D}^e \mathbf{B}^e \right) \hat{\mathbf{f}}^e + \mathbf{b}^e = 0. \quad (3.143)$$

Here, \mathbf{D}^e is the same matrix as defined in (3.133) and the vector \mathbf{b}^e is

$$\mathbf{b}^e[0] = - \left(f^{ext}(x_L) - f^{int}(x_L) \right), \quad (3.144)$$

$$\mathbf{b}^e[n(pq)] = 0, \quad \text{for } 1 \leq p, q \leq P. \quad (3.145)$$

Note that, the matrix formulation (3.143) is very similar to the matrix formulation of the continuous Galerkin discretisation (3.132). However, the significant difference is that in the DG discretisation, we do not need to assemble the global system and we can compute the solution element-by-element thanks to the coupling of the element through the boundary integral.

The solution for the continuous Galerkin method is determined by

$$\frac{d\hat{\mathbf{f}}_g}{dt} = -[\mathbf{M}_g]^{-1} \left[\mathcal{A}^T \left(\underline{[\mathbf{B}^e]^T \mathbf{W}^e \mathbf{D}^e \mathbf{B}^e} \right) \mathcal{A} \hat{\mathbf{f}}_g \right], \quad (3.146)$$

where the inversion of the global matrix is computed using the multi-static condensation technique explained in Section 3.7.1. And for the discontinuous Galerkin method the solution is determined by

$$\frac{d\hat{\mathbf{f}}^e}{dt} = -[\mathbf{M}^e]^{-1} \left[\left([\mathbf{B}^e]^T \mathbf{W}^e \mathbf{D}^e \mathbf{B}^e \right) \hat{\mathbf{f}}^e + \mathbf{b}^e \right], \quad \forall \Omega_e. \quad (3.147)$$

We solve the linear advection equation in time using a fourth-order Runge-Kutta method and transport the function $f(x, t)$ for 30000 timesteps of size $\Delta t = 10^{-4}$, i.e. until the final time $t_{fin} = 3$.

The exact solution for the advection with convection velocity V until t_{fin} of the three investigated functions (3.118)-(3.120) is then given by

- for the smooth Gaussian function

$$f_0(x) = e^{-10(x-(3+Vt_{fin}))^2}. \quad (3.148)$$

- for the hat function

$$f_0(x) = \begin{cases} x - (2 + Vt_{fin}), & \text{for } 2 + Vt_{fin} \leq x \leq 3 + Vt_{fin}, \\ 1 - (x - (3 + Vt_{fin})), & \text{for } 3 + Vt_{fin} < x \leq 4 + Vt_{fin}, \\ 0, & \text{otherwise.} \end{cases} \quad (3.149)$$

- for the square wave function

$$f_0(x) = \begin{cases} 1, & \text{for } 2 + Vt_{fin} \leq x \leq 4 + Vt_{fin}, \\ 0, & \text{otherwise.} \end{cases} \quad (3.150)$$

We observe in Figure 3.14 that for the spectral/hp element method the error for the transport of the smooth Gaussian function decreases exponentially with increasing polynomial order. Continuous Galerkin and discontinuous Galerkin yield similar results for the spectral/hp element method. The only difference is in an onset of slight oscillations in the wake of the Gaussian function for the continuous Galerkin method. For the continuous Galerkin linear finite element method, we observe numerical diffusion and strong oscillations in the wake. The discontinuous Galerkin linear finite element method performs undershoots near the Gaussian hump and the convergence rate for the finite element method is around 1.8.

Figure 3.15 reveals similar qualitative behaviour for the approximation of the hat function for the finite element method with decreased convergence rate of 1 for the L^2 error and 1.34 for the L^∞ error. However, for the spectral element method, the exponential convergence is lost as the hat function gets smoothed by the approximation at the top of the hat function and at the bottom and the convergence rate reduces to linear convergence with a rate of 1.21 for the L^2 error and 1.69 for the L^∞ error.

Figure 3.16 reveals the dramatic consequences of the Gibbs phenomenon in advection of a jump discontinuity. In the continuous Galerkin method for the spectral/hp element method the oscillations occurring around the jump discontinuity in the approximation as displayed in Figure 3.13(a) are transported across the whole domain even yielding divergence with increasing polynomial order. The discontinuous Galerkin method for the spectral/hp element prevents the oscillations from convecting into the whole domain and yields much smaller oscillations only in the direction of the advection velocity and close to the first jump discontinuity and on top of the square wave. For the finite element method, strong oscillations occur in the wake and on the top of the square wave. However, there is no divergence with decreasing mesh size. The discontinuous Galerkin linear finite element method prevents these oscillations and simply shows an undershoot near the jump continuity and an overshoot on top of the square wave. There is almost no convergence observed in terms of the L^2 error for DG for the spectral/hp element method and for the DG and the C^0 method for the finite element method. In terms of the L^∞ error the DG method for the spectral/hp method converges with a rate of 0.5, which is slightly higher than the convergence rate of 0.33 for the DG method for the finite element method.

These examples show very clearly that the DG method is superior to the continuous Galerkin method for advection dominated problems. For all three tested function the discontinuous Galerkin method for the spectral/hp element method showed the lowest error. However, spectral convergence can only be achieved for smooth functions.

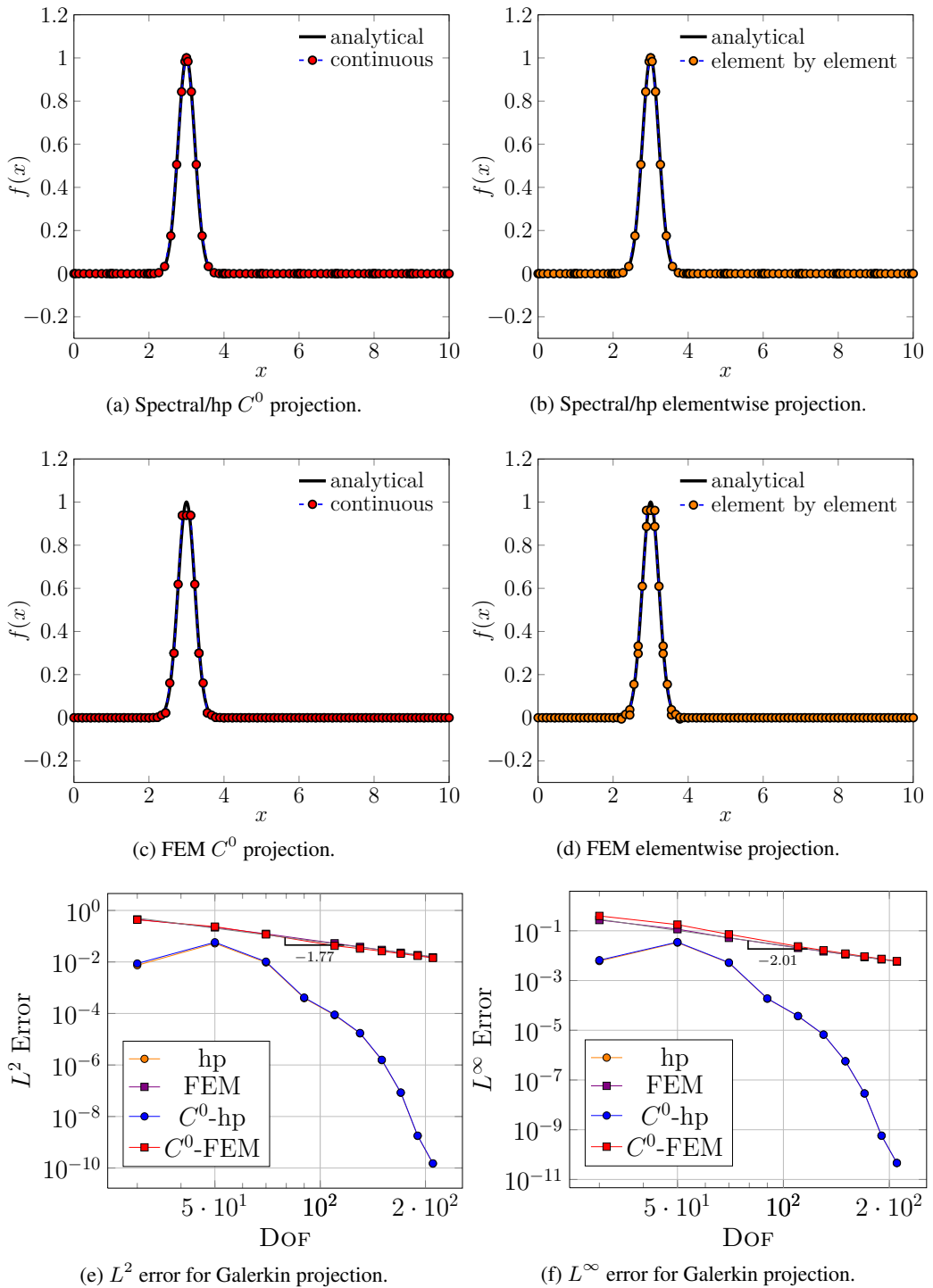


Figure 3.11.: Comparison of Galerkin projection for the Gaussian function of ((a), (b)) spectral/hp element method and ((c), (d)) linear finite element method for $DOF = 90$ and the corresponding L^2 and L^∞ error for increasing DOF ((e), (f)).

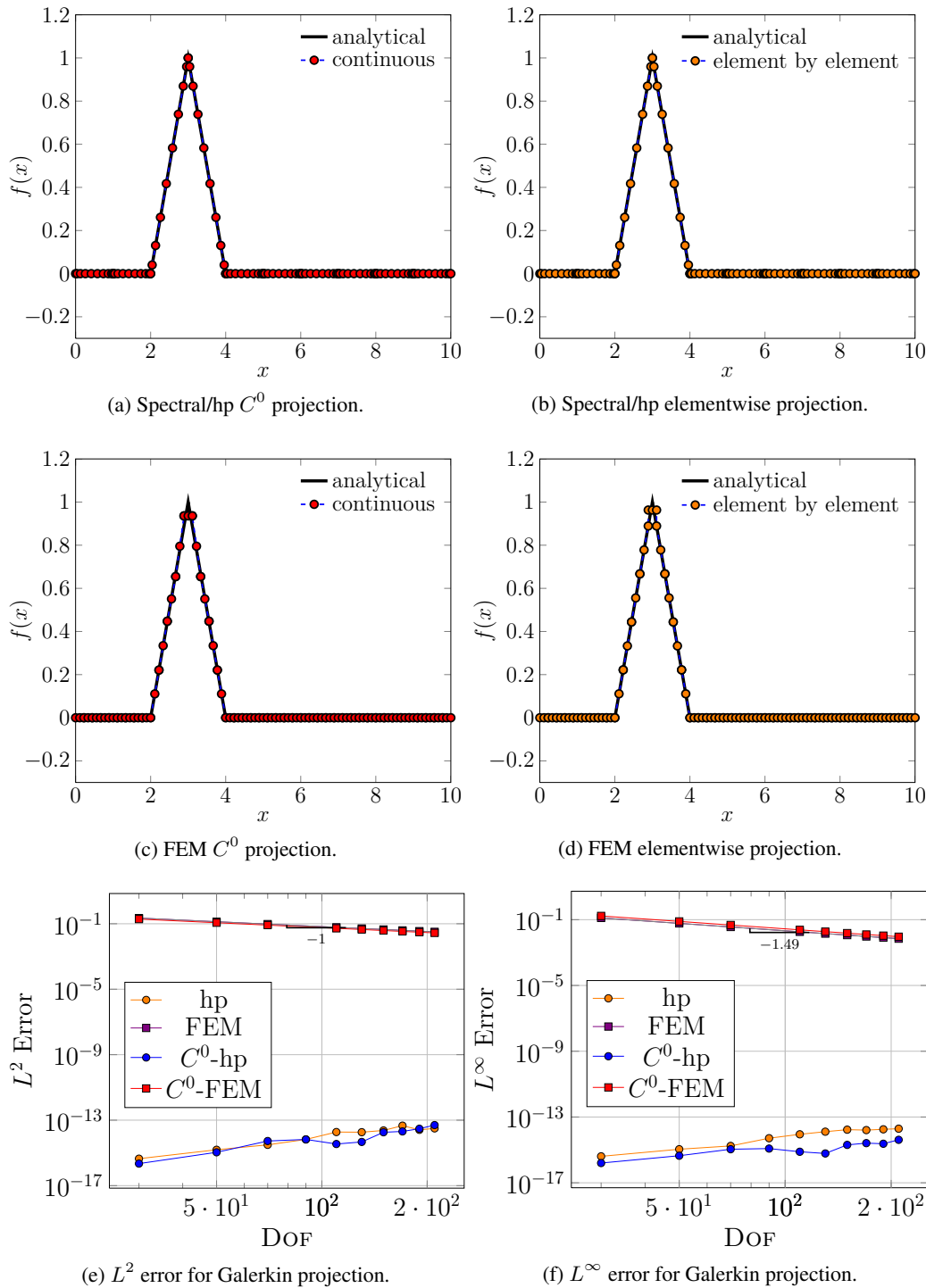


Figure 3.12.: Comparison of Galerkin projection for the hat function of ((a), (b)) spectral/hp element method and ((c), (d)) linear finite element method for $DOF = 90$ and the corresponding L^2 and L^∞ error for increasing DOF ((e), (f)).

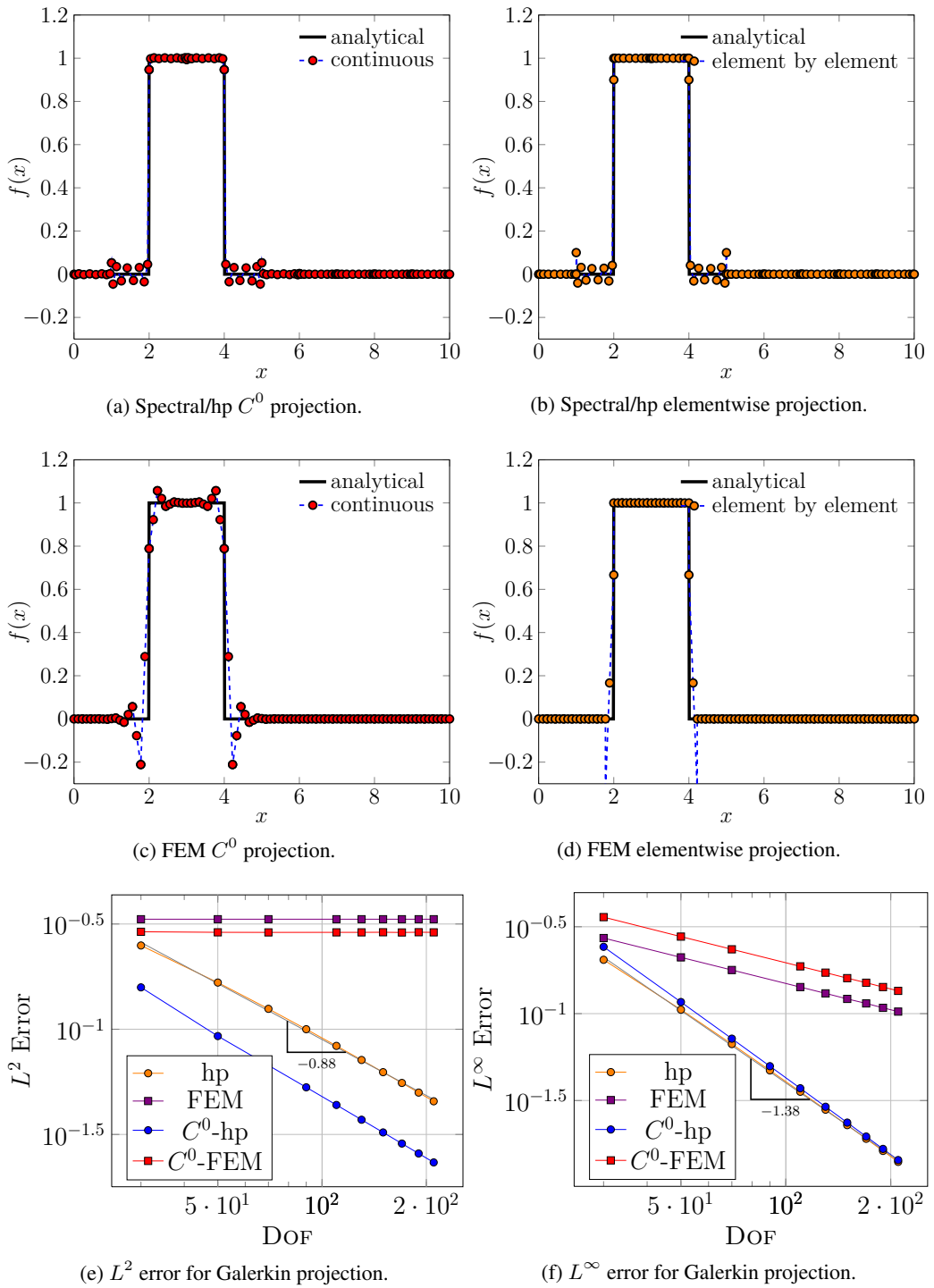


Figure 3.13.: Comparison of Galerkin projection for the square wave function of ((a), (b)) spectral/hp element method and ((c), (d)) linear finite element method for $DOF = 90$ and the corresponding L^2 and L^∞ error for increasing DOF ((e), (f)).

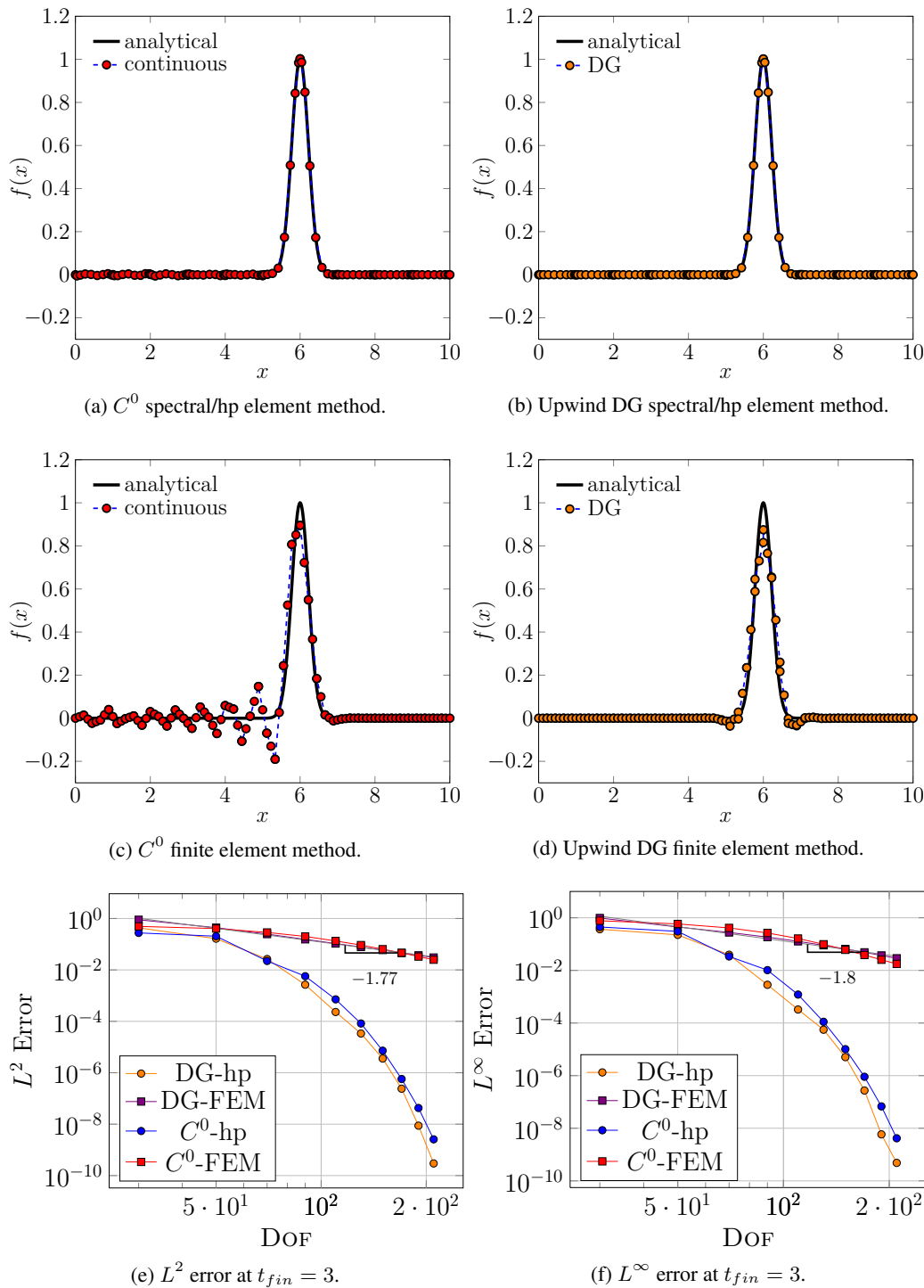


Figure 3.14.: Comparison of the numerical results for the advection equation after 30000 timesteps with $\Delta t = 10^{-4}$ using the continuous Galerkin method and the discontinuous Galerkin method for the spectral/hp element method for $P = 8$, $N_{el} = 10$ ((a), (b)) and the linear finite element method, i.e. $P = 1$, for $N_{el} = 45$ ((c), (d)) for the smooth Gaussian function and the L^2 and L^∞ error for increasing DOF ((e), (f)).

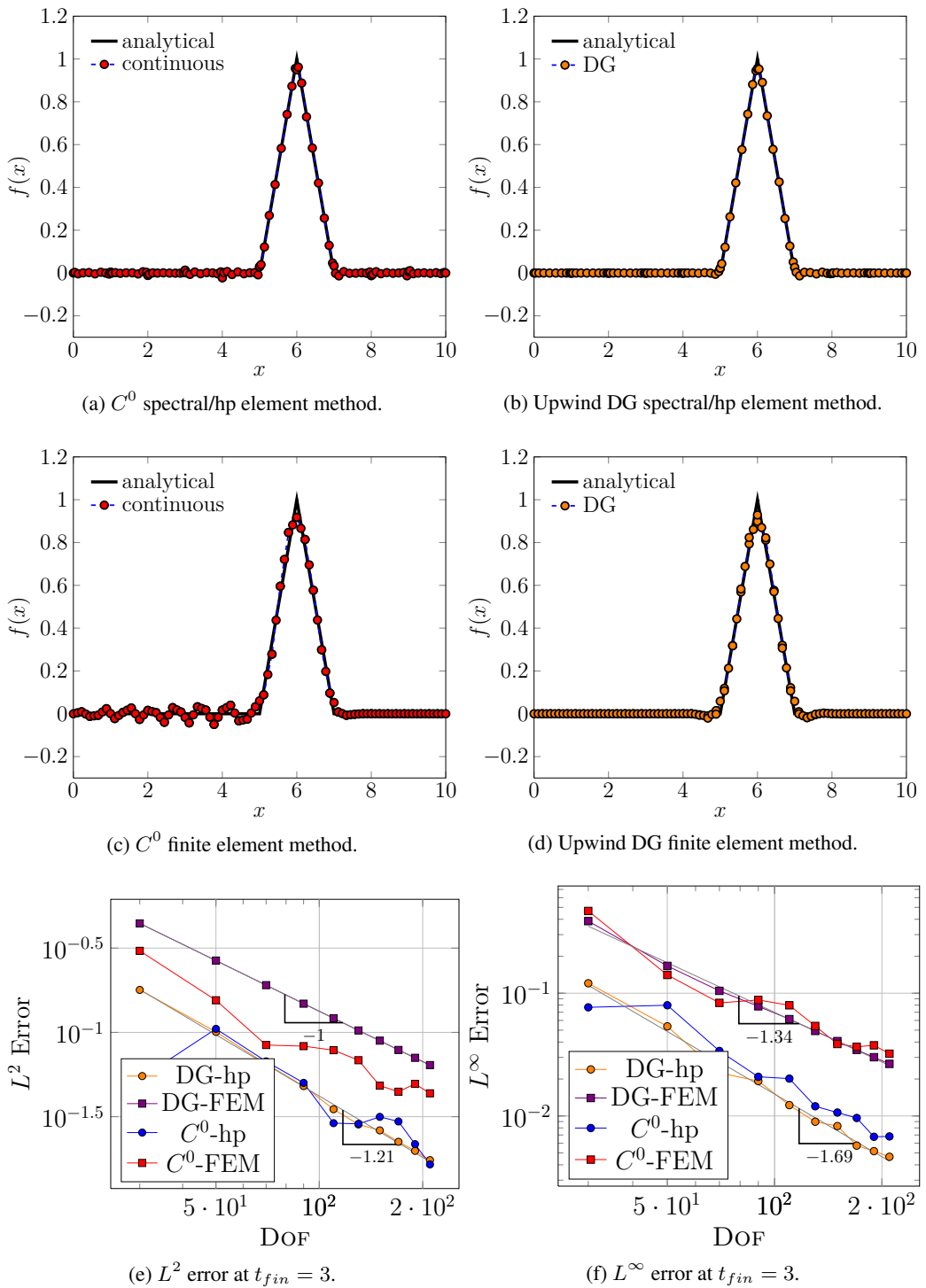


Figure 3.15.: Comparison of the numerical results for the advection equation after 30000 timesteps with $\Delta t = 10^{-4}$ using the continuous Galerkin method and the discontinuous Galerkin method for the spectral/hp element method for $P = 8$, $N_{el} = 10$ ((a), (b)) and the linear finite element method, i.e. $P = 1$, for $N_{el} = 45$ ((c), (d)) for the hat function and the L^2 and L^∞ error for increasing DOF ((e), (f)).

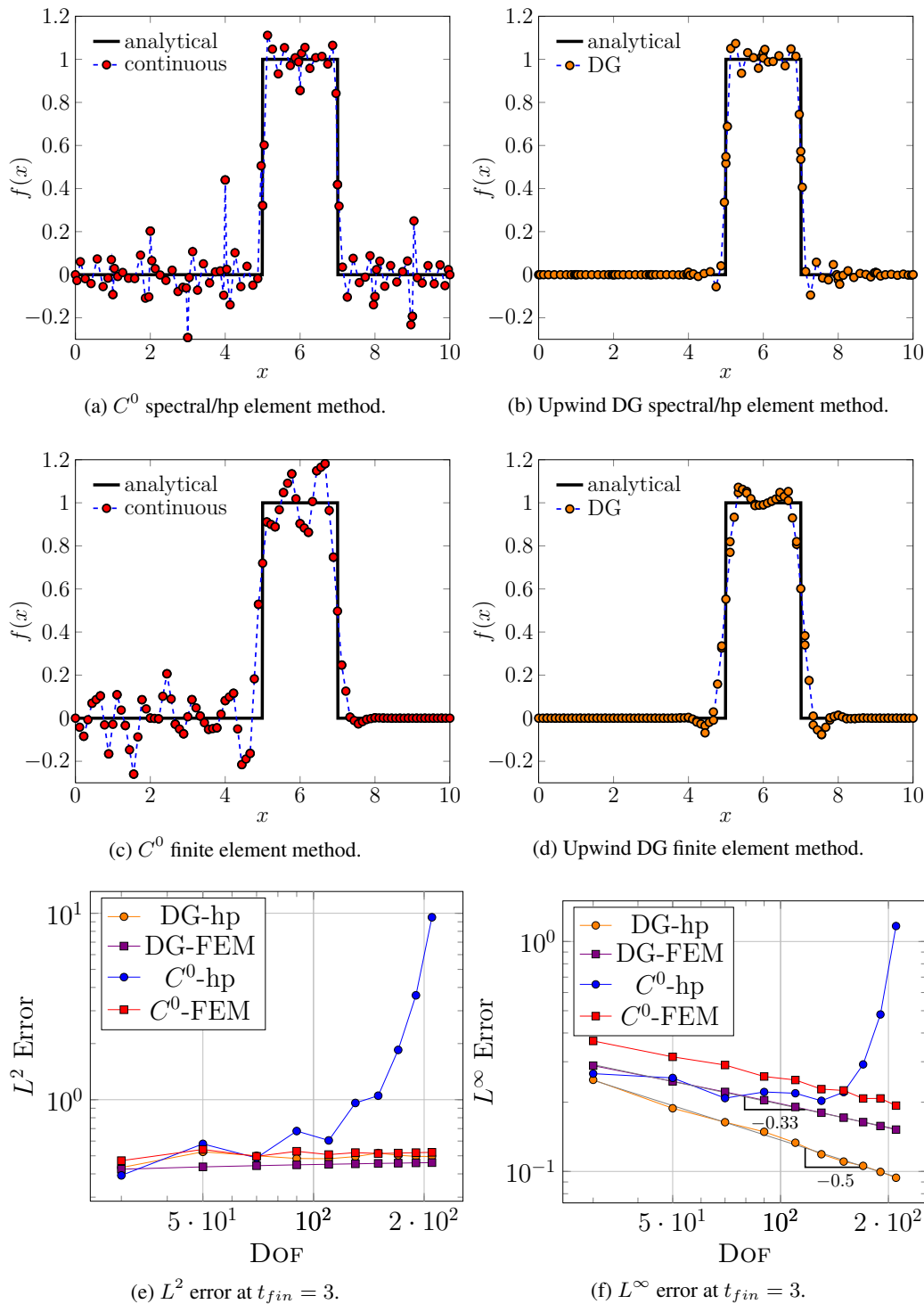


Figure 3.16.: Comparison of the numerical results for the advection equation after 30000 timesteps with $\Delta t = 10^{-4}$ using the continuous Galerkin method and the discontinuous Galerkin method for the spectral/hp element method for $P = 8$, $N_{el} = 10$ ((a), (b)) and the linear finite element method, i.e. $P = 1$, for $N_{el} = 45$ ((c), (d)) for the hat function and the L^2 and L^∞ error for increasing DOF ((e), (f)).

Chapter 4

Temporal and Spatial Approximation for Viscoelastic Flows

In this Section, we present the spatial and temporal approximations employed in this thesis to solve the weak form of the equations governing viscoelastic flows (2.178), which were introduced in Chapter 2. As mentioned in Chapter 2 the system of equations (2.178) are of mixed type: the conservation laws are of elliptic/parabolic type and the constitutive equation is hyperbolic (Gerritsma (1996); Owens and Phillips (2005)). Our numerical scheme is based on the popular decoupled approach to split the formulation into the solution of the conservation equations for velocity-pressure and into the computation of the constitutive equation for the polymeric stress. To each of these two split “solution steps”, we apply a stabilisation technique:

1. for the constitutive equation, we employ upwinding techniques in order to develop a stable scheme considering its hyperbolic nature. As demonstrated in Section 3.8.2 on a one dimensional linear advection problem, the continuous Galerkin method is not suitable for hyperbolic problems.
2. for the conservation equations, we introduce an additional elliptic operator into the momentum equation in order to enhance stability. This elliptic operator is introduced because for viscoelastic liquids, flow configurations of interest are often in a parameter range of a low Newtonian to total viscosity, i.e. $\beta \ll 1$. This means the elliptic term $\beta \Delta \mathbf{u}$ in the momentum equation is a lot weaker in the balance of terms in comparison to the Navier-Stokes equations for Newtonian liquids, i.e. $\beta = 1$.

In addition to these two stabilisation techniques, we need to consider compatibility conditions in the selection of the discrete spaces for the three variables of velocity, pressure and polymeric stress. An overview of stabilisation techniques for viscoelastic flow is given in Baaijens (1998).

In the following, we employ the following notation. Let a, b be two scalars, \mathbf{a}, \mathbf{b} be two vectors and \mathbf{A}, \mathbf{B} be two tensors. Then, the inner products $(\cdot, \cdot)_{\Omega}$ and $\langle \cdot, \cdot \rangle_{\partial\Omega}$ are defined

as follows

$$(a, b)_\Omega = \int_\Omega ab \, d\Omega, \quad (4.1)$$

$$(\mathbf{a}, \mathbf{b})_\Omega = \int_\Omega \mathbf{a} \cdot \mathbf{b} \, d\Omega, \quad (4.2)$$

$$(\mathbf{A}, \mathbf{B})_\Omega = \int_\Omega \mathbf{A} : \mathbf{B} \, d\Omega, \quad (4.3)$$

$$\langle \mathbf{A} \cdot \mathbf{n}, \mathbf{b} \rangle_\Gamma = \int_\Gamma (\mathbf{A} \cdot \mathbf{n}) \cdot \mathbf{b} \, d\Gamma. \quad (4.4)$$

4.1. Stabilisation Techniques

4.1.1. Upwinding Techniques for the Constitutive Equations

A constitutive equation of Maxwell and Oldroyd-type for the polymeric stress is hyperbolic in nature (see Owens and Phillips (2005)), which means we need to incorporate discretisation techniques suitable for hyperbolic problems such as upwinding techniques, e.g. streamline upwind/Petrov-Galerkin (SUPG, Brooks and Hughes (1982)) or discontinuous Galerkin methods (Lesaint and Raviart (1974)).

The SUPG method, first applied to viscoelastic flows by Marchal and Crochet (1987), is applied to the Oldroyd-B constitutive equation, for example, by modifying the test function space with an upwind factor

$$\left(\mathbf{W}_i \nabla + \boldsymbol{\tau} - 2(1 - \beta)\mathbf{D}, \phi_{\boldsymbol{\tau}} + \gamma \nabla \phi_{\boldsymbol{\tau}} \right)_\Omega = 0, \quad (4.5)$$

where γ is the upwind parameter. Several choices for γ have been introduced, however, all are of the form

$$\gamma = \frac{h}{U}, \quad (4.6)$$

where h is a characteristic length-scale of an element and U is a characteristic velocity, e.g. the norm of the velocity \mathbf{u} or a characteristic velocity of the flow. An SUPG method suitable for nodal spectral element methods has been presented by Owens et al. (2002). The SUPG method may produce oscillatory stress fields at steep stress boundary layers or near singularities.

Another possibility to account for the hyperbolic nature of the constitutive equation is the discontinuous Galerkin method introduced in Section 3.7.2, which we employ in this thesis in order to solve the constitutive equation. The discontinuous Galerkin method was first applied to viscoelastic flows by Fortin and Fortin (1989). We demonstrated the advantages of the discontinuous Galerkin method over the continuous Galerkin method in Section 3.8.2 on a one dimensional linear advection problem. To employ the discontinuous

Galerkin method, we integrate the convection term $\mathbf{u} \cdot \nabla \boldsymbol{\tau}$ in the constitutive equation by parts on each element Ω_e , which yields

$$\int_{\Omega_e} (\mathbf{u} \cdot \nabla \boldsymbol{\tau}) : \phi_{\boldsymbol{\tau}} d\Omega_e = - \int_{\Omega_e} (\mathbf{u} \cdot \nabla) \phi_{\boldsymbol{\tau}} : \boldsymbol{\tau} d\Omega_e + \int_{\partial\Omega_e} (\mathbf{u} \cdot \mathbf{n}) \boldsymbol{\tau} : \phi_{\boldsymbol{\tau}} d\Gamma \quad (4.7)$$

Note that the elemental domains Ω_e are now coupled through the boundary integral term and the equations can be solved element-by-element. Next, we replace the term $(\mathbf{u} \cdot \mathbf{n}) \boldsymbol{\tau}$ in the boundary integral by the boundary flux $\tilde{\mathbf{f}}^e(\boldsymbol{\tau}^{ext}(x), \boldsymbol{\tau}^{int}(x))$ given by

$$\tilde{\mathbf{f}}^e(\boldsymbol{\tau}^{int}(x), \boldsymbol{\tau}^{ext}(x)) = \begin{cases} (\mathbf{u} \cdot \mathbf{n})(\gamma \boldsymbol{\tau}^{ext} + (1 - \gamma) \boldsymbol{\tau}^{int}), & \mathbf{u} \cdot \mathbf{n} < 0, \\ (\mathbf{u} \cdot \mathbf{n})(\gamma \boldsymbol{\tau}^{int} + (1 - \gamma) \boldsymbol{\tau}^{ext}), & \mathbf{u} \cdot \mathbf{n} \geq 0, \\ (\mathbf{u} \cdot \mathbf{n}) \boldsymbol{\tau}_{in}, & \text{at inflow boundary,} \\ (\mathbf{u} \cdot \mathbf{n}) \boldsymbol{\tau}^{int}, & \text{at outflow boundary,} \end{cases} \quad (4.8)$$

where $\boldsymbol{\tau}^{ext}(x)$ is the value of $\boldsymbol{\tau}$ external to the element and $\boldsymbol{\tau}^{int}(x)$ is the value internal to the element and $\gamma \in [0, 1]$. For $\gamma = 1$, we obtain a fully upwind approximation to the flux. Here, $\boldsymbol{\tau}_{in}$ denotes the Dirichlet inflow values of the polymeric stress.

4.1.2. DEVSS-G Formulation

In order to stabilise the numerical solution by improving the ellipticity of the momentum equation, we employ a variant of the discrete elastic viscous split stress DEVSS method, the DEVSS-G scheme, first introduced by Liu et al. (1998). The DEVSS-G method is based on methods that were introduced earlier. The success of schemes introducing additional ellipticity into the momentum equations arises from the explicit form of the viscous operator in the momentum equation, which results in solving an elliptic saddle point problem. For viscoelastic liquids this viscous term is scaled with the ratio of Newtonian to total viscosity. As we are usually interested in flow configurations with dominant viscoelastic effects, the ratio of Newtonian to total viscosity as defined in (2.173) is usually chosen to be small $\beta \approx 0.1$ (i.e. 90 % polymeric viscosity to 10 % Newtonian viscosity). In these cases the elastic stress contribution can dominate the viscous term and this can lead to instabilities. The more dominant the viscous term is in the equation, relative to the elastic stress contribution, the better the performance of the method. An overview over these methods can be found in Baaijens (1998) and Owens and Phillips (2005). The idea of introducing ellipticity through a change of variables was first employed in the elastic viscous split stress (EVSS) formulation, introduced by Perera and Walters (1977), used by Mendelson et al. (1982) for second order fluids and extended for viscoelastic liquids by Beris et al. (1984). In the EVSS scheme, we perform a change of variables to the stress

variable Σ

$$\Sigma = \boldsymbol{\tau} - 2(1 - \beta)\mathbf{D}. \quad (4.9)$$

Substituting this expression into the governing equations introduced in Problem 2.11 for Oldroyd-B flow with $\frac{D\mathbf{u}}{Dt} = 0$ yields

$$\left(\Sigma + \text{Wi} \overset{\nabla}{\Sigma} + 2(1 - \beta)\text{Wi} \overset{\nabla}{\mathbf{D}}, \phi_{\Sigma} \right)_{\Omega} = 0, \quad (4.10)$$

$$(2\mathbf{D} + \Sigma, \nabla \phi_{\mathbf{u}})_{\Omega} - (p, \nabla \cdot \phi_{\mathbf{u}})_{\Omega} = 0, \quad (4.11)$$

$$(\nabla \cdot \mathbf{u}, \psi)_{\Omega} = 0. \quad (4.12)$$

Here, we assume that all boundary terms are zero. One disadvantage of this formulation is that in Equation (4.10), we need to evaluate the upper convected derivative of the rate of deformation tensor, which includes the second-order derivative of the velocity field. In order to avoid this, Rajagopalan et al. (1990), proposed treating the rate of deformation tensor as a separate unknown and computing it using an L^2 -projection of the rate of deformation tensor. Sun et al. (1996) introduced the adaptive viscoelastic split stress (AVSS) scheme, in which the viscosity in the change of variables is adapted according to the flow configuration, in such a way that the viscous contribution in Σ is of at least the same order as that of the elastic contribution.

Brown et al. (1993) used the velocity gradient tensor as an additional unknown, instead of using the rate of deformation tensor. In this method, called the EVSS-G method, we compute the additional unknown, the velocity gradient projection tensor \mathbf{G} , by an L^2 projection

$$(\mathbf{G} - \nabla \mathbf{u}, \phi_{\mathbf{G}})_{\Omega} = 0. \quad (4.13)$$

The change of variables performed in EVSS-type methods may be impossible to perform for some constitutive equations. Therefore, Guénette and Fortin (1995) introduced the discrete EVSS (DEVSS) method, in which no change of variables is required and the viscous term is introduced into the momentum equation only in an approximate sense using the numerical approximations. The discrete splitting method essentially adds and subtracts two different approximations of the same viscous contribution to increase the viscous contribution in the momentum equation that comes from the Newtonian viscosity. In the limit where these approximations are exact, the added terms cancel, giving the original equation. Introducing the discrete approximation of the rate of deformation tensor $\overline{\mathbf{D}}$, computed by an L^2 projection of the rate of deformation tensor, as an additional unknown and including this term into the Cauchy stress tensor, by adding $\theta \mathbf{D}$ and subtracting the

same amount in terms of the discrete approximation $\theta\bar{\mathbf{D}}$, that is,

$$\boldsymbol{\sigma} \approx -p\mathbf{I} + 2\beta\mathbf{D} + 2\theta(\mathbf{D} - \bar{\mathbf{D}}), \quad (4.14)$$

the DEVSS formulation for steady state flows reads

Problem 4.1 (DEVSS). Find $(\mathbf{u}, p, \bar{\mathbf{D}}, \boldsymbol{\tau}) \in [H_D^1(\Omega)]^2 \times [L_0^2(\Omega)] \times [L^2(\Omega)]^{d^2} \times [L^2(\Omega)]_s^{d^2}$ such that, for all $(\phi_{\mathbf{u}}, \psi, \phi_{\bar{\mathbf{D}}}, \phi_{\boldsymbol{\tau}}) \in [H_0^1(\Omega)]^d \times [L_0^2(\Omega)] \times [L^2(\Omega)]^{d^2} \times [L^2(\Omega)]_s^{d^2}$

$$2(\beta + \theta) (\mathbf{D}, \nabla\phi_{\mathbf{u}})_{\Omega} - (p, \nabla \cdot \phi_{\mathbf{u}})_{\Omega} + (\boldsymbol{\tau}, \nabla\phi_{\mathbf{u}})_{\Omega} - 2\theta (\bar{\mathbf{D}}, \nabla\phi_{\mathbf{u}})_{\Omega} = 0, \quad (4.15)$$

$$(\nabla \cdot \mathbf{u}, \psi)_{\Omega} = 0, \quad (4.16)$$

$$(\mathbf{D} - \bar{\mathbf{D}}, \phi_{\bar{\mathbf{D}}})_{\Omega} = 0 \quad (4.17)$$

$$Wi \left(\frac{D\boldsymbol{\tau}}{Dt} - \nabla\mathbf{u} \cdot \boldsymbol{\tau} - \boldsymbol{\tau} \cdot \nabla\mathbf{u}^T, \phi_{\boldsymbol{\tau}} \right)_{\Omega} + (\boldsymbol{\tau}, \phi_{\boldsymbol{\tau}})_{\Omega} = 2(1 - \beta) (\mathbf{D}, \phi_{\boldsymbol{\tau}})_{\Omega}, \quad (4.18)$$

where θ is the stabilisation parameter.

Here, we assume $\frac{D\mathbf{u}}{Dt} = 0$ and that all boundary terms are zero. In analogy to the EVSS-G method, the DEVSS-G method (Liu et al. (1998)) may be defined, where a projection of the velocity gradient tensor is made instead of the rate of deformation tensor, that is,

$$\boldsymbol{\sigma}^{\delta} \approx -p\mathbf{I} + 2\beta\mathbf{D} + \theta(2\mathbf{D} - (\mathbf{G} + \mathbf{G}^T)). \quad (4.19)$$

In this formulation the velocity gradient projection tensor is used in the constitutive equation as well as in the momentum equation. Sun et al. (1999) introduced the DAVSS-G formulation in analogy to the AVSS formulation employing an adaptive stabilisation viscosity that differs from element to element depending on the flow properties in an element. Sun et al. (1999) combined the DAVSS-G with the discontinuous Galerkin method.

In this thesis, we employ the DEVSS-G method in combination with the discontinuous Galerkin method for the constitutive equation. This algorithm is known as DEVSS-G/DG and has been employed in the finite element context by Baaijens (1997), Sun et al. (1999), Caola et al. (2001) and Kim et al. (2005). To the best of our knowledge, the DEVSS-G/DG method has not been applied to spectral element methods. It has been implemented in the context of spectral elements for the first time in this thesis. We choose the solution space for the velocity gradient projection tensor as $[L^2(\Omega)]^{d^2}$, to be consistent with the spaces for pressure and polymeric stress, which are chosen to be $L_0^2(\Omega)$ and $[L^2(\Omega)]_s^{d^2}$, respectively.

We employ the following DEVSS-G formulation

Problem 4.2 (Weak Formulation DEVSS-G). *Find* $(\mathbf{u}, p, \mathbf{G}, \boldsymbol{\tau}) \in [H_D^1(\Omega)]^2 \times [L_0^2(\Omega)] \times [L^2(\Omega)]^{d^2} \times [L^2(\Omega)]_s^{d^2}$ such that

$$Re \left(\frac{D\mathbf{u}}{Dt}, \phi_{\mathbf{u}} \right)_{\Omega} + (\beta + \theta) (2\mathbf{D}, \nabla \phi_{\mathbf{u}})_{\Omega} - (p, \nabla \cdot \phi_{\mathbf{u}})_{\Omega} \quad (4.20)$$

$$+ (\boldsymbol{\tau}, \nabla \phi_{\mathbf{u}})_{\Omega} - \theta \left(\mathbf{G} + \mathbf{G}^T, \nabla \phi_{\mathbf{u}} \right)_{\Omega} - \langle \boldsymbol{\sigma} \cdot \mathbf{n}, \phi_{\mathbf{u}} \rangle_{\Gamma_N} = 0, \quad (4.21)$$

$$(\nabla \cdot \mathbf{u}, \psi)_{\Omega} = 0, \quad (4.21)$$

$$(\mathbf{G} - \nabla \mathbf{u}, \phi_{\mathbf{G}})_{\Omega} = 0, \quad (4.22)$$

$$Wi \left(\frac{D\boldsymbol{\tau}}{Dt} - \mathbf{G} \cdot \boldsymbol{\tau} - \boldsymbol{\tau} \cdot \mathbf{G}^T, \phi_{\boldsymbol{\tau}} \right)_{\Omega} + (\boldsymbol{\tau}, \phi_{\boldsymbol{\tau}})_{\Omega} + \frac{\alpha Wi}{(1 - \beta)} (\boldsymbol{\tau}^2, \phi_{\boldsymbol{\tau}})_{\Omega}, \quad (4.23)$$

$$= (1 - \beta) \left(\mathbf{G} + \mathbf{G}^T, \phi_{\boldsymbol{\tau}} \right)_{\Omega},$$

for all $(\phi_{\mathbf{u}}, \psi, \phi_{\mathbf{G}}, \phi_{\boldsymbol{\tau}}) \in [H_0^1(\Omega)]^d \times [L_0^2(\Omega)] \times [L^2(\Omega)]^{d^2} \times [L^2(\Omega)]_s^{d^2}$. Here, Γ_N is the Neumann boundary.

If not stated otherwise, we choose

$$\theta = (1 - \beta) \quad (4.24)$$

for the stabilisation parameter as discussed in Fortin (2000). Fortin (2000) also contains further details on possible choices for the stabilisation parameter and admissible choices for the discrete approximation unknowns.

4.2. Spatial Approximation of Velocity, Pressure and Polymeric Stress

Before we discuss the details of suitable approximation spaces for velocity, pressure and polymeric stress, we introduce some definitions for discrete polynomial spaces. To approximate the unknowns of velocity, pressure, velocity gradient projection tensor and the polymeric stress tensor and to discretise Equations (4.20)-(4.23) in space, we use the spectral/hp element method. In the spectral/hp element method we approximate the solution using the modal expansion functions defined in Equation (3.24), which is a hierarchical set of polynomials with highest polynomial order P . In detail, each element Ω_e is mapped onto the standard element Ω_{st} using an iso-parametric mapping $\boldsymbol{\chi} : \Omega_{st} \rightarrow \Omega_e$ as explained in Section 3.4. This means, on each element, the solution is approximated in the space of polynomials of degree P defined as

$$\mathcal{P}_P(\Omega_e) := \left\{ g : g = \hat{g} \circ \boldsymbol{\chi}^{-1}, \quad \hat{g} \in \mathcal{P}_P(\Omega_{st}) \right\}. \quad (4.25)$$

To obtain the approximate solution on the whole domain Ω , different coupling strategies between the elements can be applied. In the continuous Galerkin method, we construct a globally continuous expansion basis as explained in Section 3.7.1. With this in mind, we define the globally continuous space of polynomials $\mathcal{P}_P^c(\Omega)$ as

$$\mathcal{P}_P^c(\Omega) := \left\{ g \in C^0(\overline{\Omega}) : g|_{\Omega_e} \in \mathcal{P}_P(\Omega_e), \forall \Omega_e \right\}. \quad (4.26)$$

However, if we do not seek a globally continuous solution, we can describe the approximation using the space of piecewise continuous polynomials of degree P over Ω , that is,

$$\mathcal{P}_P(\Omega) := \left\{ g \in L^2(\Omega) : g|_{\Omega_e} \in \mathcal{P}_P(\Omega_e), \forall \Omega_e \right\}. \quad (4.27)$$

Using these polynomial spaces, we can define the discrete spaces for velocity, \mathcal{V}^δ , pressure, \mathcal{Q}^δ and polymeric stress Σ^δ . However, the discrete spaces have to be chosen with care in order to ensure stability and uniqueness of the discrete solution. For Oldroyd-B flow with $\frac{D\mathbf{u}}{Dt} = 0$ and zero contribution from the boundary terms, the discrete three field formulation reads

Problem 4.3 (MIX). Find $(\mathbf{u}^\delta, p^\delta, \boldsymbol{\tau}^\delta) \in \mathcal{V}^\delta \times \mathcal{Q}^\delta \times \Sigma^\delta$ such that

$$\begin{aligned} 2\beta \int_{\Omega_t} \mathbf{D} : \nabla \phi_{\mathbf{u}} d\Omega - \int_{\Omega_t} p (\nabla \cdot \phi_{\mathbf{u}}) d\Omega + \int_{\Omega_t} \boldsymbol{\tau} : \nabla \phi_{\mathbf{u}} d\Omega &= 0, \\ \int_{\Omega_t} (\nabla \cdot \mathbf{u}) \psi d\Omega &= 0, \\ Wi \int_{\Omega_t} \overline{\boldsymbol{\tau}} : \phi_{\boldsymbol{\tau}} d\Omega + \int_{\Omega_t} \boldsymbol{\tau} : \phi_{\boldsymbol{\tau}} d\Omega - 2(1 - \beta) \int_{\Omega_t} \mathbf{D} : \phi_{\boldsymbol{\tau}} d\Omega &= 0, \end{aligned} \quad (4.28)$$

for all $(\phi_{\mathbf{u}}, \psi, \phi_{\boldsymbol{\tau}}) \in \mathcal{V}^\delta \times \mathcal{Q}^\delta \times \Sigma^\delta$.

This formulation was introduced by Crochet et al. (1984). Fortin and Pierre (1987) have shown that in the limiting case of the absence of a purely viscous contribution, i.e. $\beta = 0$, the following conditions must hold

1. The discrete spaces for velocity and pressure have to satisfy the Ladyzhenskaya-Babuška-Brezzi (LBB) condition (Brezzi, 1974) in order to avoid spurious oscillations in the pressure approximation and to ensure stability and uniqueness of the discrete solution.
2. If the space for the polymeric stress is chosen to be discontinuous, as for example in the discontinuous Galerkin method, the discrete space for the rate of deformation tensor \mathbf{D} must be contained in the discrete space for the polymeric stress $\mathbf{D} \in \Sigma^\delta$.

3. If the space for the polymeric stress is chosen to be continuous, e.g. for the SUPG method, the number of degrees of freedom for each component of $\boldsymbol{\tau}^\delta$ must be greater than or equal to the number of all degrees of freedom of each component \mathbf{u}^δ .

Baranger and Sandri (1992) demonstrated that for $\beta > 0$ the third condition does not need to be imposed. A choice of appropriate discrete spaces fulfilling the LBB condition for higher order methods is given for the velocity space by

$$\mathcal{V}^\delta = [H_0^1(\Omega)]_\delta^2 := [H_0^1(\Omega)]^2 \cap [\mathcal{P}_P^c(\Omega)]^2 \quad (4.29)$$

in combination with an approximation of the pressure with a lower-degree polynomial of order $P - 2$

$$\mathcal{Q}^\delta = [L^2(\Omega)]_\delta := [L^2(\Omega)] \cap \mathcal{P}_{P-2}(\Omega) \quad (4.30)$$

as shown by Maday et al. (1992). Gerritsma and Phillips (1999, 2001) have shown that for the three field Stokes problem (4.28), in the limit of $\beta = 0$, well-posedness of the discrete problem is guaranteed if, in addition to satisfying the LBB condition on the velocity-pressure approximation, the degree of polynomial used for the polymeric stress components is at least as great as that used for the components of velocity. Therefore, we choose for the polymeric stress

$$\Sigma^\delta = [L^2(\Omega)]_{s,\delta}^{d^2} := [L^2(\Omega)]_s^{d^2} \cap [\mathcal{P}_P(\Omega)]^{d^2}. \quad (4.31)$$

For the DEVSS-G method, we need to choose an appropriate function space for the velocity gradient projection tensor \mathbf{G} as

$$\Sigma_G^\delta = [L^2(\Omega)]_\delta^{d^2} := [L^2(\Omega)]^{d^2} \cap [\mathcal{P}_P(\Omega)]^{d^2} \quad (4.32)$$

which fulfils Requirement 2, i.e. $\mathbf{D} = 1/2(\mathbf{G} + \mathbf{G}^T) \in \Sigma^\delta$. Thus, the approximation of

the dependent variables in any parent element $(\xi_1, \xi_2) \in [-1, 1]^2$ take the form

$$u^\delta(\xi_1, \xi_2) = \sum_{p=0}^P \sum_{q=0}^P \hat{u}_{pq} \phi_p(\xi_1) \phi_q(\xi_2), \quad (4.33)$$

$$v^\delta(\xi_1, \xi_2) = \sum_{p=0}^P \sum_{q=0}^P \hat{v}_{pq} \phi_p(\xi_1) \phi_q(\xi_2), \quad (4.34)$$

$$p^\delta(\xi_1, \xi_2) = \sum_{p=0}^{P-2} \sum_{q=0}^{P-2} \hat{p}_{pq} \phi_p(\xi_1) \phi_q(\xi_2), \quad (4.35)$$

$$\tau_{kl}^\delta(\xi_1, \xi_2) = \sum_{p=0}^P \sum_{q=0}^P \hat{\tau}_{pq}^{kl} \phi_p(\xi_1) \phi_q(\xi_2), \quad k = 1, 2, l = 1, 2 \quad (4.36)$$

$$G_{kl}^\delta(\xi_1, \xi_2) = \sum_{p=0}^P \sum_{q=0}^P \hat{G}_{pq}^{kl} \phi_p(\xi_1) \phi_q(\xi_2), \quad k = 1, 2, l = 1, 2 \quad (4.37)$$

where \hat{u}_{pq} , \hat{v}_{pq} , \hat{p}_{pq} , $\hat{\tau}_{pq}^{kl}$ and \hat{G}_{pq}^{kl} are the expansion coefficients. The discrete evaluation of the integrals in the weak form of the equations is explained in detail in Chapter 3.

4.3. Temporal schemes

We discretise the Equations (2.168) in time using the first-order explicit Euler and the second-order backward differentiation formula in combination with second-order extrapolation (BDF2/EX2) time integration schemes. These two schemes can be defined as follows. Consider a system of ordinary differential equations of the form

$$\frac{d\mathbf{u}}{dt} = \mathbf{F}(\mathbf{u}) \quad (4.38)$$

which is discretised in time using the linear multi-step method

$$\frac{\gamma_0 \mathbf{u}^{n+1} - \sum_{q=0}^{J-1} \alpha_q \mathbf{u}^{n-q}}{\Delta t} = \sum_{q=0}^{J-1} \beta_q \mathbf{F}(\mathbf{u})^{n-q}, \quad (4.39)$$

where $J = 1, 2$ is the time integration order with $\gamma_0 = 1$, $\alpha_0 = 1$, $\beta_0 = 1$ for the first-order explicit Euler and $\gamma_0 = 3/2$, $\alpha_0 = 2$, $\alpha_1 = -1/2$, $\beta_0 = 2$, $\beta_1 = -1$ for second-order BDF2/EX2.

4.4. DEVSS/DG Algorithm in a Fixed Domain

In our algorithm for fixed domains, we use the fact that $\nabla \cdot \nabla \mathbf{u}^T = 0$ due to incompressibility and we adjust the DEVSS-G stabilisation accordingly. That means we stabilise the

computations only with \mathbf{G} , instead of $\mathbf{G} + \mathbf{G}^T$ as proposed by Bogaerds et al. (2002), which yields

$$\begin{cases} \operatorname{Re} \frac{D\mathbf{u}}{Dt} = -\nabla p + (\beta + \theta)\Delta\mathbf{u} - \theta \nabla \cdot \mathbf{G} + \nabla \cdot \boldsymbol{\tau}, \\ \nabla \cdot \mathbf{u} = 0, \\ \mathbf{G} - \nabla\mathbf{u} = 0, \\ \boldsymbol{\tau} + \operatorname{Wi} \overset{\nabla}{\boldsymbol{\tau}} + \frac{\alpha \operatorname{Wi}}{(1-\beta)} \boldsymbol{\tau}^2 = (1-\beta) (\mathbf{G} + \mathbf{G}^T), \end{cases} \quad (4.40)$$

where \mathbf{G} is the velocity gradient projection tensor. The upper convected derivative in the constitutive equation is computed using the velocity gradient projection tensor, that is,

$$\overset{\nabla}{\boldsymbol{\tau}} = \frac{D\boldsymbol{\tau}}{Dt} - \mathbf{G} \cdot \boldsymbol{\tau} - \boldsymbol{\tau} \cdot \mathbf{G}^T. \quad (4.41)$$

This system of equations is completed by specifying initial and boundary conditions as explained in Section 2.6.1. We employ the temporal schemes introduced in Section 4.3 in the following way

Problem 4.4 (Semi-Discretised DEVSS-G/DG Formulation).

Find $(\mathbf{u}^{n+1}, p^{n+1}, \mathbf{G}^{n+1}, \boldsymbol{\tau}^{n+1}) \in [H_D^1(\Omega)]^2 \times [L_0^2(\Omega)] \times [L^2(\Omega)]^{d^2} \times [L^2(\Omega)]_s^{d^2}$ such that, for all $(\phi_{\mathbf{u}}, \psi, \phi_{\mathbf{G}}, \phi_{\boldsymbol{\tau}}) \in [H_0^1(\Omega)]^d \times [L_0^2(\Omega)] \times [L^2(\Omega)]^{d^2} \times [L^2(\Omega)]_s^{d^2}$

$$\begin{aligned} & \operatorname{Re} \left(\frac{\gamma_0 \mathbf{u}^{n+1} - \sum_{q=0}^{J-1} \alpha_q \mathbf{u}^{n-q}}{\Delta t}, \phi_{\mathbf{u}} \right)_{\Omega} + (\beta + \theta) (\nabla \mathbf{u}^{n+1}, \nabla \phi_{\mathbf{u}})_{\Omega} - (p^{n+1}, \nabla \cdot \phi_{\mathbf{u}})_{\Omega} \\ &= \sum_{q=0}^{J-1} \beta_q [-\operatorname{Re} (\mathbf{u} \cdot \nabla \mathbf{u}, \phi_{\mathbf{u}})_{\Omega} + (\theta \mathbf{G} - \boldsymbol{\tau}, \nabla \phi_{\mathbf{u}})_{\Omega} \\ & \quad + \langle (-p + \nabla \mathbf{u} + \boldsymbol{\tau} - \theta \mathbf{G}) \cdot \mathbf{n}, \phi_{\mathbf{u}} \rangle_{\Gamma_N}]^{n-q}, \end{aligned} \quad (4.42)$$

$$(\nabla \cdot \mathbf{u}^{n+1}, \psi)_{\Omega} = 0, \quad (4.43)$$

$$(\mathbf{G}^{n+1}, \phi_{\mathbf{G}})_{\Omega_e} = (\nabla \mathbf{u}^{n+1}, \phi_{\mathbf{G}})_{\Omega_e}, \quad \forall \Omega_e, \quad (4.44)$$

$$\begin{aligned} & \operatorname{Wi} \left(\frac{\gamma_0 \boldsymbol{\tau}^{n+1} - \sum_{q=0}^{J-1} \alpha_q \boldsymbol{\tau}^{n-q}}{\Delta t}, \phi_{\boldsymbol{\tau}} \right)_{\Omega_e} - \left[\operatorname{Wi} (\mathbf{G} \boldsymbol{\tau} + \boldsymbol{\tau} \mathbf{G}^T, \phi_{\boldsymbol{\tau}})_{\Omega_e} - (\boldsymbol{\tau}, \phi_{\boldsymbol{\tau}})_{\Omega_e} \right]^{n+1} \\ & + \left[\frac{\alpha \operatorname{Wi}}{(1-\beta)} \boldsymbol{\tau}^2 \right]^{n+1} - \left[((1-\beta)(\mathbf{G} + \mathbf{G}^T), \phi_{\boldsymbol{\tau}})_{\Omega_e} \right]^{n+1} = \tilde{\mathbf{g}}, \quad \forall \Omega_e \end{aligned} \quad (4.45)$$

with

$$\tilde{\mathbf{g}} = \sum_{q=0}^{J-1} \beta_q \left[\int_{\Omega_e} (\mathbf{u} \cdot \nabla) \phi_{\boldsymbol{\tau}} : \boldsymbol{\tau} \, d\Omega_e + \int_{\partial\Omega_e} \tilde{\mathbf{f}}^e(\boldsymbol{\tau}^{int}(x), \boldsymbol{\tau}^{ext}(x)) : \phi_{\boldsymbol{\tau}} \, d\Gamma \right]^{n-q}.$$

This system of equations is solved as outlined in Algorithm 4.4.1. The different steps outlined in the algorithm are explained in the following Sections.

Algorithm 4.4.1: DEVSS-G/DG SCHEME FOR A FIXED MESH. $(\mathbf{u}^n, p^n, \boldsymbol{\tau}^n)$

$t = t_0$

while $t \leq t_{fin}$

 Set boundary conditions for \mathbf{u} .

procedure COMPUTERHS($\mathbf{u}^n, \boldsymbol{\tau}^n, \mathbf{u}^{n-1}, \boldsymbol{\tau}^{n-1}$)

 Determine explicit terms on RHS of (4.42) and (4.45).

output ($RHS(\mathbf{u}), RHS(\boldsymbol{\tau})$)

procedure SOLVECOUPLEDSYSTEM($\mathbf{u}^n, p^n, \boldsymbol{\tau}^n, RHS(\mathbf{u})$)

 Solve Coupled System of Velocity and Pressure (4.42), (4.43).

output ($\mathbf{u}^{n+1}, p^{n+1}$)

do { **procedure** COMPUTEG(\mathbf{u}^{n+1})

 Perform L^2 projection (4.44).

output (\mathbf{G}^{n+1})

 Set boundary conditions for $\boldsymbol{\tau}$.

procedure SOLVECONSTITUTIVEEQUATION($\mathbf{G}^{n+1}, RHS(\boldsymbol{\tau})$)

 Solve (4.45).

output ($\boldsymbol{\tau}^{n+1}$)

$t \leftarrow t + \Delta t$

$n + 1 \leftarrow n$

4.4.1. Solving the Coupled System of Velocity and Pressure

As outlined in Algorithm 4.4.1, we first solve the coupled system for velocity and pressure with respect to the polymeric stress at the previous time-level. We base this step on a coupled Navier-Stokes solver for Newtonian flows introduced in Ainsworth and Sherwin (1999) and Sherwin and Ainsworth (2000). Here, we will outline the steps that we take

to solve the coupled system. Further details on the coupled solver can be found in Karniadakis and Sherwin (2005).

First, as we employ a continuous global basis for the velocity, we write the conservation laws in a global matrix form given by

$$\begin{aligned}\mathbf{H}_g \hat{\mathbf{u}}_g - \mathbf{D}_g^T \hat{\mathbf{p}}_g &= \mathbf{f}, \\ \mathbf{D}_g \hat{\mathbf{u}}_g &= \mathbf{0},\end{aligned}\quad (4.46)$$

where $\hat{\mathbf{u}}_g$ and $\hat{\mathbf{p}}_g$ are the vectors of unknown global coefficients, \mathbf{H}_g is the global Helmholtz matrix and $\mathbf{D}_g = (\mathbf{D}_{x_1}, \mathbf{D}_{x_2})$ is the global discrete gradient operator based on the derivative matrices defined in (3.66) and (3.66) in Section 3.6. The global matrices can be constructed from the block diagonal matrix of all elemental matrices $\underline{\mathbf{H}}^e$ by using the permutation matrix \mathcal{A} which constructs the local vector $\hat{\mathbf{u}}_l$ from the global vector $\hat{\mathbf{u}}_g$, and its transpose \mathcal{A}^T which represents the global assembly process

$$\mathbf{H}_g = \mathcal{A}^T \underline{\mathbf{H}}^e \mathcal{A}, \quad \underline{\mathbf{H}}^e = \begin{bmatrix} \mathbf{H}^1 & 0 & 0 & 0 \\ 0 & \mathbf{H}^2 & 0 & 0 \\ 0 & 0 & \ddots & 0 \\ 0 & 0 & 0 & \mathbf{H}^{N_{el}} \end{bmatrix}, \quad \hat{\mathbf{u}}_l = \mathcal{A} \hat{\mathbf{u}}_g. \quad (4.47)$$

This global assembly procedure is explained in detail in Section 3.7.1. The elemental Helmholtz matrix for the momentum equation consists of

$$\mathbf{H}^e[m][n] = (\beta + \theta) (\nabla \phi_u^n, \nabla \phi_u^m)_{\Omega_e}^\delta + \frac{\text{Re } \gamma_0}{\Delta t} (\phi_u^n, \phi_u^m)_{\Omega_e}^\delta. \quad (4.48)$$

where the indices $m = m(pq)$, $n = n(rs)$ are ordered using the lexicographical numbering convention defined in Equation (3.57). And the elemental discrete gradient operator is given by

$$\mathbf{D}^e[n, m] = (\nabla \phi_u^n, \psi^m)_{\Omega_e}^\delta. \quad (4.49)$$

As explained in Section 3.7.1, we choose the global numbering scheme in such a way that we obtain global matrices with a structure that is optimal for solving the equations using the multi-static condensation technique. In order to apply the multi-static condensation technique explained in Section 3.7.1 to solve the coupled system (4.46), we decompose our system into boundary and interior contributions

$$\begin{bmatrix} \mathbf{H}_{bb} & -\mathbf{D}_b^T & \mathbf{H}_{bi} \\ -\mathbf{D}_b & 0 & -\mathbf{D}_i \\ \mathbf{H}_{ib} & -\mathbf{D}_i^T & \mathbf{H}_{ii} \end{bmatrix} \begin{bmatrix} \hat{\mathbf{u}}_b \\ \hat{\mathbf{p}} \\ \hat{\mathbf{u}}_i \end{bmatrix} = \begin{bmatrix} \mathbf{f}_b \\ \mathbf{0} \\ \mathbf{f}_i \end{bmatrix} \quad (4.50)$$

where $\hat{\mathbf{u}}_b, \mathbf{f}_b$ denote the degrees of freedom of the elemental velocities on the boundary of the element and $\hat{\mathbf{u}}_i, \mathbf{f}_i$ denote the interior degrees of freedom of the element.

The matrix \mathbf{H}_{bb} denotes the global assembly of the elemental boundary-boundary mode interactions, \mathbf{H}_{bi} and \mathbf{H}_{ib} correspond to the global assembly of the elemental boundary-interior coupling and \mathbf{H}_{ii} denotes the block-diagonal matrix of elemental interior-interior mode interactions. Note, that these global matrices can be constructed from the elemental matrices by

$$\mathbf{H}_{ii}^{-1} = \left[\underline{\mathbf{H}}_{ii}^e \right]^{-1}, \quad (4.51)$$

$$\mathbf{H}_{bi} = \mathcal{A}_b^T \underline{\mathbf{H}}_{bi}^e, \quad (4.52)$$

$$\mathbf{H}_{ib} = \underline{\mathbf{H}}_{ib}^e \mathcal{A}_b, \quad (4.53)$$

$$\mathbf{H}_{bb} = \mathcal{A}_b^T \underline{\mathbf{H}}_{bb}^e \mathcal{A}_b, \quad (4.54)$$

$$\mathbf{D}_b = \mathcal{A}_b^T \underline{\mathbf{D}}_b^e, \quad (4.55)$$

where $\underline{\mathbf{H}}^e$ denotes the block-diagonal concatenation of the elemental matrices as in (3.74). Here, \mathcal{A}_b is the boundary version of \mathcal{A} . It scatters the global boundary degrees of freedom to the local boundary degrees of freedom. Similarly, \mathcal{A}_b^T assembles the global boundary degrees of freedom from the local boundary degrees of freedom. The elemental matrices for each element are given by

$$\mathbf{H}_{bb}^e[n, m] = \frac{\text{Re } \gamma_0}{\Delta t} \left(\phi_u^{b,n}, \phi_u^{b,m} \right)_{\Omega_e}^\delta + (\beta + \theta) \left(\nabla \phi_u^{b,n}, \nabla \phi_u^{b,m} \right)_{\Omega_e}^\delta, \quad (4.56)$$

$$\mathbf{H}_{ib}^e[n, m] = \frac{\text{Re } \gamma_0}{\Delta t} \left(\phi_u^{i,n}, \phi_u^{b,m} \right)_{\Omega_e}^\delta + (\beta + \theta) \left(\nabla \phi_u^{i,n}, \nabla \phi_u^{b,m} \right)_{\Omega_e}^\delta, \quad (4.57)$$

$$\mathbf{H}_{bi}^e[n, m] = \frac{\text{Re } \gamma_0}{\Delta t} \left(\phi_u^{b,n}, \phi_u^{i,m} \right)_{\Omega_e}^\delta + (\beta + \theta) \left(\nabla \phi_u^{b,n}, \nabla \phi_u^{i,m} \right)_{\Omega_e}^\delta, \quad (4.58)$$

$$\mathbf{H}_{ii}^e[n, m] = \frac{\text{Re } \gamma_0}{\Delta t} \left(\phi_u^{i,n}, \phi_u^{i,m} \right)_{\Omega_e}^\delta + (\beta + \theta) \left(\nabla \phi_u^{i,n}, \nabla \phi_u^{i,m} \right)_{\Omega_e}^\delta, \quad (4.59)$$

$$\mathbf{D}_b^e[n, m] = \left(\nabla \phi_u^{b,n}, \psi^m \right)_{\Omega_e}^\delta, \quad (4.60)$$

$$\mathbf{D}_i^e[n, m] = \left(\nabla \phi_u^{i,n}, \psi^m \right)_{\Omega_e}^\delta \quad (4.61)$$

and

$$\begin{aligned} \mathbf{f} = & \left(\frac{\text{Re}}{\Delta t} \sum_{q=0}^{J-1} \alpha_q \mathbf{u}^{n-q}, \phi_u \right)_{\Omega}^\delta \\ & + \sum_{q=0}^{J-1} \beta_q \left[-\text{Re} (\mathbf{u} \cdot \nabla \mathbf{u}, \phi_u)_{\Omega}^\delta + (\theta \mathbf{G} - \boldsymbol{\tau}, \nabla \phi_u)_{\Omega}^\delta \right]^{n-q}. \end{aligned} \quad (4.62)$$

To decouple the interior degrees of freedom $\hat{\mathbf{u}}_i$ from the boundary degrees of freedom $\hat{\mathbf{u}}_b$ and pressure $\hat{\mathbf{p}}$, we premultiply the equation system (4.50) with the matrix

$$\begin{bmatrix} I & 0 & -\mathbf{H}_{bi}\mathbf{H}_{ii}^{-1} \\ 0 & I & \mathbf{D}_i\mathbf{H}_{ii}^{-1} \\ 0 & 0 & I \end{bmatrix} \quad (4.63)$$

which leads to the system

$$\begin{bmatrix} \mathbf{H}_{bb} - \mathbf{H}_{bi}\mathbf{H}_{ii}^{-1}\mathbf{H}_{ib} & -\mathbf{D}_b^T + \mathbf{H}_{bi}\mathbf{H}_{ii}^{-1}\mathbf{D}_i^T & 0 \\ -\mathbf{D}_b + \mathbf{D}_i\mathbf{H}_{ii}^{-1}\mathbf{H}_{ib} & -\mathbf{D}_i\mathbf{H}_{ii}^{-1}\mathbf{D}_i^T & 0 \\ \mathbf{H}_{ib} & -\mathbf{D}_i^T & \mathbf{H}_{ii} \end{bmatrix} \begin{bmatrix} \hat{\mathbf{u}}_b \\ \hat{\mathbf{p}} \\ \hat{\mathbf{u}}_i \end{bmatrix} = \begin{bmatrix} \mathbf{f}_b - \mathbf{H}_{bi}\mathbf{H}_{ii}^{-1}\mathbf{f}_i \\ \mathbf{D}_i\mathbf{H}_{ii}^{-1}\mathbf{f}_i \\ \mathbf{f}_i \end{bmatrix}. \quad (4.64)$$

Note that the Schur complement is determined from the matrix concatenation $\underline{\mathbf{H}}^e$ using the global boundary permutation matrix \mathcal{A}_b , that is,

$$\mathbf{H}_{bb} - \mathbf{H}_{bi}\mathbf{H}_{ii}^{-1}\mathbf{H}_{ib} = \mathcal{A}_b^T \left[\underline{\mathbf{H}}_{bb}^e - \underline{\mathbf{H}}_{bi}^e \left[\underline{\mathbf{H}}_{ii}^e \right]^{-1} \underline{\mathbf{H}}_{ib}^e \right] \mathcal{A}_b. \quad (4.65)$$

Next, we perform another step of substructuring by lumping a pressure degree of freedom containing a mean component \hat{p}_0 with the velocity boundary degrees of freedom $\hat{\mathbf{u}}_b$ into $\mathbf{b} = [\hat{\mathbf{u}}_b, \hat{p}_0]$. If \mathbf{p}_r denotes the remainder of the pressure degrees of freedom, we can write the system in the form

$$\begin{bmatrix} \hat{A} & \hat{B} \\ \hat{C} & \hat{D} \end{bmatrix} \begin{bmatrix} \mathbf{b} \\ \mathbf{p}_r \end{bmatrix} = \begin{bmatrix} \hat{\mathbf{f}}_b \\ \hat{\mathbf{f}}_p \end{bmatrix}. \quad (4.66)$$

Now, we decouple \mathbf{b} from \mathbf{p}_r by performing a second level of static condensation

$$\begin{bmatrix} \hat{A} - \hat{B}\hat{D}^{-1}\hat{C} & 0 \\ \hat{C} & \hat{D} \end{bmatrix} \begin{bmatrix} \mathbf{b} \\ \mathbf{p}_r \end{bmatrix} = \begin{bmatrix} \hat{\mathbf{f}}_b - \hat{B}\hat{D}^{-1}\hat{\mathbf{f}}_p \\ \hat{\mathbf{f}}_p \end{bmatrix}. \quad (4.67)$$

For the boundary unknowns, we obtain the equation

$$(\hat{A} - \hat{B}\hat{D}^{-1}\hat{C}) \mathbf{b} = \hat{\mathbf{f}}_b - \hat{B}\hat{D}^{-1}\hat{\mathbf{f}}_p. \quad (4.68)$$

which can be solved either iteratively or directly. Here, we solve this equation using multi-level static condensation. Once this system has been solved for $\mathbf{b} = [\hat{\mathbf{u}}_b, \hat{p}_0]$, we can then recover the rest of the pressure modes

$$\mathbf{p}_r = \hat{D}^{-1}(-\hat{C}\mathbf{b} + \hat{\mathbf{f}}_p). \quad (4.69)$$

And finally, we can use this result to obtain the interior velocity degrees of freedom using

$$\hat{\mathbf{u}}_i = \mathbf{H}_{ii}^{-1}(-\mathbf{H}_{ib}\hat{\mathbf{u}}_b + \mathbf{D}_i^T \hat{\mathbf{p}}). \quad (4.70)$$

4.4.2. Solving the Constitutive Equation

Having determined the velocity, \mathbf{u}^{n+1} , and pressure, p^{n+1} , from the coupled conservation equations using the algorithm described in the previous Section, we perform an L^2 -projection, to determine the unknown coefficients of the velocity gradient projection tensor \mathbf{G} component-by-component using

$$\begin{aligned} \hat{\mathbf{G}}_{11}^{n+1,e} &= [\mathbf{M}_{G11}^e]^{-1} \mathbf{M}_{G11u}^e \hat{\mathbf{u}}^e, & \hat{\mathbf{G}}_{12}^{n+1,e} &= [\mathbf{M}_{G12}^e]^{-1} \mathbf{M}_{G12u}^e \hat{\mathbf{u}}^e \\ \hat{\mathbf{G}}_{21}^{n+1,e} &= [\mathbf{M}_{G21}^e]^{-1} \mathbf{M}_{G21v}^e \hat{\mathbf{v}}^e, & \hat{\mathbf{G}}_{22}^{n+1,e} &= [\mathbf{M}_{G22}^e]^{-1} \mathbf{M}_{G22v}^e \hat{\mathbf{v}}^e, \quad \forall \Omega_e, \end{aligned} \quad (4.71)$$

where

$$\begin{aligned} \mathbf{M}_{G_{ij}}^e[m, n] &= \left(\phi_{G_{ij}}^n, \phi_{G_{ij}}^m \right)_{\Omega_e}^\delta, \quad i, j = 1, 2, \\ \mathbf{M}_{G11u}^e[m, n] &= - \left(\frac{\partial \phi_u^n}{\partial x}, \phi_{G11}^m \right)_{\Omega_e}^\delta, & \mathbf{M}_{G12u}^e[m, n] &= - \left(\frac{\partial \phi_u^n}{\partial y}, \phi_{G12}^m \right)_{\Omega_e}^\delta, \\ \mathbf{M}_{G21v}^e[m, n] &= - \left(\frac{\partial \phi_v^n}{\partial x}, \phi_{G21}^m \right)_{\Omega_e}^\delta, & \mathbf{M}_{G22v}^e[m, n] &= - \left(\frac{\partial \phi_v^n}{\partial y}, \phi_{G22}^m \right)_{\Omega_e}^\delta. \end{aligned} \quad (4.72)$$

The physical values of \mathbf{G} at the quadrature points are then obtained using the backward transformation defined in Equation (3.70)

$$\mathbf{G}_{ij}^{n+1,e} = \mathbf{B}^e \hat{\mathbf{G}}_{ij}^e, \quad i = 1, 2, j = 1, 2, \quad \forall \Omega_e, \quad (4.73)$$

We can now use \mathbf{G}^{n+1} to solve the constitutive equation.

However, we first evaluate the explicit terms of the RHS of Equation (4.45)

$$\tilde{\mathbf{g}}^e = \sum_{q=0}^{J-1} \beta_q \left[\int_{\Omega_e} (\mathbf{u} \cdot \nabla) \phi_{\boldsymbol{\tau}} : \boldsymbol{\tau} \, d\Omega_e + \int_{\partial\Omega_e} \tilde{\mathbf{f}}^e(\boldsymbol{\tau}^{ext}(x), \boldsymbol{\tau}^{ext}(x)) : \phi_{\boldsymbol{\tau}} \, d\Gamma \right]^{n-q}, \quad \forall \Omega_e \quad (4.74)$$

which in matrix notation is given by (see Section 3.7.2)

$$\tilde{\mathbf{g}}^e = \sum_{q=0}^{J-1} \beta_q \left[(\mathbf{D}_x^e \mathbf{B}^e)^T \mathbf{W}^e \Xi^e(f(\boldsymbol{\tau}^{n-q})) + (\mathbf{D}_y^e \mathbf{B}^e)^T \mathbf{W}^e \Xi^e(g(\boldsymbol{\tau}^{n-q})) - \mathbf{b}^e(\boldsymbol{\tau}^{n-q}) \right], \quad (4.75)$$

where \mathbf{b}^e is the vector corresponding to the surface integral

$$\mathbf{b}^e(\boldsymbol{\tau}^{n-q})[k] = \int_{\partial\Omega_e} \tilde{\mathbf{f}}^e(\boldsymbol{\tau}^{ext,(n-q)}(x), \boldsymbol{\tau}^{int,(n-q)}(x)) : \phi_{\boldsymbol{\tau}}^k d\Gamma, \quad (4.76)$$

$\Xi^e(f(\boldsymbol{\tau}^{(n-q)}))$, $\Xi^e(g(\boldsymbol{\tau}^{(n-q)}))$ are the diagonal elemental matrices containing the flux values $\mathbf{F}(\boldsymbol{\tau}^{(n-q)}) = [f(\boldsymbol{\tau}^{(n-q)}), g(\boldsymbol{\tau}^{(n-q)})]^T$ at the quadrature points given by

$$\Xi^e(f(\boldsymbol{\tau}^{(n-q)}))[m(ij)][k(rs)] = u^{(n-q)}(\xi_{1_i}, \xi_{2_j}) \cdot \boldsymbol{\tau}^{(n-q)}(\xi_{1_i}, \xi_{2_j}) \delta_{mk}, \quad (4.77)$$

$$\Xi^e(g(\boldsymbol{\tau}^{(n-q)}))[m(ij)][k(rs)] = v^{(n-q)}(\xi_{1_i}, \xi_{2_j}) \cdot \boldsymbol{\tau}^{(n-q)}(\xi_{1_i}, \xi_{2_j}) \delta_{mk}, \quad (4.78)$$

\mathbf{D}_x^e , \mathbf{D}_y^e are the discrete differentiation matrices defined in (3.66) and (3.67), u, v are the components of the velocity vector $\mathbf{u} = (u, v)$, \mathbf{M}^e is the elemental mass matrix defined in (3.74), \mathbf{B}^e is the basis matrix defined in (3.60) and \mathbf{W}^e is the elemental weight matrix defined in (3.63). Using these elemental evaluations of the RHS in the weak formulation, we compute the physical values at the quadrature points for an intermediate polymeric stress field $\tilde{\boldsymbol{\tau}}^e$

$$\tilde{\boldsymbol{\tau}}^e = \mathbf{B}^e[\mathbf{M}^e]^{-1} \left[\frac{\Delta t}{\gamma_0 \text{Wi}} \tilde{\mathbf{g}}^e + \sum_{q=0}^{J-1} \frac{\alpha_q}{\gamma_0} [\mathbf{B}^e]^T \mathbf{W}^e \boldsymbol{\tau}^{e,(n-q)} \right], \quad \forall \Omega_e. \quad (4.79)$$

This explicit treatment of the convection term, and having \mathbf{G} given, leaves us with a linear system of equations for the polymeric stress when $\alpha = 0$ (Oldroyd-B model). We solve this linear system in the strong form for each quadrature point as follows. We cast the remaining terms in the constitutive equation given by

$$\begin{aligned} & \frac{\text{Wi} \gamma_0}{\Delta t} \boldsymbol{\tau}^{n+1} - \text{Wi} [\mathbf{G}\boldsymbol{\tau} - \boldsymbol{\tau}\mathbf{G}^T]^{n+1} + \boldsymbol{\tau}^{n+1} \\ & = [(1-\beta)(\mathbf{G} + \mathbf{G}^T)]^{n+1} + \frac{\text{Wi} \gamma_0}{\Delta t} \tilde{\boldsymbol{\tau}} - \left[\frac{\alpha \text{Wi}}{(1-\beta)} \boldsymbol{\tau}^2 \right]^{(it)} \end{aligned} \quad (4.80)$$

into the form

$$\begin{bmatrix} \mathbf{A}_{xx,xx}^e & \mathbf{A}_{xx,xy}^e & 0 \\ \mathbf{A}_{xy,xx}^e & \mathbf{A}_{xy,xy}^e & \mathbf{A}_{xy,yy}^e \\ 0 & \mathbf{A}_{yy,xy}^e & \mathbf{A}_{yy,yy}^e \end{bmatrix} \begin{bmatrix} \boldsymbol{\tau}_{xx}^e \\ \boldsymbol{\tau}_{xy}^e \\ \boldsymbol{\tau}_{yy}^e \end{bmatrix} = \begin{bmatrix} \mathbf{f}_{xx}^e + \mathbf{g}_{xx}^{e,(it)} \\ \mathbf{f}_{xy}^e + \mathbf{g}_{xy}^{e,(it)} \\ \mathbf{f}_{yy}^e + \mathbf{g}_{yy}^{e,(it)} \end{bmatrix} \quad (4.81)$$

where

$$\begin{aligned}
\mathbf{A}_{xx,xx}^e[m] &= \left[\left(1 + \frac{\text{Wi} \gamma_0}{\Delta t} \right) - 2\text{Wi} G_{11}^e(\boldsymbol{\xi}_m) \right], & \mathbf{A}_{xx,xy}^e[m] &= -2\text{Wi} G_{12}^e(\boldsymbol{\xi}_m) \\
\mathbf{A}_{xy,xx}^e[m] &= -\text{Wi} G_{21}^e(\boldsymbol{\xi}_m), & \mathbf{A}_{xy,yy}^e[m] &= -\text{Wi} G_{12}^e(\boldsymbol{\xi}_m) \\
\mathbf{A}_{xy,xy}^e[m] &= \left[\left(1 + \frac{\text{Wi} \gamma_0}{\Delta t} \right) - \text{Wi} (G_{11}^e(\boldsymbol{\xi}_m) + G_{22}^e(\boldsymbol{\xi}_m)) \right], \\
\mathbf{A}_{yy,xy}^e[m] &= -2\text{Wi} G_{21}^e(\boldsymbol{\xi}_m), & \mathbf{A}_{yy,yy}^e[m] &= \left[\left(1 + \frac{\text{Wi} \gamma_0}{\Delta t} \right) - 2\text{Wi} G_{22}^e(\boldsymbol{\xi}_m) \right] \quad (4.82)
\end{aligned}$$

and

$$\begin{aligned}
\mathbf{f}_{xx}^e[m] &= 2(1 - \beta)G_{11}^e(\boldsymbol{\xi}_m) + \frac{\text{Wi} \gamma_0}{\Delta t} \tilde{\tau}_{xx}, \\
\mathbf{f}_{xy}^e[m] &= (1 - \beta)(G_{12}^e(\boldsymbol{\xi}_m) + G_{21}^e(\boldsymbol{\xi}_m)) + \frac{\text{Wi} \gamma_0}{\Delta t} \tilde{\tau}_{xy}, \\
\mathbf{f}_{yy}^e[m] &= 2(1 - \beta)G_{22}^e(\boldsymbol{\xi}_m) + \frac{\text{Wi} \gamma_0}{\Delta t} \tilde{\tau}_{yy} \\
\mathbf{g}_{xx}^{e,(it)}[m] &= -\frac{\alpha \text{Wi}}{(1 - \beta)} \left[\tau_{xx}(\boldsymbol{\xi}_m)^2 + \tau_{xy}(\boldsymbol{\xi}_m)^2 \right]^{(it)} \\
\mathbf{g}_{xy}^{e,(it)}[m] &= -\frac{\alpha \text{Wi}}{(1 - \beta)} \left[\tau_{xy}(\boldsymbol{\xi}_m)(\tau_{xx}(\boldsymbol{\xi}_m) + \tau_{yy}(\boldsymbol{\xi}_m)) \right]^{(it)} \\
\mathbf{g}_{yy}^{e,(it)}[m] &= -\frac{\alpha \text{Wi}}{(1 - \beta)} \left[\tau_{yy}(\boldsymbol{\xi}_m)^2 + \tau_{xy}(\boldsymbol{\xi}_m)^2 \right]^{(it)} \quad (4.84)
\end{aligned}$$

where the indices $m = m(ij)$ are ordered according to a lexicographical ordering along the ξ_1 direction given in (3.54) and $\boldsymbol{\xi}_{m(ij)} = (\xi_{1i}, \xi_{2j})$.

Next, we solve the system (4.81) point wise using the analytic expression for \mathbf{A}^{-1} .

When $\alpha = 0$, this gives us the solution $\boldsymbol{\tau}^{n+1}$ at the quadrature points. However, in the case when $\alpha \neq 0$, we perform a fixed point iteration by solving the same system

$$\boldsymbol{\tau}^{(it+1)} = \mathbf{A}^{-1} \left(\mathbf{f} + \mathbf{g}^{(it)} \right) \quad (4.85)$$

and updating the term $\mathbf{g}^{(it)}$ with $\boldsymbol{\tau}^{(it)}$ on the RHS in each iteration step until the residual

$$R = \max_{kl=xx,xy,yy} \left[\max_{1 \leq i,j \leq Q} \left| \tau_{kl}^{(it+1)}(\xi_{1i}, \xi_{2j}) - \tau_{kl}^{(it)}(\xi_{1i}, \xi_{2j}) \right| \right] < 10^{-10}. \quad (4.86)$$

For the first iteration, we set $[\boldsymbol{\tau}^2]^{(0)} = [\boldsymbol{\tau}^2]^n$.

Chapter 5

Numerical Results for Fixed Meshes

In this Chapter, we demonstrate the performance and accuracy of our algorithm for the unsteady Poiseuille flow of an Oldroyd-B fluid, for which an analytical solution exists, and the flow around a cylinder for the Oldroyd-B model for $Re = \{0, 0.01, 0.1, 1\}$ and for the Giesekus model for $\alpha = \{0.001, 0.01, 0.1\}$. Throughout this Chapter, we choose $\gamma = 1$ in the numerical flux term (4.8).

5.1. Unsteady Poiseuille Flow of an Oldroyd-B Fluid

In this Section, we investigate the Poiseuille flow of an Oldroyd-B fluid in a plane channel. For this flow configuration an analytical solution exists for both steady and unsteady Poiseuille flow. It is therefore an ideal first benchmark to evaluate the quality of numerical algorithms for Oldroyd-B fluids. In this Section, we first present the analytical solution. Then, we investigate the numerical solution at fixed points in the channel domain and compare the results to the analytical solution.

5.1.1. Analytical Solution

Poiseuille flow is the flow of a fluid through a channel of length L and height H driven by a constant pressure gradient. Let this constant pressure gradient be denoted by

$$\frac{\partial p}{\partial x} = \kappa. \quad (5.1)$$

Next, we assume a velocity distribution of the form

$$(u(y, t), 0, 0) \text{ with } 0 < y < H \text{ and } t > 0 \quad (5.2)$$

with boundary conditions

$$u(0, t) = 0 \text{ and } u(H, t) = 0 \quad (5.3)$$

and initial condition

$$u(y, 0) = 0 \text{ with } 0 < y < H. \quad (5.4)$$

For this velocity field the equation of continuity is automatically satisfied and the flow field is described by the momentum equation

$$\rho \frac{\partial u}{\partial t} = -\kappa + \frac{\partial T_{xy}}{\partial y}, \quad (5.5)$$

where T_{xy} is the shear stress component of the extra stress tensor \mathbf{T} . Waters and King (1970) derived the solution for this problem and employed the following non-dimensionalisation

$$y^* = \frac{y}{H}, \quad u^* = \frac{u}{U}, \quad U = -\frac{\kappa H^2}{8\eta_0}, \quad t^* = \frac{\eta_0 t}{\rho H^2}. \quad (5.6)$$

Using the dimensionless numbers

$$\text{El} = \frac{\lambda \eta_0}{\rho H^2} = \frac{\text{Wi}}{\text{Re}}, \quad \beta = \frac{\eta_S}{\eta_0}, \quad \text{Wi} = \lambda \frac{U}{H}, \quad \text{Re} = \frac{UH\rho}{\eta_0}. \quad (5.7)$$

The solution of Waters and King (1970) is given by

$$u^*(y^*, t^*) = 4y^*(1 - y^*) - 32 \sum_{n=1}^{\infty} \frac{\sin(Ny^*)}{N^3} G_N(\text{El}, t^*), \quad (5.8)$$

where

$$G_N(\text{El}, t^*) = \exp\left(-\frac{\alpha_N t^*}{2\text{El}}\right) \left[\cosh\left(\frac{\beta_N t^*}{2\text{El}}\right) + \frac{\gamma_N}{\beta_N} \sinh\left(\frac{\beta_N t^*}{2\text{El}}\right) \right] \quad (5.9)$$

and

$$\begin{aligned} N &= (2n - 1)\pi, & \alpha_N &= 1 + \text{El}N^2, \\ \beta_N^2 &= \alpha_N^2 - 4N^2\text{El}, & \beta_N &= \sqrt{\beta_N^2}, \\ \gamma_N &= 1 + N^2\text{El}(\beta - 2). \end{aligned} \quad (5.10)$$

If $\beta_N^2 < 0$, then $G_N(\text{El}, t^*)$ changes to

$$G_N(\text{El}, t^*) = \exp\left(-\frac{\alpha_N t^*}{2\text{El}}\right) \left[\cos\left(\frac{\beta_N t^*}{2\text{El}}\right) + \frac{\gamma_N}{\beta_N} \sin\left(\frac{\beta_N t^*}{2\text{El}}\right) \right] \quad (5.11)$$

with

$$\beta_N = \sqrt{-\beta_N^2}. \quad (5.12)$$

The corresponding Newtonian solution is given by

$$u^*(y^*, t^*) = 4y^*(1 - y^*) - 32 \sum_{n=1}^{\infty} \frac{\sin(Ny^*)}{N^3} \exp(-N^2 t^*). \quad (5.13)$$

Note that the non-dimensional time scale ($t_{our}^* = (U/H)t$) in our numerical scheme has to be fitted to the time scale of the analytic solution ($t_{ana}^* = (\eta_0 t)/(\rho H^2)$), which yields

$$t_{ana}^* = \frac{\eta_0 t}{\rho H^2} = \text{El} \frac{t}{\lambda} = \text{El} \frac{tU}{\text{Wi} H} = \frac{t_{our}^*}{\text{Re}}. \quad (5.14)$$

For $t \rightarrow \infty$, the same steady state solution for the velocity field for the Newtonian and the Oldroyd-B fluid is recovered, which is given by

$$A(y) = u^*(y^*) = 4y^*(1 - y^*). \quad (5.15)$$

In the following, the star notation will be dropped for the sake of simplicity. The stress components of the Oldroyd-B equation have the steady state solution

$$\begin{aligned} \tau_{xx} &= 2 \text{Wi} \frac{\partial u}{\partial y} \tau_{xy} = 2 \text{Wi} (1 - \beta) \left(\frac{\partial u}{\partial y} \right)^2 = 2 \text{Wi} (1 - \beta) A'(y)^2, \\ \tau_{xy} &= (1 - \beta) \frac{\partial u}{\partial y} = (1 - \beta) A'(y), \\ \tau_{yy} &= 0, \end{aligned} \quad (5.16)$$

where

$$A'(y) = \frac{dA(y)}{dy}. \quad (5.17)$$

Carew et al. (1994) derived the transient analytical expressions for the stress components using the solution of Waters and King (1970)

$$\begin{aligned} \tau_{yy} &= 0, \\ \tau_{xy} &= \frac{(1 - \beta)}{\text{El}} \left[\text{El} A'(y) - 32 \sum_{n=1}^{\infty} \frac{\cos(Ny)}{N^2} H_N(\text{El}, t) \right] + C_{xy}(\text{El}, y) \exp\left(-\frac{t}{\text{El}}\right), \end{aligned} \quad (5.18)$$

$$\begin{aligned}
\tau_{xx} = & 2\text{Re } C_{xy}(\text{El}, y) \left[A'(y) \exp\left(-\frac{t}{\text{El}}\right) t - 32 \sum_{n=1}^{\infty} \frac{\cos(Ny)}{N^2} I_N(\text{El}, t) \right] \\
& + 2\text{Re}(1 - \beta) A'(y) \left[A'(y) \text{El} - 32 \sum_{n=1}^{\infty} \frac{\cos(Ny)}{N^2} H_N(\text{El}, t) \right] \\
& - \frac{64 \text{Re } A'(y)(1 - \beta)}{\text{El}} \sum_{n=1}^{\infty} \frac{\cos(Ny)}{N^2} J_N(\text{El}, t) \\
& + \frac{2 \cdot 32^2 \text{Re}(1 - \beta)}{\text{El}} \sum_{n,m=1}^{\infty} \frac{\cos(Ny)}{N^2} \frac{\cos(My)}{M^2} K_{NM}(\text{El}, t) \\
& + C_{xx}(\text{El}, y) \exp\left(-\frac{t}{\text{El}}\right),
\end{aligned} \tag{5.19}$$

where $M = (2m - 1)\pi$, and C_{xy} and C_{xx} are time-independent functions defined by the requirement that τ_{xy} and τ_{xx} are zero at time $t = 0$, respectively. Here, t is the non-dimensional time scale defined in Equation (5.14). The coefficients $H_N(\text{El}, t)$, $I_N(\text{El}, t)$, $J_N(\text{El}, t)$ and $K_{NM}(\text{El}, t)$ are given in Carew et al. (1994).

5.1.2. Transient Numerical Solution

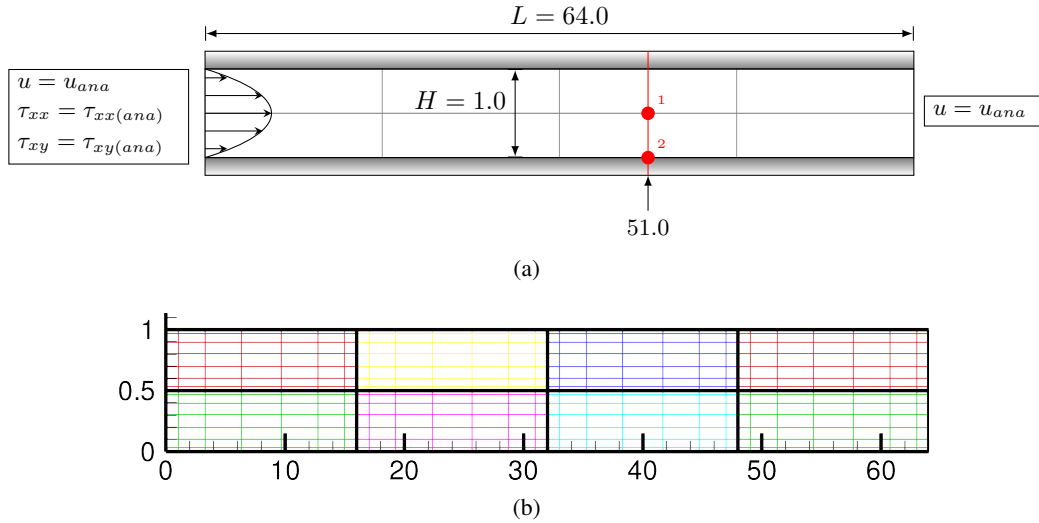


Figure 5.1.: Schematics (a) and mesh configuration (b) for Poiseuille channel flow.

Consider the flow through a channel of length $L = 64$ and height $H = 1.0$ as illustrated in Figure 5.1. At $t = 0$, we start our computation with a fluid at rest ($\mathbf{u} = \mathbf{0}$, $\boldsymbol{\tau} = \mathbf{0}$). For $t > 0$, we set the velocity at inflow and outflow to the time-dependent analytical solution of Waters and King (1970) given by the time-dependent Poiseuille flow (5.8). For the polymeric stress components, we impose Dirichlet inflow values given by (5.19).

We choose a mesh consisting of $N_{el} = 8$ elements (see Figure 5.1(b)) and perform the computation for a polynomial order of $P = 6$. We observe the time-dependent Poiseuille flow at two quadrature points in the channel domain: one point at the channel wall ($P_2 = (51.2664, 0)$), where we observe the numerical solution of the stress components τ_{xx} and τ_{xy} ; and one point in the middle of the channel ($P_1 = (51.2664, 0.5)$), where we observe the velocity component u . At these two points, we investigate the quality of the solution in the time interval $t \in [0, 100]$. We set the Reynolds number to 1.0 and $\beta = 0.1$ and solve the problem with the second order time integration scheme (BDF2/EX2) with a timestep of $\Delta t = 10^{-2}$ as detailed in Chapter 4. Figure 5.2 displays the comparison of the analytical and the numerical solution at point P_1 (a), (b) and point P_2 (c) for a range of stabilisation parameters θ of the DEVSS-G stabilisation scheme. Undershoots and overshoots of the velocity and stress components can be observed in the solution before the steady state solution is reached. In Figure 5.2, we discover that an increase in the stabilisation parameter amplifies the overshoots and undershoots for the stress components and dampens the oscillations in the velocity. However, the steady state solution is not polluted by the stabilisation parameter and coincides with the analytical solution up to machine precision for all tested θ . The amplification in the stress oscillations and the damping of the velocity oscillations is due to the amount of artificial viscosity, controlled by θ , that is added and subtracted in the momentum equation in order to stabilise the computations. The artificial increase in the viscosity yields lower velocity and higher stress values.

We evaluate the deviation of the numerical solution from the analytical solution at each overshoot and undershoot in terms of maximum relative error defined as

$$e_{\infty}^t(u) := \max_{t \in I} \left(\frac{|u_{ana}(t) - u_{num}(t)|}{|u_{ana}(t)|} \right), \quad (5.20)$$

where $u_{ana}(t)$ is the analytical solution at time t , $u_{num}(t)$ is the numerical solution at time t and $\max(\cdot)$ is the maximum value over all $t \in I$, where I is the time interval of an overshoot or undershoot. Table 5.1 lists these relative errors in percent for a range of stabilisation parameters. The maximum relative error is the greatest for the first overshoot and then dampens down quickly with the following overshoots and undershoots. The relative error increases significantly with θ for the first overshoot. However, the maximum error decreases with each overshoot and undershoot and the difference between stabilised and non-stabilised computations decreases until the difference vanishes for the steady state solution, which coincides with the analytical solution with machine precision for all θ . However, even though the errors increase slightly with θ , θ has a significant stabilising effect and computations can be performed up to much higher Weissenberg numbers than without the stabilisation. Table 5.2 lists the critical Weissenberg number beyond which

Table 5.1.: Dependence of maximum relative error at each overshoot and undershoot in percent on the stabilisation parameter θ .

	$e_{\infty}^t(\tau_{xx})$ in %			$e_{\infty}^t(\tau_{xy})$ in %		
	$\theta = 0$	$\theta = 0.5$	$\theta = 0.9$	$\theta = 0$	$\theta = 0.5$	$\theta = 0.9$
overshoot ₁	0.0863	5.2077	6.2491	0.1335	3.6341	4.2056
undershoot ₁	0.0765	0.8733	0.9647	0.1399	1.6265	1.9093
overshoot ₂	0.0390	0.8171	0.9411	0.0151	0.6002	0.6831
undershoot ₂	0.0284	0.0319	0.0474	0.0164	0.1579	0.1918
overshoot ₃	0.0108	0.1339	0.1456	0.0019	0.0849	0.0938

	$e_{\infty}^t(u)$ in %		
	$\theta = 0$	$\theta = 0.5$	$\theta = 0.9$
overshoot ₁	0.0401	3.4277	3.6516
undershoot ₁	0.1247	6.5624	7.2907
overshoot ₂	0.0057	0.6273	0.7169
undershoot ₂	0.0003	0.3265	0.3617
overshoot ₃	0.0001	0.0913	0.1046

Table 5.2.: Dependence of critical Weissenberg number yielding numerical breakdown on stabilisation parameter θ within the time interval $t \in [0, 100]$.

θ	Wi_c
0	3.3
0.1	4.6
0.5	9.2
0.9	9.8

computations fail in the time interval $t \in [0, 100]$. Without the DEVSS-G stabilisation in the momentum equation computations fail beyond $Wi_c = 3.3$. However, for a stabilisation parameter of $\theta = (1 - \beta) = 0.9$ computations can be performed up until $Wi_c = 9.8$, which is a significant improvement. Figure 5.3 displays the numerical and analytical solution for a large range of Weissenberg numbers. With a stabilisation parameter of $\theta = 0.9$, computations follow the analytical solution up to $Wi = 7$. Beyond $Wi = 7$, oscillations in the stress components occur that grow overtime and become more violent with increasing Weissenberg number until the computation fail for $Wi = 9.8$ in the time interval $t \in [0, 100]$.

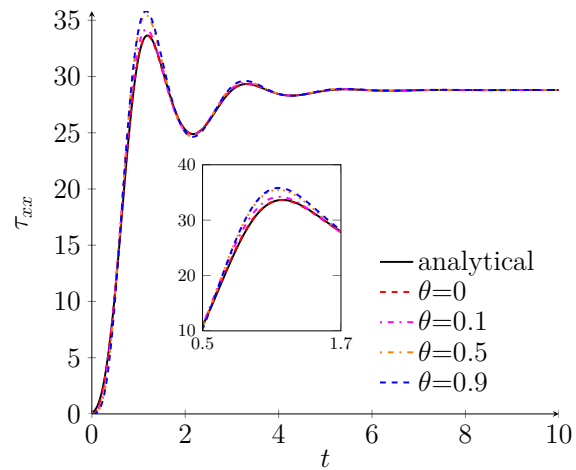
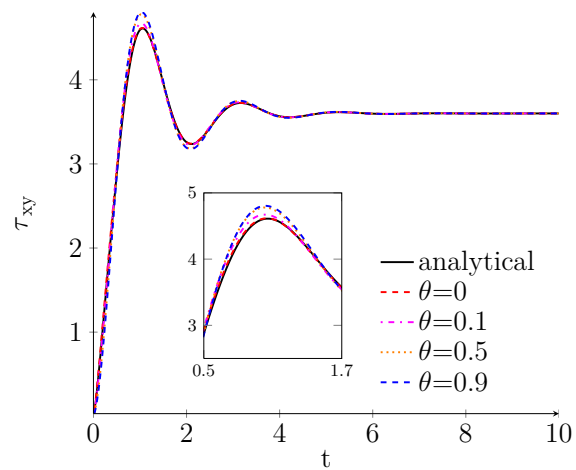
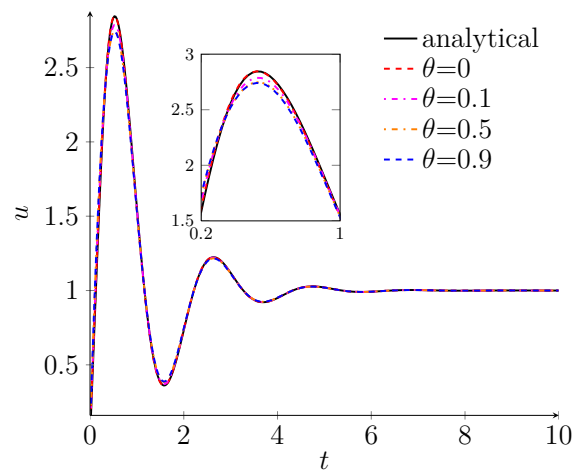
(a) τ_{xx} (b) τ_{xy} (c) u

Figure 5.2.: Comparison of numerical and analytical solution for $Wi = 1.0$ for increasing stabilisation parameter θ at point P_1 (a), (b) and point P_2 (c).

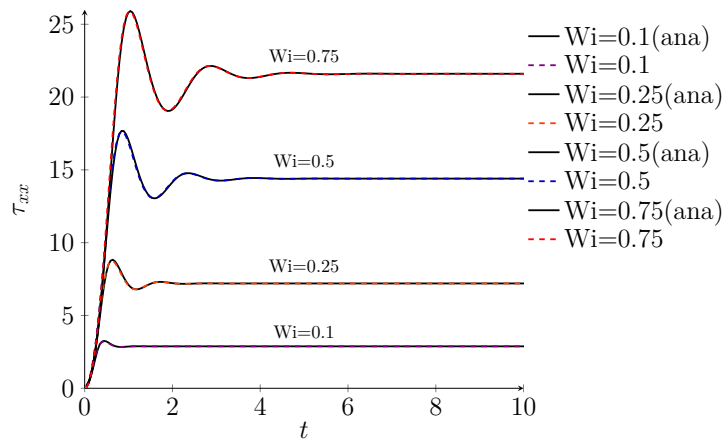
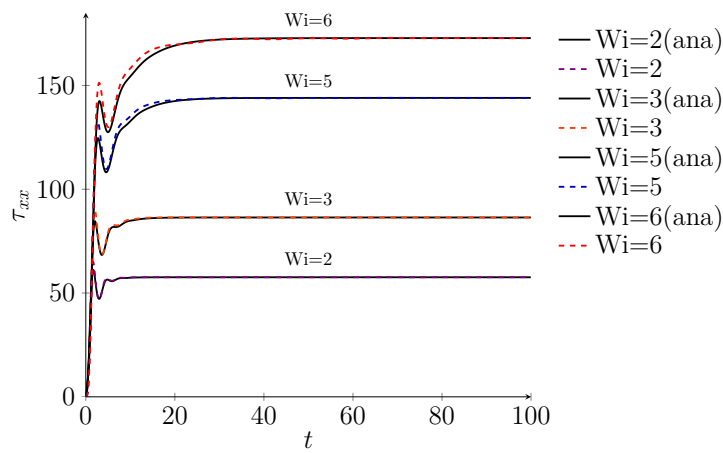
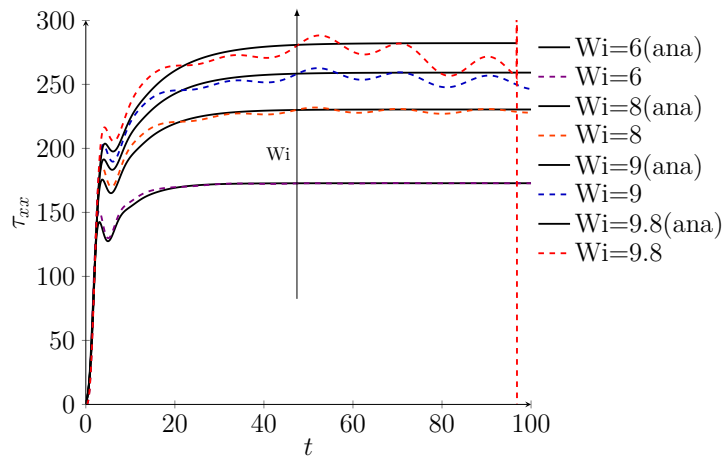
(a) $\tau_{xx}, \theta = 0$ (b) $\tau_{xx}, \theta = 0.9$ (c) $\tau_{xx}, \theta = 0.9$

Figure 5.3.: Comparison of analytical and numerical solution for a range of Weissenberg numbers.

5.2. Flow around a Confined Cylinder

In this Section, we investigate the performance of our DEVSS-G/DG algorithm on the well established flow around a cylinder in a confined channel benchmark problem. The results of the investigation in this Section have been published in essence in Claus and Phillips (2013a). Even though this flow configuration has been tested thoroughly for different numerical methods and solution schemes (see Liu et al. (1998), Fan et al. (1999), Fan et al. (2005), Alves et al. (2001), Owens et al. (2002), Ma et al. (2003), Kim et al. (2004), Caola et al. (2001), Phan-Thien and Dou (1999), Sun et al. (1999), Hulsen et al. (2005), for example), there remain unresolved issues. The use of very fine meshes and stabilisation techniques are essential in order to capture the formation of thin boundary layers with steep stress gradients around the cylinder and the formation of a thin birefringent strand in the wake behind the cylinder.

The most reported property for numerical simulations of flow around a cylinder is the drag coefficient. Values of the drag coefficient up to a Weissenberg number $Wi = 1$ for an Oldroyd-B fluid can be found in all the mentioned works above. However, converged solutions in the wake downstream of the cylinder are difficult or impossible to achieve for $Wi \geq 0.7$. In addition, all numerical algorithms start to diverge with spatial refinement for some $Wi \leq 1$ for the Oldroyd-B fluid. The cause for this loss of convergence and the numerical failure is still unknown. Some of the possible sources include

1. unphysical predictions of the viscoelastic models and the ill-posedness of the underlying initial-boundary value problem.
2. propagation of numerical errors introduced by the approximation scheme.
3. onset of physical viscoelastic instabilities.

Concerning the first point, we demonstrated in Chapter 2.5.4 that the Oldroyd-B model predicts a singularity in the elongational viscosity even for low elongation rates, which leads to unphysical predictions of the flow behaviour and possible instabilities in the numerical solution. This makes the Oldroyd-B model unsuitable for the simulation of flows undergoing elongational deformations. For the flow around a cylinder, there are regions of the flow which experience elongational deformation and therefore the results achieved with the Oldroyd-B model have to be interpreted with care.

In addition to exploring the flow of an Oldroyd-B fluid around a cylinder, we will present results using the Giesekus model, which does not exhibit a singularity in the elongational viscosity. Numerical predictions are compared with those of the Oldroyd-B fluid for different values of the mobility parameter α in the Giesekus model. The Giesekus model for the flow around a confined cylinder has been investigated by Liu et al. (1998), Sun et al.

(1999) and Hulsen et al. (2005). However, these investigations were mostly concerned with the reduction of the drag coefficient. We give detailed tables of drag coefficients for increasing spatial refinement for $\alpha = 0.001, 0.01, 0.1$, contour plots and plots along different paths in the fluid domain.

We present our results using the flow directed shear and normal stress measures proposed by Bollada and Phillips (2008). These reveal that the flow dependent normal stress dominates the flow for the Oldroyd-B fluid and its magnitude increases significantly with Wi , while the flow dependent shear stress decreases slightly with increasing Wi . This means the flow around a cylinder is increasingly characterised by normal stress effects, which include the elongational contributions. For the Giesekus fluid, we show that with increasing α , the shear stress contributions become more and more important in comparison to the normal stress until the flow is dominated by the shear stress component for $\alpha = 0.1$. In addition, we investigate the effect of the Reynolds number on the drag and flow patterns for the Oldroyd-B fluid.

Concerning the second point, Hulsen et al. (2005) identified the region downstream close to the rear stagnation point as a critical point for exponential stress growth. This exponential growth in stress is poorly approximated by polynomial expansion bases. This leads to large numerical errors. However, this problem can be alleviated using the log-conformation approach. Hulsen et al. (2005) demonstrated that when the log-conformation reformulation is used, results for larger values of Wi can be achieved especially for the Giesekus model. However, loss of convergence in the wake remains a problem.

Concerning the third point, there is experimental evidence of an onset of a physical viscoelastic instability. The experimental work of McKinley et al. (1993) and Byars (1996) suggest that there is an onset of viscoelastic instabilities in the flow around a cylinder at a critical Weissenberg number. They found that beyond a critical Weissenberg number large downstream shifts in the velocity profiles are generated progressively. Then, beyond another critical value the steady planar stagnation flow in the downstream wake becomes unstable and evolves into a steady, three-dimensional cellular structure. Byars (1996) reported a transition at around $Wi=0.5$. At this critical Weissenberg number the instability was observed to be confined to the vicinity of the wake of the cylinder. Measurements near to the cylinder beyond the critical Weissenberg number showed that the instability also existed along the cylinder upstream of the rear stagnation point. The experimental evidence seems to suggest that the instability, generated by normal stresses on the cylinder due to fluid elasticity, is convected downstream into the wake region. Numerical evidence suggests that there are three distinct regimes. In the first regime ($Wi \leq 0.6$), the flow is stable and convergent values of the drag coefficient are obtained. Excellent agreement is obtained across a wide range of numerical schemes. In the second regime ($Wi \in [0.6, 1]$), there is a transition to an oscillatory flow near the rear stagnation point.

Steady state values of the drag can be determined provided the mesh is not too fine. For a given mesh, a convergent steady state approximation is obtained. However, there is a lack of convergence with mesh refinement. In the third regime ($Wi > 1$), the flow becomes unstable and numerical schemes fail to converge. Some form of turbulence model is required in this regime. In order to obtain predictions in the second regime, transient algorithms are required since there is not a convergent steady state solution. This may explain why algorithms that are designed to compute steady state solutions fail to do so above a critical Weissenberg number.

The evidence that such a transient regime can be predicted by numerical simulations becomes more and more apparent with the enhancement of numerical algorithms and the use of high-resolution meshes. Oliveira and Miranda (2005) simulated the flow around a cylinder of a FENE-CR fluid and observed that the flow becomes unsteady for $Wi \approx 1.3$ for an extensibility parameter of $L^2 = 144$. Oliveira and Miranda (2005) also observed that the transient flow is characterised by a small pulsating recirculation zone of size approximately equal to 0.15 times the cylinder radius attached to the downstream face of the cylinder and that the drag value undergoes a sinusoidal motion in time. Very little is known about how this instability develops. The most common assumption is that the instability develops due to the presence of a thin extensional wake characterised by high longitudinal stresses τ_{xx} in the downstream wake of the cylinder. Another possible explanation is that the instability is caused by oscillations in the shear layer on top of the cylinder, which are then convected downstream into the wake. In our computations, we predict the onset of oscillations on top of the cylinder and observe a small recirculation zone of radius less than 1% of the cylinder radius for $Wi \gtrsim 0.62$. This critical Wi is consistent with the observations by Dou and Phan-Thien (2007).

Dou and Phan-Thien (2007, 2008) developed a theory aiming to explain the onset of a viscoelastic instability in the shear layer on the top of the cylinder. They investigated this shear layer numerically and analytically using boundary layer analysis and interpreted their results in terms of energy gradients. They identified the ratio, K , of the total mechanical energy $E = p + \frac{1}{2}\rho\mathbf{u}^2$ in the direction normal to the streamlines to the gradient of the total energy loss in the streamwise direction, denoted by H , as a critical parameter for the onset of an instability. For large ratios the flow is dominated by the transverse energy gradient which can amplify a disturbance if the energy loss, H , along the streamline is not large enough to dampen the disturbance. As a result the disturbance is transported downstream and amplified. For Newtonian flow, the energy loss along the streamline is due to viscous friction along the streamwise direction. Dou and Phan-Thien (2007) point out that an inflection in the velocity profile results in a zero energy loss along the streamlines which leads to infinite K . This causes the flow to become unstable when it is

subjected to a finite disturbance. In Dou and Phan-Thien (2007), they find a velocity inflection for $Wi \approx 0.6$ for an Oldroyd-B fluid, which lies very close to the cylinder surface at $y/R \approx 1.02$. Because this velocity inflection occurs very close to the cylinder surface only fine meshes can capture it. This might provide one possible explanation, why computations performed on coarse meshes converge to steady state solutions but convergence problems occur for finer meshes. We find the onset of oscillations in the drag coefficient for $Wi \gtrsim 0.6$ only for the finest meshes. We investigate the velocity and pressure on top of the cylinder and demonstrate the development of a velocity inflection with increasing Wi .

5.2.1. Benchmark Geometry

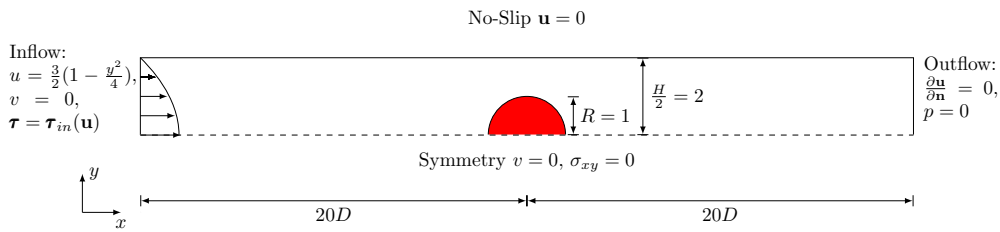


Figure 5.4.: Schematic diagram of flow around a cylinder.

We investigate the flow around a confined cylinder of radius $R = 1$ in a channel of height $H = 4$ resulting in a 50% blockage ratio (see Figure 5.4). At inflow, we impose a parabolic velocity profile with an average inlet fluid speed of 1. The average fluid speed is defined as

$$\langle u \rangle := \frac{1}{b-a} \int_a^b u(x) dx = 1. \quad (5.21)$$

Table 5.3.: Parameters for flow around a confined cylinder.

Re	0, 0.01, 0.1, 1
Wi	0.1, 0.2, 0.3, 0.4, 0.5, 0.6, 0.7, 0.8, 0.9, 1.0
β	0.59
θ	$(1 - \beta)$
γ	1
α	0, 0.001, 0.01, 0.1
Δt	10^{-3}
T_{fin}	40
Time integration	BDF2/EX2

This results in a parabolic velocity profile given by

$$u = \frac{3}{2} \left(1 - \frac{y^2}{4} \right), \quad v = 0. \quad (5.22)$$

Furthermore, we set the polymeric stress components at inflow to the steady state solution of Poiseuille flow of the Oldroyd-B fluid given by Equation (5.16). At the outflow boundary Γ_{out} , we assume a fully developed unidirectional flow field, i.e. we impose

$$\nabla \mathbf{u} \cdot \mathbf{n} = 0, \quad (5.23)$$

through the boundary integral in Equation (4.42) in combination with a reference pressure of zero. This means the boundary integral in Equation (4.42) reduces at outflow to

$$\langle (\boldsymbol{\tau} - (1 - \beta)\mathbf{G}) \cdot \mathbf{n}, \phi_{\mathbf{u}} \rangle_{\Gamma_{out}}. \quad (5.24)$$

On symmetry boundaries, we impose a combination of Dirichlet and Neumann conditions

$$\begin{aligned} \mathbf{u} \cdot \mathbf{n} &= 0, \\ \mathbf{t} \cdot \boldsymbol{\sigma} \cdot \mathbf{n} &= 0. \end{aligned} \quad (5.25)$$

Here, $\boldsymbol{\sigma}$ is the Cauchy stress tensor, \mathbf{n} is the unit outward normal vector and \mathbf{t} is the unit tangent vector on the boundary. For the cylinder geometry displayed in Figure 5.4, Equation (5.25) reduces to setting $v = 0$ in combination with $\sigma_{xy} = 0$ along the symmetry boundary. These boundary conditions mean that there is no contribution of the boundary integral term in the momentum equation (4.42) along the symmetry line. At the wall and along the cylinder surface, we impose no-slip boundary conditions, i.e. $\mathbf{u} = \mathbf{0}$. We assume the fluid to be at rest initially, i.e. $\mathbf{u} = \mathbf{0}$ and $\boldsymbol{\tau} = \mathbf{0}$ at $t = 0$.

In the flow around the cylinder benchmark problem, we define the Reynolds and Weissenberg number by

$$\text{Re} = \frac{\rho \langle u \rangle R}{\eta_0}, \quad (5.26)$$

$$\text{Wi} = \lambda \frac{\langle u \rangle}{R}, \quad (5.27)$$

where $\eta_0 = \eta_p + \eta_N$ is the total viscosity given by the sum of polymeric viscosity η_p and Newtonian viscosity η_N , λ is the relaxation time and ρ is the fluid density. The characteristic length scale is given by the radius R of the cylinder and the characteristic velocity is given by the average fluid inlet speed $\langle u \rangle$. The parameters chosen in our computations are listed in Table 5.3. To investigate the quality of our numerical solution, we compute the

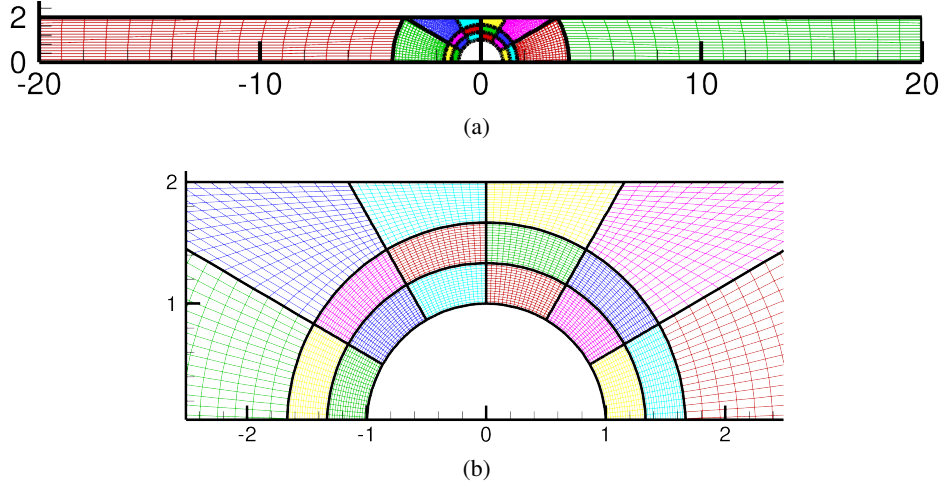


Figure 5.5.: Mesh for $N_{el} = 20$, (a) complete computational domain, (b) zoom of region around the cylinder.

drag coefficient around the cylinder. The drag coefficient is defined as the x -component of the traction force around the cylinder given by

$$\mathbf{F} = \int_{\Gamma_c} \boldsymbol{\sigma} \cdot \mathbf{n} \, d\Gamma, \quad (5.28)$$

where Γ_c is the cylinder surface, \mathbf{n} is the unit outward normal to the cylinder surface and $\boldsymbol{\sigma} = -p\mathbf{I} + \beta(\nabla\mathbf{u} + \nabla\mathbf{u}^T) + \boldsymbol{\tau}$ is the Cauchy stress tensor. With $\boldsymbol{\sigma}^* = \frac{R}{\eta_0 \langle u \rangle} \boldsymbol{\sigma}$, we obtain the dimensionless traction force

$$\mathbf{F}^* = \frac{1}{\langle u \rangle \eta_0} \int_{\Gamma_c} \boldsymbol{\sigma}^* \cdot \mathbf{n}^* \, d\Gamma. \quad (5.29)$$

The x -component of \mathbf{F}^* gives the **drag coefficient**

$$C_D^* = \frac{1}{\langle u \rangle \eta_0} \int_{\Gamma_c} \boldsymbol{\sigma}^* \cdot \mathbf{n}^* \cdot \hat{\mathbf{x}} \, d\Gamma, \quad (5.30)$$

where $\hat{\mathbf{x}}$ is the unit vector in the x -direction. In two-dimensional components, it is given by

$$C_D^* = \frac{1}{\langle u \rangle \eta_0} \int_{\Gamma_c} \left\{ \left(-p + \tau_{xx} + 2\beta \frac{\partial u}{\partial x} \right) n_x + \left(\tau_{xy} + \beta \left(\frac{\partial u}{\partial y} + \frac{\partial v}{\partial x} \right) \right) n_y \right\} d\Gamma, \quad (5.31)$$

We use a mesh with $N_{el} = 20$ as illustrated in Figure 5.5 and investigate the quality of our solution for increasing order of the polynomial expansion basis. The number of degrees of freedom for the dependent variables and the distance of the closest quadrature point to

Table 5.4.: Number of degrees of freedom for dependent variables and the distance of the closest quadrature point to the cylinder surface, h_q , on a mesh consisting of 20 elements for increasing polynomial order.

P	\mathbf{u}	$\boldsymbol{\tau}, \mathbf{G}$	p	Total	h_q
12	3013	3380	2420	32106	$2.77 \cdot 10^{-2}$
14	4075	4500	3380	43030	$2.38 \cdot 10^{-2}$
16	5297	5780	4500	55554	$2.08 \cdot 10^{-2}$
18	6679	7220	5780	69678	$1.85 \cdot 10^{-2}$

the cylinder surface, h_q , for the employed mesh are listed in Table 5.4. We compare the drag results with those of Owens et al. (2002), Fan et al. (1999) and Alves et al. (2001). Owens et al. (2002) used a spectral method with LUST upwinding, a variant of SUPG for nodal spectral methods, with a maximum polynomial order $P = 20$, $N_{dof} = 8239$ for the velocities and a total number of degrees of freedom of $N_{dof} = 48415$. Fan et al. (1999) employed a high order FEM and used $N_{dof} = 29206$ for a mesh with elements of maximum polynomial order $P = 5$. Alves et al. (2001) used the finite volume method with high order upwinding and 69600 control volumes in their finest mesh.

We display the stress tensor results using flow dependent shear and normal stress measures as proposed by Bollada and Phillips (2008). The decomposition in the streamwise and cross stream direction was first introduced by Wapperom and Renardy (2005) for the configuration tensor in the Oldroyd B model. This decomposition, when applied to the total stress tensor (Cauchy stress), is the subject of the contribution of Bollada and Phillips (2008). This has the advantage of decomposing the principal stresses into shear and normal stresses in a natural way. An example of the physical importance of such quantities is suggested in Lodge (1956): “in shear flow, in addition to the usual hydrostatic and shear stress components, there is a tensile stress in the direction of the streamline” and also the Weissenberg hypothesis: the stress tensor rotates towards the direction of the streamlines of flow as the rate of shear increases (Weissenberg et al., 1947). First, we remove the isotropic part from the Cauchy stress

$$\mathbf{T} = \boldsymbol{\sigma} - \left(\frac{1}{2}\text{tr}\boldsymbol{\sigma}\right)\mathbf{I}. \quad (5.32)$$

Then, we decompose the traceless symmetric stress \mathbf{T} into a flow directed shear and normal stress using the direction of the streamlines $\mathbf{u}_{\parallel} = \frac{\mathbf{u}}{|\mathbf{u}|}$ and their unit normals in the cross stream direction \mathbf{u}_{\perp} . We define the flow dependent shear stress as

$$S_1 = \mathbf{u}_{\perp} \cdot \mathbf{T} \cdot \mathbf{u}_{\parallel} \quad (5.33)$$

and the flow dependent normal stress

$$S_2 = \mathbf{u}_{\parallel} \cdot \mathbf{T} \cdot \mathbf{u}_{\parallel}. \quad (5.34)$$

Additionally, we define the principal stress as

$$T = \sqrt{S_1^2 + S_2^2}. \quad (5.35)$$

5.2.2. Oldroyd-B Model

Drag Coefficient

The computed values of the drag coefficient for different values of P for an Oldroyd-B fluid ($0 \leq Wi \leq 1$, $\beta = 0.59$) are tabulated in Table 5.5 and plotted in Figure 5.6 in comparison with the results of Alves et al. (2001), Fan et al. (1999) and Owens et al. (2002). The predicted drag coefficients are in very good agreement with the existing literature. Converged values for the drag are obtained for $Wi \leq 0.7$ on all meshes. However, for finer meshes, the drag oscillates about a mean value for $Wi \geq 0.6$. The amplitude of these time-dependent but stable oscillations in the drag value is very small initially but increases with increasing polynomial order. For $Wi = 0.6$, the drag exhibits the sinusoidal behaviour from $P = 16$, while for $Wi = 0.7$ the evolution of the drag exhibits oscillatory behaviour from $P = 14$. Figure 5.7 shows the development of the drag with time for increasing values of Wi . The drag reaches an apparent steady state value, i.e. it either reaches a constant value or it oscillates around a mean value, for $t \approx 7$. However, for $Wi \geq 0.8$ the computations diverge after an apparent drag value is reached from $P = 16$ (marked with a (D) in Table 5.5). For $Wi = 1$, we fail to obtain a steady state solution for the polynomial orders investigated. However, the drag reaches its apparent steady state value before the computations fail.

The time dependent behaviour of the drag for $Wi \geq 0.6$ may be due to the onset of velocity fluctuations in the shear layer on top of the cylinder initiated by an inflection in the velocity profile near the cylinder surface as described by Dou and Phan-Thien (2007). The velocity inflection occurs very close to the cylinder and can therefore only be captured by meshes that are sufficiently fine. In the next Section, we present plots of the velocity components and the pressure in the gap between the top of the cylinder and the channel wall that confirm the development of a velocity inflection on top of the cylinder for increasing Wi .

Moreover, in our computations, we observe the formation of a small pulsating recirculation zone attached to the rear of the cylinder for $Wi \geq 0.62$. A similar recirculation region was found by Oliveira and Miranda (2005) for a FENE-CR fluid with $Wi \gtrsim 1.3$ and an

Table 5.5.: Comparison of computed values of the drag coefficient for an Oldroyd-B fluid ($\beta = 0.59$) with results in the literature. (D) means computations diverge after an apparent converged drag value is reached.

Wi	$P = 12$	$P = 14$	$P = 16$	$P = 18$	Alves et al. (2001)	Fan et al. (1999)	Owens et al. (2002)
0.1	130.364	130.360	130.364	130.364	130.355	130.36	-
0.2	126.627	126.623	126.626	126.626	126.32	126.62	-
0.3	123.193	123.189	123.192	123.192	123.210	123.19	-
0.4	120.592	120.589	120.592	120.593	120.607	120.59	-
0.5	118.826	118.822	118.826	118.826	118.838	118.83	118.827
0.6	117.775	117.773	117.775	117.776	117.787	117.77	117.775
0.7	117.306	117.319	117.319	117.316	117.323	117.32	117.291
0.8	117.307	117.352	117.369 (D)	117.368 (D)	117.357	117.36	117.237
0.9	117.688	117.776	117.817 (D)	117.812 (D)	117.851	117.79	117.503
1	118.372 (D)	118.508 (D)	118.558 (D)	118.550 (D)	118.518	118.49	118.030

extensibility parameter of $L^2 = 144$. Oliveira and Miranda (2005) found a recirculation zone of size approximately equal to $0.15R$ attached to the rear of the cylinder. We observe a recirculation zone for $Wi \gtrsim 0.62$ for the Oldroyd-B model of size less than $0.01R$. This zone is only captured on the finer meshes. This demonstrates the capability of the spectral/hp method to capture fast and small spatial and temporal variations in the solution.

Plots along Paths

In this Section, the behaviour of the polymeric stress component τ_{xx} along the symmetry line and around the cylinder surface, the horizontal velocity in the wake region along the symmetry line and the pressure and velocity components on top of the cylinder between the cylinder surface and the channel wall are investigated. Figure 5.8 shows the profile of the polymeric stress τ_{xx} along the centreline and on the cylinder surface for increasing values of Wi on the mesh with $P = 14$. The maximum value of τ_{xx} on top of the cylinder increases with Wi and a tail in the wake of the cylinder is formed. The maximum value of τ_{xx} in the wake of the cylinder increases sharply with increasing Wi . In Figure 5.9, the convergence behaviour of the polymeric stress component τ_{xx} along this path with increasing polynomial order for $Wi = 0.5, 0.6, 0.7$ is presented. Convergence of τ_{xx} is achieved on the cylinder surface and the drag converges with increasing P for up to $Wi = 0.5$. For $Wi = 0.6$, we observe a trend indicating convergence in the wake. However, there is a loss of convergence with increasing P in the downstream wake for

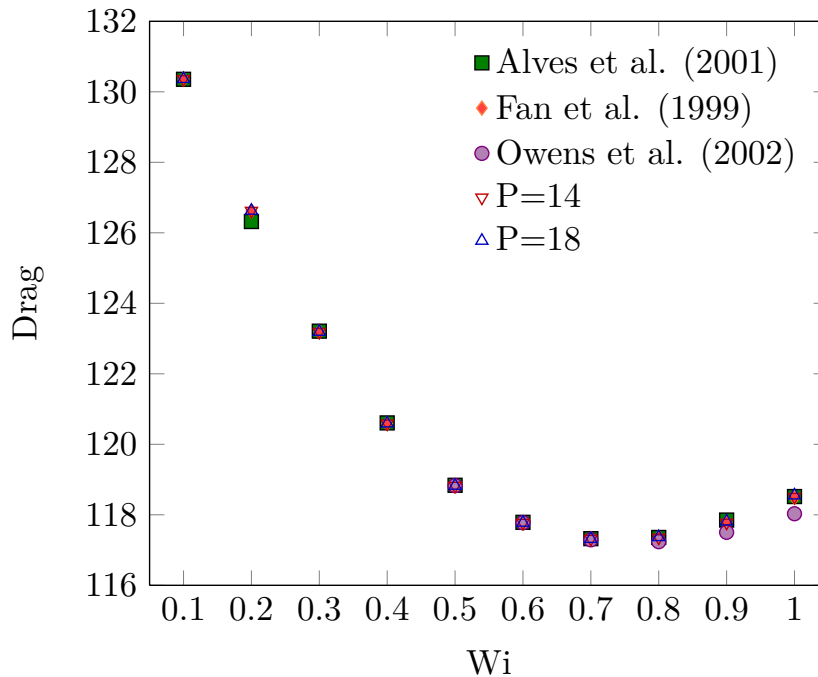


Figure 5.6.: Comparison of the dependence of the drag coefficient on Wi computed using the spectral/hp element method with results in the literature. Oldroyd-B fluid with $\beta = 0.59$.

$Wi = 0.7$. As loss of convergence is observed in the wake, the drag does not provide a good sole measure for the convergence behaviour for simulations of an Oldroyd-B fluid for the flow around a cylinder for large values of Wi .

Examining the horizontal velocity component in the wake of the cylinder along the symmetry line (see Figure 5.10(a)) for increasing values of Wi , reveals that the horizontal velocity component experiences an upstream shift with respect to the Newtonian velocity near the rear of the cylinder followed by a downstream shift further downstream of the cylinder wake. These shifts in the velocity profile increase with increasing Wi and the point where the upstream shift is followed by the downstream shift lie closer to the rear of the cylinder with increasing Wi (see Figure 5.10(b)).

Additionally, we investigate the velocity components and the pressure on top of the cylinder. According to the theory of Dou and Phan-Thien (2007, 2008) oscillations in the shear stress layer on the top of the cylinder may be the origin of transient viscoelastic behaviour. They identified the occurrence of a velocity inflection on the top of the cylinder as a possible cause for the onset of a viscoelastic instability. They identify the viscoelastic flow with an energy gradient field and determine the ratio of the energy gradient normal to the streamlines, E , and the energy loss gradient in the streamwise direction, H , as a critical

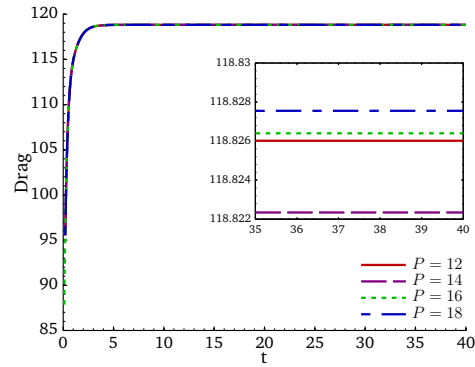
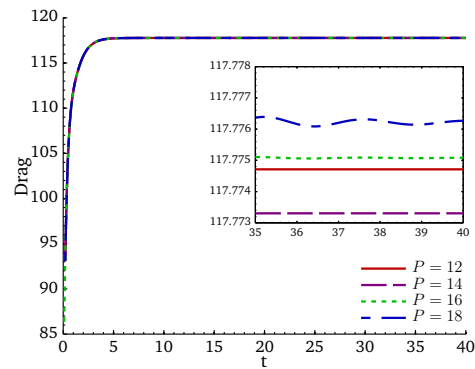
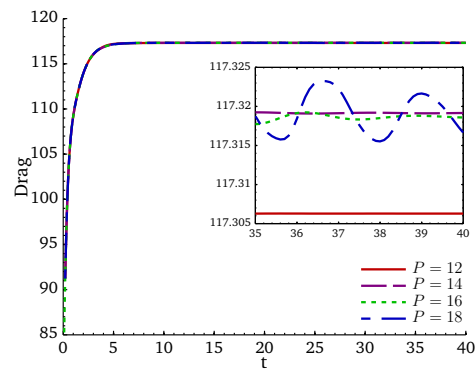
(a) $Wi = 0.5$ (b) $Wi = 0.6$ (c) $Wi = 0.7$

Figure 5.7.: Dependence of the evolution of the drag coefficient on P for (a) $Wi = 0.5$, (b) $Wi = 0.6$, (c) $Wi = 0.7$.

value that determines the stability of the flow. In the shear layer around the cylinder, the kinetic energy is negligible and the ratio of the energy gradients in the transverse direction to that in the streamwise direction becomes the ratio of pressure derivatives. Using the two dimensional cylindrical coordinate system (r, θ) , with origin at the centre of the cylinder, to express the pressure gradient in cross-stream and streamwise direction in the region around the cylinder, K becomes

$$K = \frac{\partial E / \partial \mathbf{n}}{\partial H / \partial \mathbf{s}} = \frac{\frac{\partial p}{\partial r}}{\frac{1}{r} \frac{\partial p}{\partial \theta}}. \quad (5.36)$$

As depicted in Figure 5.11, K can be expressed in terms of the angle γ between the cross-stream and streamwise pressure derivative. Figure 5.11 shows that this angle between the cross-stream and streamwise pressure derivative grows with increasing values of Wi . This increasing distortion of the pressure causes the velocity profile to deform and eventually causes a velocity inflection, which is associated with the onset of the transient flow regime. In Figures 5.12 and 5.13, we see that the magnitude of the horizontal velocity component is reduced near the cylinder in comparison to the parabolic Newtonian profile and is increased near the middle of the gap between the cylinder and the channel wall. The vertical velocity component (see Figure 5.13(b)) increases near the cylinder surface and decreases near the channel wall with increasing Wi . The vertical velocity component experiences a change in the velocity gradient when leaving the shear layer at $y \approx 1.02$ that increases with increasing Wi . These findings are in agreement with Dou and Phan-Thien (2007), who also found a significant change in the velocity gradient at $y \approx 1.02$. Note that, in our case, this change in the velocity gradient does not occur on an element boundary but inside one high order element. Therefore, this change is not a numerical artefact occurring from coupling one element to the other. According to Dou and Phan-Thien (2007), the sudden change in the vertical velocity component will eventually allow particles to leave the shear layer and will cause a disturbance of the flow. This disturbance will be amplified and transported downstream if the energy gradient in the transverse direction dominates the energy gradient loss in the streamwise direction.

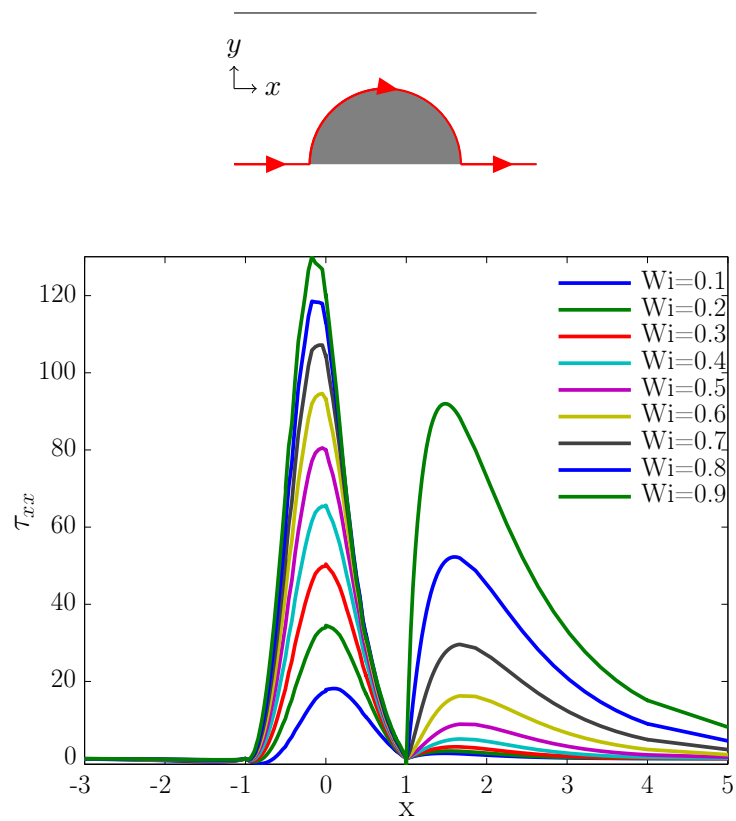


Figure 5.8.: Profiles of τ_{xx} along centreline and cylinder surface for increasing Wi for $P = 14$.

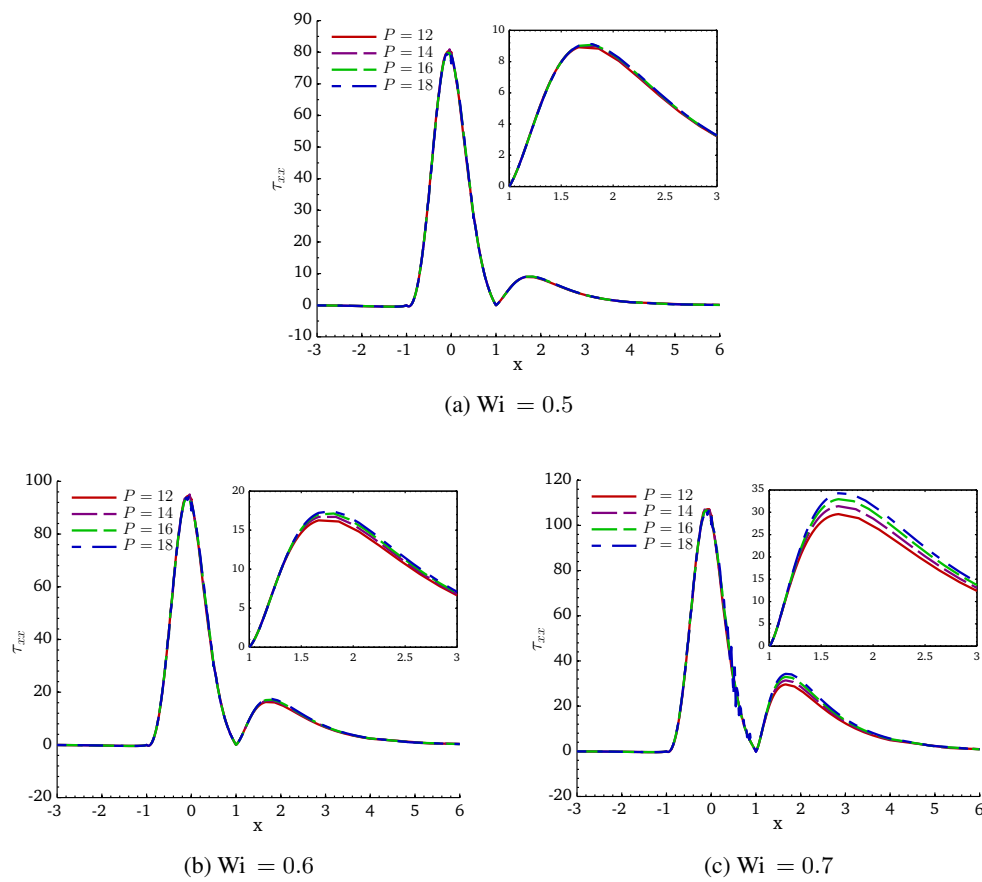


Figure 5.9.: Convergence of the profiles of τ_{xx} along the centerline and around the cylinder with P for (a) $Wi = 0.5$, (b) $Wi = 0.6$, and (c) $Wi = 0.7$

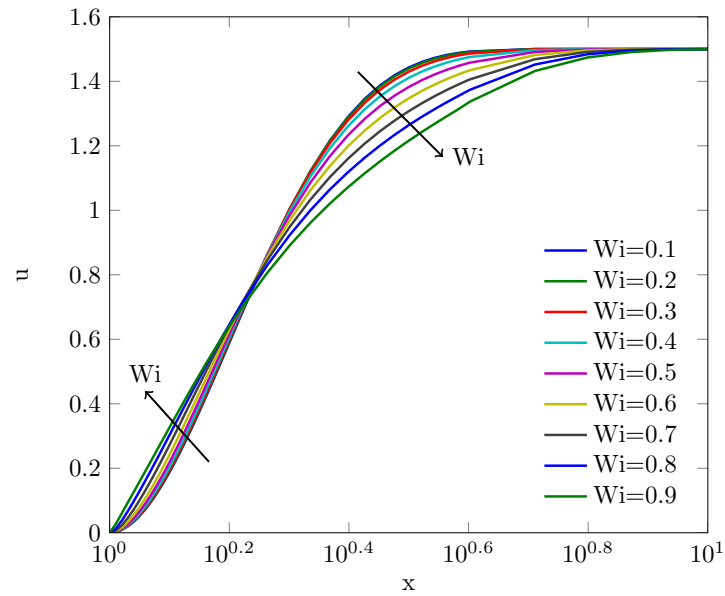
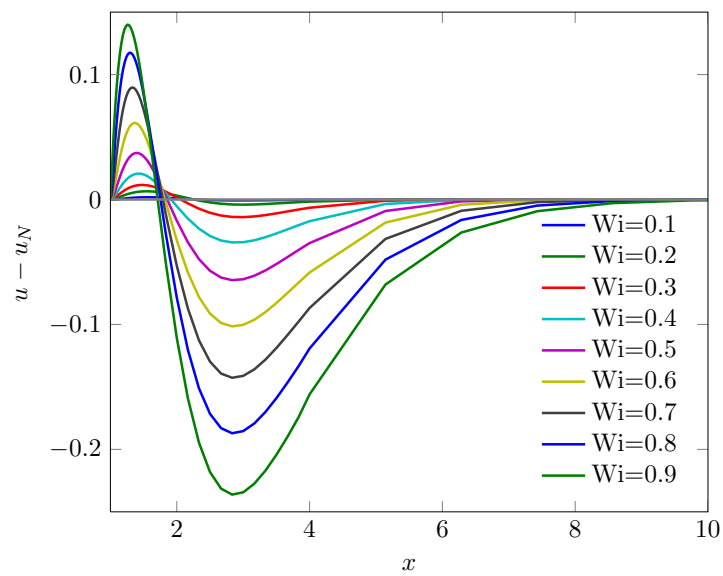
(a) u in the wake(b) $u - u_N$ in the wake

Figure 5.10.: Dependence of (a) u and (b) $u - u_N$ (the velocity shift with respect to the Newtonian velocity profile), on Wi along the downstream centreline.

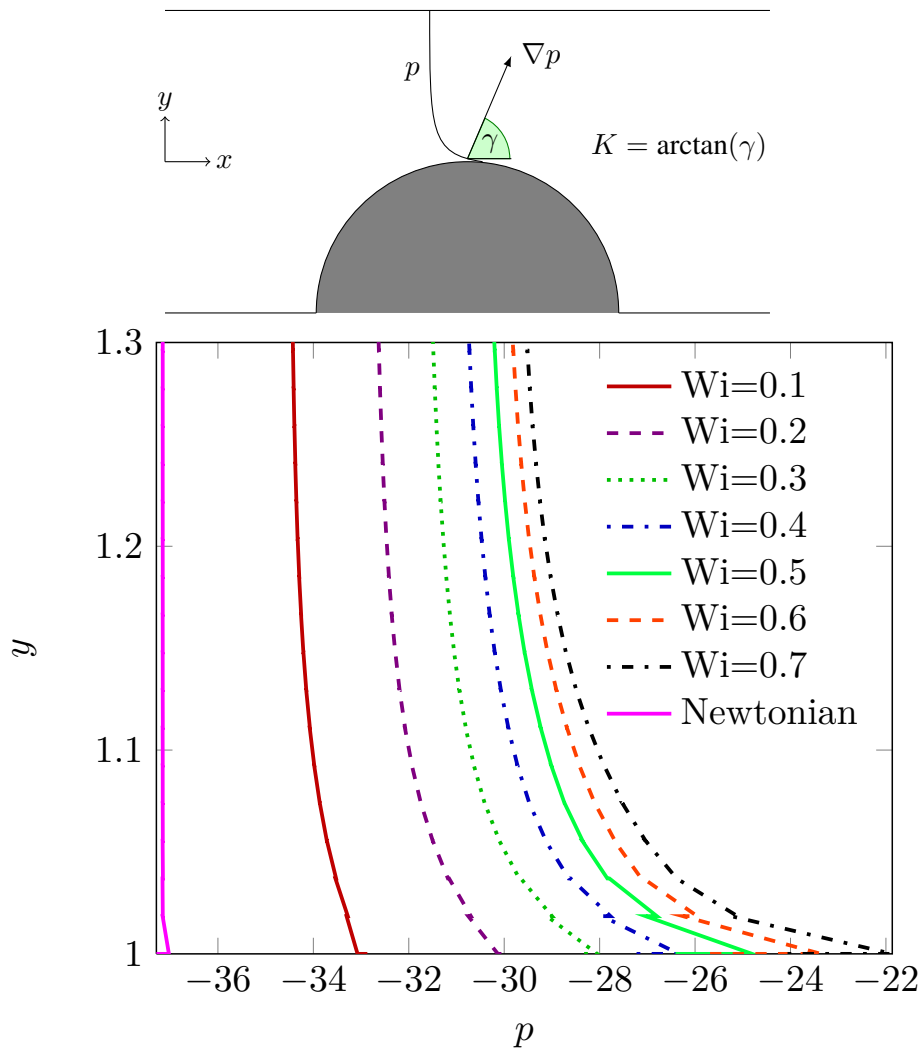


Figure 5.11.: Dependence of the pressure profiles on top of the cylinder on Wi . In the boundary layer near the cylinder the ratio of energy gradients, K , can be expressed as the ratio of the pressure gradient in the transverse and streamwise direction, which is given the inverse tangent of the angle γ depicted above. As this angle increases with increasing Wi , K increases with increasing Wi and therefore the tendency of the flow to develop an instability increases.

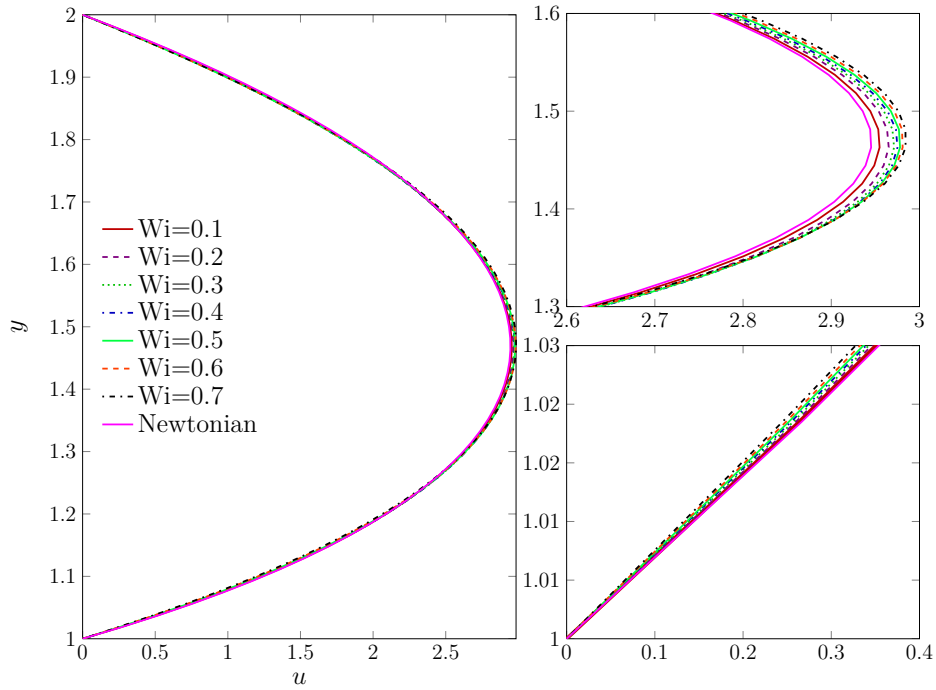


Figure 5.12.: Dependence of horizontal velocity u on top of the cylinder on Wi .

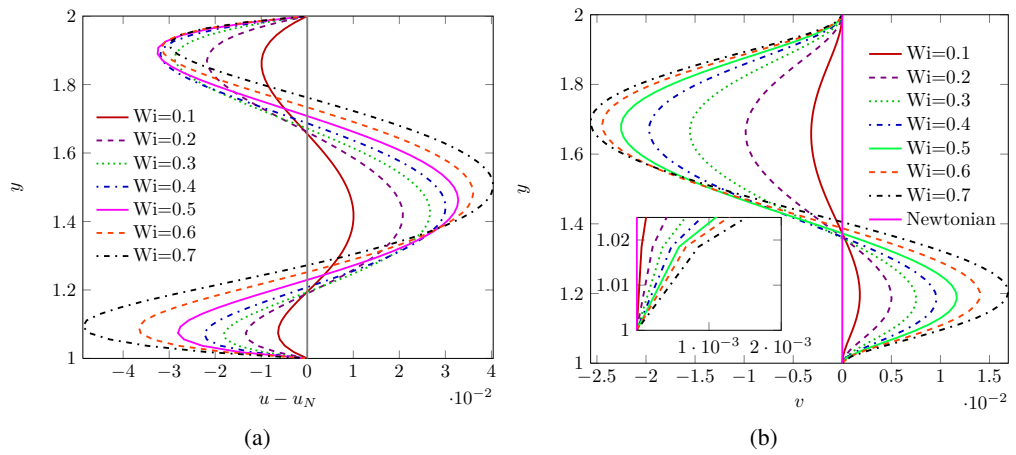


Figure 5.13.: Dependence of (a) $u - u_N$ and (b) v on Wi along the shortest path from the top of the cylinder to the channel wall.

Contour Plots

Figure 5.14 displays contour plots of the pressure and the horizontal velocity component. As Wi increases, we observe a pressure concentration at the front and at the rear stagnation point and the formation of strong pressure gradients near the cylinder surface. The horizontal velocity component experiences an upstream shift in comparison to the Newtonian flow profile near the rear stagnation point and a downstream shift further downstream of the wake. The shifts are strongest along the symmetry line. The contour plots of the polymeric stress component τ_{xx} and the flow dependent normal stress S_2 are displayed in Figure 5.15. The polymeric stress component τ_{xx} forms thin and steep boundary layers on top of the cylinder and along the channel wall above the cylinder. In addition, the polymeric stress component τ_{xx} forms a region of high stress along the symmetry line in the rear of the cylinder forming a thin tail in the downstream region of the cylinder. The boundary layers and the tail increase in strength with increasing values of Wi .

These observations are consistent with the literature (see Caola et al. (2001) and Sun et al. (1999), for example). However, in addition to the pressure and the components of velocity and stress, we investigate the behaviour of the flow dependent normal and shear stress contributions as defined in (5.33) and (5.34). The right hand column of Figure 5.15 displays the contour plots of the flow dependent normal stress and Figure 5.16 shows the flow dependent shear stress and the principal stress. Looking at this flow dependent stress decomposition, we observe that the major contribution to the total stress is given by the flow dependent normal stress which means the flow around a cylinder is dominated by normal stress effects. The flow dependent normal stress S_2 exhibits qualitatively all the features of the polymeric stress component τ_{xx} , i.e. sharp increase of the normal stress value in the boundary layers around the cylinder and formation of a tail with increasing Wi . However, in addition to that, S_2 shows a low normal stress region near the front stagnation point of the cylinder. In contrast to the sharp increase of the normal stresses with increasing Wi , the flow dependent shear stress S_1 decreases slightly with increasing Wi . Furthermore, S_1 exhibits the development of a high shear stress region a small distance upstream of the front stagnation point. The decrease in the shear stress might be explained by the small decrease in $\frac{\partial u}{\partial y}$ on top of the cylinder. For example, at the top of the cylinder at $(x_1, x_2) = (0, 1)$, we find $\frac{\partial u}{\partial y} = 14.637$ for $Wi = 0.1$, $\frac{\partial u}{\partial y} = 13.739$ for $Wi = 0.5$ and $\frac{\partial u}{\partial y} = 13.228$ for $Wi = 0.7$. The principal stress T is almost symmetric for low values of Wi and then gradually becomes asymmetric with the formation of the thin bi-refringence strand downstream of the cylinder and low stress regions close to the front and rear stagnation points. The contribution of the flow dependent normal stress S_2 is much higher than the contribution of the flow dependent shear stress S_1 to the principal

stress T . Therefore, the flow around a cylinder for the Oldroyd-B fluid will be dominated by normal stress phenomena, due to both normal stress differences and elongational flow properties, rather than shear stress phenomena.

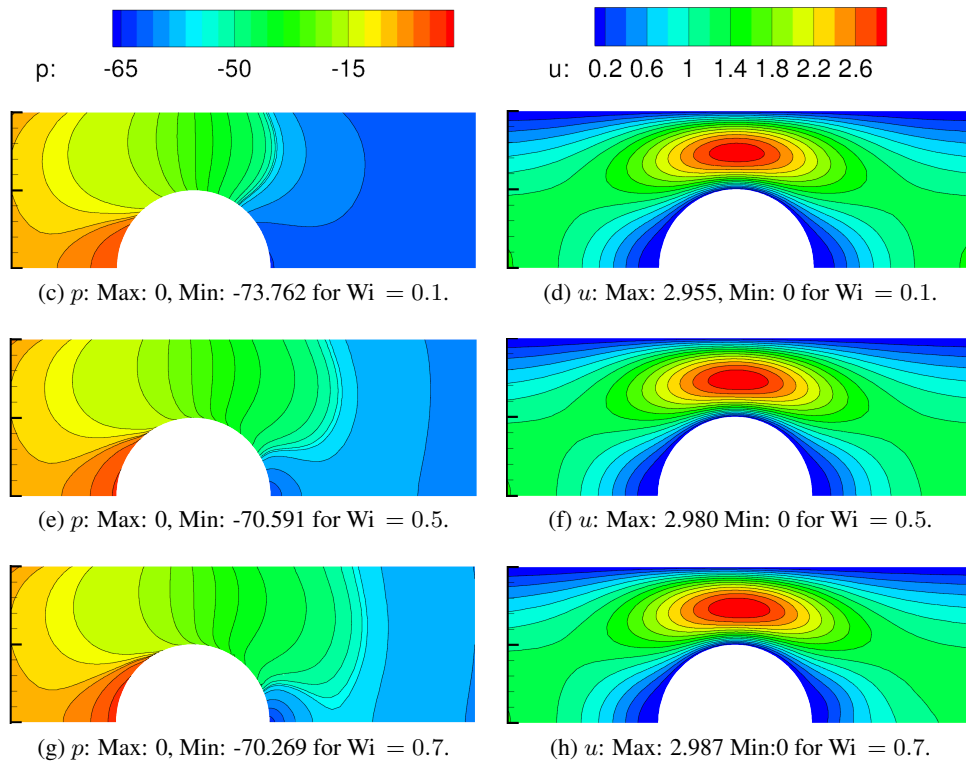


Figure 5.14.: Contour plots of pressure p (left) and velocity component u in x -direction (right) for $P = 18$ for an Oldroyd-B fluid.

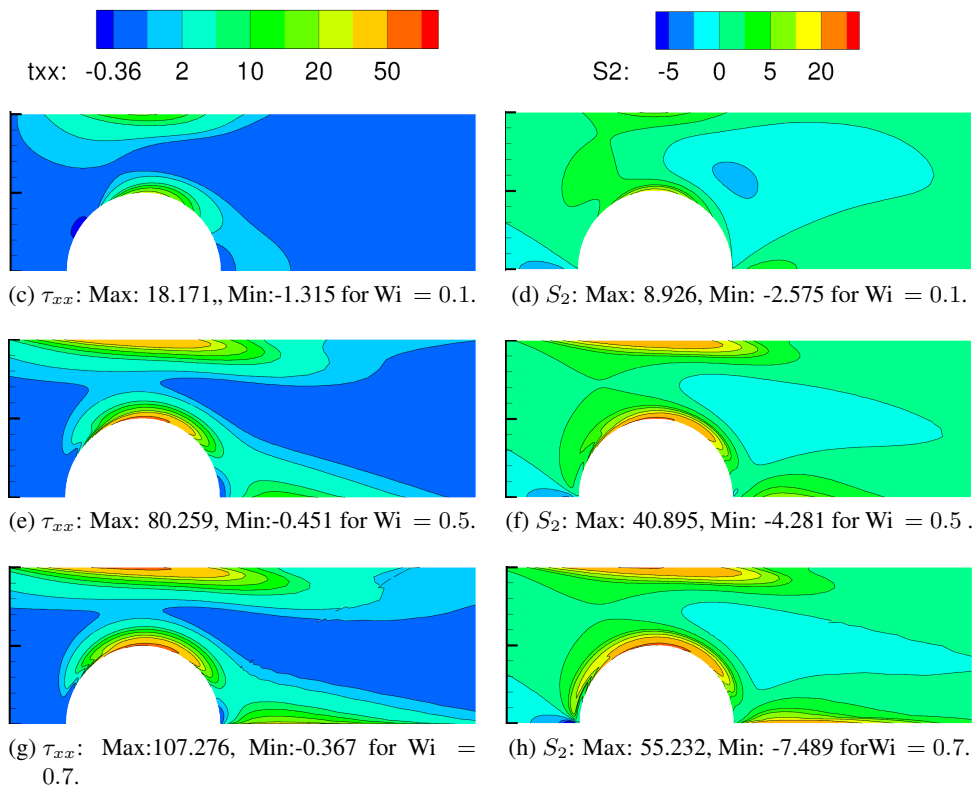


Figure 5.15.: Contour plots of polymeric stress component τ_{xx} (left) and flow dependent normal stress S_2 (right) for an Oldroyd-B fluid.

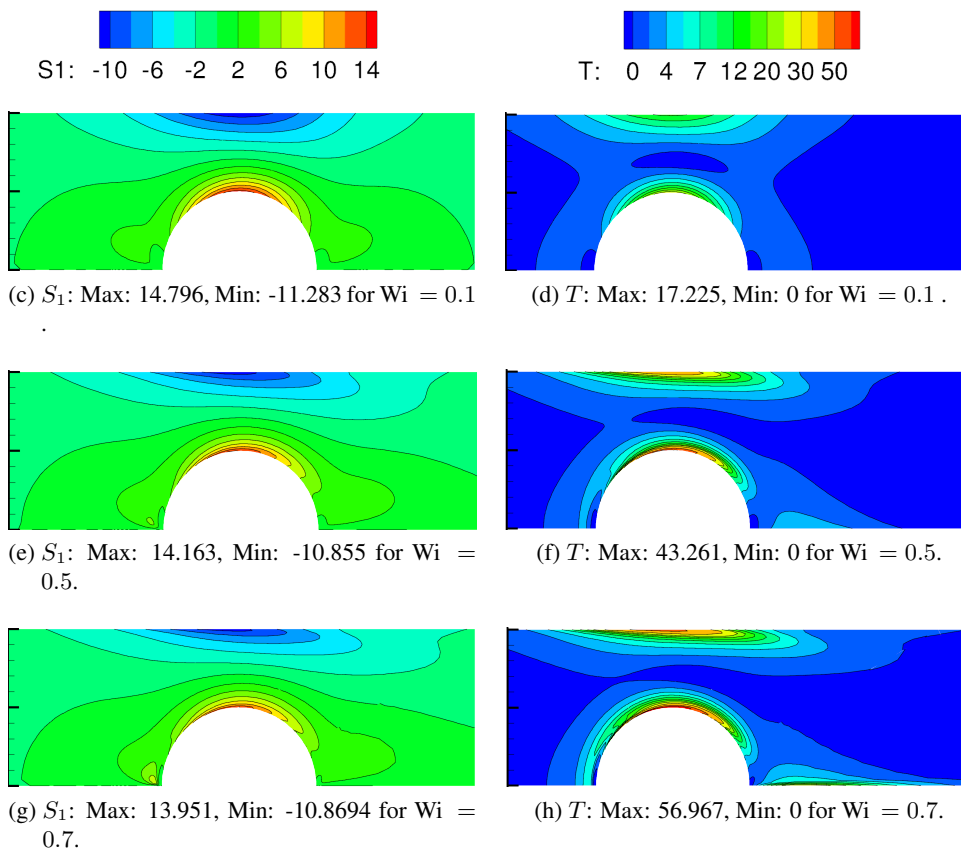


Figure 5.16.: Contour plots of flow dependent shear stress S_1 (left) and flow dependent principal stress T for an Oldroyd-B fluid.

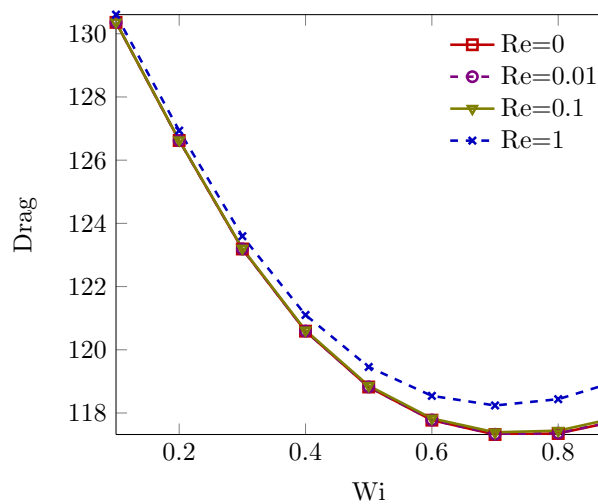
5.2.3. Oldroyd-B Model for higher Reynolds numbers

We investigate the effect of inertia on the flow around a cylinder. The computed drag coefficient values for $Re = 0.01, 0.1, 1$, are tabulated in Table 5.6 and illustrated in Figure 5.17. The drag values increase with increasing values of Re . The drag reduction effect caused by increasing Wi decreases with increasing Re . For $Wi = 0.7$, the drag value for $Re = 0.01$ differs from the drag value for $Re = 0$ by 0.006%, for $Re = 0.1$ by 0.06% and for $Re = 1$ by 1.18%. The cause for the increase of the drag value with increasing Re is increasing velocity gradients. Table 5.7 displays the maximum and minimum values of the dependent variables as a function of Re . While the maximum values of τ_{xy} and τ_{yy} increase for increasing Re , the maximum value of τ_{xx} decreases. Figure 5.18(a) shows that τ_{xx} decreases only slightly on top of the cylinder surface for all tested Re . However, the values in the wake behind the cylinder strongly decrease when $Re = 1$. The horizontal velocity component in the downstream region in the wake of the cylinder is depicted in Figure 5.18(b) and the difference between the viscoelastic and the Newtonian horizontal velocity is displayed in Figure 5.18(c). The horizontal velocity component in the wake of the cylinder experiences an overshoot near the cylinder ($x \approx 1.5$) in comparison to the Newtonian velocity profile and an undershoot further downstream ($x \approx 3$). The overshoot increases with increasing Re and the undershoot decreases with increasing Re . In addition, the maximum of the overshoot and the minimum of the undershoot occur further and further downstream with increasing Re .

The changes of the velocity profiles with increasing Re in the gap between the top of the cylinder and the channel wall are shown in Figure 5.19. The horizontal velocity profile decreases near the top of the cylinder and increases in the middle of the gap with increasing Re . In contrast, the vertical velocity increases near the top of the cylinder and decreases near the wall with increasing Re . This reduced horizontal velocity and amplified vertical velocity explains the increase of the drag value as well as the increase in τ_{xy} and τ_{yy} and the decrease τ_{xx} .

Table 5.6.: Computed values of the drag coefficient for an Oldroyd-B fluid for $0 \leq Wi \leq 1$ and $Re = 0.01, 0.1, 1$.

Wi	Re = 0.01		Re = 0.1		Re = 1	
	$P = 14$	$P = 18$	$P = 14$	$P = 18$	$P = 14$	$P = 18$
0.1	130.361	130.364	130.365	130.368	130.605	130.609
0.2	126.624	126.627	126.633	126.636	126.935	126.938
0.3	123.191	123.194	123.208	123.211	123.594	123.597
0.4	120.591	120.595	120.617	120.622	121.102	121.106
0.5	118.826	118.831	118.863	118.868	119.456	119.460
0.6	117.779	117.781	117.828	117.831	118.542	118.542
0.7	117.326	117.323	117.390	117.387	118.238	118.233
0.8	117.360	117.379 (D)	117.440	117.459 (D)	118.437	118.455 (D)
0.9	117.786	117.827 (D)	117.883	117.925 (D)	119.047	119.096 (D)
1	118.520 (D)	118.563 (D)	118.635 (D)	118.697 (D)	119.992 (D)	120.057 (D)

Figure 5.17.: Dependence of the drag coefficient on Wi and Re for $P = 14$.Table 5.7.: Minimum and maximum values for dependent variables for $P = 18$ and $Wi = 0.7$ for $Re = \{0.01, 0.1, 1\}$.

Re	$\text{Max}(\tau_{xx})$	$\text{Min}(\tau_{xx})$	$\text{Max}(\tau_{xy})$	$\text{Min}(\tau_{xy})$	$\text{Max}(\tau_{yy})$	$\text{Min}(\tau_{yy})$
0.01	107.251	-0.368	37.027	-20.734	24.673	-0.495
0.1	107.032	-0.369	37.172	-20.385	24.909	-0.533
1.0	104.871	-0.380	38.588	-17.783	27.511	-0.695

Re	$\text{Max}(u)$	$\text{Min}(u)$	$\text{Max}(v)$	$\text{Min}(v)$	$\text{Max}(p)$	$\text{Min}(p)$
0.01	2.988	0.000	0.884	-0.944	0	-70.272
0.1	2.988	0.000	0.888	-0.942	0	-70.288
1.0	2.994	0.000	0.929	-0.920	0	-70.522

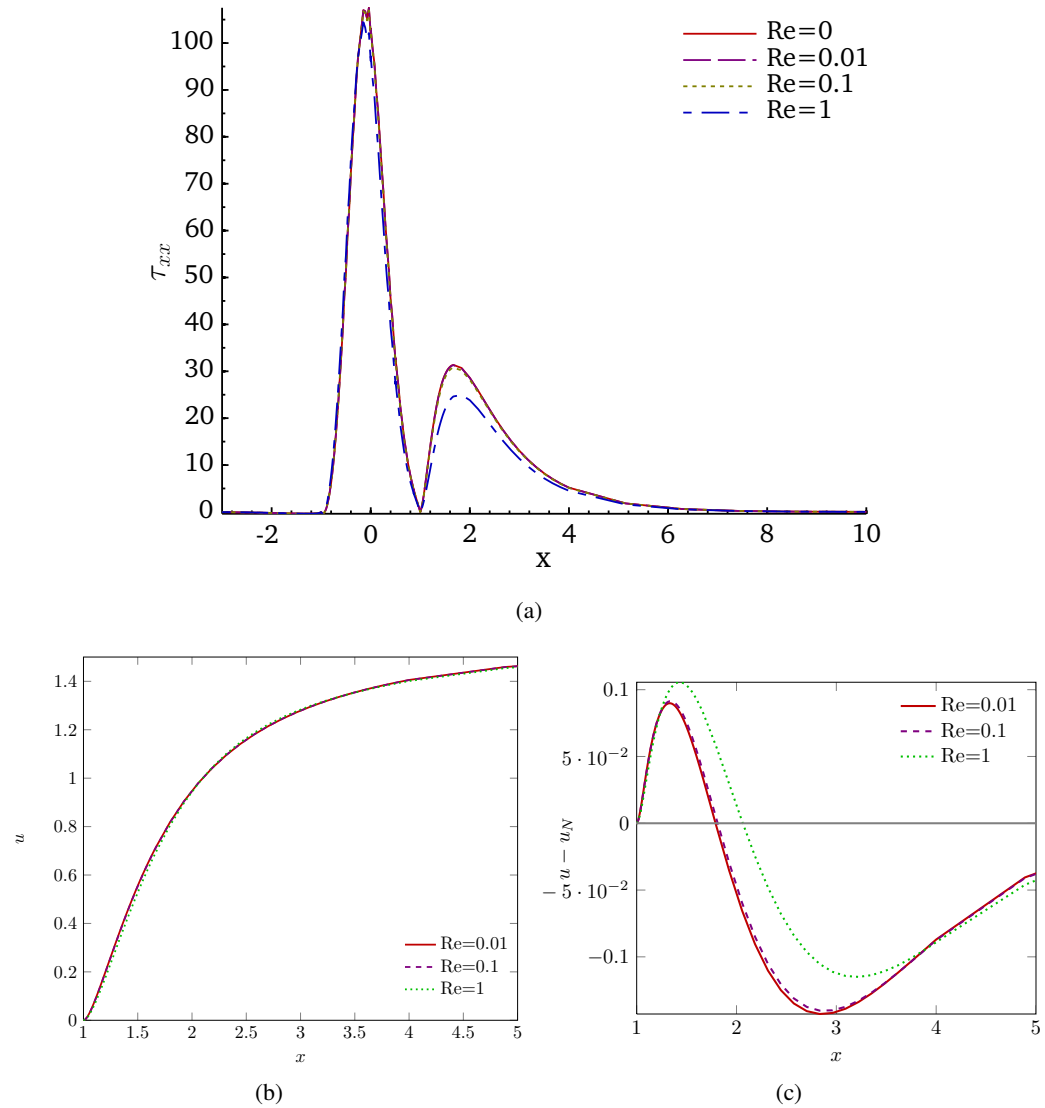
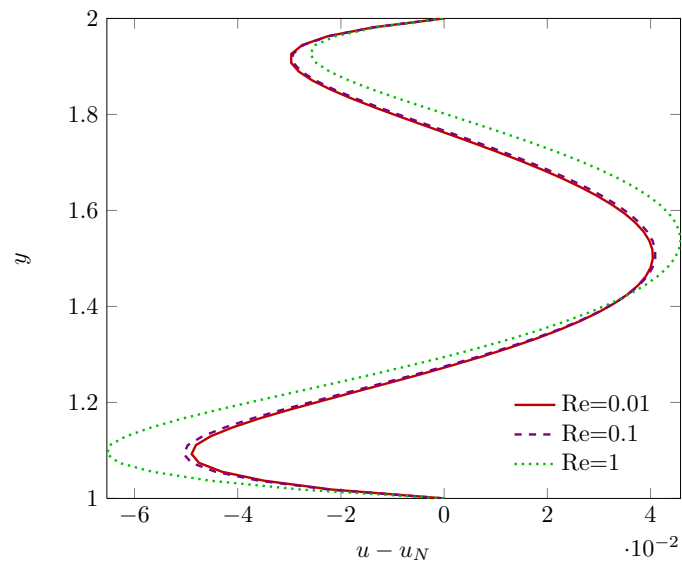
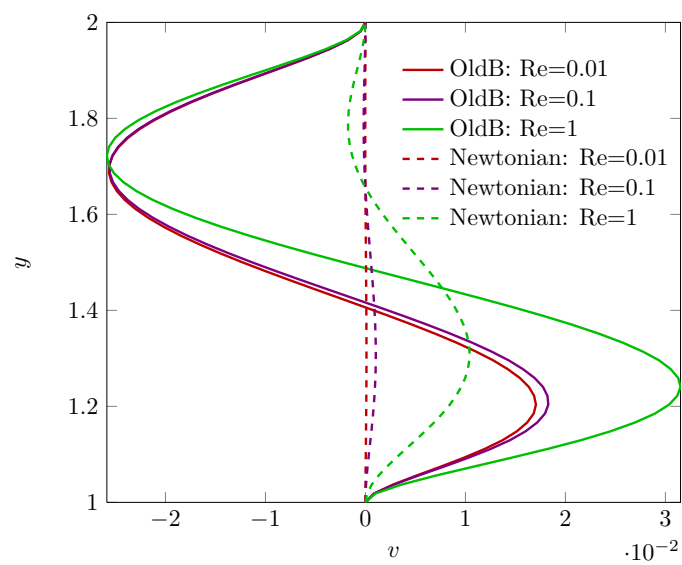


Figure 5.18.: Dependence on Re of the profiles of (a) τ_{xx} along the centreline and cylinder surface, (b) u along the downstream centreline, (c) $u - u_N$ along the downstream centreline for $P = 14$.



(a)



(b)

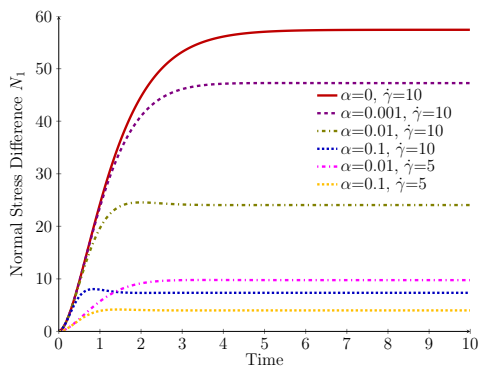
Figure 5.19.: Dependence of (a) $u - u_N$ and (b) v on Re along the shortest path from the top of the cylinder to the channel wall for $Wi = 0.7$.

5.2.4. Giesekus Model

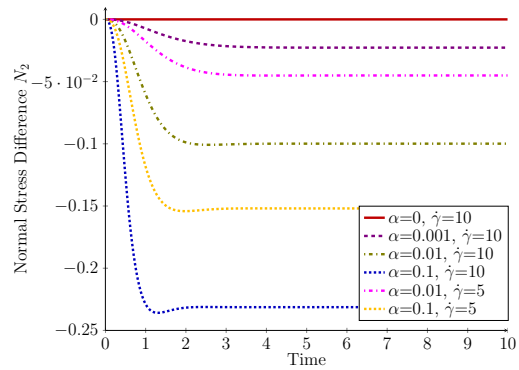
The Giesekus model for the flow around a confined cylinder has been investigated by Liu et al. (1998), Sun et al. (1999) and Hulsen et al. (2005). However, these investigations were mostly concerned with the reduction of the drag coefficient for the Giesekus model and whether the Giesekus model provided improved results in comparison to the Oldroyd-B model concerning elongational flow properties. We investigate the dependence of the flow properties for the Giesekus model for a range of mobility parameters $\alpha = 0.001, 0.01, 0.1$ for $Re = 0$. With increasing α the critical value of Wi , Wi_c , above which the computations fail to converge, increases. For $P = 12$, we obtain $Wi_c = 1.0$ for $\alpha = 0.001$, the same value as for the Oldroyd-B model, $Wi_c = 1.4$ for $\alpha = 0.01$ and $Wi_c = 8.5$ for $\alpha = 0.1$. Figure 5.20 shows the influence of the mobility parameter α on the first and second normal stress difference and the shear and elongational viscosities for $\beta = 0.59$ and $Wi = 0.7$ for two fixed shear rates ($\dot{\gamma} = 10$ and $\dot{\gamma} = 5$), and a fixed elongation rate ($\dot{\epsilon} = 1$) in time-dependent simple shear and uniaxial elongation. Increasing the value of α yields a decrease in the shear and elongational viscosities. Additionally, the transient shear viscosity goes through a maximum in time before attaining a constant value. The magnitude of this overshoot in the transient shear viscosity increases with increasing α . The elongational viscosity for the Oldroyd-B model ($\alpha = 0$) becomes unbounded at finite time when it is subjected to a fixed elongation rate of 1. An elongation rate of this magnitude can be expected to occur in the cylinder benchmark problem.

Drag Coefficient

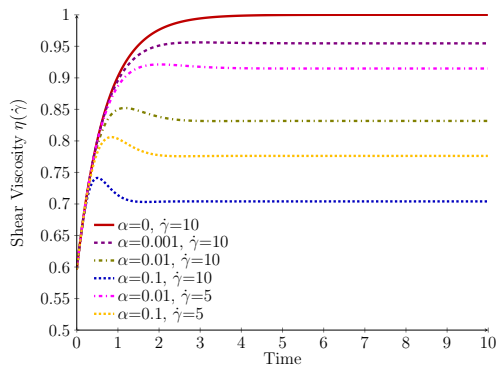
The drag coefficients for the Giesekus model for increasing α are tabulated in Table 5.8 and displayed in Figure 5.21. Figure 5.21 shows that, for a fixed value of Wi , the drag coefficient decreases with increasing α which means that α has a strong drag reduction effect. This drag reduction is due to the shear-thinning properties of the Giesekus model. The drag values for increasing Wi show that a minimum value is attained before they increase again for higher Wi for the Oldroyd-B model ($\alpha = 0$) and for the Giesekus model with $\alpha = 0.001$. This upturn in the drag value for higher Wi is not present for $\alpha = 0.01$ and $\alpha = 0.1$ for this range of Wi .



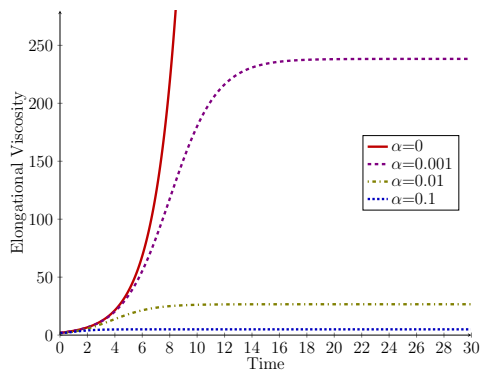
(a) First Normal Stress Difference $N_1 = \sigma_{xx} - \sigma_{yy}$



(b) Second Normal Stress Difference $N_2 = \sigma_{yy} - \sigma_{zz}$



(c) Shear Viscosity



(d) Elongational Viscosity

Figure 5.20.: Dependence of transient viscometric functions on parameter α for a shear rate of $\dot{\gamma} = 10$ and $\dot{\gamma} = 5$ and an elongation rate of $\dot{\epsilon} = 1$ for $\beta = 0.59$ and $Wi = 0.7$.

Table 5.8.: Comparison of drag coefficients for the Giesekus fluid for different values of α .

Wi	$\alpha = 0.001$		$\alpha = 0.01$		$\alpha = 0.1$	
	$P = 14$	$P = 18$	$P = 14$	$P = 18$	$P = 14$	$P = 18$
0.1	130.287	130.291	129.667	129.671	125.585	125.587
0.2	126.392	126.396	124.666	124.670	117.110	117.113
0.3	122.775	122.778	120.082	120.085	111.096	111.098
0.4	119.978	119.981	116.513	116.517	106.853	106.855
0.5	118.002	118.005	113.861	113.867	103.732	103.733
0.6	116.719	116.719	111.895	111.906	101.341	101.341
0.7	115.991	115.982	110.409	110.422	99.449	99.448
0.8	115.687	115.679 (D)	109.247	109.258	97.910	97.909
0.9	115.678	115.664 (D)	108.302	108.307	96.632	96.631
1	115.887 (D)	115.868 (D)	107.508	107.505	95.552	95.552

Plots along Paths

Figure 5.22 shows the profile of the polymeric stress component τ_{xx} along the symmetry line and the cylinder surface for increasing values of α for $Wi = 0.7$. We observe that the maximum values of τ_{xx} on top of the cylinder and in the wake behind the cylinder decrease drastically with increasing α . In fact, the maximum value of all three polymeric stress components decrease with increasing α as displayed in Table 5.9. The maximum values of τ_{xx} decrease by 23.9% for $\alpha = 0.001$, by 66% for $\alpha = 0.01$ and by 90.7% for $\alpha = 0.1$.

To understand the mechanism behind this decrease in the polymeric stress value, we investigate the velocity in the downstream wake of the cylinder and in the gap between the top of the cylinder and the channel wall. Figure 5.23 shows that the horizontal velocity profile for the Giesekus fluid exhibits an overshoot near the rear stagnation point in comparison to the Newtonian velocity profile and an undershoot further downstream before the constant Newtonian velocity value along the centreline is reached. These velocity shifts in the horizontal velocity in the wake of the cylinder are reduced with increasing α . For $\alpha = 0.1$ the undershoot disappears completely and the velocity profile only performs a slight overshoot near the rear stagnation point before it approaches a constant lower than the Newtonian value. This reduced limiting value of u along the centreline is caused by the flattening of the velocity profile due to shear-thinning.

This onset of the dominance of shear thinning effects for $\alpha = 0.1$ can also be observed in Figure 5.24 and Figure 5.25 in the gap between the top of the cylinder and the channel wall. The values of the horizontal velocity component in the middle of the gap decrease with increasing α until the viscoelastic velocity overshoot of the parabolic profile disap-

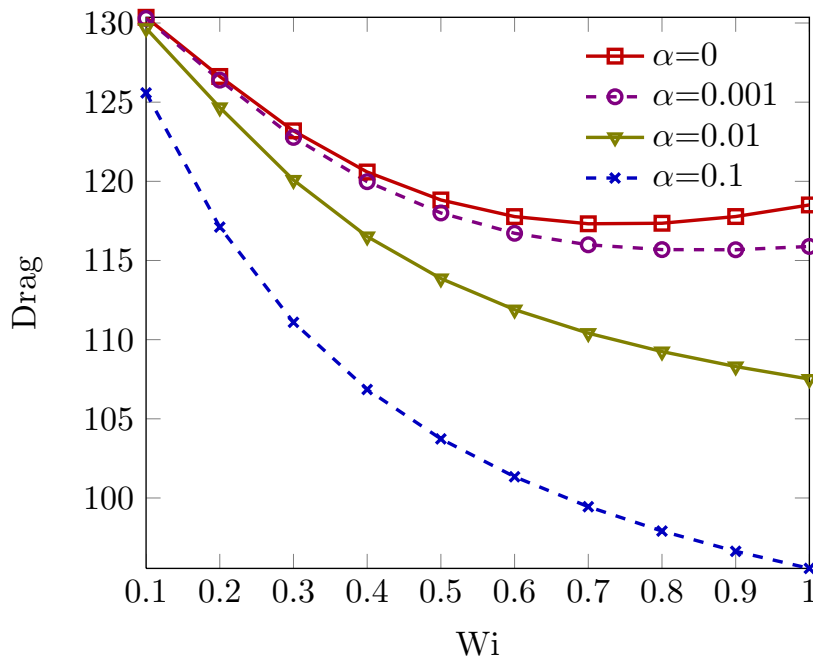


Figure 5.21.: Dependence of the drag coefficient on Wi and α for Giesekus fluid for $P = 14$.

pears and the horizontal velocity profile flattens for $\alpha = 0.1$. This flattening of the velocity profile can be observed more clearly, in Figure 5.25, which illustrates the behaviour of the velocity components with respect to the Newtonian velocity. With increasing α , the decrease in the horizontal velocity near the cylinder surface due to the elasticity of the fluid lessens with increasing α and for $\alpha = 0.1$ the horizontal velocity near the cylinder even increases. Similarly, the increase of the vertical velocity component near the cylinder wall due to elasticity lessens with increasing α until the vertical velocity profile decreases for $\alpha = 0.1$. This reduction in the magnitude of the overshoots and undershoots for the velocity components delays the onset of the formation of a velocity inflection on top of the cylinder and therefore the onset of viscoelastic instabilities. Furthermore, it reduces the magnitude of the velocity gradients and therefore the magnitude of the polymeric stress components. To confirm that the onset of a viscoelastic instability will be delayed with increasing α , we consider the Dou and Phan-Thien (2008) criterion, that the ratio between the streamwise component and the cross streamwise component of the pressure derivative gives us a critical value for the onset of an instability. The pressure profile plotted in Figure 5.26 shows that the pressure derivative in the cross-stream direction decreases significantly with increasing α , which means that increasing α leads to stable flow fields for wider ranges of elasticity.

To illustrate the influence of the value of α on the convergence properties of the scheme,

the axial component of the polymeric stress τ_{xx} is plotted along the axis of symmetry and around the cylinder for $Wi = 0.7$ in Figure 5.27. The convergence behaviour in the wake improves as α increases. When $\alpha = 0.1$ converged results are obtained with $P = 12$. As α tends to zero, we recover the convergence properties associated with the Oldroyd-B model.

Table 5.9.: Minimum and maximum values of the polymeric stress components for the Giesekus model for $P = 18$, $Wi = 0.7$.

α	Max(τ_{xx})	Min(τ_{xx})	Max(τ_{xy})	Min(τ_{xy})	Max(τ_{yy})	Min(τ_{yy})
0	107.276	-0.367	37.011	-20.772	24.646	-0.489
0.001	81.675	-0.367	28.193	-17.455	20.508	-0.375
0.01	36.462	-0.368	13.033	-10.430	11.197	-0.374
0.1	9.982	-0.377	4.039	-3.364	3.889	-0.427

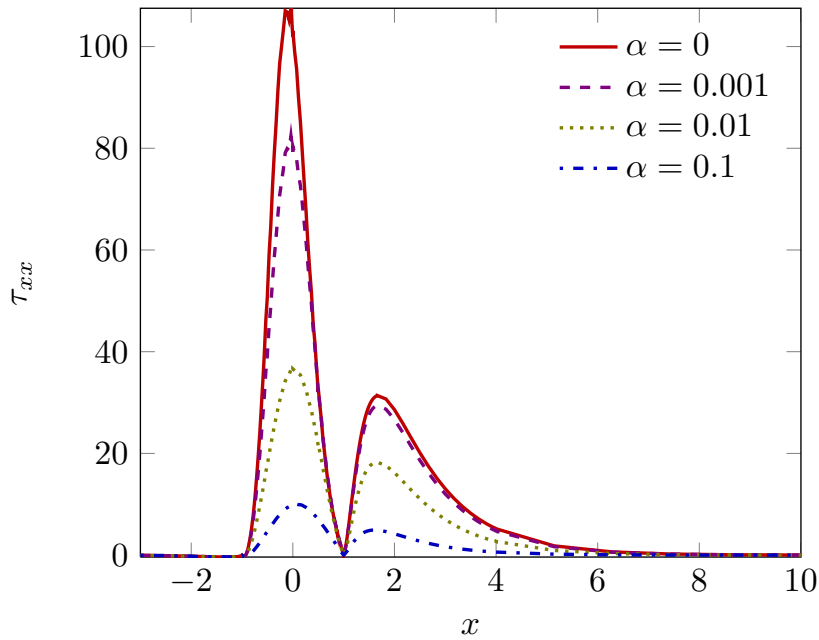


Figure 5.22.: Profile of τ_{xx} along symmetry line and cylinder surface for $Wi = 0.7$, $P = 14$ and increasing α .

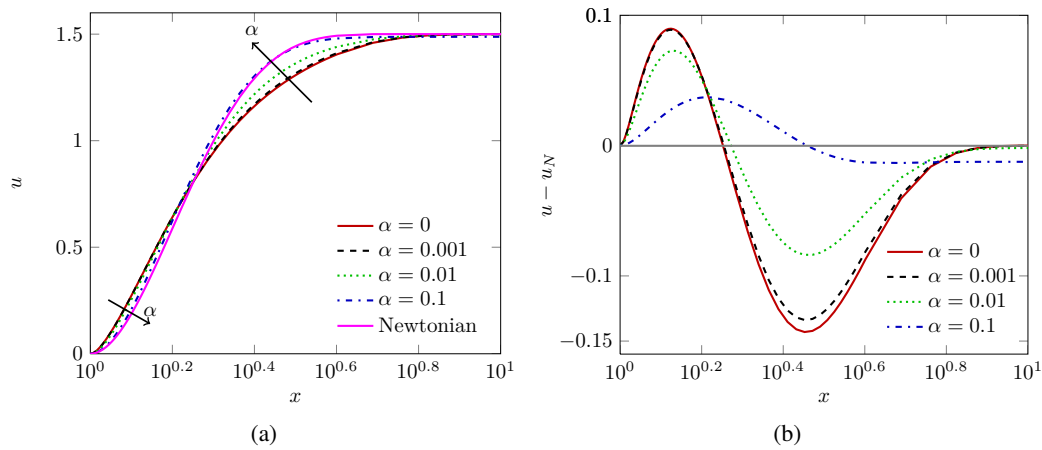


Figure 5.23.: Dependence of (a) u and (b) $u - u_N$ (the velocity shift with respect to the Newtonian velocity profile), on Wi along the downstream centreline.

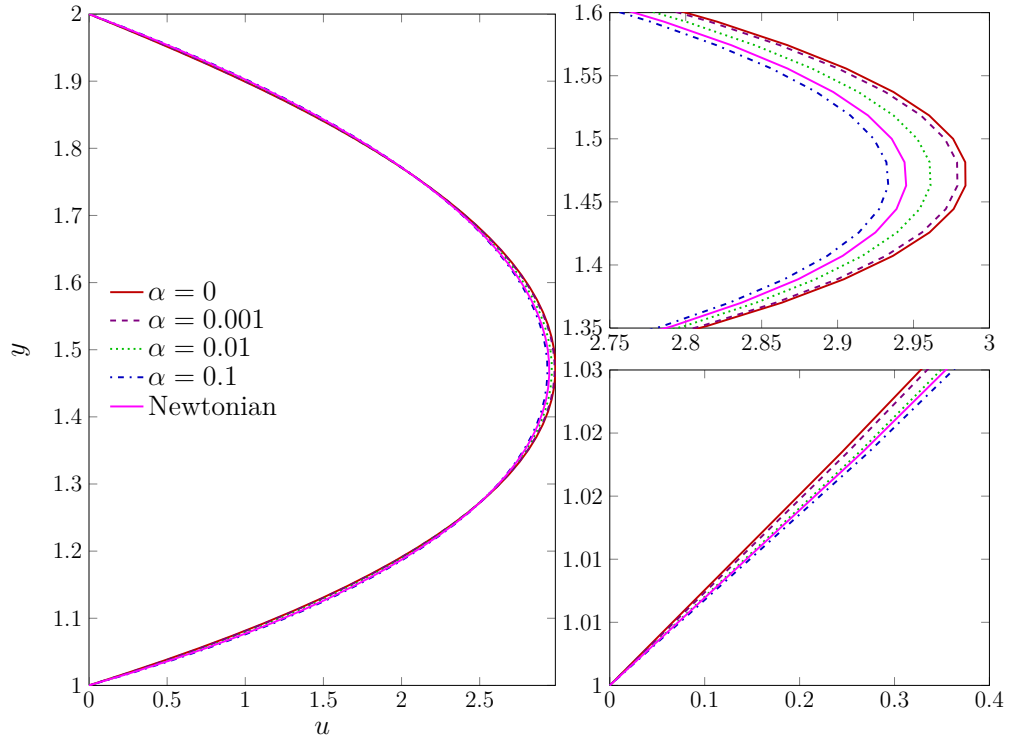


Figure 5.24.: Dependence of u on top of the cylinder on α for $Wi = 0.7$.

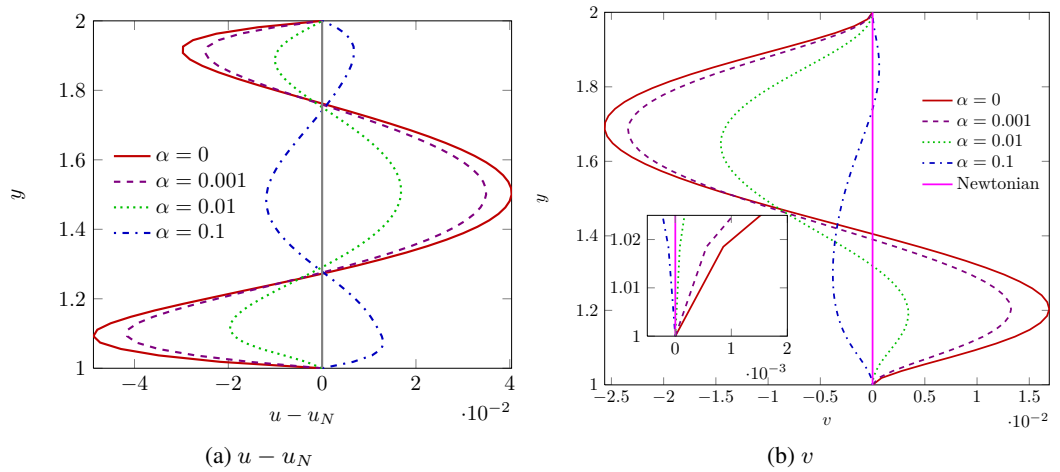


Figure 5.25.: Dependence of (a) $u - u_N$ and (b) v on α along the shortest path from the top of the cylinder to the channel wall for $Wi = 0.7$.

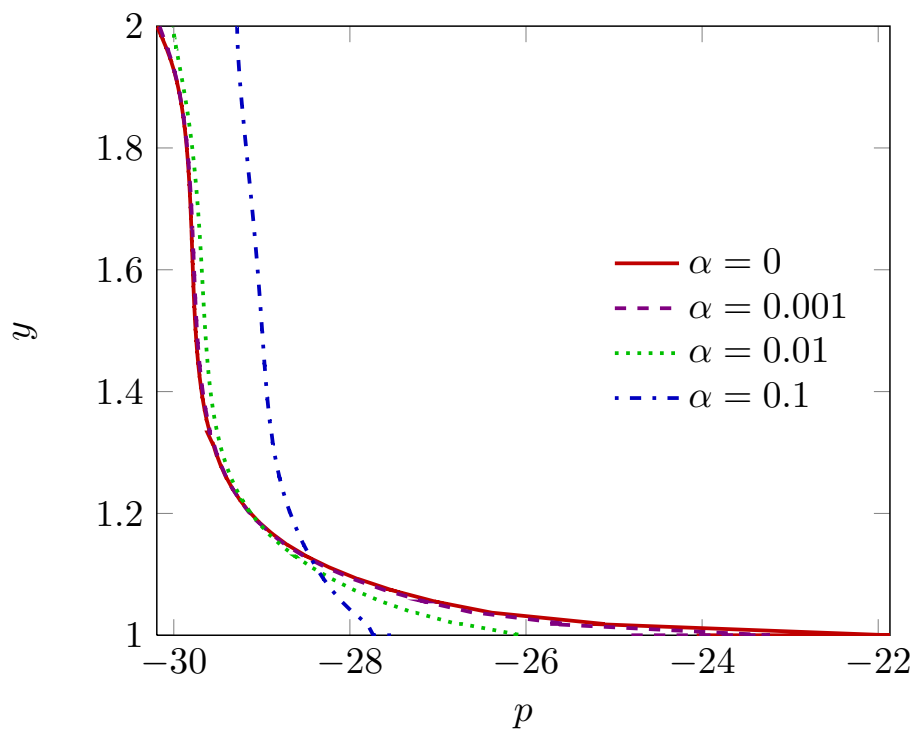


Figure 5.26.: Dependence of the pressure profile on top of the cylinder on α for $Wi = 0.7$. The pressure derivative in cross stream direction decreases with increasing α . This means for higher α , the flow field is more stable.

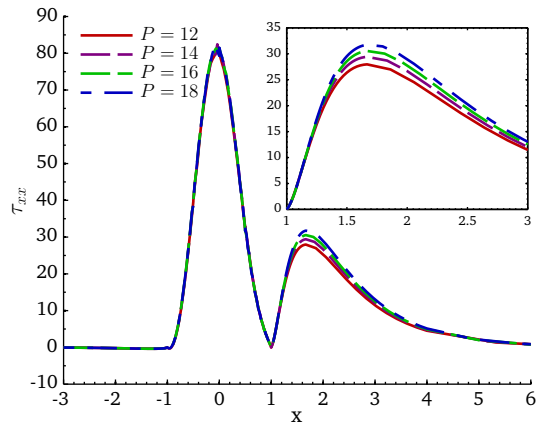
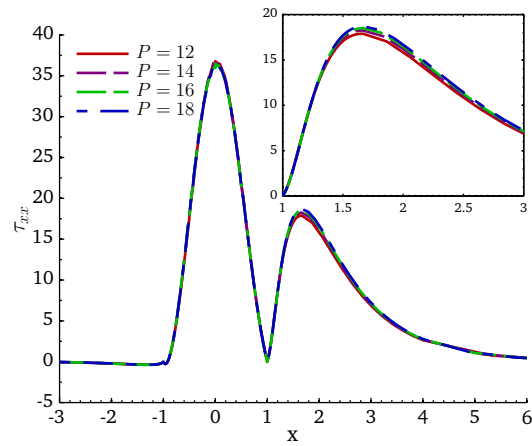
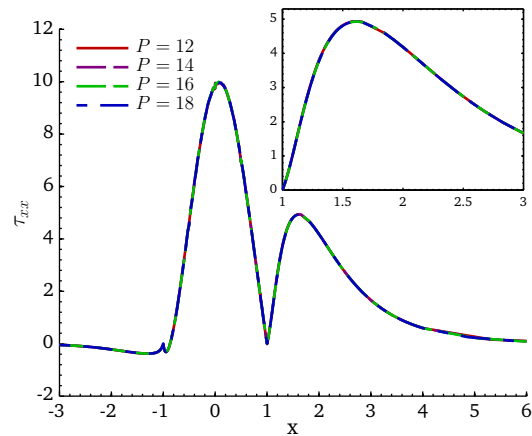
(a) $\alpha = 0.001$ (b) $\alpha = 0.01$ (c) $\alpha = 0.1$

Figure 5.27.: Dependence of the profiles of τ_{xx} along the centreline and around the cylinder on P for $Wi = 0.7$ for (a) $\alpha = 0.001$, (b) $\alpha = 0.01$ and (c) $\alpha = 0.1$.

Contour Plots

Figure 5.28 displays the contour plots of the pressure p and the horizontal velocity component for increasing α . With increasing α the high pressure concentrations in the regions close to the stagnation points are dissipated. The pressure derivatives close to the cylinder surface are reduced with increasing α . Additionally, we observe a smaller pressure concentration near the stagnation points with increasing α . The horizontal velocity shifts upstream with increasing α in the downstream region of the cylinder and the maximum value decreases with increasing α . This is due to the flattening of the velocity profile with increasing α . Figure 5.29 shows that the magnitude of the axial polymeric stress component τ_{xx} and the flow dependent normal stress S_2 decrease significantly in the boundary layers around the cylinder and the channel walls and in the downstream wake of the cylinder with increasing α . The magnitude of S_2 decreases by 24.6% for $\alpha = 0.001$, by 66.9% for $\alpha = 0.01$ and by 90.8% for $\alpha = 0.1$, which is very similar to the decrease in τ_{xx} . The magnitude of the low normal stress region of S_2 near the front stagnation point decreases with increasing α . The decrease in the flow dependent shear stress S_1 (see Figure 5.30) is more gentle with increasing α than the decrease in the flow dependent normal stress S_2 . The magnitude of S_1 decreases by 5.1% for $\alpha = 0.001$, by 16% for $\alpha = 0.01$ and by 25.9% for $\alpha = 0.1$ with respect to the shear stress of the Oldroyd-B fluid ($\alpha = 0$). To interpret the results, for the flow dependent stress decomposition for the Giesekus model, we turn to the predictions of the viscometric functions in simple shear and uniaxial elongation as plotted in Figure 5.20. For increasing α , the first normal stress difference N_1 , the shear viscosity $\eta(\dot{\gamma})$ and the elongational viscosity decrease with increasing α . Figure 5.20 shows the viscometric shear functions for a shear rate of $\dot{\gamma} = 10$, which is the order of magnitude of the shear rate on top of the cylinder in the benchmark problem and for an elongation rate of $\dot{\epsilon} = 1$, which is the order of magnitude of the elongation rate in the wake behind the cylinder. Examining the values of the first normal stress difference N_1 for $Wi = 0.7$ shows that N_1 decreases by 17.7% for $\alpha = 0.001$, by 58.1% for $\alpha = 0.01$ and by 87.2% for $\alpha = 0.1$. In addition, the elongational viscosity decreases sharply with increasing α . The combination of the significant decreases in the first normal stress difference and the elongational viscosity lead to the sharp decrease in the flow dependent normal stress S_2 and τ_{xx} and therefore also in the principal stress T . The shear viscosity for the simple shear flow with $\dot{\gamma} = 10$ decreases by 4.5% for $\alpha = 0.001$, by 16.8% for $\alpha = 0.01$ and by 29.6% for $\alpha = 0.1$ with respect to the Oldroyd-B fluid. This decrease is of the same order of magnitude as the decrease of the flow dependent shear stress S_1 . Therefore, we deduce the flow dependent shear stress is reduced due to the shear thinning of the shear viscosity of the fluid. In contrast to the Oldroyd-B fluid, the contribution of S_1 to T increases with increasing α until the flow dependent shear stress dominates the

principal stress for $\alpha = 0.1$. Therefore, the impact of S_1 on the flow patterns in comparison to S_2 increases with increasing α . This gives rise to the manifestation of typical shear thinning phenomena such as the flattening of the parabolic velocity profile, which was observed in the simulations presented in the previous Subsection.

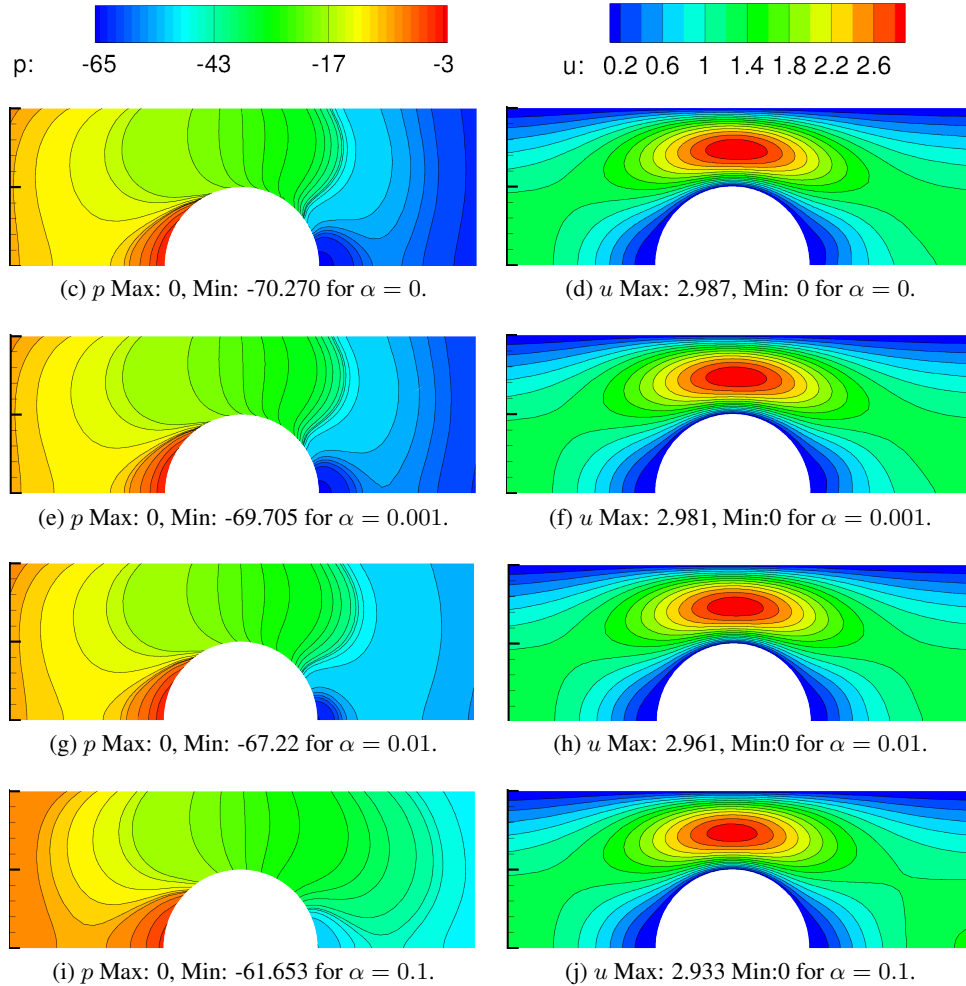


Figure 5.28.: Contour plots for Giesekus fluid for different values of α : pressure p (left) and horizontal velocity component u (right) for $Wi = 0.7$ and $P = 18$.

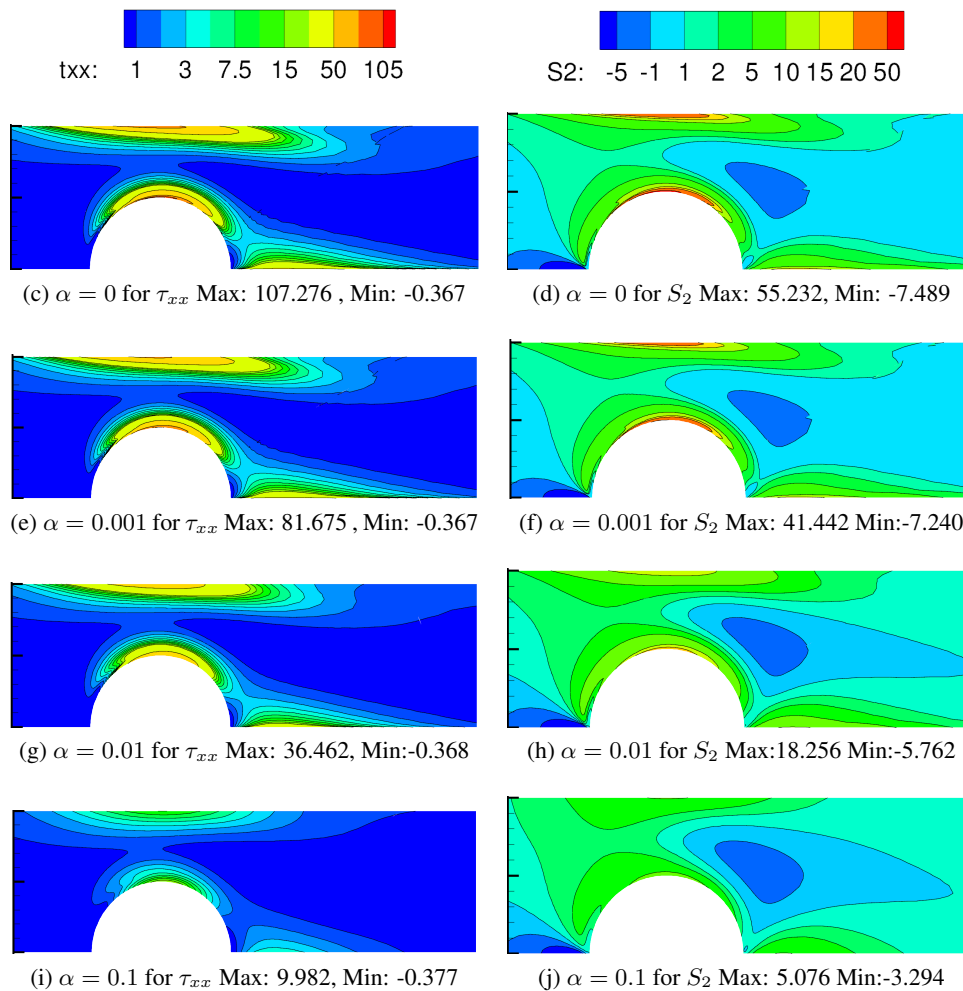


Figure 5.29.: Contour plots for Giesekus fluid for different values of α : polymeric stress component τ_{xx} (left) and flow dependent normal stress S_2 (right) for $Wi = 0.7, P = 18$.

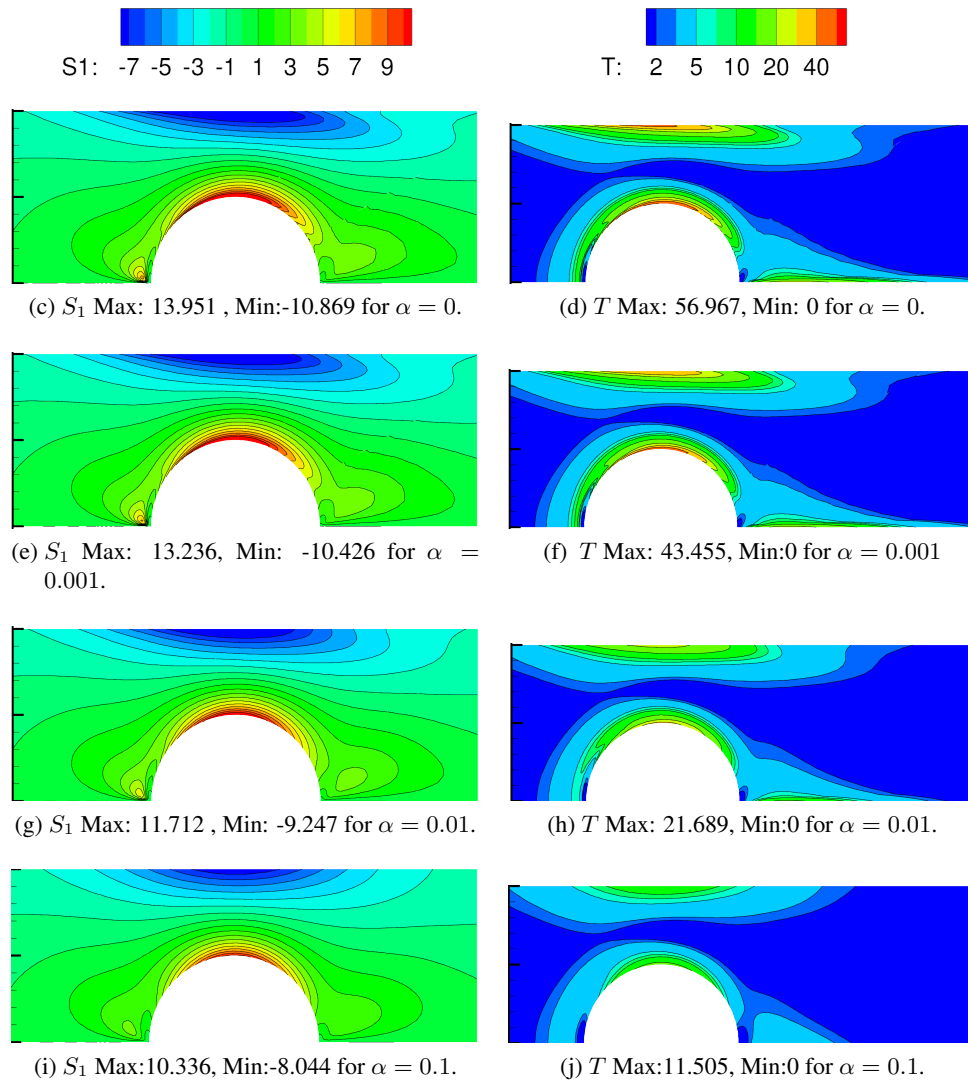


Figure 5.30.: Contour plots for Giesekus fluid for different values of α : flow dependent shear stress S_1 (left) and flow dependent principal stress T (right) for $Wi = 0.7$, $P = 18$.

Chapter 6

DEVSS/DG Algorithm for Viscoelastic Free Surface Flows

In this Chapter, we first introduce the DEVSS-G/DG formulation in the ALE framework. Then, we discuss the details of the algorithm used to move the mesh in order to trace the free surface boundary movement. We employ a cubic spline representation of the free surface boundary in order to guarantee the smoothness of the free surface to obtain continuous normals and curvature across several spectral elements. Then, we discuss the algorithm used to solve the discrete coupled system of velocity, pressure and velocity gradient projection tensor and the discretised constitutive equation.

6.1. Weak DEVSS/DG Formulation in the ALE framework

In this Section, we describe the DEVSS-G/DG algorithm that we employed to simulate viscoelastic free surface flows. We use mesh particles to trace the deformation of the domain employing the arbitrary Lagrangian Eulerian (ALE) introduced in Section 2.1.2. Here, we trace the deformation of the free surface by moving the grid points at the free surface with the normal fluid velocity, thus ensuring that particles do not cross the interface. In the interior of the domain, we move the mesh points in an arbitrary fashion to avoid mesh distortion. The movement of the mesh introduces a referential frame or ALE-frame which is connected to the Eulerian and Lagrangian frames as described in Section 2.1. Here, we provide a summary of some of the key definitions, that we introduced in Section 2.1.2, for the ALE-frame:

1. the ALE-map

$$\begin{aligned}\mathcal{R}_t : \hat{\Omega}_{t_0} &\rightarrow \Omega_t, \quad \forall t \geq 0, \\ \mathbf{Y} &\mapsto \mathbf{x}(\mathbf{Y}, t) = \mathcal{R}_t(\mathbf{Y}), \quad \forall \mathbf{Y} \in \hat{\Omega}_{t_0}.\end{aligned}\tag{6.1}$$

which is the parametrized family of diffeomorphisms relating the reference con-

figuration, $\hat{\Omega}_{t_0}$, to the Eulerian configuration Ω_t . Here, \mathbf{x} are the coordinates in the Eulerian frame and the coordinates \mathbf{Y} are associated with the positions of the nodes.

2. the mesh velocity

$$\mathbf{w}(\mathbf{x}, t) := \left. \frac{\partial \mathbf{x}(\mathbf{Y}, t)}{\partial t} \right|_{\mathbf{Y}} = \left. \frac{\partial \mathcal{R}_t(\mathbf{Y})}{\partial t} \right|_{\mathbf{Y}}. \quad (6.2)$$

3. the material time derivative in terms of time derivative with respect to the ALE-frame

$$\frac{Df(\mathbf{x}, t)}{Dt} = \left. \frac{\partial f}{\partial t} \right|_{\mathbf{Y}} + (\mathbf{u} - \mathbf{w}) \cdot \nabla_{\mathbf{x}} f \quad (6.3)$$

In Section 2.2, we presented the conservation laws in fixed and moving domains. In this Section, we base our definitions of the solution spaces in the weak formulation on the thesis of Nobile (2001) and Pena (2009).

The governing equations of free surface incompressible viscoelastic flows for moving domains in dimensionless form over the time interval $I = [t_0, t_{fin}]$ is given by

$$\begin{aligned} \text{Re} \left(\left. \frac{\partial \mathbf{u}}{\partial t} \right|_{\mathbf{Y}} + (\mathbf{u} - \mathbf{w}) \cdot \nabla_{\mathbf{x}} \mathbf{u} \right) &= -\nabla_{\mathbf{x}} p + 2\beta \nabla_{\mathbf{x}} \cdot \mathbf{D}_{\mathbf{x}} + \nabla_{\mathbf{x}} \cdot \boldsymbol{\tau}, \\ \nabla_{\mathbf{x}} \cdot \mathbf{u} &= 0, \end{aligned} \quad (6.4)$$

$$\boldsymbol{\tau} + \text{Wi} \left(\left. \frac{\partial \boldsymbol{\tau}}{\partial t} \right|_{\mathbf{Y}} + (\mathbf{u} - \mathbf{w}) \cdot \nabla_{\mathbf{x}} \boldsymbol{\tau} - \nabla_{\mathbf{x}} \mathbf{u} \cdot \boldsymbol{\tau} - \boldsymbol{\tau} \cdot \nabla_{\mathbf{x}} \mathbf{u}^T \right) + \frac{\alpha \text{Wi}}{(1 - \beta)} \boldsymbol{\tau}^2 = 2(1 - \beta) \mathbf{D}_{\mathbf{x}}, \quad (6.5)$$

subject to appropriate boundary and initial conditions. Here, $\mathbf{D}_{\mathbf{x}} = 1/2(\nabla_{\mathbf{x}} \mathbf{u} + \nabla_{\mathbf{x}} \mathbf{u}^T)$ is the rate of deformation tensor in the Eulerian frame of reference.

To derive the weak formulation of the equations including the DEVSS-G stabilisation, we first define the trial and test functions spaces on the reference configuration $\hat{\Omega}_{t_0}$, which are the same as the ones we chose for the equations in fixed meshes

$$\begin{aligned} \hat{\mathcal{V}}(\hat{\Omega}_{t_0}) &= [H_0^1(\hat{\Omega}_{t_0})]^d, \quad \hat{\mathcal{V}}_D(\hat{\Omega}_{t_0}) = [H_D^1(\hat{\Omega}_{t_0})]^d \\ \hat{\mathcal{Q}}(\hat{\Omega}_{t_0}) &= L^2(\hat{\Omega}_{t_0}), \quad \hat{\mathcal{Q}}_0(\hat{\Omega}_{t_0}) = L_0^2(\hat{\Omega}_{t_0}) \\ \Sigma(\hat{\Omega}_{t_0}) &= [L^2(\hat{\Omega}_{t_0})]_s^{d^2}, \quad \Sigma_G(\hat{\Omega}_{t_0}) = [L^2(\hat{\Omega}_{t_0})]^{d^2} \end{aligned} \quad (6.6)$$

Using the ALE-map \mathcal{R}_t , we extend these trial and test function spaces over the referential domain to the spaces defined over the Eulerian domain Ω_t

$$\mathcal{V}_D(\Omega_t) = \left\{ \mathbf{u} : \Omega_t \times I \rightarrow \mathbb{R}^d : \mathbf{u} = \hat{\mathbf{u}} \circ \mathcal{R}_t^{-1}, \hat{\mathbf{u}} \in \hat{\mathcal{V}}(\hat{\Omega}_{t_0}) \right\}, \quad (6.7)$$

$$\mathcal{Q}(\Omega_t) = \left\{ q : \Omega_t \times I \rightarrow \mathbb{R}^d : q = \hat{q} \circ \mathcal{R}_t^{-1}, \hat{q} \in \hat{\mathcal{Q}}(\hat{\Omega}_{t_0}) \right\}, \quad (6.8)$$

$$\Sigma(\Omega_t) = \left\{ \boldsymbol{\tau} : \Omega_t \times I \rightarrow \mathbb{R}^{d \times d} : \boldsymbol{\tau} = \hat{\boldsymbol{\tau}} \circ \mathcal{R}_t^{-1}, \hat{\boldsymbol{\tau}} \in \Sigma(\hat{\Omega}_{t_0}) \right\}, \quad (6.9)$$

$$\Sigma_G(\Omega_t) = \left\{ \mathbf{G} : \Omega_t \times I \rightarrow \mathbb{R}^{d \times d} : \mathbf{G} = \hat{\mathbf{G}} \circ \mathcal{R}_t^{-1}, \hat{\mathbf{G}} \in \Sigma_G(\hat{\Omega}_{t_0}) \right\}. \quad (6.10)$$

Similar definitions hold for $\hat{\mathcal{V}}(\Omega_t)$ and $\hat{\mathcal{Q}}_0(\Omega_t)$. For these spaces to be admissible for the weak formulation of the system of equations (6.4)-(6.5), we need to ensure that $\mathcal{V}(\Omega_t) \subseteq [H_D^1(\Omega_t)]^d$, $\mathcal{Q}(\Omega_t) \subseteq L^2(\Omega_t)$ and $\Sigma(\Omega_t) \subseteq [L^2(\Omega_t)]_s^{d^2}$. Nobile (2001) showed that $\mathcal{V}(\Omega_t) \subseteq [H_D^1(\Omega)]^d$ and $\mathcal{Q}(\Omega_t) \subseteq L^2(\Omega_t)$ if $\hat{\Omega}_{t_0}$ and $\Omega_t = \mathcal{R}_t(\hat{\Omega}_{t_0})$ are bounded domains with Lipschitz continuous boundaries and

$$\mathcal{R}_t \in W^{1,\infty}(\hat{\Omega}_{t_0}), \quad \mathcal{R}_t^{-1} \in W^{1,\infty}(\Omega_t), \quad (6.11)$$

which means that we have restrictions on the regularity of the ALE-map \mathcal{R}^t . Moreover, Nobile (2001) demonstrated that $\|\mathbf{u}\|_{[H^1(\Omega_t)]^d}$ is equivalent to $\|\hat{\mathbf{u}}\|_{[H^1(\hat{\Omega}_{t_0})]^d}$ for all $\mathbf{u} \in [H^1(\Omega_t)]^d$ under these conditions.

In order to stabilise our computation, we employ the DEVSS-G method specified in Problem 4.2. However, in contrast to the fixed domain DEVSS/DG algorithm introduced in Section 4.4, we can no longer simplify the equations by noting that $\nabla \cdot \nabla \mathbf{u}^T = 0$ due to the incompressibility of the fluid. We require this term in computations involving a free surface to obtain the right force balance of the Cauchy stress at the free surface of $\boldsymbol{\sigma} \cdot \mathbf{n} = \sigma \kappa \mathbf{n}$ after the integration by parts.

The weak formulation of the system of equations (6.4)-(6.5) including the DEVSS-G/DG stabilisation with $\theta = (1 - \beta)$ in the ALE framework reads

Problem 6.1 (Weak DEVSS-G/DG Formulation in the ALE framework). *For almost every $t \in I$ find $t \rightarrow (\mathbf{u}(t), p(t), \mathbf{G}(t), \boldsymbol{\tau}(t)) \in \mathcal{V}(\Omega_t) \times \mathcal{Q}(\Omega_t) \times \Sigma_G(\Omega_t) \times \Sigma(\Omega_t)$ such that, for all $(\phi_{\mathbf{u}}, \psi, \phi_{\mathbf{G}}, \phi_{\boldsymbol{\tau}}) \in \mathcal{V}(\Omega_t) \times \mathcal{Q}(\Omega_t) \times \Sigma_G(\Omega_t) \times \Sigma(\Omega_t)$*

$$\begin{aligned} & Re \left(\frac{\partial \mathbf{u}}{\partial t} \Big|_{\mathbf{Y}} + ((\mathbf{u} - \mathbf{w}) \cdot \nabla_{\mathbf{x}}) \mathbf{u}, \phi_{\mathbf{u}} \right)_{\Omega_t} + (2\mathbf{D}_{\mathbf{x}}, \nabla_{\mathbf{x}} \phi_{\mathbf{u}})_{\Omega_t} - (p, \nabla_{\mathbf{x}} \cdot \phi_{\mathbf{u}})_{\Omega_t} \\ & + (\boldsymbol{\tau}, \nabla_{\mathbf{x}} \phi_{\mathbf{u}})_{\Omega_t} - (1 - \beta) \left(\mathbf{G} + \mathbf{G}^T, \nabla_{\mathbf{x}} \phi_{\mathbf{u}} \right)_{\Omega_t} \end{aligned} \quad (6.12)$$

$$\begin{aligned} & - \langle \boldsymbol{\sigma} \cdot \mathbf{n}, \phi_{\mathbf{u}} \rangle_{\Gamma_N(t)} - \langle \sigma \kappa \cdot \mathbf{n}, \phi_{\mathbf{u}} \rangle_{\Gamma_f(t)} = 0, \\ & (\nabla_{\mathbf{x}} \cdot \mathbf{u}, \psi)_{\Omega_t} = 0, \end{aligned} \quad (6.13)$$

$$(\mathbf{G} - \nabla_{\mathbf{x}} \mathbf{u}, \phi_{\mathbf{G}})_{\Omega_t^e} = 0, \quad (6.14)$$

$$\begin{aligned} & Wi \left(\frac{\partial \boldsymbol{\tau}}{\partial t} \Big|_{\mathbf{Y}}, \phi_{\boldsymbol{\tau}} \right)_{\Omega_t^e} - Wi (\boldsymbol{\tau}, ((\mathbf{u} - \mathbf{w}) \cdot \nabla_{\mathbf{x}}) \phi_{\boldsymbol{\tau}})_{\Omega_t^e} \\ & + Wi \left\langle [(\mathbf{u} - \mathbf{w}) \cdot \mathbf{n}] \tilde{f}(\boldsymbol{\tau}^{ext}, \boldsymbol{\tau}^{int}), \phi_{\boldsymbol{\tau}} \right\rangle_{\partial \Omega_t^e} \\ & - Wi \left(\mathbf{G} \cdot \boldsymbol{\tau} + \boldsymbol{\tau} \cdot \mathbf{G}^T, \phi_{\boldsymbol{\tau}} \right)_{\Omega_t^e} + (\boldsymbol{\tau}, \phi_{\boldsymbol{\tau}})_{\Omega_t^e} + \frac{\alpha Wi}{(1 - \beta)} (\boldsymbol{\tau}^2, \phi_{\boldsymbol{\tau}})_{\Omega_t^e} \\ & = (1 - \beta) \left(\mathbf{G} + \mathbf{G}^T, \phi_{\boldsymbol{\tau}} \right)_{\Omega_t^e}, \end{aligned} \quad (6.15)$$

where $\Gamma_N(t)$ is the Neumann boundary and $\Gamma_f(t)$ is the free surface boundary.

Note that, Problem 6.1 is in the so-called *non-conservative* form due to the fact that the ALE time derivative is under the integral over Ω_t . The conservative form of the Navier-Stokes equations in the ALE framework can be found, for example, in Nobile (2001). In Equation (6.15), the numerical flux is defined as

$$\tilde{f}(\boldsymbol{\tau}^{ext}, \boldsymbol{\tau}^{int}) = \begin{cases} \gamma \boldsymbol{\tau}^{ext} + (1 - \gamma) \boldsymbol{\tau}^{int}, & (\mathbf{u} - \mathbf{w}) \cdot \mathbf{n} < 0, \\ \gamma \boldsymbol{\tau}^{int} + (1 - \gamma) \boldsymbol{\tau}^{ext}, & (\mathbf{u} - \mathbf{w}) \cdot \mathbf{n} \geq 0, \\ \boldsymbol{\tau}_D & \text{at inflow,} \\ \boldsymbol{\tau}^{int} & \text{at outflow.} \end{cases} \quad (6.16)$$

The discrete spaces are defined in analogy to Section 4.2 as

$$\begin{aligned} \mathcal{V}^\delta(\Omega_t) &= \mathcal{V}(\Omega_t) \cap [\mathcal{P}_P^c(\Omega_t)]^2, \\ \mathcal{Q}^\delta(\Omega_t) &= \mathcal{Q}(\Omega_t) \cap \mathcal{P}_{P-2}(\Omega_t), \\ \Sigma^\delta(\Omega_t) &= \Sigma(\Omega_t) \cap [\mathcal{P}_P(\Omega_t)]^{d^2}, \\ \Sigma_G^\delta(\Omega_t) &= \Sigma_G(\Omega_t) \cap [\mathcal{P}_P(\Omega_t)]^{d^2}. \end{aligned} \quad (6.17)$$

6.2. Domain Movement

We employ the ALE-scheme in order to trace the movement of the free surface boundary. In general, the domain movement is characterised by the movement of its boundary $\partial\Omega_t$ and can be described using the domain or mesh velocity \mathbf{w} (Ho and Rønquist (1994), Robertson et al. (2004)), the ALE-mapping $\mathcal{R}(t)$ (Nobile (2001), Pena (2009)) or the displacement $\mathbf{d} = \Delta t \mathbf{w}$ (Choi and Hulsen (2011)).

In this thesis, we describe the movement of the domain in terms of the mesh velocity \mathbf{w} . We wish to use the domain deformation to trace the movement of the free surface. The movement of the free surface boundary is characterised by the kinematic boundary condition, which ensures that no particle crosses the interface, that is,

$$\mathbf{u} \cdot \mathbf{n} = \mathbf{w}_f \cdot \mathbf{n} \quad \text{on } \Gamma_f \quad (\text{kinematic boundary condition}) \quad (6.18)$$

where \mathbf{w}_f is the velocity of the free surface. In our implementation, we can satisfy this boundary condition and use it to trace the free surface profile by moving the mesh nodes at the free surface with the normal fluid velocity, that is,

$$\mathbf{w} \cdot \mathbf{n} = \mathbf{u} \cdot \mathbf{n} \quad \text{on } \Gamma_f. \quad (6.19)$$

The remaining boundary conditions and the movement of the mesh in the interior of the domain are chosen in order to prevent strong deformations of the elements Ω_e . In general, we choose the following set of boundary conditions for the mesh velocity

$$\begin{cases} \mathbf{w} \cdot \mathbf{n} = \mathbf{u} \cdot \mathbf{n}, \\ \mathbf{w} \cdot \mathbf{s} = 0 \end{cases} \quad \text{at } \Gamma_f, \\ \nabla \mathbf{w} \cdot \mathbf{n} = \mathbf{0} \quad \text{at outflow,} \\ \mathbf{w} = \mathbf{0} \quad \text{elsewhere,} \end{cases} \quad (6.20)$$

where \mathbf{s} is the unit tangent vector on the free surface boundary. In order to guarantee smooth mesh movement in the interior, we solve an elliptic problem for the mesh velocity, given by

$$\Delta \mathbf{w} = 0, \quad (6.21)$$

subject to the boundary conditions (6.20). This approach delivers good results when considering mesh movements with small displacements and has been employed, for instance, by Ho and Rønquist (1994), Nobile (2001) and Pena (2009). However, for larger mesh deformations, other elliptic problems may be solved for the movement of the domain, such as elliptic operators arising from Stokes or elasticity problems (see the monograph

of Deville et al. (2002) for further details).

We choose the same trial and test function space for the mesh velocity as for the fluid velocity, i.e. we choose

$$\mathcal{W} \equiv \mathcal{V} \quad (6.22)$$

and we solve Equation (6.21) with the boundary conditions (6.20) using a continuous Galerkin method. That means the weak formulation reads

Problem 6.2 (Weak Formulation Mesh Velocity). *For almost every $t \in I$ find $t \rightarrow \mathbf{w}(t) \in \mathcal{V}_D(\Omega_t)$ such that, for all $\phi_{\mathbf{w}} \in \mathcal{V}(\Omega_t)$*

$$(\nabla \mathbf{w}, \nabla \phi_{\mathbf{w}})_{\Omega_e} = 0, \quad (6.23)$$

subject to the boundary conditions (6.20). Note that, we suppose that $\nabla \mathbf{w} \cdot \mathbf{n} = 0$ on all Neumann boundaries.

The position of the new nodes of the mesh can be obtained via Equation (6.2), that is,

$$\left. \frac{\partial \mathbf{x}(\mathbf{Y}, t)}{\partial t} \right|_{\mathbf{Y}} = \left. \frac{\partial \mathcal{R}_t(\mathbf{Y})}{\partial t} \right|_{\mathbf{Y}} = \mathbf{w}(\mathbf{x}, t). \quad (6.24)$$

Even though solving Problem 6.2 yields continuous mesh movement, the free surface boundary might not be sufficiently smooth. The free surface boundary undergoes the largest deformations and its movement involves the evaluations of the outward normal, \mathbf{n} , in Equation (6.19), across multiple elements. In our computations, we experienced peaks appearing in the free surface boundary, which may lead to the violation of the restrictions on the regularity of the mapping (see Equation (6.11)) and to instabilities. To ensure a higher degree of smoothness of the free surface, we could consider a Hermite mapping, instead of the iso-parametric mapping introduced in Section 3.4, which yields continuous derivatives of grid lines over element boundaries. However, we found that the interior mesh nodes and element boundaries were kept sufficiently smooth using (6.21). Therefore, we found a smooth representation of the free surface sufficient to obtain a sufficiently smooth mapping for our numerical examples.

In order to obtain a smooth free surface representation, we represent the free surface using a cubic spline, and we use it to determine the normals in the kinematic free surface boundary condition (6.19) and the curvature and normals in the dynamic boundary condition term $\langle \sigma \kappa \cdot \mathbf{n}, \phi_{\mathbf{u}} \rangle_{\Gamma_f(t)}$ in Equation (6.12).

6.3. Free Surface Representation



Figure 6.1.: Cubic spline free surface representation.

As mentioned above, we represent the free surface using a cubic spline, $S(x, t) \in \mathcal{C}^2(\Gamma_f)$ in order to guarantee the smoothness of the free surface boundary. This guarantees continuous outward normals and curvature of the free surface boundary across several spectral elements.

The cubic spline is constructed through all the quadrature points on the free surface. Let (x_i, y_i) , $1 \leq i \leq N$, be the physical coordinates of the N quadrature points along the free surface. Then, we construct a cubic spline $S(x, t) = S_i(x, t)$ for each $x_i \leq x \leq x_{i+1}$ through

$$S_i(x, t) = a_i(x - x_i)^3 + b_i(x - x_i)^2 + c_i(x - x_i) + d_i \quad (6.25)$$

where we enforce **continuity**

$$\begin{aligned} S_{i-1}(x_i, t) &= S_i(x_i, t), \\ S_i(x_{i+1}, t) &= S_{i+1}(x_{i+1}, t) \end{aligned} \quad (6.26)$$

and **smoothness**

$$\begin{aligned} S'_{i-1}(x_i, t) &= S'_i(x_i, t), \\ S''_{i-1}(x_i, t) &= S''_i(x_i, t), \\ S'_i(x_{i+1}, t) &= S'_{i+1}(x_{i+1}, t), \\ S''_i(x_{i+1}, t) &= S''_{i+1}(x_{i+1}, t). \end{aligned} \quad (6.27)$$

Here, S' denotes the partial differentiation with respect to x . We have

$$S_i(x_i, t) = d_i(t) = y_i(t), \quad S'_i(x_i, t) = c_i(t), \quad S''_i(x_i, t) = 2b_i(t). \quad (6.28)$$

From the continuity and smoothness conditions, we can derive expressions for the coeffi-

icients $a_i(t)$, $b_i(t)$, $c_i(t)$, $d_i(t)$ in terms of the second derivative of S , $M_i := S''_i(x_i, t)$,

$$a_i(t) = \frac{M_{i+1} - M_i}{6h_i}, \quad (6.29)$$

$$b_i(t) = \frac{M_i}{2}, \quad (6.30)$$

$$c_i(t) = \frac{y_{i+1} - y_i}{h_i} - \left(\frac{M_{i+1} + 2M_i}{6} \right) h_i, \quad (6.31)$$

$$d_i(t) = y_i, \quad (6.32)$$

where $h_i = x_{i+1} - x_i$. Substituting these expressions into the smoothness condition $S'_i(x_i) = S'_{i-1}(x_i)$ yields the system of equations

$$(2h_{i-1} + 2h_i) M_i + h_{i-1} M_{i-1} + h_i M_{i+1} = 6 \left(\frac{y_{i+1} - y_i}{h_i} - \frac{y_i - y_{i-1}}{h_{i-1}} \right), \quad (6.33)$$

for $1 < i < N - 1$, which can be solved if we specify boundary conditions for $i = 1$ and $i = N - 1$. We employ the following boundary conditions

1. the **natural** boundary condition

$$M_1 = 0, \quad M_{N-1} = 0; \quad (6.34)$$

2. the **not-a-knot** boundary condition

$$S'''_1(x_2) = S'''_2(x_2), \quad \text{i.e. } a_1 = a_2, \quad (6.35)$$

$$S'''_{N-1}(x_{N-1}) = S'''_{N-2}(x_{N-1}); \quad (6.36)$$

3. the **clamped** boundary condition

$$S'_1(x_1) = c_1 = c_L, \quad S'_{N-1}(x_N) = c_N = c_R, \quad (6.37)$$

where c_L and c_R are arbitrary values. To obtain the values c_L or c_R for the clamped boundary condition, we determine the value of the derivative of a Lagrange polynomial through the first or last three nodes, respectively. For c_L , that means

$$c_L = \frac{2x_1 - (x_2 + x_3)}{(x_1 - x_2)(x_1 - x_3)} y_1 + \frac{x_1 - x_3}{(x_2 - x_1)(x_2 - x_3)} y_2 + \frac{x_1 - x_2}{(x_3 - x_1)(x_3 - x_2)} y_3. \quad (6.38)$$

The system of equations (6.33) with corresponding boundary conditions forms a tridiagonal matrix, which can be inverted to obtain M_i . Using M_i , we obtain the coefficients a_i , b_i , c_i and d_i , which define the cubic spline. The cubic spline can then be used to determine

the unit outward normals \mathbf{n} and the curvature κ of the free surface using

$$\mathbf{n}_S(t) = \frac{1}{\sqrt{S'(x,t)^2 + 1}} \begin{pmatrix} -S'(x,t) \\ 1 \end{pmatrix}, \quad (6.39)$$

$$\kappa_S(t) = \frac{|S''(x,t)|}{(1 + S'(x,t)^2)^{3/2}}. \quad (6.40)$$

These expressions are then used to evaluate the free surface boundary condition for the mesh velocity given by Equation (6.20) and the free surface boundary integral in the momentum equation

$$\int_{\Gamma_f} \sigma \kappa_S \mathbf{n}_S \phi_{\mathbf{u}} d\Gamma. \quad (6.41)$$

6.4. Spatial discretisation

The spectral element approximation of Problem 6.1 involves the discretisation of the equations describing viscoelastic flow and the discretisation of the domain motion. Here, we describe the domain motion in terms of the mesh velocity.

Consider a fixed reference mesh $\hat{\Omega}_{t_0}^\delta$ consisting of the union of N_{el} mesh elements $\hat{\Omega}_{t_0}^e$, that is,

$$\hat{\Omega}_{t_0}^\delta = \bigcup_{e=1}^{N_{el}} \hat{\Omega}_{t_0}^e, \quad \hat{\Omega}_{t_0}^{e_1} \cap \hat{\Omega}_{t_0}^{e_2} = \emptyset \text{ for } e_1 \neq e_2. \quad (6.42)$$

Furthermore, let Ω_t^δ be the union of all mesh elements in the Eulerian frame at time t .

The discrete ALE-mapping \mathcal{R}_t^δ can be identified with the geometrical mappings of the standard element Ω_{st} onto each element Ω_t^e , χ^e , defined in Section 3.4 as follows. Let $\chi^e(t_0)$ be the parametric mapping from Ω_{st} to $\hat{\Omega}_{t_0}^e$ defined as

$$\mathbf{Y}(\xi_1, \xi_2) = \chi^e(t_0; \xi_1, \xi_2) = \sum_{p=0}^P \sum_{q=0}^P \hat{\mathbf{Y}}_{pq} \phi_p(\xi_1) \phi_q(\xi_2). \quad (6.43)$$

Similar to the definitions of the spaces of polynomials in Section 4.2, we define the globally continuous space of polynomials of degree P over the reference mesh as

$$\mathcal{P}_P^c(\hat{\Omega}_{t_0}^\delta) = \left\{ g^\delta : \hat{\Omega}_{t_0}^\delta \rightarrow \mathbb{R} \mid g^\delta \in \mathcal{C}^0(\hat{\Omega}_{t_0}^\delta), \quad g^\delta|_{\hat{\Omega}_{t_0}^e} \circ [\chi^e(t_0)]^{-1} \in \mathcal{P}_P(\Omega_{st}) \right\}, \quad (6.44)$$

and the space of piecewise continuous polynomials of degree P over the reference mesh as

$$\mathcal{P}_P(\hat{\Omega}_{t_0}^\delta) = \left\{ g^\delta : \hat{\Omega}_{t_0}^\delta \rightarrow \mathbb{R} \mid g^\delta \in L^2(\hat{\Omega}_{t_0}^\delta), g^\delta \Big|_{\hat{\Omega}_{t_0}^e} \circ [\boldsymbol{\chi}^e(t_0)]^{-1} \in \mathcal{P}_P(\Omega_{st}) \right\}. \quad (6.45)$$

Here, $g^\delta \Big|_{\hat{\Omega}_{t_0}^e}$ indicates the restrictions of g^δ to the spectral element $\hat{\Omega}_{t_0}^e$, $\mathcal{P}_P(\Omega_{st})$ is the space of polynomials of degree P defined on the standard element. At each time t , we define the elemental mapping on the elements of the Eulerian mesh as

$$\begin{aligned} \boldsymbol{\chi}^e(t) : \Omega_{st} &\rightarrow \hat{\Omega}_{t_0}^e \\ \mathbf{x}(\xi_1, \xi_2) &= \boldsymbol{\chi}^e(t; \xi_1, \xi_2) = \sum_{p=0}^P \sum_{q=0}^P \hat{\mathbf{x}}_{pq}(t) \phi_p(\xi_1) \phi_q(\xi_2). \end{aligned} \quad (6.46)$$

where $\hat{\mathbf{x}}_{pq}(t)$ denotes the expansion coefficients at time t ; the globally continuous polynomial space over the Eulerian mesh as

$$\mathcal{P}_P^c(\Omega_t^\delta) = \left\{ g^\delta : \Omega_t^\delta \rightarrow \mathbb{R} \mid g^\delta \in C^0(\Omega_t^\delta), g^\delta \Big|_{\Omega_t^e} \circ [\boldsymbol{\chi}^e(t)]^{-1} \in \mathcal{P}_P(\Omega_{st}) \right\}, \quad (6.47)$$

and the piecewise continuous polynomial space over the Eulerian mesh as

$$\mathcal{P}_P(\Omega_t^\delta) = \left\{ g^\delta : \Omega_t^\delta \rightarrow \mathbb{R} \mid g^\delta \in L^2(\Omega_t^\delta), g^\delta \Big|_{\Omega_t^e} \circ [\boldsymbol{\chi}^e(t)]^{-1} \in \mathcal{P}_P(\Omega_{st}) \right\}. \quad (6.48)$$

Nobile (2001) showed that if the discrete ALE-map is constructed as

$$\mathcal{R}_t^\delta \Big|_{\hat{\Omega}_{t_0}^e} \circ \boldsymbol{\chi}^e(t_0) = \boldsymbol{\chi}^e(t), \quad \forall \hat{\Omega}_{t_0}^e, \quad \Omega_t^e = \mathcal{R}_t \quad (6.49)$$

or equivalently

$$\mathcal{R}_t^\delta \Big|_{\hat{\Omega}_{t_0}^e} = \boldsymbol{\chi}^e(t) \circ [\boldsymbol{\chi}^e(t_0)]^{-1} \quad (6.50)$$

and is globally continuous then if the discrete space over the reference mesh is given by

$$\mathcal{X}^\delta(\hat{\Omega}_{t_0}^\delta) = \mathcal{P}_P^c(\hat{\Omega}_{t_0}^\delta), \quad t = t_0, \quad (6.51)$$

the discrete space over the Eulerian mesh

$$\mathcal{X}^\delta(\Omega_t^\delta) = \left\{ g : \Omega_t \times I \rightarrow \mathbb{R}^d : g = \hat{g} \circ [\mathcal{R}_t^\delta]^{-1}, \hat{g} \in \mathcal{X}^\delta(\hat{\Omega}_{t_0}^\delta) \right\}, \quad \forall t \in I \quad (6.52)$$

is given by

$$\mathcal{X}^\delta(\Omega_t^\delta) = \mathcal{P}_P^c(\Omega_t^\delta). \quad (6.53)$$

An analogous results holds for the discontinuous spaces.

With these definitions, we can now define the discrete trial and test function spaces for the unknowns consisting of the velocity, pressure, velocity gradient projection, polymeric stress and the mesh velocity. Appropriate discrete spaces fulfilling the compatibility conditions presented in Section 4.2 are given by

$$\mathcal{V}^\delta(\Omega_t^\delta) = \left\{ \mathbf{u} : \Omega_t^\delta \times I \rightarrow \mathbb{R}^d : \mathbf{u} = \hat{\mathbf{u}} \circ [\mathcal{R}_t^\delta]^{-1}, \hat{\mathbf{u}} \in [H_D^1(\hat{\Omega}_{t_0}^\delta)]^d \cap [\mathcal{P}_P^c(\hat{\Omega}_{t_0}^\delta)]^d \right\}, \quad (6.54)$$

$$\mathcal{Q}^\delta(\Omega_t^\delta) = \left\{ q : \Omega_t^\delta \times I \rightarrow \mathbb{R} : q = \hat{q} \circ [\mathcal{R}_t^\delta]^{-1}, \hat{q} \in L^2(\hat{\Omega}_{t_0}^\delta) \cap [\mathcal{P}_{P-2}(\hat{\Omega}_{t_0}^\delta)]^d \right\}, \quad (6.55)$$

$$\Sigma_G^\delta(\Omega_t^\delta) = \left\{ \mathbf{G} : \Omega_t^\delta \times I \rightarrow \mathbb{R}^{d \times d} : \mathbf{G} = \hat{\mathbf{G}} \circ [\mathcal{R}_t^\delta]^{-1}, \hat{\mathbf{G}} \in [L^2(\hat{\Omega}_{t_0}^\delta)]^{d^2} \cap [\mathcal{P}_P(\hat{\Omega}_{t_0}^\delta)]^d \right\}, \quad (6.56)$$

$$\Sigma^\delta(\Omega_t^\delta) = \left\{ \boldsymbol{\tau} : \Omega_t^\delta \times I \rightarrow \mathbb{R}^{d \times d} : \boldsymbol{\tau} = \hat{\boldsymbol{\tau}} \circ [\mathcal{R}_t^\delta]^{-1}, \hat{\boldsymbol{\tau}} \in [L^2(\hat{\Omega}_{t_0}^\delta)]_s^{d^2} \cap [\mathcal{P}_P(\hat{\Omega}_{t_0}^\delta)]^d \right\}. \quad (6.57)$$

Alternatively, these spaces can be expressed as (see Pena (2009))

$$\mathcal{V}^\delta(\Omega_t^\delta) = [H_D^1(\Omega_t^\delta)]^d \cap [\mathcal{P}_P^c(\Omega_t^\delta)]^d, \quad (6.58)$$

$$\mathcal{Q}^\delta(\Omega_t^\delta) = L^2(\Omega_t^\delta) \cap [\mathcal{P}_{P-2}(\Omega_t^\delta)]^d, \quad (6.59)$$

$$\Sigma_G^\delta(\Omega_t^\delta) = [L^2(\Omega_t^\delta)]^{d^2} \cap [\mathcal{P}_P(\Omega_t^\delta)]^d, \quad (6.60)$$

$$\Sigma^\delta(\Omega_t^\delta) = [L^2(\Omega_t^\delta)]_s^{d^2} \cap [\mathcal{P}_P(\Omega_t^\delta)]^d. \quad (6.61)$$

The unknowns are approximated by the expansion series given in Equation (4.37) and the spatial approximation of the Weak DEVSS/DG formulation becomes

Problem 6.3 (Spatial Discretisation of the Weak DEVSS-G/DG Formulation in the ALE framework). *For almost every $t \in I$ find $t \rightarrow (\mathbf{w}_\delta(t), \mathbf{u}_\delta(t), p_\delta(t), \mathbf{G}_\delta(t), \boldsymbol{\tau}_\delta(t)) \in \mathcal{V}_D^\delta(\Omega_t) \times \mathcal{V}_D^\delta(\Omega_t) \times \mathcal{Q}^\delta(\Omega_t) \times \Sigma_G^\delta(\Omega_t) \times \Sigma^\delta(\Omega_t)$ such that, for all $(\phi_w, \phi_u, \psi, \phi_G, \phi_\tau) \in \mathcal{V}^\delta(\Omega_t) \times \mathcal{V}^\delta(\Omega_t) \times \mathcal{Q}^\delta(\Omega_t) \times \Sigma_G^\delta(\Omega_t) \times \Sigma^\delta(\Omega_t)$*

$$(\nabla \mathbf{w}_\delta, \nabla \phi_w)_{\Omega_t} = 0, \quad (6.62)$$

$$\begin{aligned} & Re \left(\frac{\partial \mathbf{u}_\delta}{\partial t} \Big|_{\mathbf{Y}} + ((\mathbf{u}_\delta - \mathbf{w}_\delta) \cdot \nabla_{\mathbf{x}}) \mathbf{u}_\delta, \phi_u \right)_{\Omega_t} + (2\mathbf{D}_{\mathbf{x}, \delta}, \nabla_{\mathbf{x}} \phi_u)_{\Omega_t} - (p_\delta, \nabla_{\mathbf{x}} \cdot \phi_u)_{\Omega_t} \\ & + (\boldsymbol{\tau}_\delta, \nabla_{\mathbf{x}} \phi_u)_{\Omega_t} - (1 - \beta) (\mathbf{G}_\delta + [\mathbf{G}_\delta]^T, \nabla_{\mathbf{x}} \phi_u)_{\Omega_t} \end{aligned} \quad (6.63)$$

$$\begin{aligned} & - \langle \boldsymbol{\sigma}_\delta \cdot \mathbf{n}, \phi_u \rangle_{\Gamma_N(t)} - \langle \sigma \kappa_S \cdot \mathbf{n}_S, \phi_u \rangle_{\Gamma_f(t)} = 0, \\ & (\nabla_{\mathbf{x}} \cdot \mathbf{u}, \psi)_{\Omega_t} = 0, \end{aligned} \quad (6.64)$$

$$(\mathbf{G}_\delta - \nabla_{\mathbf{x}} \mathbf{u}_\delta, \phi_G)_{\Omega_t^e} = 0, \quad (6.65)$$

$$\begin{aligned} & Wi \left(\frac{\partial \boldsymbol{\tau}_\delta}{\partial t} \Big|_{\mathbf{Y}}, \phi_\tau \right)_{\Omega_t^e} - Wi (\boldsymbol{\tau}_\delta, ((\mathbf{u}_\delta - \mathbf{w}_\delta) \cdot \nabla_{\mathbf{x}}) \phi_\tau)_{\Omega_t^e} \\ & + Wi \left\langle [(\mathbf{u}_\delta - \mathbf{w}_\delta) \cdot \mathbf{n}] \tilde{f}(\boldsymbol{\tau}^{ext}, \boldsymbol{\tau}^{int}), \phi_\tau \right\rangle_{\partial \Omega_t^e} \\ & - Wi (\mathbf{G}_\delta \cdot \boldsymbol{\tau} + \boldsymbol{\tau}_\delta \cdot \mathbf{G}_\delta^T, \phi_\tau)_{\Omega_t^e} + (\boldsymbol{\tau}, \phi_\tau)_{\Omega_t^e} + \frac{\alpha Wi}{(1 - \beta)} (\boldsymbol{\tau}_\delta^2, \phi_\tau)_{\Omega_t^e} \\ & = (1 - \beta) (\mathbf{G}_\delta + \mathbf{G}_\delta^T, \phi_\tau)_{\Omega_t^e}, \end{aligned} \quad (6.66)$$

where $\Gamma_N(t)$ is the Neumann boundary and $\Gamma_f(t)$ is the free surface boundary.

The matrix notation and the temporal discretisation schemes used to solve system of equations of Problem 6.3 are detailed in the following Sections. Here, we just briefly outline the solution procedure in Algorithm 6.4.1

Algorithm 6.4.1: ALE/DEVSS-G/DG SCHEME. $(\mathbf{u}^n, p^n, \boldsymbol{\tau}^n)$

```

t = t0
while t ≤ tfin
  procedure MOVEMESH( $\mathbf{u}^n, p^n, \boldsymbol{\tau}^n$ )
    Construct Cubic Spline through Free Surface Boundary.
    Set BC for Mesh Velocity (see (6.20)).
    Solve Elliptic Problem for Mesh Velocity (6.62).
    output ( $\mathbf{w}^{n+1}$ )
    Compute New Mesh Coordinates  $\mathbf{X}^{n+1}$ .
    Construct New Parametric Mappings  $\boldsymbol{\chi}^e(t_{n+1})$ .
    output ( $\Omega_{t_{n+1}}$ )

  Set Boundary Conditions for  $\mathbf{u}$  and  $p$ .
  do { procedure SOLVECOUPLEDSYSTEM( $\mathbf{u}^n, p^n, \boldsymbol{\tau}^n, \mathbf{w}^{n+1}$ )
    Solve Coupled System of Velocity, Pressure
    and Velocity Gradient Projection Tensor (6.63), (6.64) and (6.65).
    output ( $\mathbf{u}^{n+1}, p^{n+1}, \mathbf{G}^{n+1}$ )

    Set Boundary Conditions for  $\boldsymbol{\tau}$ .
    procedure SOLVECONSTITUTIVEEQUATION( $\mathbf{G}^{n+1}, \mathbf{u}^{n+1}, \mathbf{w}^{n+1}$ )
    Solve the Constitutive Equation (4.45).
    output ( $\boldsymbol{\tau}^{n+1}$ )

  tn+1 ← tn + Δt
  n + 1 ← n

```

6.5. Mesh Movement

For given \mathbf{u}^n , we perform the mesh movement in the following way. First, we determine the cubic spline through all the quadrature points along the free surface as described in Section 6.3 from which we compute the normals along the free surface \mathbf{n}_S . Here, the index S indicates that the normal is determined using the cubic spline according to Equation (6.39). Then, solve the elliptic problem using the continuous Galerkin method

Problem 6.4. Find $t \rightarrow \mathbf{w}_\delta(t) \in \mathcal{V}_D^\delta(\Omega_t)$, such that

$$(\nabla \mathbf{w}_\delta, \nabla \phi_{\mathbf{w}})_{\Omega_t} = 0, \quad \forall \phi_{\mathbf{w}} \in \mathcal{V}^\delta(\Omega_t) \quad (6.67)$$

subject to the boundary conditions

$$\begin{cases} \mathbf{w} \cdot \mathbf{n}_S = \mathbf{u} \cdot \mathbf{n}_S, \\ \mathbf{w} \cdot \mathbf{s}_S = 0, \end{cases} \quad \text{at } \Gamma_f, \\ \nabla \mathbf{w} \cdot \mathbf{n} = \mathbf{0} \quad \text{at outflow}, \\ \mathbf{w} = \mathbf{0} \quad \text{elsewhere}, \end{cases} \quad (6.68)$$

where \mathbf{n}_S is the outward unit normal and \mathbf{s}_S is the unit tangent vector on the cubic spline representing the free surface boundary.

The mesh velocity resulting from the solution of Problem 6.4, denoted by $\tilde{\mathbf{w}}$, is then used to update the coordinates of the mesh nodes using a third order Adams-Bashforth-Scheme for Equation (6.2).

$$\mathbf{X}^{n+1} = \mathbf{X}^n + \frac{\Delta t}{12}(23\tilde{\mathbf{w}} - 16\mathbf{w}^n + 5\mathbf{w}^{n-1}). \quad (6.69)$$

This equation is solved pointwise in the strong form for each quadrature point. However, in practice, we do not move all the mesh nodes of every element. We only move all the quadrature points along the free surface boundary. In the interior of the domain, we just move the corner vertices of every element keeping the interior edges of the domain straight.

The movement of all the quadrature points along the free surfaces, means that we introduce curved edges along the free surface boundary. These curved edges are approximated by a polynomial expansion of the same order as the unknowns (see Section 3.4 for details), e.g.

$$\Gamma_f^e(t_{n+1}; \xi_1) = \sum_{p=0}^P \hat{\mathbf{x}}_{p0} \phi_p(\xi_1). \quad (6.70)$$

From these edge representations along the free surface and from the new coordinates of the interior corner vertices of the elements, we construct the geometrical mappings $\boldsymbol{\chi}^e(t_{n+1})$ using the blending technique described in Section 3.4. These mappings then specify the new location of all mesh nodes and their continuous union describes $\Omega_{t_{n+1}}^\delta$. Using these new coordinates of all mesh nodes, we compute the mesh velocity at the new time level pointwise as

$$\mathbf{w}^{n+1} = \frac{\mathbf{X}^{n+1} - \mathbf{X}^n}{\Delta t}. \quad (6.71)$$

6.6. Solving the Coupled System of Velocity, Pressure and \mathbf{G}

In the next step, we solve the coupled system of equations (6.63) - (6.65) for velocity, pressure and velocity gradient projection tensor. We discretise the equations in time using an implicit Euler scheme for velocity, pressure and the velocity gradient projection tensor and the resulting problem reads

Problem 6.5. For each n , let $t_n = t_0 + n\Delta t$, find $(\mathbf{u}_\delta^{n+1}, p_\delta^{n+1}, \mathbf{G}_\delta^{n+1}) \in (\mathcal{V}_D^\delta(\Omega_{t_{n+1}}^\delta) \times \mathcal{Q}^\delta(\Omega_{t_{n+1}}^\delta) \times \Sigma_G^\delta(\Omega_{t_{n+1}}^\delta))$ with $\mathbf{u}_\delta^0 = \mathbf{u}_{0,\delta}$ in $\hat{\Omega}_{t_0}^\delta$ such that

$$\begin{aligned} & \text{Re} \left(\frac{\mathbf{u}_\delta^{n+1} - \mathbf{u}_\delta^n}{\Delta t}, \phi_{\mathbf{u}} \right)_{\Omega_{t_{n+1}}^\delta} + \left([(\mathbf{u}_\delta^* - \mathbf{w}_\delta^{n+1}) \cdot \nabla_{\mathbf{x}}] \mathbf{u}_\delta^{n+1}, \phi_{\mathbf{u}} \right)_{\Omega_{t_{n+1}}^\delta} \\ & + \left(2\mathbf{D}_{\mathbf{x},\delta}^{n+1}, \nabla_{\mathbf{x}} \phi_{\mathbf{u}} \right)_{\Omega_{t_{n+1}}^\delta} - \left(p_\delta^{n+1}, \nabla_{\mathbf{x}} \cdot \phi_{\mathbf{u}} \right)_{\Omega_{t_{n+1}}^\delta} \\ & + \left(\boldsymbol{\tau}_\delta^*, \nabla_{\mathbf{x}} \phi_{\mathbf{u}} \right)_{\Omega_{t_{n+1}}^\delta} - (1 - \beta) \left(\mathbf{G}_\delta^{n+1} + [\mathbf{G}_\delta^{n+1}]^T, \nabla_{\mathbf{x}} \phi_{\mathbf{u}} \right)_{\Omega_{t_{n+1}}^\delta} \end{aligned} \quad (6.72)$$

$$\begin{aligned} & - \left\langle \boldsymbol{\sigma}_\delta^{n+1} \cdot \mathbf{n}, \phi_{\mathbf{u}} \right\rangle_{\Gamma_N(t_{n+1})} - \left\langle \boldsymbol{\sigma}_{\kappa_S} \cdot \mathbf{n}_S, \phi_{\mathbf{u}} \right\rangle_{\Gamma_f(t_{n+1})} = 0, \\ & \left(\nabla_{\mathbf{x}} \cdot \mathbf{u}_\delta^{n+1}, \psi \right)_{\Omega_{t_{n+1}}^\delta} = 0, \end{aligned} \quad (6.73)$$

$$\left(\mathbf{G}_\delta^{n+1} - \nabla_{\mathbf{x}} \mathbf{u}_\delta^{n+1}, \phi_{\mathbf{G}} \right)_{\Omega_i^\delta} = 0, \quad (6.74)$$

for all $(\phi_{\mathbf{u}}, \psi, \phi_{\mathbf{G}}) \in (\mathcal{V}^\delta(\Omega_{t_{n+1}}^\delta) \times \mathcal{Q}^\delta(\Omega_{t_{n+1}}^\delta) \times \Sigma_G^\delta(\Omega_{t_{n+1}}^\delta))$. Here, we linearise the convective term in the momentum equation by setting $\mathbf{u}_\delta^* = \mathbf{u}_\delta^n$, which is an extrapolation of the velocity of the same order as the implicit Euler scheme.

For the linear advection diffusion problem, Nobile (2001) showed that the implicit Euler method in the non-conservative form is only conditionally stable. The stability condition

restricts the time step and involves only geometrical quantities

$$\Delta t < \left(\|\nabla \cdot \mathbf{w}_\delta^n\|_{L^\infty(\Omega_{t_n}^\delta)} + \sup_{t \in (t_n, t_{n+1})} \|J_{\mathcal{R}_{t_n, t_{n+1}}} \nabla \cdot \mathbf{w}_\delta\|_{L^\infty(\Omega_t^\delta)} \right)^{-1} \quad (6.75)$$

where $\mathcal{R}_{t_n, t_{n+1}}$ is the mapping between Ω_{t_n} and $\Omega_{t_{n+1}}$. If the mesh velocity is divergence free, then the scheme is unconditionally stable and this is a sufficient condition to satisfy the so-called geometric conservation law (GCL). The Geometric Conservation Law demands that a numerical scheme is able to reproduce a constant solution accurately and independently of the mesh motion. The system of equations describing viscoelastic flow is geometrically conserving. However, this is not clearly the case for the discrete form of the equations. Let us suppose $\mathbf{u}_\delta^n = \mathbf{u}_0$ and $p_\delta^n = 0$ are constant for all $t_n \in I$. Then, the discrete momentum equation (6.72) reduces to

$$\left(\mathbf{u}^{n+1}, \phi_{\mathbf{u}} \right)_{\Omega_{t_{n+1}}^\delta} = \left(\mathbf{u}^n, \phi_{\mathbf{u}} \right)_{\Omega_{t_n}^\delta} . \quad (6.76)$$

which fulfils the geometric conservation. However, this means geometric conservation requires that the terms arising from the time derivative have to be integrated over the same domain $\Omega_{t_{n+1}}^\delta$ at the same instant in time. This means all the governing equations need to be tested and integrated within the same configuration in time (see Förster et al. (2006)). In addition to this condition, the mesh deformation is subject to some restrictions in order to guarantee geometric conservation. Consider the mesh Jacobian defined in Equation (2.10), that is,

$$\hat{J}_t = \det \left(\frac{\partial \mathbf{x}}{\partial \mathbf{Y}} \right), \quad (6.77)$$

which describes the ratio between the differential volume elements in the current configuration Ω_t and the referential configuration $\hat{\Omega}_{t_0}$. Then, the time derivative of the Jacobian, known from continuum mechanics (see e.g. Scovazzi and Hughes (2007)), gives the relationship of volume transformation and relative velocity between the two systems \mathbf{Y} and \mathbf{x}

$$\frac{\partial \hat{J}_t}{\partial t} = \hat{J}_t \nabla \cdot \mathbf{w}. \quad (6.78)$$

Therefore for an algorithm to satisfy the geometric conservation law, Equation (6.78) should be satisfied in addition to Equation (6.76). Hence, a divergence free mesh velocity is sufficient to satisfy Equation (6.78). However, even though the GCL could be linked to convergence properties in numerical schemes using the finite volume method by Farhat et al. (2001) and Lesoinne and Farhat (1996), Mavriplis and Yang (2006) noted that there is no evidence that makes the GCL a sufficient or necessary condition for convergence or

stability in the context of the Navier-Stokes equations in the ALE framework.

Introducing the following matrices

$$\mathbf{M}^e(t)[j][i] = \frac{\text{Re}}{\Delta t} \left(\phi_{\mathbf{u}}^i, \phi_{\mathbf{u}}^j \right)_{\Omega_t^e}^\delta, \quad (6.79)$$

$$\begin{aligned} \mathbf{K}^e(t)[j][i] &= \left(\nabla_{\mathbf{x}} \phi_{\mathbf{u}}^i + [\nabla_{\mathbf{x}} \phi_{\mathbf{u}}^i]^T, \nabla_{\mathbf{x}} \phi_{\mathbf{u}}^j \right)_{\Omega_t^e}^\delta, \\ &\quad - \left\langle \left(\nabla_{\mathbf{x}} \phi_{\mathbf{u}}^i + [\nabla_{\mathbf{x}} \phi_{\mathbf{u}}^i]^T \right) \cdot \mathbf{n}, \phi_{\mathbf{u}}^j \right\rangle_{\Gamma_N(t)}, \end{aligned} \quad (6.80)$$

$$\mathbf{B}^e(t; \mathbf{u}_\delta, \mathbf{w}_\delta)[j][i] = \left([(\mathbf{u}_\delta - \mathbf{w}_\delta) \cdot \nabla_{\mathbf{x}}] \phi_{\mathbf{u}}^i, \phi_{\mathbf{u}}^j \right)_{\Omega_t^e}^\delta, \quad (6.81)$$

$$\mathbf{D}^e(t)[j][i] = \left(\nabla_{\mathbf{x}} \phi_{\mathbf{u}}^i, \psi^j \right)_{\Omega_t^e}^\delta, \quad (6.82)$$

$$\begin{aligned} \mathbf{M}_{\mathbf{uG}}^e(t)[j][i] &= -(1 - \beta) \left(\phi_{\mathbf{G}}^i + [\phi_{\mathbf{G}}^i]^T, \nabla_{\mathbf{x}} \phi_{\mathbf{u}}^j \right)_{\Omega_t^e}^\delta, \\ &\quad + (1 - \beta) \left\langle \left(\phi_{\mathbf{G}}^i + [\phi_{\mathbf{G}}^i]^T \right) \cdot \mathbf{n}, \phi_{\mathbf{u}}^j \right\rangle_{\Gamma_N(t)}, \end{aligned} \quad (6.83)$$

$$\mathbf{b}(t)[j] = \left\langle \sigma \kappa_S \cdot \mathbf{n}_S, \phi_{\mathbf{u}}^j \right\rangle_{\Gamma_f(t)},$$

$$\mathbf{f}(t; \boldsymbol{\tau})[j] = - \left(\boldsymbol{\tau}_\delta, \nabla_{\mathbf{x}} \phi_{\mathbf{u}}^j \right)_{\Omega_t^e}^\delta + \left\langle \boldsymbol{\tau}_\delta \cdot \mathbf{n}, \phi_{\mathbf{u}}^j \right\rangle_{\Gamma_N(t)}, \quad (6.84)$$

$$\mathbf{M}_{\mathbf{Gu}}^e(t)[j][i] = - \left(\nabla_{\mathbf{x}} \phi_{\mathbf{u}}^i, \phi_{\mathbf{G}}^j \right)_{\Omega_t^e}^\delta, \quad (6.85)$$

$$\mathbf{M}_{\mathbf{GG}}^e(t)[j][i] = - \left(\phi_{\mathbf{G}}^i, \phi_{\mathbf{G}}^j \right)_{\Omega_t^e}^\delta, \quad (6.86)$$

and introducing a modified Helmholtz matrix

$$\mathbf{H}^e(t)[j][i] := \mathbf{M}^e(t)[j][i] + \mathbf{K}^e(t)[j][i] + \mathbf{B}^e(t; \mathbf{u}_\delta, \mathbf{w}_\delta)[j][i], \quad (6.87)$$

this system of equations can be written for each element in algebraic form as

$$\begin{aligned} \mathbf{H}_g(t_{n+1}) \hat{\mathbf{u}}_g^{n+1} - \mathbf{D}_g(t_{n+1})^T \hat{\mathbf{p}}_g^{n+1} + \mathbf{M}_{\mathbf{uG}}(t_{n+1}) \hat{\mathbf{G}}^{n+1} &= \mathbf{M}(t_{n+1}) \hat{\mathbf{u}}_g^n \\ &\quad + \mathbf{f}(t_{n+1}; \boldsymbol{\tau}^n) + \mathbf{b}(t_{n+1}), \\ \mathbf{D}_g(t_{n+1}) \hat{\mathbf{u}}_g^{n+1} &= \mathbf{0}, \\ \mathbf{M}_{\mathbf{Gu}}(t_{n+1}) \hat{\mathbf{u}}_g^{n+1} + \mathbf{M}_{\mathbf{GG}}(t_{n+1}) \hat{\mathbf{G}}^{n+1} &= \mathbf{0}, \end{aligned} \quad (6.88)$$

where $\hat{\mathbf{u}}_g$ and $\hat{\mathbf{p}}_g$ are the vectors of unknown global coefficients, $\mathbf{H}_g, \mathbf{D}_g = (\mathbf{D}_{x_1}, \mathbf{D}_{x_2})$ are the global matrices assembled from the elemental matrix contributions by

$$\mathbf{H}_g = \mathcal{A}^T \underline{\mathbf{H}}^e \mathcal{A}, \quad (6.89)$$

as explained in Section 3.7.1 and Section 4.4.1. The matrices are listed component-wise

in Appendix B.2. In a first step, we eliminate $\hat{\mathbf{G}}$ in the momentum equation and obtain

$$\begin{aligned} \left[\mathbf{H}_g - \mathbf{M}_{\mathbf{uG}} [\mathbf{M}_{\mathbf{GG}}]^{-1} \mathbf{M}_{\mathbf{Gu}} \right] \hat{\mathbf{u}}_g^{n+1} - \mathbf{D}_g^T \hat{\mathbf{p}}_g^{n+1} &= \mathbf{M}(t_{n+1}) \hat{\mathbf{u}}_g^n \\ &+ \mathbf{f}(t_{n+1}; \boldsymbol{\tau}^n) + \mathbf{b}(t_{n+1}), \end{aligned} \quad (6.90)$$

$$\mathbf{D}_g \hat{\mathbf{u}}_g^{n+1} = \mathbf{0}, \quad (6.91)$$

$$\hat{\mathbf{G}}^{n+1} = -[\mathbf{M}_{\mathbf{GG}}]^{-1} \mathbf{M}_{\mathbf{Gu}} \hat{\mathbf{u}}_g^{n+1}. \quad (6.92)$$

Introducing the matrix

$$\tilde{\mathbf{H}} := \mathbf{H}_g - \mathbf{M}_{\mathbf{uG}} [\mathbf{M}_{\mathbf{GG}}]^{-1} \mathbf{M}_{\mathbf{Gu}}, \quad (6.93)$$

the system of equations is of a similar form to the system of equations introduced in Section 4.4.1 and we can proceed by solving the system of equations analogously to the coupled solver algorithm explained in Section 4.4.1.

6.7. Solving the Constitutive Equation

Having obtained $(\mathbf{u}_\delta^{n+1}, p_\delta^{n+1}, \mathbf{G}_\delta^{n+1})$ and \mathbf{w}_δ^{n+1} , we solve the constitutive equation using a semi-implicit Euler scheme, which is formulated in the following problem

Problem 6.6. For each n , let $t_n = t_0 + n\Delta t$, and given $(\mathbf{u}_\delta^{n+1}, \mathbf{w}_\delta^{n+1}, p_\delta^{n+1}, \mathbf{G}_\delta^{n+1})$, find $\boldsymbol{\tau}_\delta^{n+1} \in \Sigma^\delta(\Omega_{t_{n+1}}^\delta)$ with $\boldsymbol{\tau}_\delta^0 = \boldsymbol{\tau}_{0,\delta}$ in $\Omega_{t_0}^\delta$ such that, for all $\phi_\boldsymbol{\tau} \in \Sigma^\delta(\Omega_{t_{n+1}}^\delta)$

$$\begin{aligned}
& Wi \left(\frac{\boldsymbol{\tau}_\delta^{n+1} - \boldsymbol{\tau}_\delta^n}{\Delta t}, \phi_{\mathbf{u}} \right)_{\Omega_{t_{n+1}}^\delta} - Wi \left(\boldsymbol{\tau}_\delta^{n+1}, \left((\mathbf{u}_\delta^{n+1} - \mathbf{w}_\delta^{n+1}) \cdot \nabla \mathbf{x} \right) \phi_\boldsymbol{\tau} \right)_{\Omega_{t_{n+1}}^\delta} \\
& - Wi \left(\mathbf{G}_\delta^{n+1} \cdot \boldsymbol{\tau}_\delta^{n+1} + \boldsymbol{\tau}_\delta^{n+1} \cdot [\mathbf{G}_\delta^{n+1}]^T, \phi_\boldsymbol{\tau} \right)_{\Omega_{t_{n+1}}^\delta} + \left(\boldsymbol{\tau}_\delta^{n+1}, \phi_\boldsymbol{\tau} \right)_{\Omega_{t_{n+1}}^\delta} \\
& = (1 - \beta) \left(\mathbf{G}_\delta^{n+1} + [\mathbf{G}_\delta^{n+1}]^T, \phi_\boldsymbol{\tau} \right)_{\Omega_{t_{n+1}}^\delta} \\
& - Wi \left\langle \left[(\mathbf{u}_\delta^{n+1} - \mathbf{w}_\delta^{n+1}) \cdot \mathbf{n} \right] \tilde{f}(\boldsymbol{\tau}^{*,ext}, \boldsymbol{\tau}^{*,int}), \phi_\boldsymbol{\tau} \right\rangle_{\partial\Omega_{t_{n+1}}^\delta} \\
& - \frac{\alpha Wi}{(1 - \beta)} \left([\boldsymbol{\tau}_\delta^*]^2, \phi_\boldsymbol{\tau} \right)_{\Omega_{t_{n+1}}^\delta},
\end{aligned} \tag{6.94}$$

where the flux across the element boundary

$$\tilde{f}(\boldsymbol{\tau}^{*,ext}, \boldsymbol{\tau}^{*,int}) = \begin{cases} \gamma \boldsymbol{\tau}^{*,ext} + (1 - \gamma) \boldsymbol{\tau}^{*,int}, & (\mathbf{u}_\delta^{n+1} - \mathbf{w}_\delta^{n+1}) \cdot \mathbf{n} < 0, \\ \gamma \boldsymbol{\tau}^{*,int} + (1 - \gamma) \boldsymbol{\tau}^{*,ext}, & (\mathbf{u}_\delta^{n+1} - \mathbf{w}_\delta^{n+1}) \cdot \mathbf{n} \geq 0, \\ \boldsymbol{\tau}_D & \text{at inflow,} \\ \boldsymbol{\tau}^{*,int} & \text{at outflow,} \end{cases} \tag{6.95}$$

and the non-linear term arising for $\alpha > 0$ are computed at the new time level using a Picard iteration scheme, that is, $\boldsymbol{\tau}^* \approx \boldsymbol{\tau}^{(it)}$.

We cast Equation (6.94) into the form

$$\mathbf{A}(t_{n+1}) \hat{\boldsymbol{\tau}} = \hat{\mathbf{f}}(t_{n+1}) + \hat{\mathbf{g}}(t_{n+1}; \boldsymbol{\tau}^{(it)}), \tag{6.96}$$

where we solve the component-wise system given by

$$\begin{aligned}
& \begin{bmatrix} \underline{\mathbf{A}}_{xx,xx}(t_{n+1}) & \underline{\mathbf{A}}_{xx,xy}(t_{n+1}) & 0 \\ \underline{\mathbf{A}}_{xy,xx}(t_{n+1}) & \underline{\mathbf{A}}_{xy,xy}(t_{n+1}) & \underline{\mathbf{A}}_{xy,yy}(t_{n+1}) \\ 0 & \underline{\mathbf{A}}_{yy,xy}(t_{n+1}) & \underline{\mathbf{A}}_{yy,yy}(t_{n+1}) \end{bmatrix} \begin{bmatrix} \hat{\boldsymbol{\tau}}_{xx} \\ \hat{\boldsymbol{\tau}}_{xy} \\ \hat{\boldsymbol{\tau}}_{yy} \end{bmatrix} \\
& = \begin{bmatrix} \hat{\mathbf{f}}_{xx}(t_{n+1}) + \hat{\mathbf{g}}_{xx}(t_{n+1}; \boldsymbol{\tau}^{(it)}) \\ \hat{\mathbf{f}}_{xy}(t_{n+1}) + \hat{\mathbf{g}}_{xy}(t_{n+1}; \boldsymbol{\tau}^{(it)}) \\ \hat{\mathbf{f}}_{yy}(t_{n+1}) + \hat{\mathbf{g}}_{yy}(t_{n+1}; \boldsymbol{\tau}^{(it)}) \end{bmatrix}.
\end{aligned} \tag{6.97}$$

Here, $\underline{\mathbf{A}}$ is the concatenation of the following elemental matrices

$$\begin{aligned}
\mathbf{A}_{xx,xx}^e(t_{n+1})[j, i] &= \left(\left[\left(1 + \frac{\text{Wi} \gamma_0}{\Delta t} \right) - 2\text{Wi} \mathbf{G}_{11,\delta}^{n+1} \right] \phi_{\tau_{xx}}^i, \phi_{\tau_{xx}}^j \right)_{\Omega_t^e}^\delta \\
&\quad - \text{Wi} \left((\mathbf{u}_\delta^{n+1} - \mathbf{w}_\delta^{n+1}) \phi_{\tau_{xx}}^i, \nabla \phi_{\tau_{xx}}^j \right)_{\Omega_t^e}^\delta, \\
\mathbf{A}_{xx,xy}^e(t_{n+1})[j, i] &= - \left(2\text{Wi} \mathbf{G}_{12,\delta}^{n+1} \phi_{\tau_{xy}}^i, \phi_{\tau_{xx}}^j \right)_{\Omega_t^e}^\delta, \\
\mathbf{A}_{xy,xx}^e(t_{n+1})[j, i] &= - \left(\text{Wi} \mathbf{G}_{21,\delta}^{n+1} \phi_{\tau_{xx}}^i, \phi_{\tau_{xy}}^j \right)_{\Omega_t^e}^\delta, \\
\mathbf{A}_{xy,xy}^e(t_{n+1})[j, i] &= \left(\left[\left(1 + \frac{\text{Wi} \gamma_0}{\Delta t} \right) - \text{Wi} \left(\mathbf{G}_{11,\delta}^{n+1} + \mathbf{G}_{22,\delta}^{n+1} \right) \right] \phi_{\tau_{xy}}^i, \phi_{\tau_{xy}}^j \right)_{\Omega_t^e}^\delta \\
&\quad - \text{Wi} \left((\mathbf{u}_\delta^{n+1} - \mathbf{w}_\delta^{n+1}) \phi_{\tau_{xy}}^i, \nabla \phi_{\tau_{xy}}^j \right)_{\Omega_t^e}^\delta, \\
\mathbf{A}_{xy,yy}^e(t_{n+1})[j, i] &= - \left(\text{Wi} \mathbf{G}_{12,\delta}^{n+1} \phi_{\tau_{yy}}^i, \phi_{\tau_{xy}}^j \right)_{\Omega_t^e}^\delta,
\end{aligned} \tag{6.98}$$

$$\begin{aligned}
\mathbf{A}_{yy,xy}^e(t_{n+1})[j, i] &= - \left(2\text{Wi} \mathbf{G}_{21,\delta}^{(n)} \phi_{\tau_{xy}}^i, \phi_{\tau_{yy}}^j \right)_{\Omega_t^e}^\delta, \\
\mathbf{A}_{yy,yy}^e(t_{n+1})[j, i] &= \left(\left[\left(1 + \frac{\text{Wi} \gamma_0}{\Delta t} \right) - 2\text{Wi} \mathbf{G}_{22,\delta}^{n+1} \right] \phi_{\tau_{yy}}^i, \phi_{\tau_{yy}}^j \right)_{\Omega_t^e}^\delta \\
&\quad - \text{Wi} \left((\mathbf{u}_\delta^{n+1} - \mathbf{w}_\delta^{n+1}) \phi_{\tau_{yy}}^i, \nabla \phi_{\tau_{yy}}^j \right)_{\Omega_t^e}^\delta,
\end{aligned} \tag{6.99}$$

and the right hand side terms are given by

$$\hat{\mathbf{f}}^e(t_{n+1})[j] = (1 - \beta) \left(\mathbf{G}_\delta^{n+1} + [\mathbf{G}_\delta^{n+1}]^T, \phi_\tau^j \right)_{\Omega_t^e}^\delta + \frac{\text{Wi}}{\Delta t} \left(\boldsymbol{\tau}_\delta^n, \phi_\tau^j \right)_{\Omega_t^e}^\delta, \tag{6.100}$$

$$\begin{aligned}
\hat{\mathbf{g}}^e(t_{n+1}; \boldsymbol{\tau}^{(it)})[j] &= -\text{Wi} \left\langle \left[(\mathbf{u}_\delta^{n+1} - \mathbf{w}_\delta^{n+1}) \cdot \mathbf{n} \right] \tilde{f} \left(\boldsymbol{\tau}^{(it),ext}, \boldsymbol{\tau}^{(it),int} \right), \phi_\tau^j \right\rangle_{\partial\Omega_{t_{n+1}}^{e,\delta}} \\
&\quad - \frac{\alpha \text{Wi}}{(1 - \beta)} \left([\boldsymbol{\tau}_\delta^{(it)}]^2, \phi_\tau^j \right)_{\Omega_t^e}^\delta.
\end{aligned} \tag{6.101}$$

We solve the system (6.97) element by element by first, eliminating $\hat{\boldsymbol{\tau}}_{xx}$ and $\hat{\boldsymbol{\tau}}_{yy}$ in the equation for $\hat{\boldsymbol{\tau}}_{xy}$, which results in

$$\begin{aligned}
&\left[\mathbf{A}_{xy,xy}^e - \mathbf{A}_{xy,xx}^e \left[\mathbf{A}_{xx,xx}^e \right]^{-1} \mathbf{A}_{xx,xy}^e - \mathbf{A}_{xy,yy}^e \left[\mathbf{A}_{yy,yy}^e \right]^{-1} \mathbf{A}_{yy,xy}^e \right] \hat{\boldsymbol{\tau}}_{xy} \\
&= \hat{\mathbf{f}}_{xy}^e(t_{n+1}) + \hat{\mathbf{g}}_{xy}^e(t_{n+1}; \boldsymbol{\tau}^{(it)}) \\
&\quad - \mathbf{A}_{xy,xx}^e \left[\mathbf{A}_{xx,xx}^e \right]^{-1} \left(\hat{\mathbf{f}}_{xx}^e(t_{n+1}) + \hat{\mathbf{g}}_{xx}^e(t_{n+1}; \boldsymbol{\tau}^{(it)}) \right) \\
&\quad - \mathbf{A}_{xy,yy}^e \left[\mathbf{A}_{yy,yy}^e \right]^{-1} \left(\hat{\mathbf{f}}_{yy}^e(t_{n+1}) + \hat{\mathbf{g}}_{yy}^e(t_{n+1}; \boldsymbol{\tau}^{(it)}) \right),
\end{aligned} \tag{6.102}$$

and which we solve to obtain the coefficients of the polymeric shear stress component $\hat{\boldsymbol{\tau}}_{xy}$. Using $\hat{\boldsymbol{\tau}}_{xy}$, we then compute the coefficients of the polymeric normal stress components $\hat{\boldsymbol{\tau}}_{xx}$ and $\hat{\boldsymbol{\tau}}_{yy}$ by

$$\hat{\boldsymbol{\tau}}_{xx} = [\mathbf{A}_{xx,xx}^e]^{-1} \left((\hat{\mathbf{f}}_{xx}^e(t_{n+1}) + \hat{\mathbf{g}}_{xx}^e(t_{n+1}; \boldsymbol{\tau}^{(it)})) - \mathbf{A}_{xx,xy}^e \hat{\boldsymbol{\tau}}_{xy} \right), \quad (6.103)$$

$$\hat{\boldsymbol{\tau}}_{yy} = [\mathbf{A}_{yy,yy}^e]^{-1} \left((\hat{\mathbf{f}}_{yy}^e(t_{n+1}) + \hat{\mathbf{g}}_{yy}^e(t_{n+1}; \boldsymbol{\tau}^{(it)})) - \mathbf{A}_{yy,xy}^e \hat{\boldsymbol{\tau}}_{xy} \right). \quad (6.104)$$

Solving this system, we obtain the polymeric stress components $\hat{\boldsymbol{\tau}} = \hat{\boldsymbol{\tau}}^{(it+1)}$ at the next iteration level. We start the Picard iteration with $\hat{\boldsymbol{\tau}}^{(it=0)} = \hat{\boldsymbol{\tau}}^n$. We then update $\hat{\mathbf{g}}(t_{n+1}; \boldsymbol{\tau}^{(it)})$ and compute

$$\hat{\boldsymbol{\tau}}^{(it+1)} = \mathbf{A}(t_{n+1})^{-1} \left(\hat{\mathbf{f}}(t_{n+1}) + \hat{\mathbf{g}}(t_{n+1}; \boldsymbol{\tau}^{(it)}) \right) \quad (6.105)$$

in each iteration step until the residual satisfies

$$R = \max_{kl=xx,xy,yy} \left[\max_{1 \leq i,j \leq Q} \left| \tau_{kl}^{(it+1)}(\xi_{1i}, \xi_{2j}) - \tau_{kl}^{(it)}(\xi_{1i}, \xi_{2j}) \right| \right] < 10^{-10}. \quad (6.106)$$

Here, we perform a backward transformation as defined in Section 3.6.3 in order to evaluate the residual in terms of the values of $\boldsymbol{\tau}$ in physical space.

Chapter 7

Die Swell Simulations

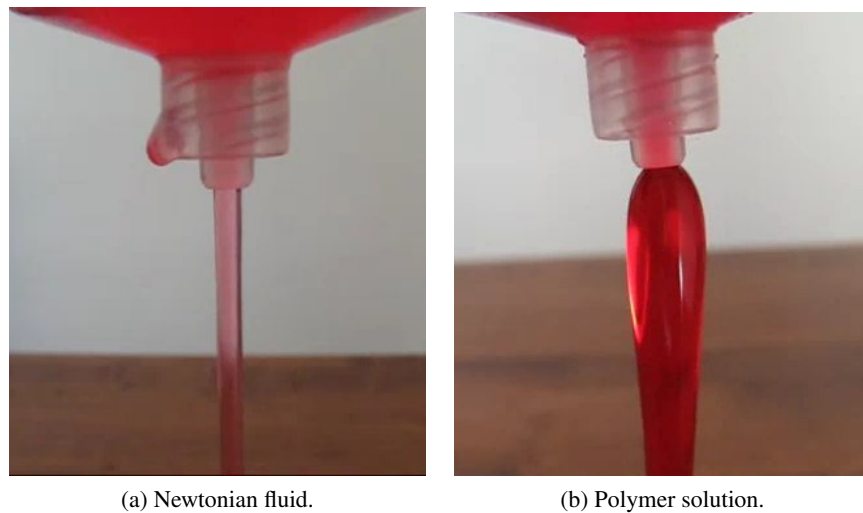
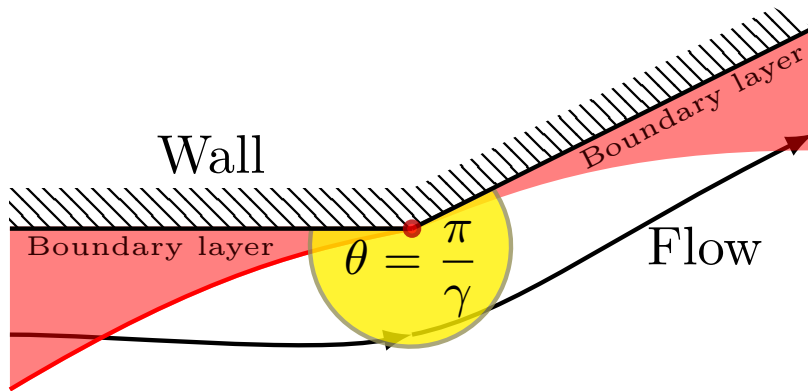
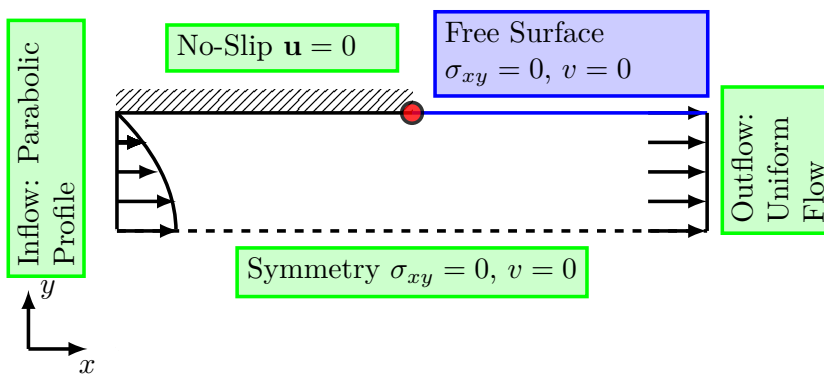


Figure 7.1.: Extrudate or die swell phenomenon for a Newtonian (a) and a viscoelastic fluid (b).

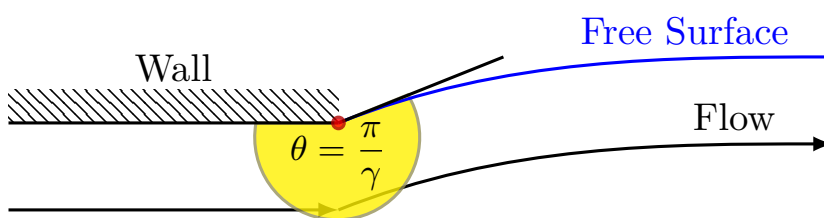
In this Chapter, we investigate the extrudate swell phenomenon, which is exhibited by viscous fluids exiting long die slits. While Newtonian fluids show relatively small swelling ratios of the exiting jet of liquid, non-Newtonian fluids show significant swelling ratios of up to twice the diameter of the die. A better understanding of this phenomenon is therefore of great importance in many industrial extrusion processes involving polymers and other viscoelastic materials. Numerical simulations of the extrudate or die swell phenomenon are very challenging due to the presence of a stress singularity at the exit of the die. This singularity originates from the sudden change in the boundary condition from the wall of the die to the free surface of the exiting jet (see Figure 7.2(c)). This "jump" in the boundary condition and the singularity in the boundary geometry, which can be characterised by the angle θ between the wall and the free surface at the singular points, yields infinite stress values at the singular point. The behaviour of velocity and polymeric stress for Oldroyd-B and Giesekus fluids near corner singularities with angle θ along a wall boundary, as



(a) Re-entrant corner singularity.



(b) Stick-slip flow.



(c) Separation point between wall and free surface.

Figure 7.2.: Schematic diagrams of (a) the re-entrant corner singularity between two walls, (b) the stick-slip problem and (c) the separation point between wall and free surface, which yield stress singularities.

depicted in Figure 7.2(a), has been investigated by Evans (2005, 2010). Let r denote radial distance from the corner of angle $\theta = \pi/\gamma$, $\gamma \in [1/2, 1)$ in the wall boundary. Evans (2005, 2010) examined the local asymptotic solution at the singularity and found the following behaviour for the velocity and the stress near the singularity as $r \rightarrow 0$

$$\boldsymbol{\tau} = \begin{cases} O(r^{-2(1-\gamma)}), & \text{Oldroyd-B,} \\ O(r^{-(1-\lambda_0)(3-\lambda_0)/4}), & \text{Giesekus,} \end{cases} \quad (7.1)$$

$$\mathbf{T}_N = \begin{cases} O(r^{-(1-\gamma)(2-\gamma)}), & \text{Oldroyd-B,} \\ O(r^{-(1-\lambda_0)}), & \text{Giesekus,} \end{cases} \quad (7.2)$$

$$\mathbf{u} = \begin{cases} O(r^{(3-\gamma)\gamma-1}), & \text{Oldroyd-B,} \\ O(r^{\lambda_0}), & \text{Giesekus,} \end{cases} \quad (7.3)$$

$$\text{Boundary layer thickness} = \begin{cases} O(r^{(2-\gamma)}), & \text{Oldroyd-B,} \\ O(r^{(3-\lambda_0)/2}), & \text{Giesekus,} \end{cases} \quad (7.4)$$

Here, $\lambda_0 \in [1/2, 1)$ is the Newtonian flow field eigenvalue given by the smallest positive root of the transcendental equation

$$\sin\left(\frac{\lambda_0\pi}{\gamma}\right) = -\lambda_0\sin\left(\frac{\pi}{\gamma}\right) \quad (\text{no-slip/ no-slip corner}). \quad (7.5)$$

For a Newtonian liquid the asymptotic behaviour of the velocity and pressure near the corner singularity is given by

$$u = O(r^{\lambda_0}), \quad p = O(r^{\lambda_0-1}). \quad (7.6)$$

For the intersection of a no-slip boundary with a shear-free surface boundary, the local asymptotic solution for the singular behaviour of velocity and pressure can be derived in an analogous manner to the no-slip corner case. Moffatt (1964) demonstrated that for the intersection of a no-slip and a shear-free surface boundary the Newtonian flow field is characterised by the smallest eigenvalue, $\lambda_0 \in (0, 0.5]$, that satisfies

$$\sin(2\lambda_0\theta) = \lambda_0\sin(2\theta), \quad (\text{no-slip/ shear-free corner}), \quad (7.7)$$

and the condition (7.6) holds (see also Salamon et al. (1997)). In the case of $\theta = 180^\circ$, the jump from no-slip to shear-free boundary is called the stick-slip problem as depicted in Figure 7.2(b). Richardson (1970) provided an analytical solution for the stick-slip problem and showed that the pressure and the velocity gradient around the singularity are

characterised by an inverse square root, that is,

$$\nabla \mathbf{u} = O(r^{-1/2}), \quad p = O(r^{-1/2}). \quad (7.8)$$

The investigation of an intersection of a Navier's slip and shear free surface is considerably more complicated and has been investigated by Salamon et al. (1995, 1997). They demonstrated that Navier's slip boundary condition behaves at leading-order like a shear-free surface in the local asymptotic solution. Moffatt (1964) showed that a wedge of angle θ formed from two shear-free surfaces has asymptotics described by the characteristic equation

$$\lambda_0 \cos\left(\frac{(\lambda_0 + 1)\theta}{2}\right) \cos\left(\frac{(\lambda_0 - 1)\theta}{2}\right) = 0, \quad (\text{Navier's slip/ shear-free corner}), \quad (7.9)$$

where $\lambda_0 \in (0, 0.5]$ and again the velocity and pressure are characterised by (7.6). In all these cases the stress values at the singularity are infinite. These infinite stress values near the singularity impact the accuracy of the numerical solution. As the computed stress and pressure values cannot be infinite at the singular point, we have large discretisation errors near the singularity and the numerical solution is tainted by Gibbs-type spurious oscillations that occur in the approximation of rapidly changing functions using polynomials. These Gibbs-type oscillations further pollute the numerical solution and destroy the rate of convergence of the solution with mesh refinement.

For Newtonian flows, the high discretisation errors in the vicinity of the singularity stay confined to this area. This is due to the fact that the flow near the corner singularity can be assumed to be creeping as the inertia terms are negligible near the no slip boundary and the flow is described by the Stokes equation, which is elliptic and therefore has no real characteristics. This means the discretisation errors are not propagated downstream along the streamlines and even though the numerical solution is highly polluted near the singularity due to large discretisation errors, the error can be controlled by mesh refinement (Blum (1990)).

However, for viscoelastic flows the discretisation error originating at the singularity can be propagated along the characteristics, i.e. the stream lines, into the whole domain (see Owens and Phillips (2005) for further explanation) due to the hyperbolic nature of the constitutive equations. This propagated error can grow downstream causing large scale oscillations in the solution. For the die swell problem, this can cause large oscillations to appear near the singularity at the die exit and these oscillations are then convected downstream and cause violent oscillations in the free surface shape which can cause the simulations to breakdown. This makes the numerical solution of viscoelastic flows in the presence of geometric singularities particularly challenging.

To improve the stability and quality of the numerical solution, special numerical techniques have been developed such as the singular finite element method (Georgiou et al., 1989; Georgiou and Boudouvis, 1999). Alternatively, the problem can be modified by introducing slip along the die wall to alleviate the strength of the singularity. Introducing slip along the wall is experimentally justified (see Denn (2001)). However, despite some early successes of Silliman and Scriven (1980), who showed that for Newtonian extrudate swell, the use of Navier's slip boundary condition yields bounded stresses and Wesson and Papanastasiou (1988), who demonstrated that the maximum attainable Weissenberg number for the UCM and Oldroyd-B model could be increased using a slip condition given by $u = \beta_{sl}\tau_w^m$, where τ_w is the wall shear stress, the use of the slip condition as a "cure" for the singularity remains questionable. Salamon et al. (1995) pointed out that the results of Silliman and Scriven (1980) were obtained before more advanced finite element techniques and faster computers allowed careful mesh refinement. Salamon et al. (1995) investigated planar Newtonian die swell involving Navier's slip condition using extremely fine meshes around the singularity to capture and resolve the behaviour of velocity and stress at the singularity. Their results revealed that while the singularity in the shear stress is alleviated at the die exit edge, the pressure and viscous normal stress remain singular. In addition, they pointed out that the length scales for the flow structure are extremely small even as the slip parameter is increased and therefore accurate calculations remain extremely difficult. Moreover, in further investigations, Salamon et al. (1997) found that the slip condition along the wall can yield more singular behaviour than the no-slip condition. This behaviour is also predicted by the local asymptotic analysis as depicted in Figure 7.3. Figure 7.3 displays the values of the eigenvalue λ_0 for a range of angles $180^\circ \leq \theta < 270^\circ$ for the corner singularity of an intersection between no-slip/no-slip boundaries, no-slip/shear-free boundaries and slip/shear-free boundaries. The eigenvalues for the intersection of slip/shear-free boundaries are smaller than for the no-slip/shear-free boundary intersection hence leading to sharper increases of the pressure and stress values near the singularity. Nevertheless, the use of the slip condition along the die wall is highly relevant due to its existence in experiments.

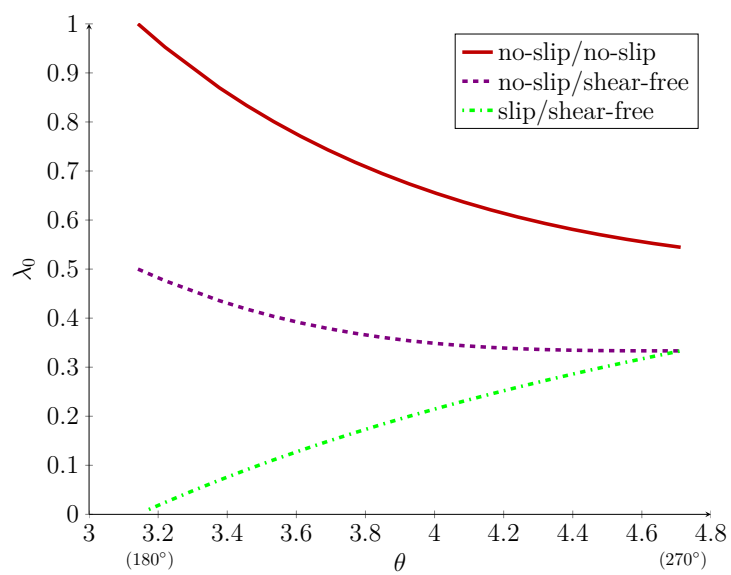


Figure 7.3.: Dependency of the smallest Newtonian eigenvalue on the angle θ of a corner singularity between no-slip/no-slip, no-slip/shear-free and slip/shear-free boundaries.

7.1. Computational Domain and Quantities of Interest

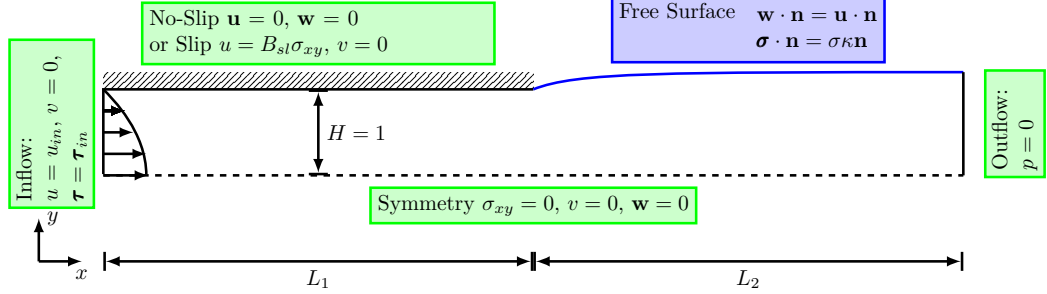


Figure 7.4.: Schematics of the die swell flow configuration including boundary conditions.

In this thesis, we consider the extrusion of Newtonian, Oldroyd-B and Giesekus fluids from a planar die. The schematics of the employed planar die geometry is depicted in Figure 7.4. We consider a die of length L_1 and height H , and an exit region of length L_2 . The length of the die is chosen sufficiently long in order to guarantee a fully developed flow far upstream of the exit plane.

In the next Section, we mainly investigate two quantities of interest: the swelling ratio and the exit pressure correction factor. These two quantities are commonly investigated in the literature. This is due to their importance for practitioners. The extrudate swell ratio is of importance in extrusion processes and the excess pressure loss gives an indication how much extra pressure has to be applied to achieve certain swell ratios. The swelling ratio, χ_R , is defined as

$$\chi_R = \frac{h_f}{H}, \quad (7.10)$$

where H is the half-height of the die and h_f is the maximum height of the free surface with respect to the symmetry line. The swelling ratio is a function of several parameters

$$\chi(H, \langle u \rangle, \text{Re}, \text{Ca}, B_{sl}, \text{Wi}, \alpha), \quad (7.11)$$

where H is the half height of the die, $\langle u \rangle$ is the average inflow velocity, Re is the Reynolds number, Ca is the capillary number, B_{sl} is the slip parameter along the die wall, Wi is the Weissenberg number and α is the mobility parameter.

The dimensionless exit pressure correction factor, n_{ex} , is defined as

$$n_{ex} = \frac{\Delta p - \Delta p_0}{2\sigma_w}, \quad (7.12)$$

where Δp is the pressure drop between the inlet and the outlet plane, Δp_0 is the pressure drop between the inlet and the exit of the die for fully developed Poiseuille flow and σ_w

is the shear stress at the channel wall corresponding to fully developed Poiseuille flow. In this thesis, we take the pressure differences along the centreline. The pressure drops are given by (Tanner (2002))

$$\Delta p_0 = p|_{x=-L_1} = 2\sigma_w \frac{L_1}{H} \quad (\text{Poiseuille flow for } x \in [-L_1, 0]), \quad (7.13)$$

$$\Delta p = p|_{x=-L_1} - p|_{x=L_2} \quad (\text{Extrudate Swell for } x \in [-L_1, L_2]), \quad (7.14)$$

where H is the total height of the channel.

In our computations, we employ the following boundary as depicted in Figure 7.4 for a half-channel height of $H/2 = 1$. We assume the flow is symmetric and along the symmetry line, we set $v = 0$ and $\sigma_{xy} = 0$. Note that, $\sigma_{xy} = 0$ is set through the boundary integral in the momentum equation (4.42). For the die swell geometry this means there is no contribution of the Neumann boundary integral in the momentum equation along the symmetry line. At the die wall we either impose no-slip boundary conditions, i.e. $\mathbf{u} = \mathbf{0}$, or Navier's slip condition. Navier's slip boundary condition is a mixed boundary condition of Dirichlet and Neumann type. For the extrudate swell geometry depicted in Figure 7.4, we set $v = 0$ and impose $\sigma_{xy} = \frac{1}{B_{sl}}u$ through the Neumann boundary term in the momentum equation. This means for the velocity component u along the slip boundary Γ_{sl} , we obtain the boundary integral

$$\int_{\Gamma_{sl}} (\boldsymbol{\sigma} \cdot \mathbf{n} \phi_{\mathbf{u}}) \mathbf{e}_x d\Gamma = \int_{\Gamma_{sl}} \frac{1}{B_{sl}} u \phi_u d\Gamma, \quad (7.15)$$

where \mathbf{e}_x is the unit vector in the x -direction. At outflow, we employ an open outflow boundary condition. We assume a reference pressure of $p = 0$ along the outflow boundary and the remaining terms in the Neumann boundary integral along the outflow boundary in the momentum equation are evaluated along with the volume integrals. In practice, this means that the boundary terms along the outflow boundary are integrated into the corresponding global matrices of system (6.88) of the coupled solver for velocity, pressure and velocity gradient projection tensor. We also integrate the boundary integral resulting from the slip condition (7.15) into the system (6.88). At inflow, we either impose the parabolic profile

$$u = \frac{3}{2} (1 - y^2), \quad v = 0, \quad (7.16)$$

in combination with no-slip along the die wall or the profile (Kountouriotis et al. (2013))

$$u = \frac{3}{2(1 + 3B_{sl})} (1 - y^2 + 2B_{sl}), \quad \frac{\partial u}{\partial y} = \frac{-3y}{(1 + 3B_{sl})}, \quad v = 0, \quad (7.17)$$

in combination with the slip boundary condition. For the elastic stress, we impose

$$\tau_{xx} = 2 \text{Wi} (1 - \beta) \left(\frac{\partial u}{\partial y} \right)^2, \quad (7.18)$$

$$\tau_{xy} = (1 - \beta) \frac{\partial u}{\partial y}, \quad (7.19)$$

$$\tau_{yy} = 0 \quad (7.20)$$

at the inflow boundary.

Concerning the mesh velocity, we employ the following boundary conditions. We consider the mesh to be fixed at inflow, the die wall and along the symmetry line, i.e. homogeneous Dirichlet conditions, $\mathbf{w} = (w_x, w_y) = \mathbf{0}$, are imposed for the mesh-velocity along these boundaries. At the outflow boundary, we allow the mesh to move in the y -direction, i.e. $\nabla w_y \cdot \mathbf{n} = 0$, and fix it in the x -direction, $w_x = 0$. At the free surface, we enforce the kinematic boundary condition through the mesh velocity in terms of a Dirichlet boundary condition for the mesh-velocity, i.e.

$$\mathbf{w} \cdot \mathbf{n} = \mathbf{u} \cdot \mathbf{n}. \quad (7.21)$$

To avoid mesh distortion, we choose to move the mesh along the free surface boundary only in the y -direction. The mesh is moved with sufficient velocity w_y into the y -direction to ensure that no particle crosses the interface, that is,

$$w_x = 0, \quad w_y = v + u \frac{n_x}{n_y}. \quad (7.22)$$

The spline representing the free surface is employed using the not-a-knot conditions at both ends of the spline as explained in Section 6.3.

7.2. Newtonian Die Swell

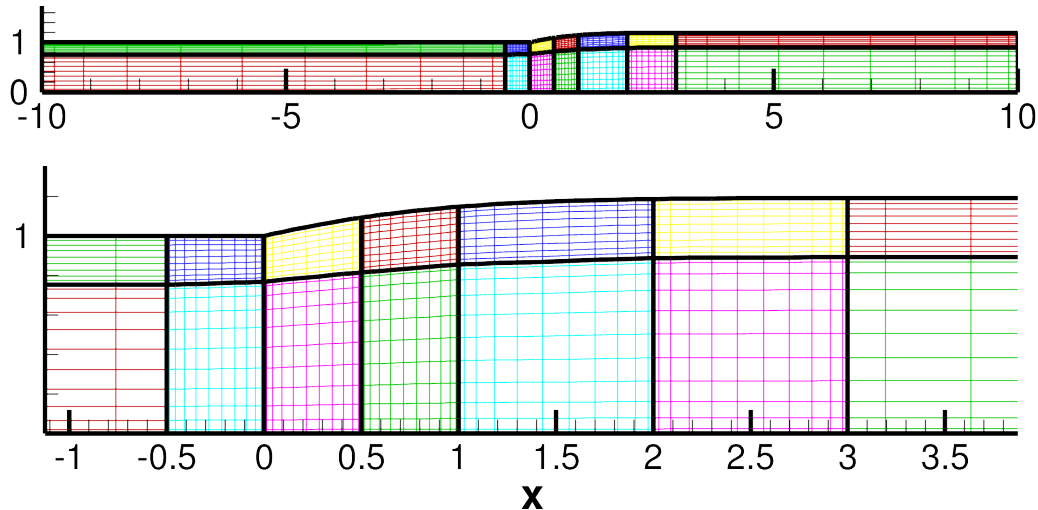


Figure 7.5.: Mesh configuration used for the Newtonian die swell computation.

In this Section, we consider the swell of Newtonian fluids and investigate the impact of inertia on the swelling ratio. A journal article detailing the findings in this Section is in preparation (Claus and Phillips, 2013b). We consider a die of length $L_1 = 10$ and an exit region of length $L_2 = 10$. The entry length is sufficient for the fluid to guarantee a fully developed flow far upstream from the exit of the die. The exit length is chosen sufficiently long to allow the free surface to reach a constant downstream height for a large range of Reynolds numbers. The chosen mesh consists of $N_{el} = 14$ elements as shown in Figure 7.5 and we increase the polynomial order to refine the mesh. We choose a time step of 5×10^{-3} .

The Newtonian die swell is mainly influenced by the reorganisation of the velocity profile from the parabolic Poiseuille flow inside the die to plug flow downstream (Tanner (2002)). This transition is characterised by the sudden jump in the shear stress at the die exit (Russo (2009)). Inside the die, the shear stress at the wall is at its maximum with particles sticking to the wall (for the no-slip boundary condition). Then immediately after the die exit, the removal of the wall shear stress causes a boundary layer to form at the free surface. In this layer, the parabolic velocity profile adjusts itself so as to satisfy the condition of zero shear stress at the free surface. This sudden jump in the shear stress at the die exit causes an instantaneous acceleration of the particles at the free surface causing the fluid jet to swell. Due to the conservation of energy (there is no gain or loss of energy since gravity is neglected and the free surface boundary is frictionless) the flow rate in the die has to be

the same as in the uniform plug flow, which yields

$$u_{plug} = \frac{1}{2h_{plug}} \int_{-H}^H u(y) dy, \quad (7.23)$$

where h_{plug} is the height of the fluid jet in the uniform flow region and $u(y)$ is the parabolic Poiseuille flow profile. We have $0 < u_{plug} < u_{max}$, which means that while particles at the free surface accelerate when exiting the die the flow near the centreline decelerates.

Inertialess Newtonian extrudate swell was first investigated in the mid 1970s by Tanner (1973) and Nickell et al. (1974). In a series of articles, Tanner (1973); Tanner et al. (1975); Reddy and Tanner (1978) performed comparisons with experiments. Tanner (2002) summarises a range of results for Newtonian die swell with $Re = 0$ and negligible surface tension and gives extrapolated values from these results. For axisymmetric die swell Tanner's extrapolated swelling ratio is $\chi_R = 1.127 \pm 0.003$ and for planar die swell $\chi_R = 1.190 \pm 0.002$. Table 7.1 summarises some swelling ratios obtained in the literature for plane Newtonian die swell. In general, an increase in the degrees of freedom yields less swelling. The effect of inertia and surface tension on the Newtonian extrudate swell was first investigated by Omodei (1980, 1979). Later, Georgiou and Boudouvis (1999) compared the singular finite element method to standard FEM for the simulation of Newtonian die swell including inertia and surface tension. The latest detailed investigations of the impact of inertia and surface tension was provided Mitsoulis et al. (2012), who in addition to these factors used FEM to investigate the impact of slip, gravity and compressibility. Inertia causes a decrease of the swelling and the liquid jet eventually contracts for sufficiently high Reynolds numbers.

We performed computations for Reynolds numbers ranging from 0 to 100. We start computing the extrudate swell for Reynolds number 0 and initialise this computation with the solution of the corresponding stick-slip problem (Figure 7.2(b)). After having obtained the extrudate swell for Reynolds number 0, we increase the Reynolds number in steps of 1 from 1 to 10 and in steps of 10 from 10 to 100, each time using the result of the converged

Table 7.1.: Newtonian swelling ratios for $Re = 0$

	Method	DOF	χ_R
Crochet and Keunings (1982)	FEM	562	1.200
		1178	1.196
Reddy and Tanner (1978)	FEM	254	1.199
Mitsoulis et al. (2012)	FEM	11270	1.191
		30866	1.186
Georgiou and Boudouvis (1999)	FEM (SFEM)	7528	1.1919 (1.1863)
	FEM (SFEM)	12642	1.1888 (1.1863)

extrudate swell of the previous lower Reynolds number as the initial condition. As the convergence criterion, we choose a change of the maximum absolute value of all variables including the mesh velocity of less than 10^{-6} . Figure 7.6 and Table 7.2 shows the comparison of the swelling ratios obtained with our algorithm to the results of Mitsoulis et al. (2012), which are in excellent agreement.

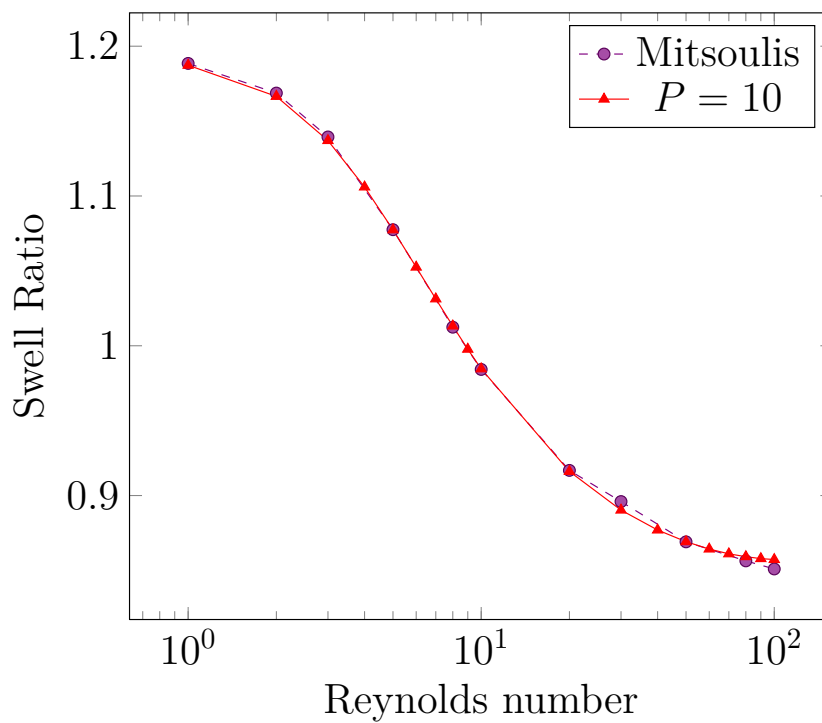


Figure 7.6.: Swell ratios for Newtonian fluid for $P = 10$ in comparison with Mitsoulis et al. (2012)

Table 7.2.: Comparison of Newtonian die swell ratio for increasing Reynolds number with Mitsoulis et al. (2012).

Re	Mitsoulis et al. (2012)	$P = 10$	Re	Mitsoulis et al. (2012)	$P = 10$
0	1.1915	1.1912	10	0.9842	0.9846
1	1.1885	1.1873	20	0.9168	0.9161
2	1.1687	1.1665	30	0.8960	0.8903
3	1.1394	1.1370	40		0.877
4		1.1060	50	0.8691	0.8692
5	1.0775	1.0774	60		0.8643
6		1.0525	70		0.8611
7		1.0313	80	0.8564	0.8592
8	1.0124	1.0132	90		0.8579
9		0.9977	100	0.85103	0.8573

Figure 7.7 displays the corresponding free surface spline profiles. We observe that the swelling ratio decreases at an accelerating pace with increasing Reynolds number until a Reynolds number of 6. For a Reynolds number equal to 6, we see the onset of a delayed die swell this means the fluid surface first goes through a minimum before it swells again. The delay in the swelling of the jet increases with increasing Reynolds number from $Re = 6$ to $Re = 10$. For $Re = 9$ and $Re = 10$, the fluid contracts ($\chi_R < 1$) but still experiences some swelling after going through a minimum near the die exit. For $Re = 20$ to $Re = 100$ the fluid does not experience any delayed swelling and contracts. For $10 < Re < 40$ the fluid contracts very fast with increasing Reynolds number. This trend in the contraction rate with increasing Reynolds number then slows down and approaches a limit for $40 < Re < 100$. The limit for infinite Reynolds number was estimated by Tillett (1968) who performed a boundary layer analysis for a free Newtonian jet and predicted a limiting value of $\chi_R = 0.8333$ for an infinite Reynolds number.

We explore the contour plots of the velocity field for a range of Reynolds numbers in Figures 7.8 (horizontal velocity component u) and 7.9 (vertical velocity component v). With increasing Reynolds number the horizontal velocity increases along the centreline, the vertical velocity near the singularity induced by the sudden change in the boundary condition decreases and the transition zone under the free surface from Poiseuille flow in the die to plug flow is extended downstream. This shows that with increasing Reynolds number the particles along the centreline are accelerated and decelerated near the free surface yielding the contraction of the free fluid jet. This is indeed the behaviour we would expect as particles leaving the die will deviate less from their initial path for increasing inertia. As pointed out by Mitsoulis et al. (2012) in order to accommodate the whole transition zone the domain length of the free fluid jet should be chosen as $L_2 = Re$. However, we employ open boundary conditions at outflow which enable us to compute the extrudate swell accurately in the truncated domain with $L_2 = 10$. As demonstrated by Mitsoulis and Malamataris (2011) the results for extrudate swell with a domain length $L_2 = 6$ are virtually identical with those from long domains with $L_2 = Re$, for all variables, when using the open boundary condition at outflow. However, in this case, the swell ratio results are only correct up to the truncated length as they continuously drop beyond the truncated domain. A small discrepancy between swell ratios for different domain lengths can therefore be expected.

To investigate the transition from Poiseuille flow to plug flow for increasing Reynolds number further, we plot the velocity and pressure along different paths in the domain. Figure 7.10 displays the velocity components along the symmetry line (i.e. $v = 0$) and along the free surface boundary. In Figure 7.10(a), we see the smooth transition of the velocity field from the maximum of the parabolic profile to the average plug flow velocity

given by (7.23), i.e. $u_{plug} = 1/\chi_R$. As the swell decreases with increasing Reynolds number the plug flow value of the velocity increases with increasing Reynolds number. With increasing Reynolds number the change from the maximum parabolic value of the velocity component u to the plug flow value shifts further downstream. For $Re = 0$, the velocity reaches the plug flow value at around $x \approx 3$, for $Re = 10$ at $x \approx 6$ and for $Re = 50$ the plug flow value is not reached within our computational domain. However, as pointed out above, due to the use of open boundary conditions at outflow, the velocity and pressure profiles stay accurate even if they are truncated at outflow. Along the free surface boundary (Figure 7.10(b), (c)), the velocity component u increases sharply near the die exit until it reaches the plug flow value, the velocity component v goes through a maximum near the die exit for $Re = 0$ and $Re = 3$ and through a minimum for $Re > 7$, when particles are no longer constrained by the no-slip boundary condition. This causes the swell (for $v > 0$) or the contraction (for $v < 0$) of the free surface near the die exit until the surface is sufficiently curved to obtain a zero total shear stress (i.e. $\mathbf{t} \cdot \boldsymbol{\sigma} \cdot \mathbf{n} = 0$). Further downstream when the free surface boundary has reached its maximum swelling value, the vertical velocity component reaches zero in accordance with the condition of no particle penetration along the surface (horizontal free surface boundary has outward normal $\mathbf{n} = (0, 1)$ and therefore $\mathbf{u} \cdot \mathbf{n} = v = 0$). The maximum value of v along the free surface decreases with increasing Reynolds number ($0 \leq Re \leq 5$). For the range of Reynolds number that causes a delayed die swell the velocity component v first undergoes a sharp minimum and then goes through a maximum ($6 \leq Re \leq 10$). For the range of Reynolds numbers that cause a contraction of the free Newtonian jet, the velocity component v goes through a minimum and then slowly approaches zero ($Re > 10$). Figure 7.11 shows the velocity components in the cross stream wise direction at inflow ($x = -10$), near the die exit ($x = -0.2, x = 0.2$), further downstream in the free jet region $x = 1$ and at outflow $x = 10$. The velocity component u , is parabolic at inflow, shortly before the die exit ($x = -0.2$) the parabolic profile flattens inside the die, after the die exit the parabolic profile flattens further and builds a boundary layer in which it goes through a minimum $x = 0.2$, then flattens increasingly until the plug flow value is reached. The vertical velocity component, which is zero at inflow, forms a parabolic like profile with a small boundary layer near the die exit inside the die, which first sharpens shortly after exiting the die and then relaxes back to the zero value.

On the contour plots for the pressure p displayed in Figure 7.12, we observe that the pressure isobars are curved near the die exit and in the free jet region in the downstream direction for low Reynolds number ($Re = 0, 3, 7$) and in the upstream direction for higher Reynolds numbers ($Re > 10$). The change in the pressure becomes more apparent when we explore the pressure values along the symmetry line (Figure 7.13(a)). Inside the die, the pressure gradient is constant as expected for Poiseuille flow. However, near the die

exit ($x = 0$) the pressure curves smoothly and approaches zero for the plug flow. For higher Reynolds numbers the pressure on the centreline goes through a minimum. This behaviour of the pressure yields a shift in the pressure values at inflow, which is expressed by the exit pressure correction as defined in Equation (7.12). Table 7.3 lists a comparison of the exit pressure correction for $Re = 0$ of our scheme and the swell ratio for increasing mesh refinement with the results obtained by Taliadorou et al. (2007). We obtain close agreement for a much smaller number of degrees of freedom, which demonstrates that p -refinement is effective for the Newtonian extrudate swell even though the result is polluted by Gibbs oscillations in the pressure around the singularity (Figure 7.14(c)). The Gibbs oscillations in the pressure stay confined to the elements adjacent to the singularity.

Increasing the Reynolds number leads to a dampening in the oscillations in the elements adjacent to the singularity and the extreme values of the pressure at the singularity decrease significantly (Figure 7.13(b)). As demonstrated in Section 3.8.2 increasing the polynomial order yields an increase in the number of oscillations. However, the amplitude of each oscillation is reduced with increasing polynomial order P . Increasing the polynomial order also has the effect of exponentially increasing the maximum value of the pressure and sharply increasing the minimum value of the pressure at the singularity which reflects an improved approximation of the infinite pressure value at the singularity (Figure 7.14(d)). While the infinite pressure values at the singularity hamper the rate of convergence of the numerical pressure solution, the values of the velocity components along the free surface are converged for $P \geq 10$ (see Figure 7.14(a), (b)).

Table 7.3.: Comparison of swell ratios and exit pressure corrections for increasing number of degrees for freedom (DOF) between our algorithm and that of Taliadorou et al. (2007).

P	Spectral/hp method			Taliadorou et al. (2007) FEM		
	DOF	h_f	n_{ex}	DOF	h_f	n_{ex}
8	2624	1.1928	0.1507			
10	4116	1.1912	0.1503	37208	1.1953	0.1514
12	5944	1.1901	0.1497	43320	1.1908	0.1491
14	8108	1.1900	0.1491	49864	1.1893	0.1482
16	10608	1.1891	0.1485	60490	1.1878	0.1473

To alleviate the pressure singularity at the die exit, we investigate the effect of slip along the die wall on the dependent variables. We therefore change the inflow profile according to Equation (7.17) and employ the slip condition (7.15) along the die wall. We explore the velocity field and the pressure along the free surface for a slip parameter of $B_{sl} = 0.01$, $B_{sl} = 0.1$ and $B_{sl} = 0$ (no-slip) in Figure 7.15. With the introduction of slip along the wall, the horizontal velocity component experiences a smooth transition at the die exit

in vast contrast to the kink at the singularity that is observed for the no-slip condition ($B_{sl} = 0$) along the wall (Figure 7.15(a)). The change for the vertical velocity remains sudden and features a kink at the singularity. However, the maximum value of the vertical velocity component decreases with increasing slip (Figure 7.15(c)). The pressure profile at the singularity is changed drastically with slip along the wall and the Gibbs oscillations disappear (Figure 7.15(e), (f)). Even though the minimum of the pressure does not show a converging trend in the range of the employed polynomial orders, its value only increases slightly with increasing P (Figure 7.15(f)). Table 7.4 lists the swelling ratios for increasing polynomial order, P , for $B_{sl} = 0.1$ and $B_{sl} = 0.01$. The swelling ratios are converged to three decimal places. Figure 7.15(b), (d) shows that the velocity values are converged for $P \geq 10$. The free surface spline for increasing slip parameter is shown in Figure 7.16. Increasing the slip parameter yields a decrease in swelling.

Table 7.4.: Dependence of the swelling ratio on P for $B_{sl} = 0.1$ and $B_{sl} = 0.01$.

P	$B_{sl} = 0.1$	$B_{sl} = 0.01$
10	1.1041	1.1671
12	1.1041	1.1673
14	1.1040	1.1670

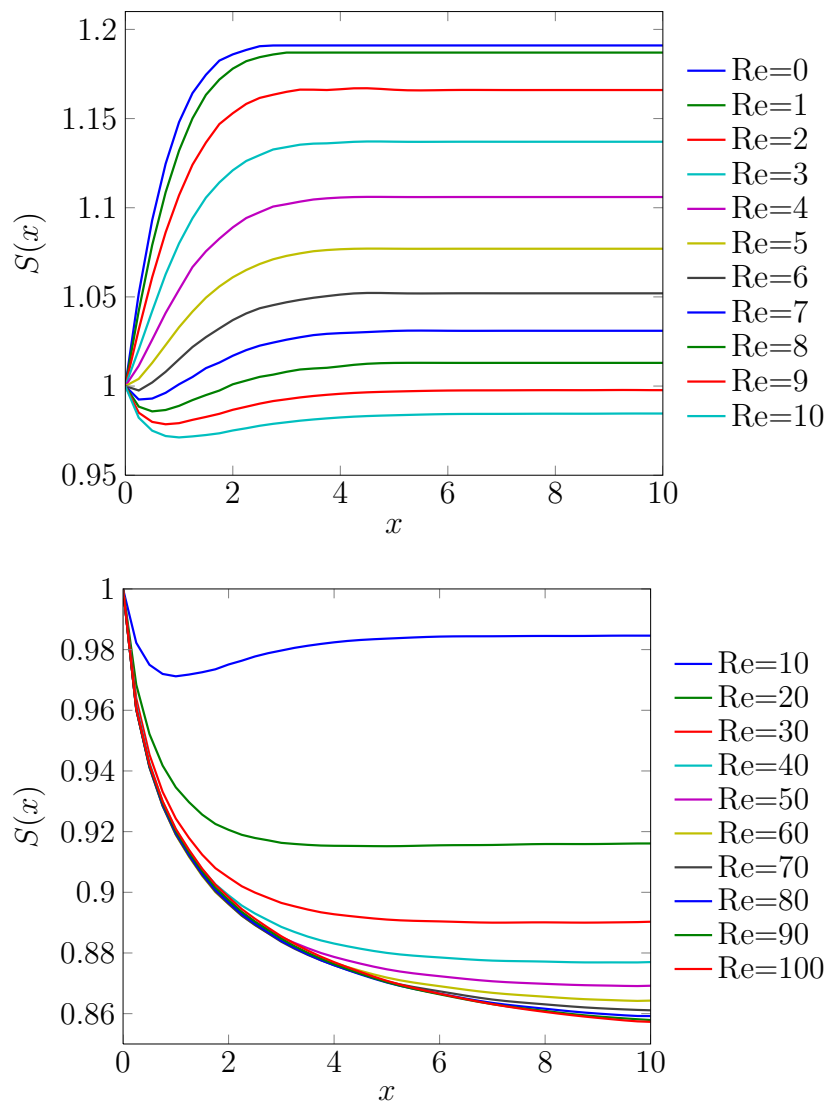


Figure 7.7.: Free surface spline profiles for Newtonian extrudate swell for $P = 10$ for a range of Reynolds numbers.

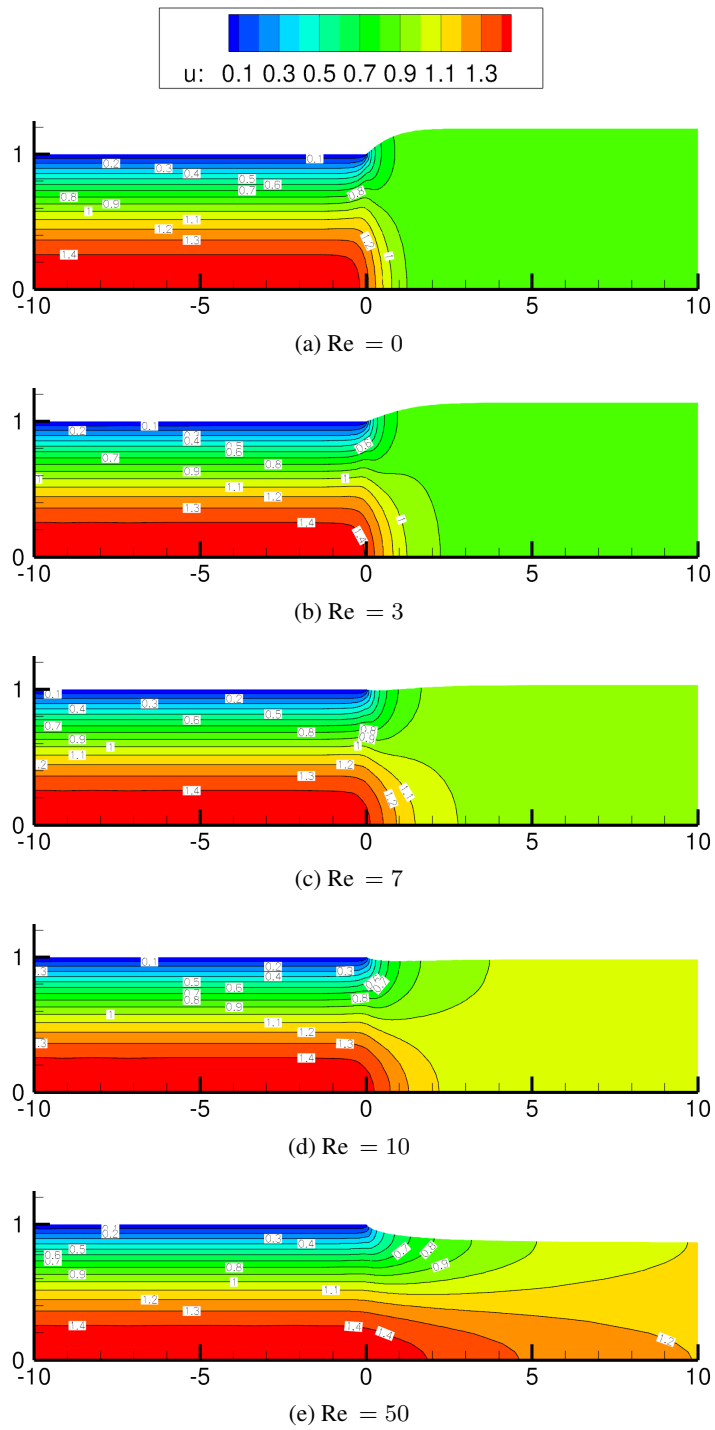


Figure 7.8.: Contour plots of horizontal velocity component u for $P = 10$ for a range of Reynolds numbers.

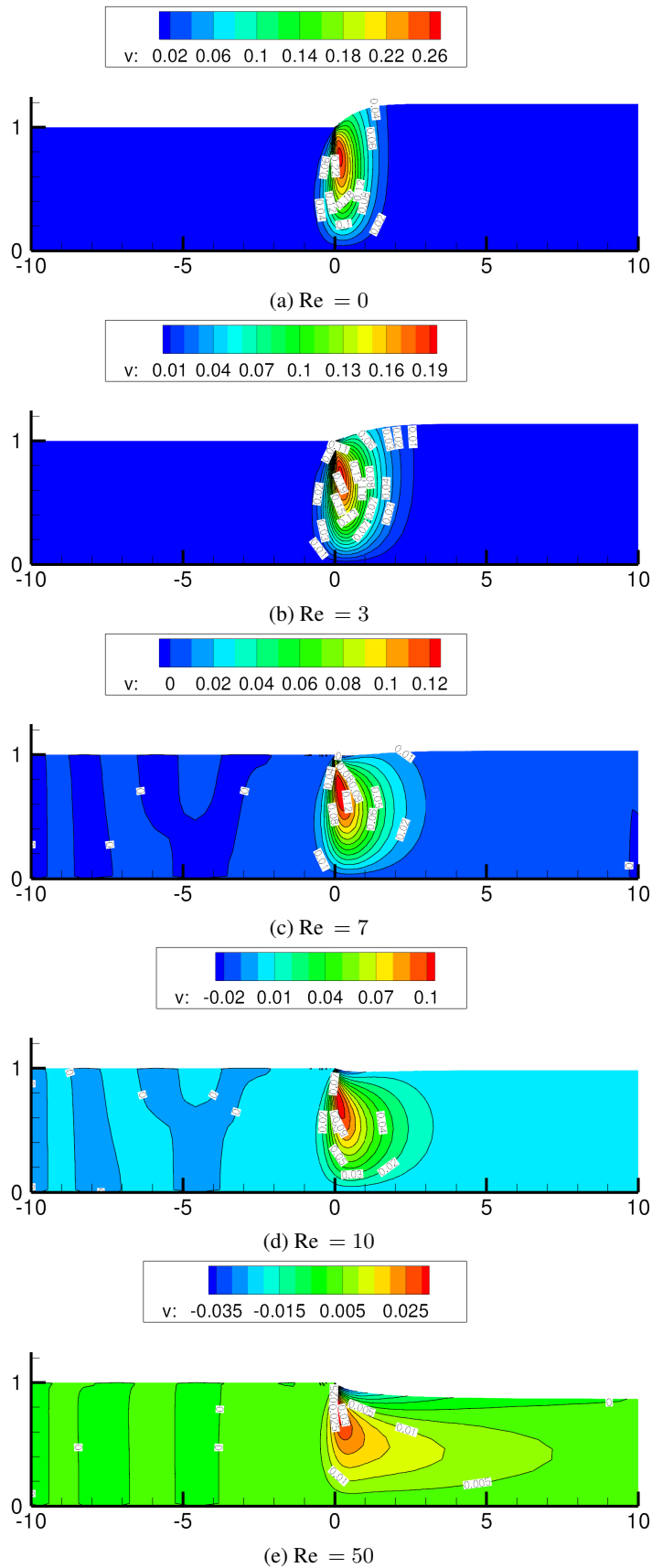


Figure 7.9.: Contour plots of vertical velocity component v for $P = 10$ for a range of Reynolds numbers.

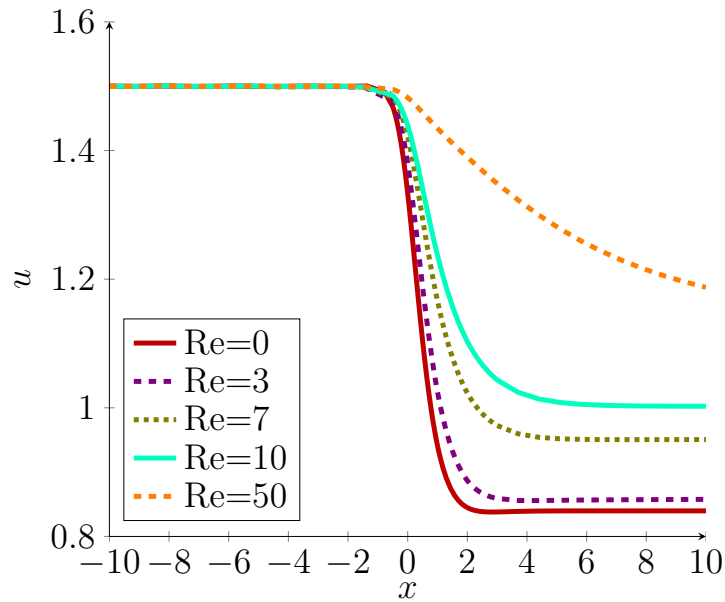
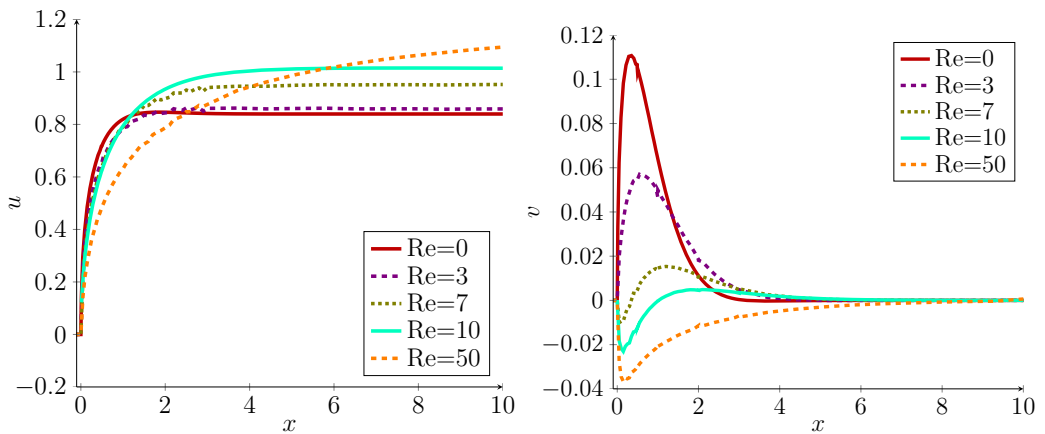
(a) Velocity component u along symmetry line ($v = 0$).(b) Velocity component u along free surface.(c) Velocity component v along free surface.

Figure 7.10.: Dependency of velocity components along (a) the symmetry line and (b)- (c) along the free surface on the Reynolds number.

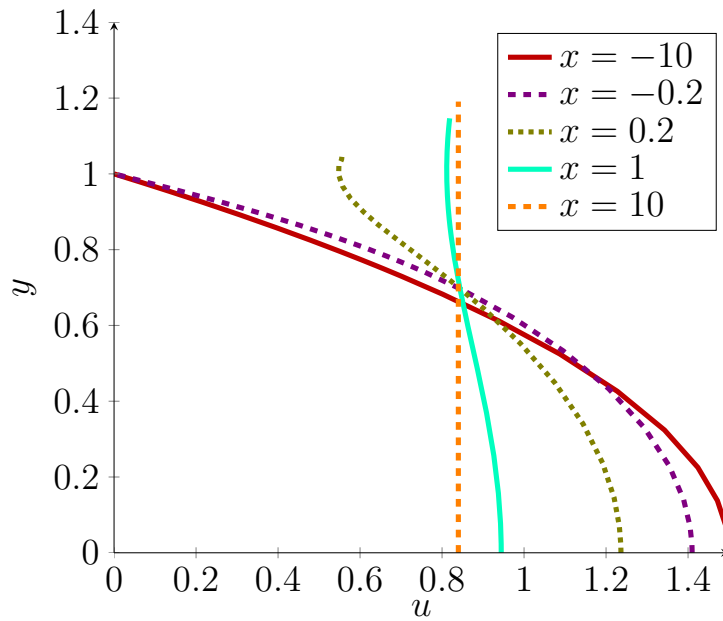
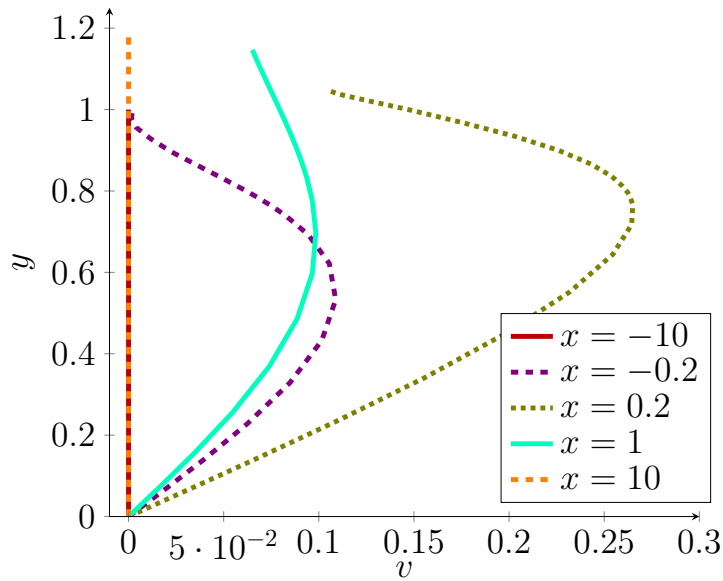
(a) Velocity component u in cross streamwise direction.(b) Velocity component v in cross streamwise direction.

Figure 7.11.: Velocity components in cross stream wise direction at inflow ($x = -10$), near the die exit ($x = -0.2$, $x = -0.2$), further downstream in the free jet region $x = 1$ and at outflow $x = 10$.

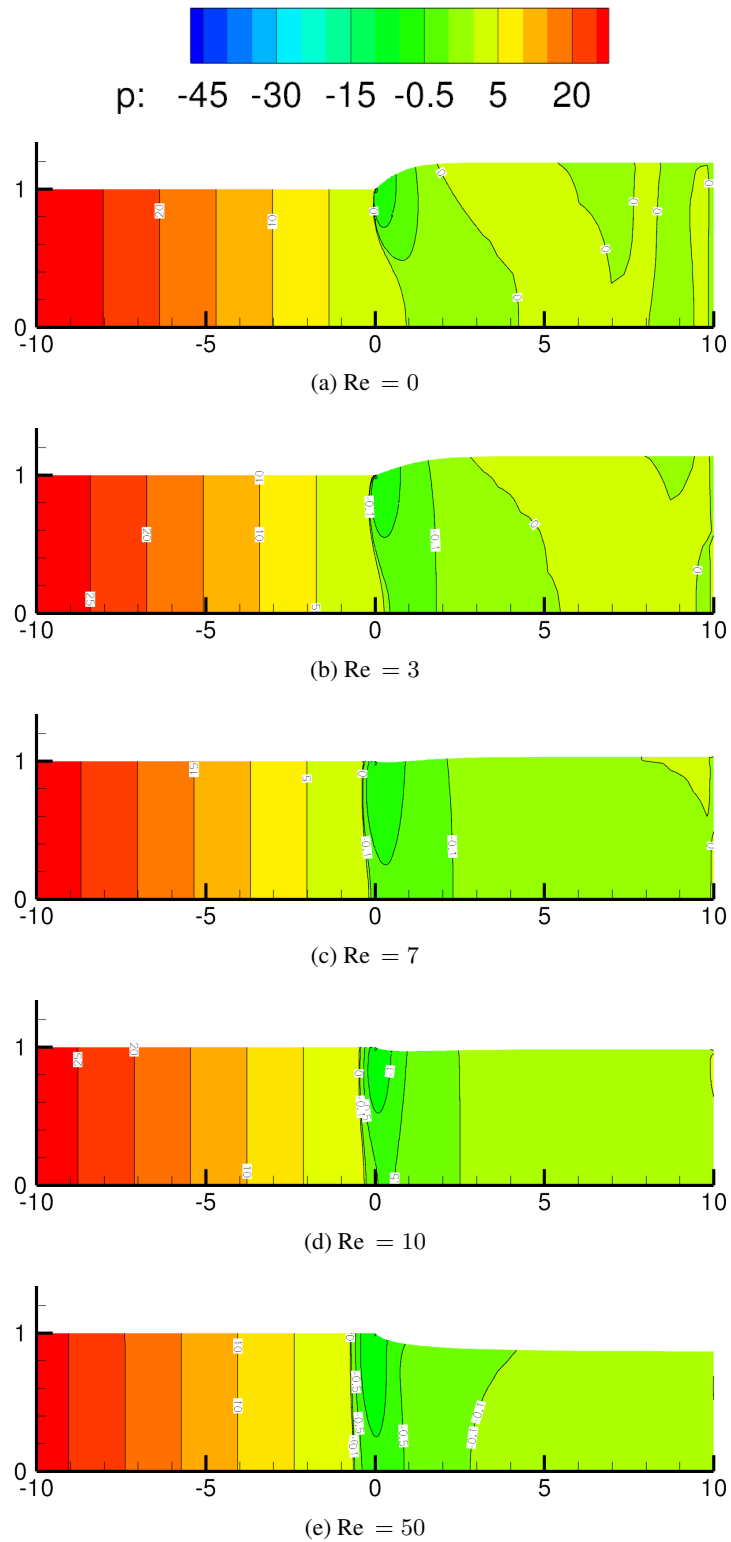
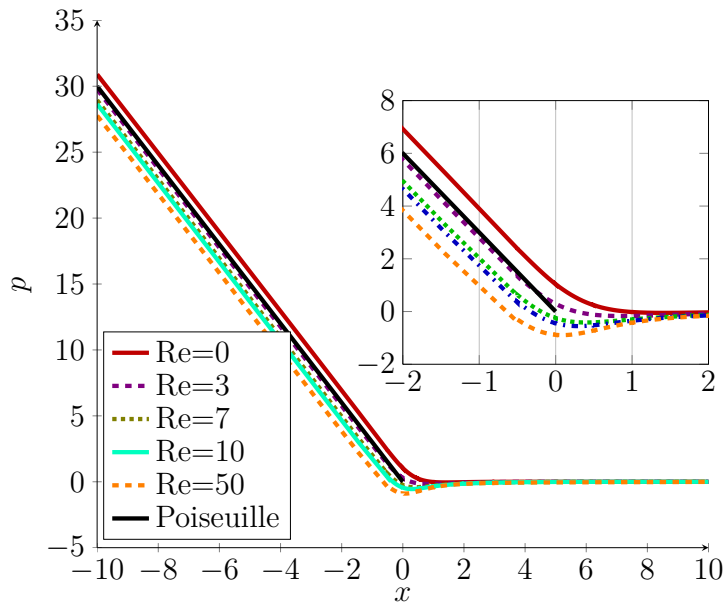
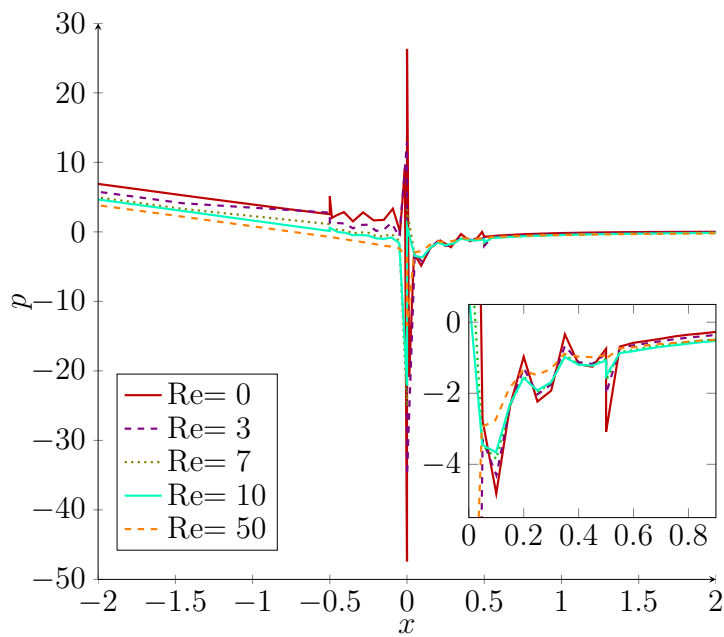
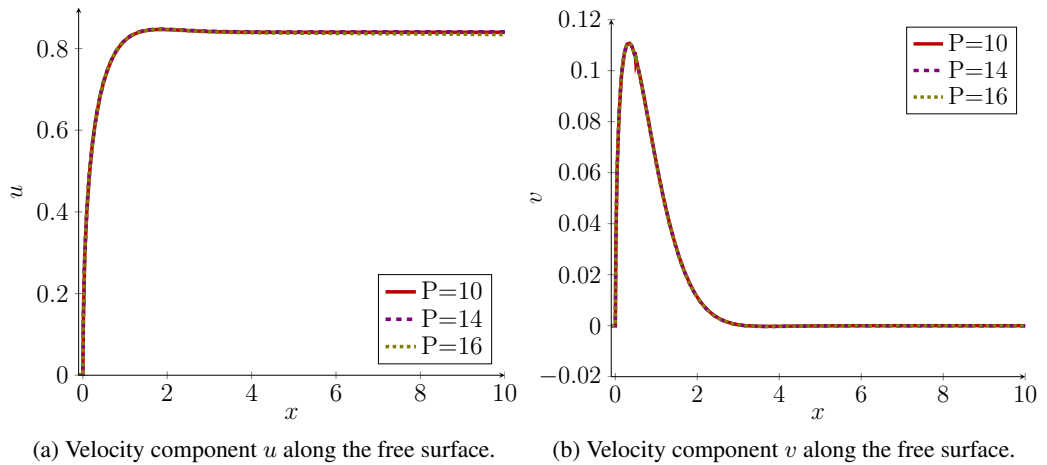
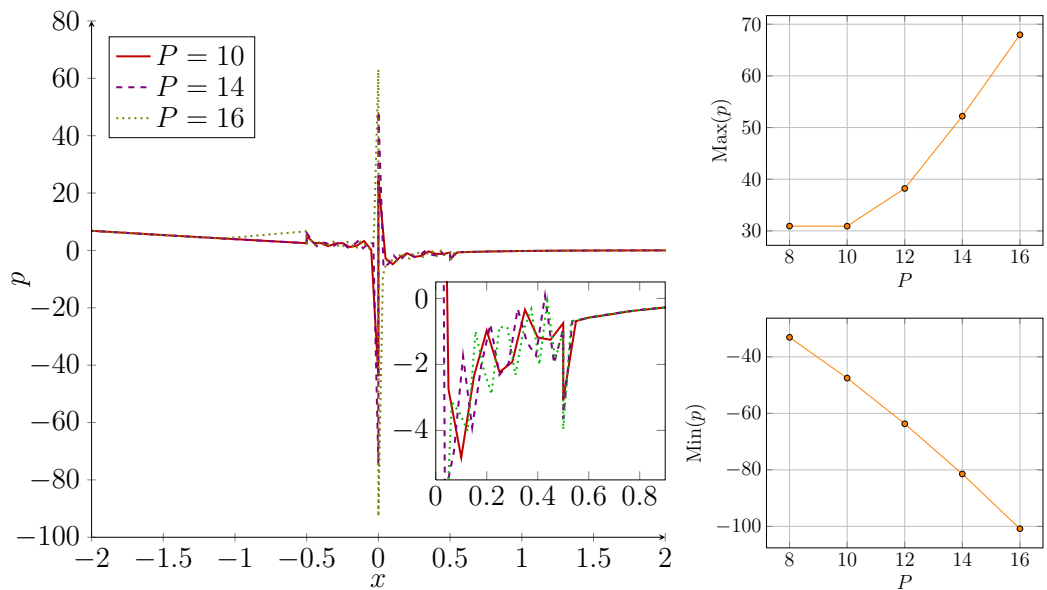


Figure 7.12.: Contour plots of pressure p for $P = 10$ for a range of Reynolds numbers.

(a) Pressure p along centreline.(b) Pressure p around the singularity at the die exit.Figure 7.13.: Plots of pressure p along (a) the centreline and (b) the wall and the free surface.

(a) Velocity component u along the free surface.(b) Velocity component v along the free surface.(c) Pressure p along the die wall and the free surface.

(d) Pressure minima and maxima.

Figure 7.14.: Influence of P -mesh refinement on (a) the velocity components u , (b) v and (c) pressure p along the free surface and the increase of maximum and minimum values of the pressure at the singularity with increasing polynomial order (d).

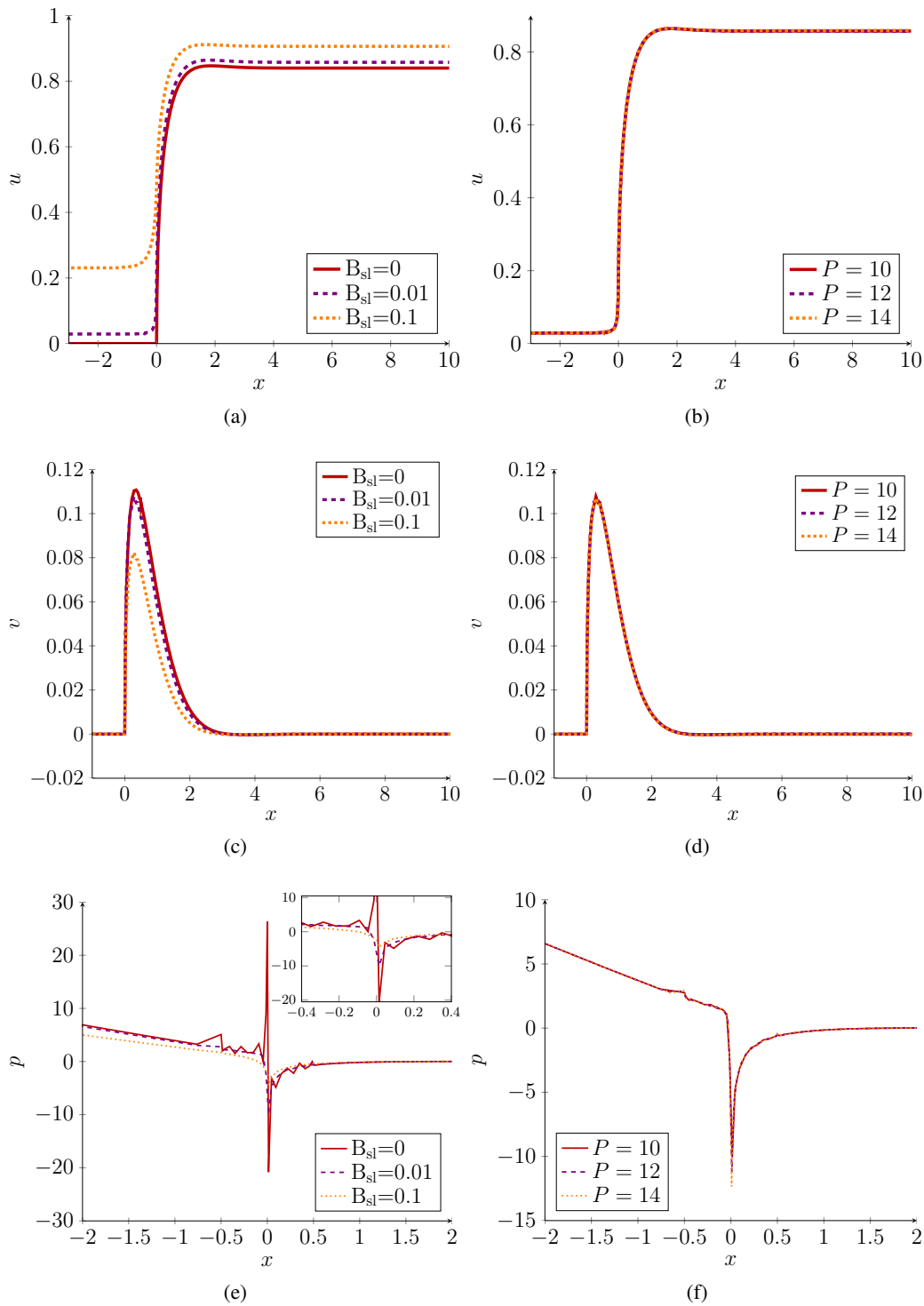


Figure 7.15.: Dependence of (a) velocity components u , (c) v and (e) pressure on the slip parameter for $P = 10$ and on mesh refinement for $B_{sl} = 0.01$ ((b),(d),(f))

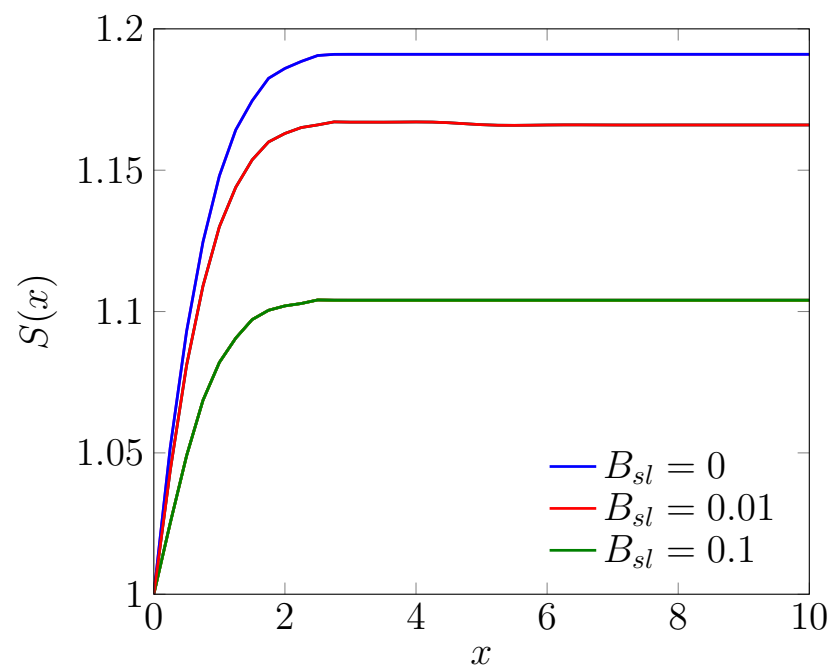


Figure 7.16.: Free surface spline profile for increasing slip parameter.

7.3. Viscoelastic Die Swell

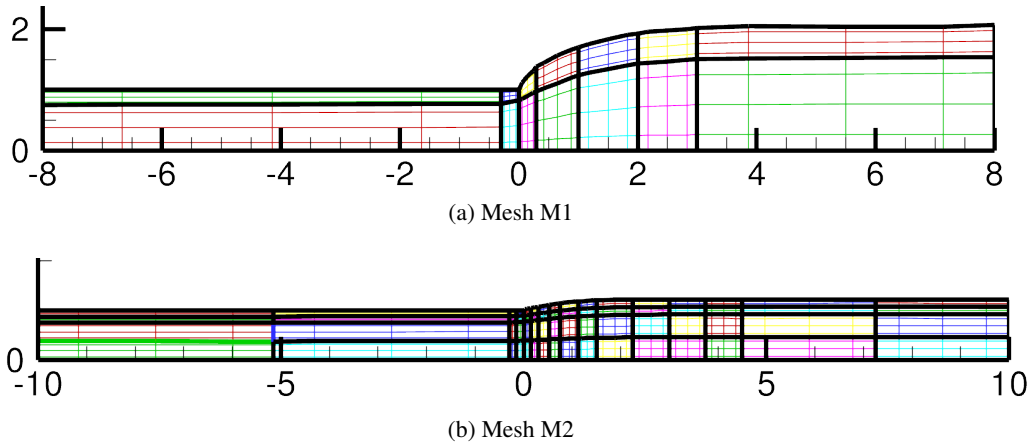


Figure 7.17.: Computational meshes employed for the viscoelastic extrudate swell computations.

In this Section, we present results for the viscoelastic extrudate swell for Oldroyd-B and Giesekus fluids. As detailed in the beginning of this Chapter, the computations of viscoelastic flows in the presence of the jump singularity at the boundary between the wall and the free surface, which yields infinite stresses, is very challenging. Discretisation errors originating at the singularity can be convected downstream for viscoelastic flows due to the hyperbolic nature of the constitutive equation in contrast to the Newtonian flow, where the error stays confined. Indeed, we find that the extrudate swell computations could only be successfully performed for a very narrow range of parameters and success is highly dependent on the mesh configuration. For the mesh configuration detailed in Figure 7.17 consisting of $N_{el} = 14$ (Mesh M1) and for $P = 3$, we obtain swelling ratios up to 2.067 for $Wi = 0.85$. For an increase in the polynomial order or for a decrease in the mesh size ($N_{el} = 64$ (Mesh M2)), the numerical algorithm breaks down at a much lower Weissenberg number due to oscillations on the free surface boundary. These oscillations originate at the singularity and are convected downstream. We attempted to alleviate the problem associated with the singularity using the slip condition. Even though this seems to cure the breakdown of the computation with mesh refinement for the tested polynomial orders, the computations break down at $Wi = 0.6$ even for the coarsest mesh. In addition to the Oldroyd-B model, we investigate the extrudate swell of Giesekus fluids. For the Giesekus fluid, we were able to obtain converged results up to $Wi = 1.5$ for a mobility parameter of $\alpha = 0.1$ on the coarsest mesh.

Subsequently, we will first present the results that we obtain with mesh M1 ($P = 3$). Then, in order to shed some light on possible causes for the failure of the numerical algo-

rithm with increasing Weissenberg number and mesh refinement, we will investigate the behaviour of the stress components in the vicinity of the singularity.

The computations are performed employing the boundary conditions specified in Figure 7.4 and detailed in Section 7.1 and the following parameters. We choose $\Delta t = 10^{-3}$, $\beta = 0.1$ and investigate the swell ratio and the exit pressure correction for increasing Weissenberg numbers. For the Oldroyd-B fluid, we compute the steady state results by incrementing Wi by 0.05. For the Giesekus model, we perform the computations in increments of $\Delta Wi = 0.1$. The first computation is performed for $Wi = 0.1$ with the stick-slip solution for $Wi = 0.1$ as the initial condition. Every other computation is then initialised with the steady state solution from the previous Wi -step.

For viscoelastic fluids, the extrudate swell is caused by a combination of several effects: the reorganisation of the velocity profile from Poiseuille flow inside the die to uniform plug flow (as in the Newtonian case); the elastic recoil from the relaxation of molecules passing from a stressed viscometric state in the die to an unstressed state; and inelastic swelling due to, for example, thermal effects (Tanner, 1980). In this thesis, we will neglect thermal effects. The contribution of the remaining effects were estimated by Tanner (2002). Tanner (2002) estimates the swelling ratio caused by the rearrangement of the velocity profile from Poiseuille to plug flow as

$$\chi_R(\text{velocity rearrangement}) = 0.19, \quad (7.24)$$

assuming that the swelling in the case of a Newtonian liquid is mainly determined by the rearrangement of the velocity field. For the contribution of the elastic recoil mechanism, Tanner (2002) demonstrates that the swelling caused by the elastic recoil mechanism exiting from a plane die can be estimated as

$$\chi_R(\text{elastic recoil}) = \left[1 + \frac{1}{12} \left(\frac{N_1}{\sigma_{xy}} \right)_w^2 \right]^{\frac{1}{4}}. \quad (7.25)$$

Here, $N_1 = \sigma_{xx} - \sigma_{yy}$ is the first normal stress difference and σ_{xy} is the shear stress, both of which are evaluated at the wall of the die. The quantity

$$S_R := \left[\frac{N_1}{2\sigma_{xy}} \right]_w \quad (7.26)$$

at the upstream wall is called **recoverable shear**. To derive formula (7.25), Tanner (2002) assumed that the elastic behaviour can be modeled by a K-BKZ integral equation, which has $\tau_{xy} \sim \dot{\gamma}_w$ and $N_1 \sim \dot{\gamma}_w^2$, where $\dot{\gamma}_w = \frac{\partial u}{\partial y}$ is the wall shear rate, but $N_2 = 0$. This is a reasonable assumption for the Oldroyd-B model. Combining the two effects, the total

estimate for the swell ratio is

$$\chi_R = 0.19 + \left[1 + \frac{1}{3} S_R^2 \right]^{\frac{1}{4}}. \quad (7.27)$$

Equation (7.27) is called **Tanner's formula**.

For fully developed Poiseuille flow, the recoverable shear for the Oldroyd-B model is given by

$$S_R = \left[\frac{2(1-\beta)\text{Wi} \dot{\gamma}_w^2}{2((1-\beta)\dot{\gamma}_w + \beta\dot{\gamma}_w)} \right]_w = (1-\beta)\text{Wi} \dot{\gamma}_w \quad (7.28)$$

where the Weissenberg number is defined as

$$\text{Wi} = \frac{\lambda \langle u \rangle}{L}. \quad (7.29)$$

Here, we define the half channel height H as the characteristic length L and the average fluid inlet speed $\langle u \rangle$ as the characteristic velocity. In addition, we define the *effective Weissenberg number*

$$\text{Wi}_{\text{eff}} := \lambda \dot{\gamma}_w = \lambda \frac{U}{L} \dot{\gamma}_w^* = \text{Wi} \dot{\gamma}_w^*. \quad (7.30)$$

where $\dot{\gamma}_w^*$ is the non-dimensionalised $\dot{\gamma}_w$ using the non-dimensionalisation $u^* = u/U$, $y^* = y/L$. The combination of elasticity and wall shear rate is an important measure for the extrudate swell problem (see also S_R (7.28)).

For our flow configuration with an inflow profile given by Equation (7.16), we obtain $\langle u \rangle = 1$ and $\dot{\gamma}_w = 3$ and our half-channel height is $L = H = 1$. Therefore, the recoverable shear (7.28) becomes

$$S_R = (1-\beta)\text{Wi} \dot{\gamma}_w = 3(1-\beta)\text{Wi}. \quad (7.31)$$

7.3.1. Swelling Ratio and Exit Pressure Correction Factor

We compare our numerical results for the planar Oldroyd-B extrudate swell with Crochet and Keunings (1982), Tomé et al. (2002) and Russo and Phillips (2011), which to our knowledge are the only authors so far to have presented results for the planar Oldroyd-B die swell. However, the comparison with these authors has to be interpreted with care and is not fully conclusive as different geometries and different parameters were varied in order to achieve a range of swell ratios (Figure 7.18). We choose the geometry definition closely to Crochet and Keunings (1982) as this geometry is commonly used for the Newtonian extrudate swell benchmark computations.

Crochet and Keunings (1982) used a channel of half-height $H = 1$, a channel and free jet domain length of $L_1 = L_2 = 16$, an inflow profile of $u = \frac{3}{2}(1 - y^2)$, which results

in $\langle u \rangle = 1$ and $\dot{\gamma}_w = 3$ (Figure 7.18(a)). They used a coarse Taylor-Hood (i.e. $P = 2$ for velocity and stress, $P = 1$ for pressure) finite element mesh of 75 elements and 357 nodes resulting in 1889 degrees of freedom. They used the governing equations in their dimensional form and increased elasticity in terms of $\lambda\dot{\gamma}$ in increments of 0.25. Crochet and Keunings (1982) obtained a maximum swell ratio of $h/h_0 = 2.19$ for $\lambda\dot{\gamma} = 4.5$, ($S_R = 4$ for $\beta = 1/9$). For Crochet and Keunings (1982) the recoverable shear is given by

$$S_R = (1 - \beta)\lambda\dot{\gamma}_w = 3(1 - \beta)\lambda. \quad (7.32)$$

The results were given in terms of $\lambda\dot{\gamma}_w$.

Tomé et al. (2002) employed a finite difference method with a mesh size of $\Delta x = \Delta y = 0.025m$. They solved the equation in the dimensionless form but chose a very different domain as depicted in Figure 7.18(b). They defined the full channel height as the characteristic length (in contrast to the standard choice of half channel height) and the average velocity as the characteristic velocity. As their full channel height is chosen to be $L = 1$ an average inlet velocity of $\langle u \rangle = 1$ is given by the velocity profile $u = -6y(y - 1)$ yielding a wall shear rate of $\dot{\gamma}_w = 6$. To increase the swell ratio, they varied the Weissenberg number. For Tomé et al. (2002), the recoverable shear becomes

$$S_R = (1 - \beta)Wi\dot{\gamma}_w = 6(1 - \beta)Wi. \quad (7.33)$$

They listed their results in terms of $Wi\dot{\gamma}_w$.

Russo and Phillips (2011) employed a nodal spectral element technique and varied the mesh with $N_{el} = 8, 10, 12, 14$ and $P = 6, 7, 8, 10$. They chose a geometry of half-channel height $H = 2$ and varying length $L_1 = 10, L_2 = 6, 10$ and varied the fluid inlet speed to vary the wall shear stress $\dot{\gamma} = 2, 4, 6, 8$ and they varied the Weissenberg number accordingly in order to obtain a range of swell ratios (Figure 7.18(c)). They used the dimensionless version of the equations. However, they fixed $\lambda = 0.125$, varied the maximum of the inflow profile $u(y) = u_{max}(1 - y^2/4)$, which yields $\langle u \rangle = 2/3u_{max}$, $\dot{\gamma} = \partial_y u|_{y=2} = u_{max}$ and thus varied $Wi = \lambda\dot{\gamma}$. Results are given in terms of Wi . For Russo and Phillips (2011) the recoverable shear becomes

$$S_R = (1 - \beta)Wi\dot{\gamma}_w \quad (7.34)$$

Russo and Phillips (2011) presented results for the cases

$$(\dot{\gamma}_w, Wi) = (2, 0.25), (4, 0.5), (6, 0.75), (8, 1) \quad (7.35)$$

yielding $S_R = (1 - \beta)/2, 2(1 - \beta), 9/2(1 - \beta), 8(1 - \beta)$.

As we performed our computations with the same dimensionless form as Tomé et al. (2002) and Russo and Phillips (2011), we will compare our results in terms of Wi . To compare our results with those of Crochet and Keunings (1982), we need to relate the Weissenberg number to the relaxation time λ . For our geometry and for Crochet and Keunings (1982) geometry, we obtain

$$Wi = \lambda \frac{U}{L} = \lambda \quad \text{as } U = 1, L = 1. \quad (7.36)$$

Figure 7.19(a) shows the comparison of swell ratios for the Oldroyd-B model using our algorithm for $P = 3$ (Mesh M1) with those in the above mentioned articles by Crochet and Keunings (1982), Tomé et al. (2002) and Russo and Phillips (2011) and Tanner's formula given by Equation (7.27). Crochet and Keunings (1982) and Tomé et al. (2002) observe a quasi-linear growth of the swelling ratio with a change in slope at a critical Weissenberg number, while Russo and Phillips (2011)'s calculations predict quasilinear increase in the swelling ratio without a slope change. We predict a quasi-quadratic growth (polynomial regression fitting yields $p(x) = 0.9372x^2 + 0.2511x + 1.1659$) in the swelling ratio. Tanner's formula underpredicts the swelling ratio. For $P = 3$, we obtain a maximum swell ratio of 2.067 for $Wi = 0.85$. This discrepancy with Tanner's formula could be due to the derivation of the formula using the K-BKZ model instead of Oldroyd-B. Our results are closest to those obtained by Russo and Phillips (2011) and the swelling ratio lies in between the results of Crochet and Keunings (1982) and Tomé et al. (2002). We predict a linear growth in the exit correction factor (7.12) for the Oldroyd-B model for $P = 3$, which also lies in between the results of Crochet and Keunings (1982) and Tomé et al. (2002) (Figure 7.19(b)). However, as detailed above it is very difficult to draw conclusions from the comparison of extrudate swell data with the existing literature as many variations in the geometry and in the technique to increase swelling have been employed. In addition to the Oldroyd-B model, we investigate the die swell of Giesekus fluids. To our knowledge, results for the two dimensional extrudate swell of a Giesekus model in a planar die have not been presented in the standard geometry used for planar Newtonian extrudate swell. However, the swell of Giesekus fluids has been investigated in a range of other geometries. Tanoue et al. (1995) and Otsuki and Kajiwara (1999) used the Giesekus model to predict swelling in blow molding specific geometries, Delvaux and Crochet (1990) computed delayed die swell with the Oldroyd-B and Giesekus constitutive equation and Adrian (2010) used three-dimensional finite elements to investigate the extrudate swell for the Oldroyd-B and Giesekus model. Other models that have been studied for extrudate swell include the K-BKZ model (e.g. Mitsoulis (2010)), the Phan-Thien-Tanner model (e.g. Ganvir et al. (2009)) and the XPP model (Russo and Phillips (2010)).

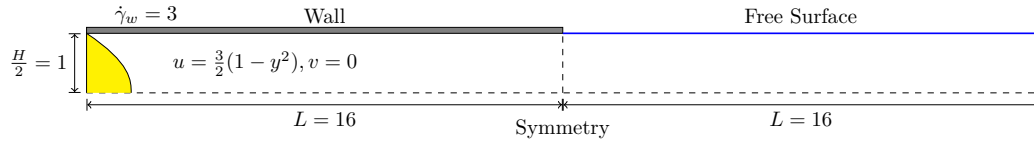
Note that most of the above listed computations have been performed using finite elements. Nodal spectral methods have only been employed for die swell flow by Ho and Rønquist (1994) for Newtonian fluids and by Russo (2009) for Newtonian, XPP and Oldroyd-B fluids. To our knowledge, modal spectral methods have not yet been employed to investigate extrudate swell. A review about numerical techniques and results for Newtonian and viscoelastic extrudate swell problems for axisymmetric and planar dies can be found in Tanner (2002).

Figure 7.20(a) displays the comparison of the swell ratio for the Giesekus model with a mobility parameter of $\alpha = 0.1$ and the Oldroyd-B model for no-slip and slip boundary conditions. The increase in the swelling ratio with increasing Weissenberg number for the Giesekus model is much lower than for the Oldroyd-B model and computations are successful for much higher Weissenberg numbers ($Wi = 1.5$). To explain the reduction in the swelling ratio for the Giesekus model, we explore the values of the recoverable shear for simple shear flow (see Section 2.5.4 and 2.5.5) with $\dot{\gamma}_w = 3$ for a no-slip wall boundary condition and $\dot{\gamma}_w^{sl} = 3/(1 + 3B_{sl})$ (see Equation (7.17)) for the slip condition. The values of the recoverable shear for increasing Weissenberg number are plotted in Figure 7.20(b). For the Giesekus model the recoverable shear is lower than for the Oldroyd-B model and it is bounded. This is due to the shear-thinning behaviour and the boundedness of the first normal stress difference of the Giesekus model (see Section 2.5.5). As the recoverable shear has been established as one of the main factors for swelling (Tanner (2002)), we would expect lower swelling for the Giesekus model and a bounded swelling ratio with increasing elasticity. In contrast, for the Oldroyd-B model, we can expect that the swelling ratio increases without bound. Figure 7.21 shows the exit pressure correction factor for the Giesekus model and the plots of the pressure values along the centreline for the Giesekus and Oldroyd-B models. The exit pressure correction factor for the Giesekus model is positive up to $Wi = 0.25$ and negative for $Wi \geq 0.3$, which is in stark contrast to the Oldroyd-B model. For the Oldroyd-B model the pressure at inflow is always greater than the Poiseuille flow value (hence $n_{ex} > 0$) and increases with increasing Wi , while for the Giesekus model the pressure value at inflow decreases with increasing Wi , which is due to the shear-thinning properties of the Giesekus model.

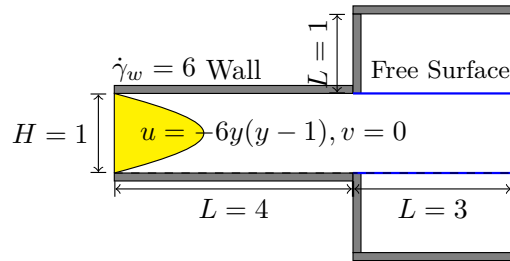
The introduction of slip along the wall reduces the recoverable shear as the wall shear rate decreases and for $B_{sl} = 0.1$, we obtain

$$\dot{\gamma}_w = \frac{3}{1 + 3B_{sl}} = 2.3077. \quad (7.37)$$

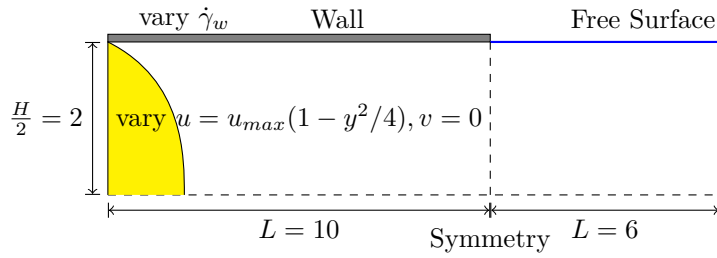
This decreases the swelling ratio (Figure 7.20) and the slope of the increase with increasing Weissenberg number is smaller than the slope for the no-slip boundary condition.



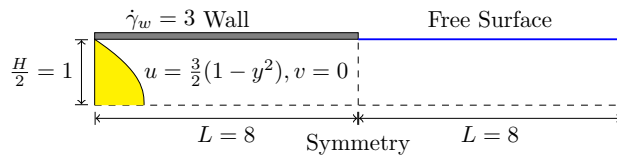
(a) Crochet and Keunings (1982): $\lambda \dot{\gamma}_w$, $S_R = (1 - \beta) \lambda \dot{\gamma}_w$, vary λ



(b) Tomé et al. (2002): $Wi \dot{\gamma}_w$, vary Wi

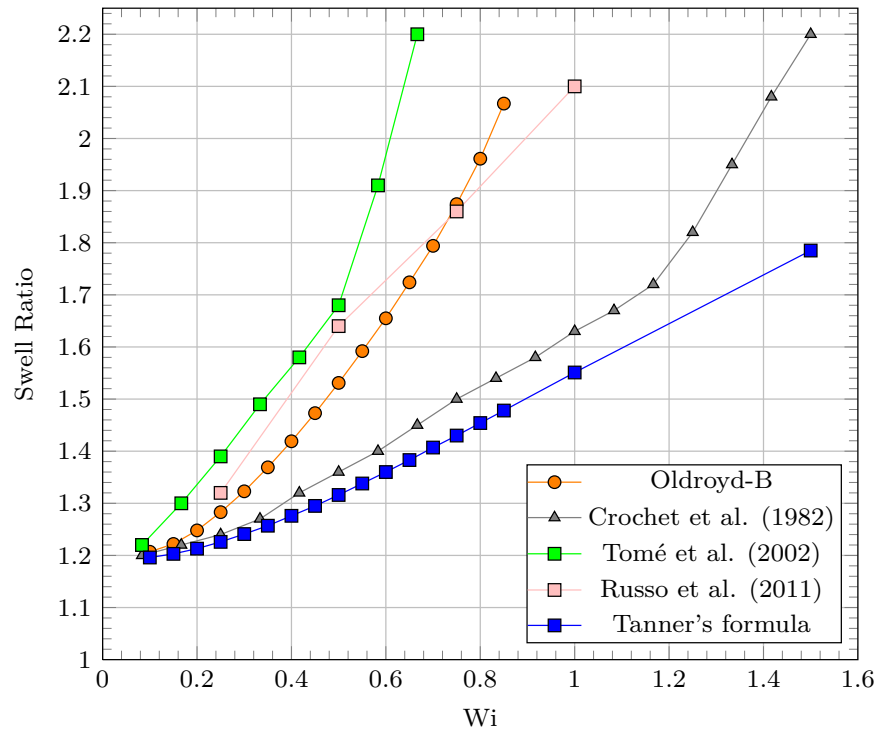


(c) Russo and Phillips (2011): Wi , vary $\dot{\gamma}_w$ and Wi

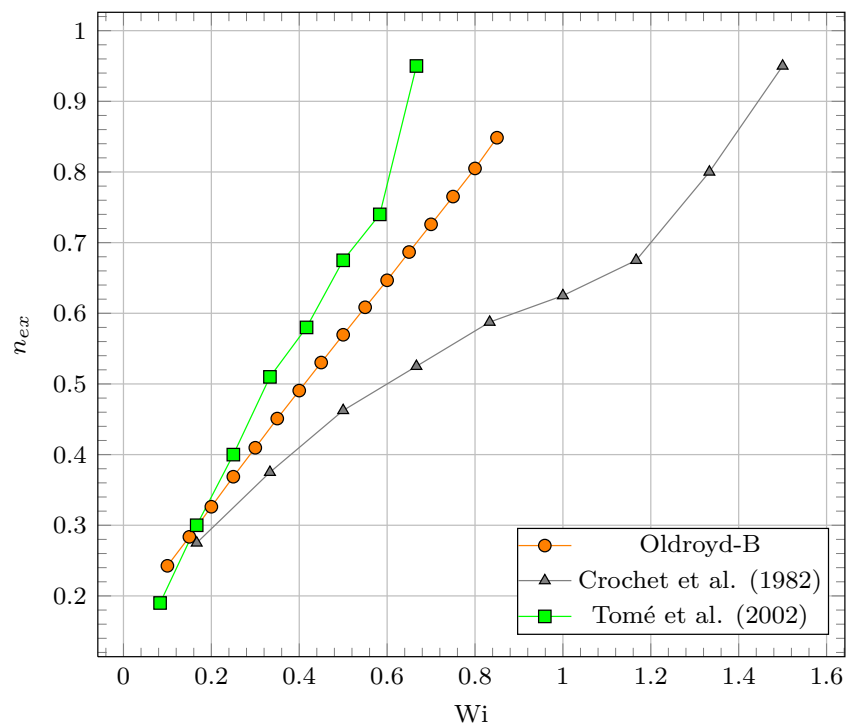


(d) Present Work: Wi , vary $Wi = \lambda U/L$

Figure 7.18.: Comparison of geometries employed by (a) Crochet and Keunings (1982), (b) Tomé et al. (2002), (c) Russo and Phillips (2011) and (d) our computational domain.

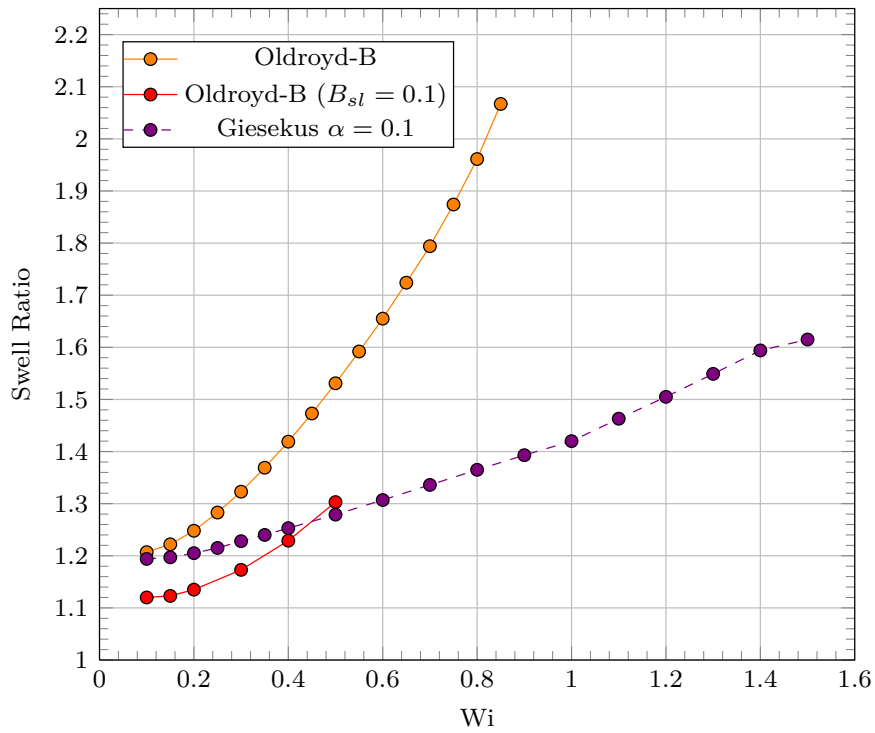


(a)

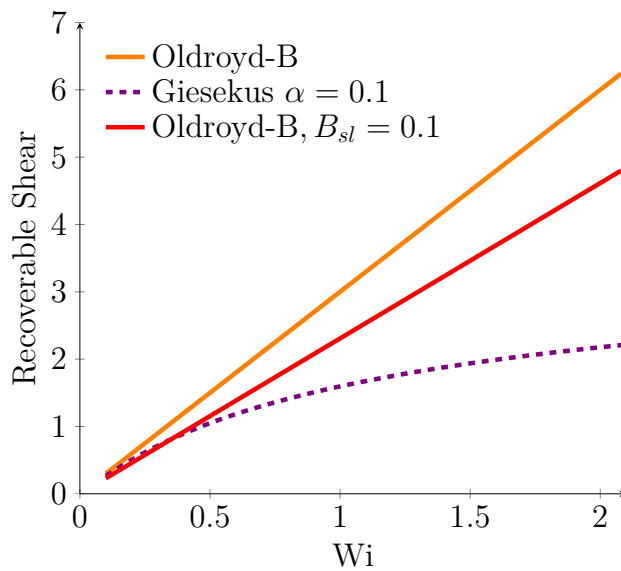


(b)

Figure 7.19.: Swelling Ratio (a) and exit pressure correction factor (b) for Oldroyd-B fluid in comparison with literature.



(a)



(b)

Figure 7.20.: Comparison of (a) swelling ratio for Oldroyd-B, Oldroyd-B with slip along the wall and the Giesekus model and (b) values of recoverable shear, S_R , at the upstream wall determined from simple shear flow.

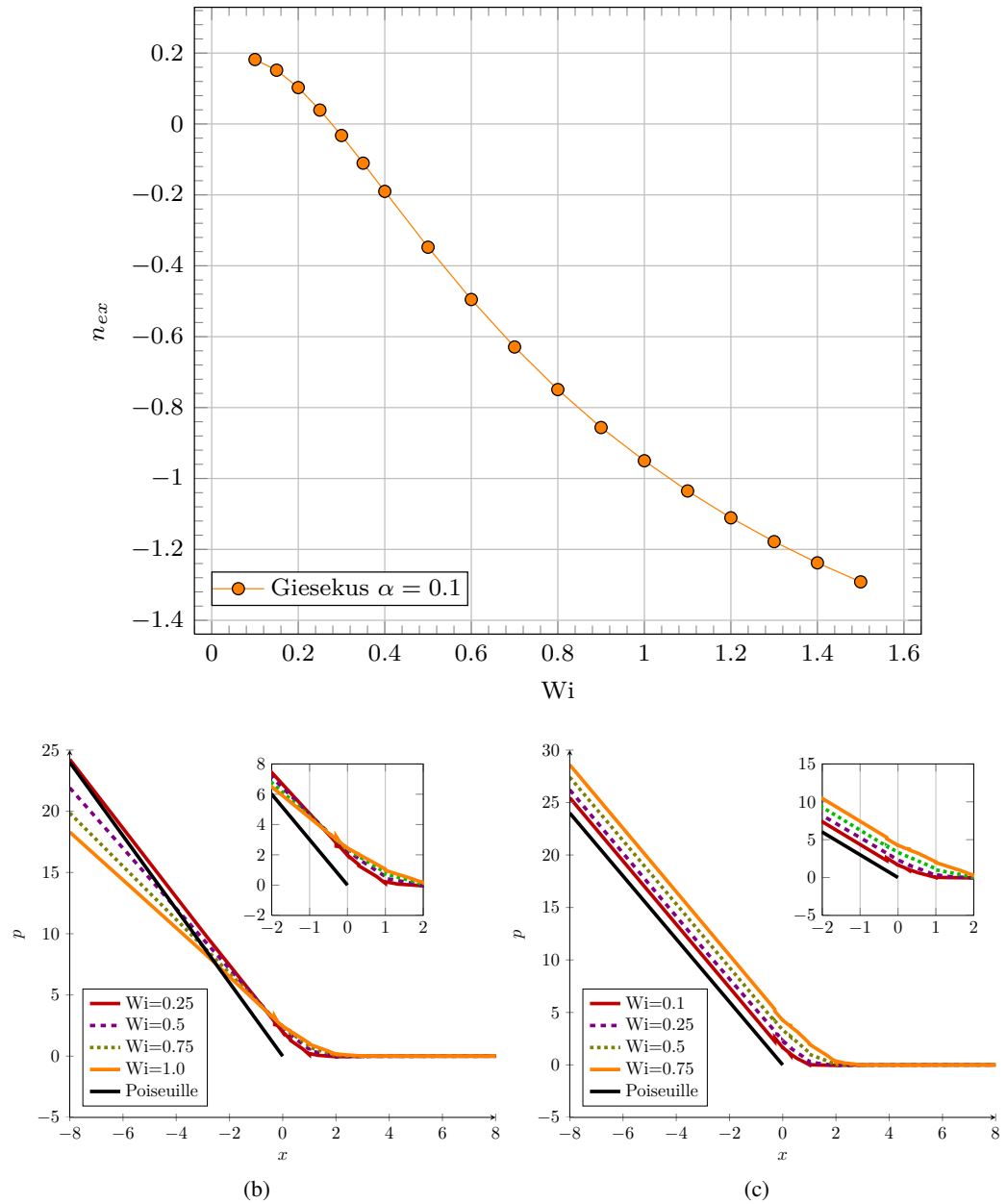
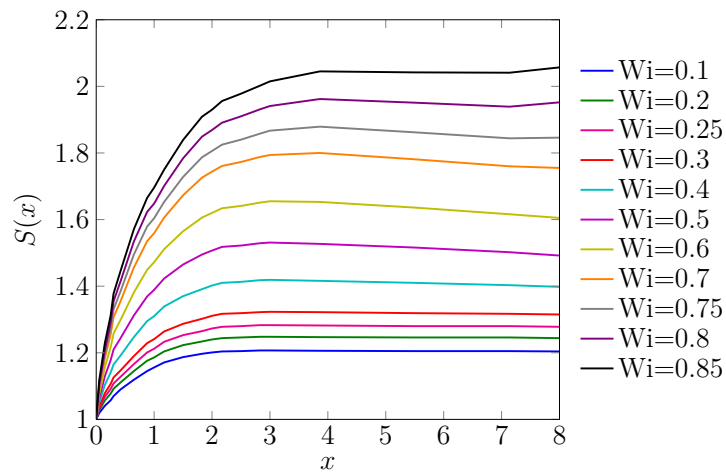


Figure 7.21.: Dependency of exit pressure correction factor on the Weissenberg number for the Giesekus model (a) and plot of pressure values along the symmetry line for $P = 3$ for the Giesekus model (b) and the Oldroyd-B model (c).

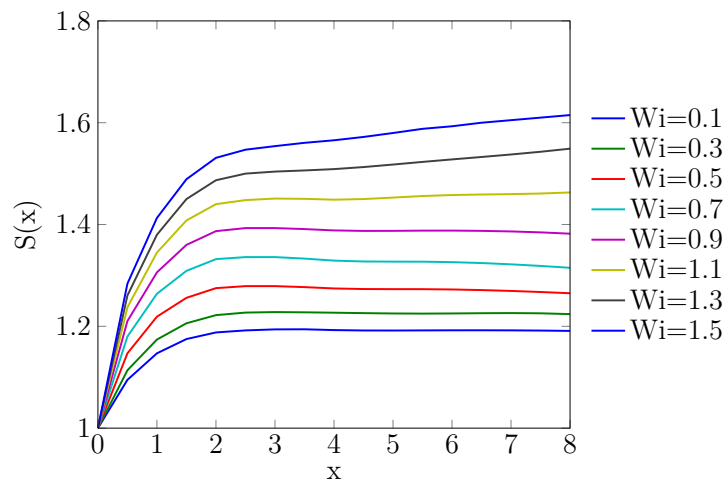
7.3.2. Spline Profiles and Contour Plots

The free surface shape in terms of the spline representing the free surface are plotted in Figure 7.22 for the Oldroyd-B and Giesekus model for a range of Weissenberg numbers for the mesh M1 for $P = 3$. The swell caused by the elasticity is a sharp increase in the free surface profile at the die exit and with increasing elasticity the free surface reaches its constant value further and further downstream.

These free surface shapes can also be seen for the Oldroyd-B model in Figure 7.23 displays the contour plots for the velocity components u for $Wi=0.1, 0.25, 0.5, 0.75, 0.85$ and v for $Wi=0.25, 0.5$. With increasing Wi , the velocity component u deforms increasingly along the whole height of channel at the die exit and increasingly upstream inside the die near the die exit. The velocity component v increases with increasing Wi causing the increase in the swelling. For both velocity components, the length of the transition zone from Poiseuille flow to plug flow increases with increasing elasticity. These effects show the increase in the fluid memory with elasticity, i.e. the flow is impacted increasingly further upstream and downstream from the point where a considerable change in the flow configuration occurs. Figure 7.24 shows the contour plots of the pressure p , the flow dependent shear stress S_1 (see Equation (5.33)) and the flow dependent normal stress S_2 (see Equation (5.34)). The pressure has a circular low pressure region attached the die exit that increases in size with increasing Wi and is increasingly bent in the downstream direction. The flow dependent shear stress undergoes a radial relaxation into the free jet region originating from a low shear stress value at the die exit. This radial relaxation reaches increasingly downstream with increasing elasticity reflecting the increase in the relaxation time of the fluid. The flow dependent normal stress also undergoes a relaxation from its maximum value at the die exit. However, this relaxation is very fast in the cross stream direction and is counteracted by the formation of a low normal stress region forming along the centreline (lowest values) and reaching over a large percentage of the whole height of the free jet domain.



(a)



(b)

Figure 7.22.: Free surface spline profiles for the Oldroyd-B (a) and Giesekus model (b) for increasing Weissenberg number.

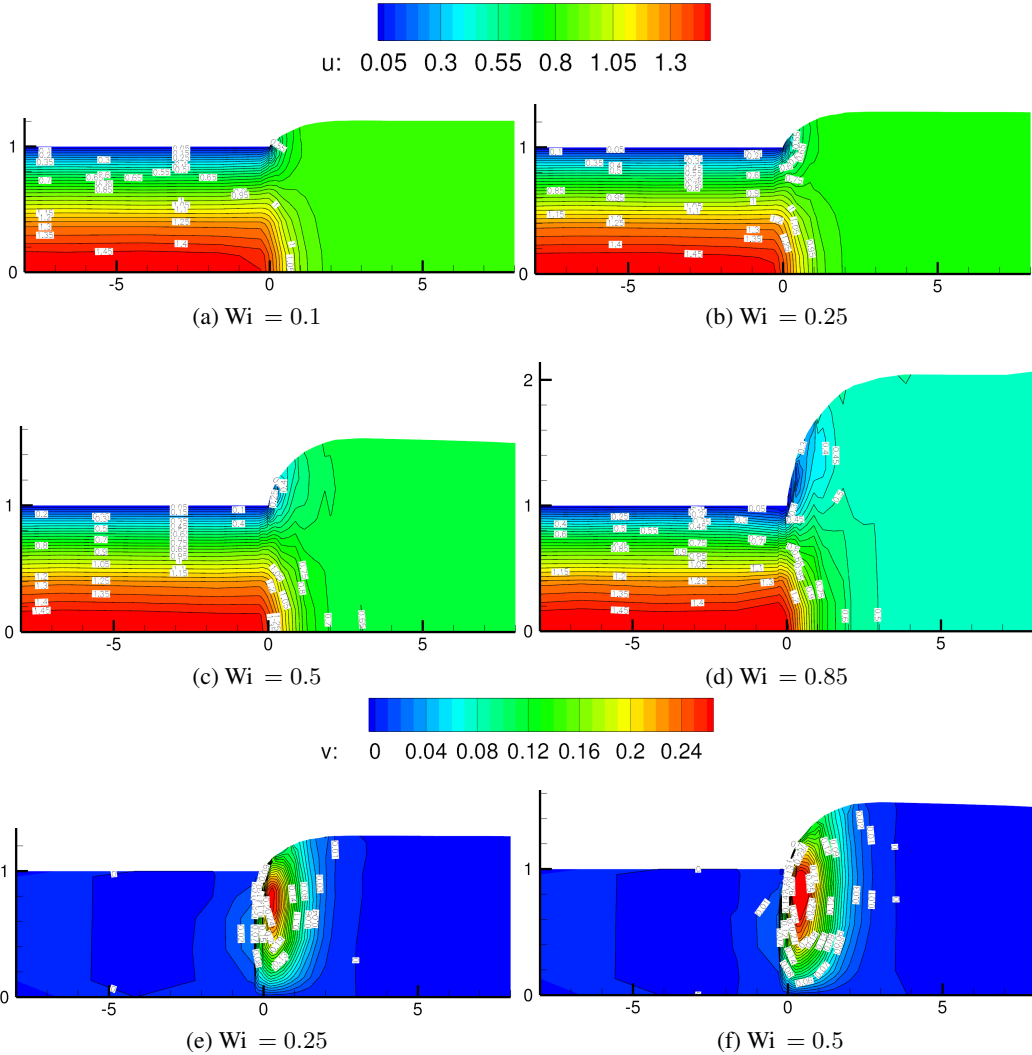


Figure 7.23.: Contour plots of velocity components u (a)-(d) and v (e)-(f) for Oldroyd-B model for a range of Weissenberg numbers.

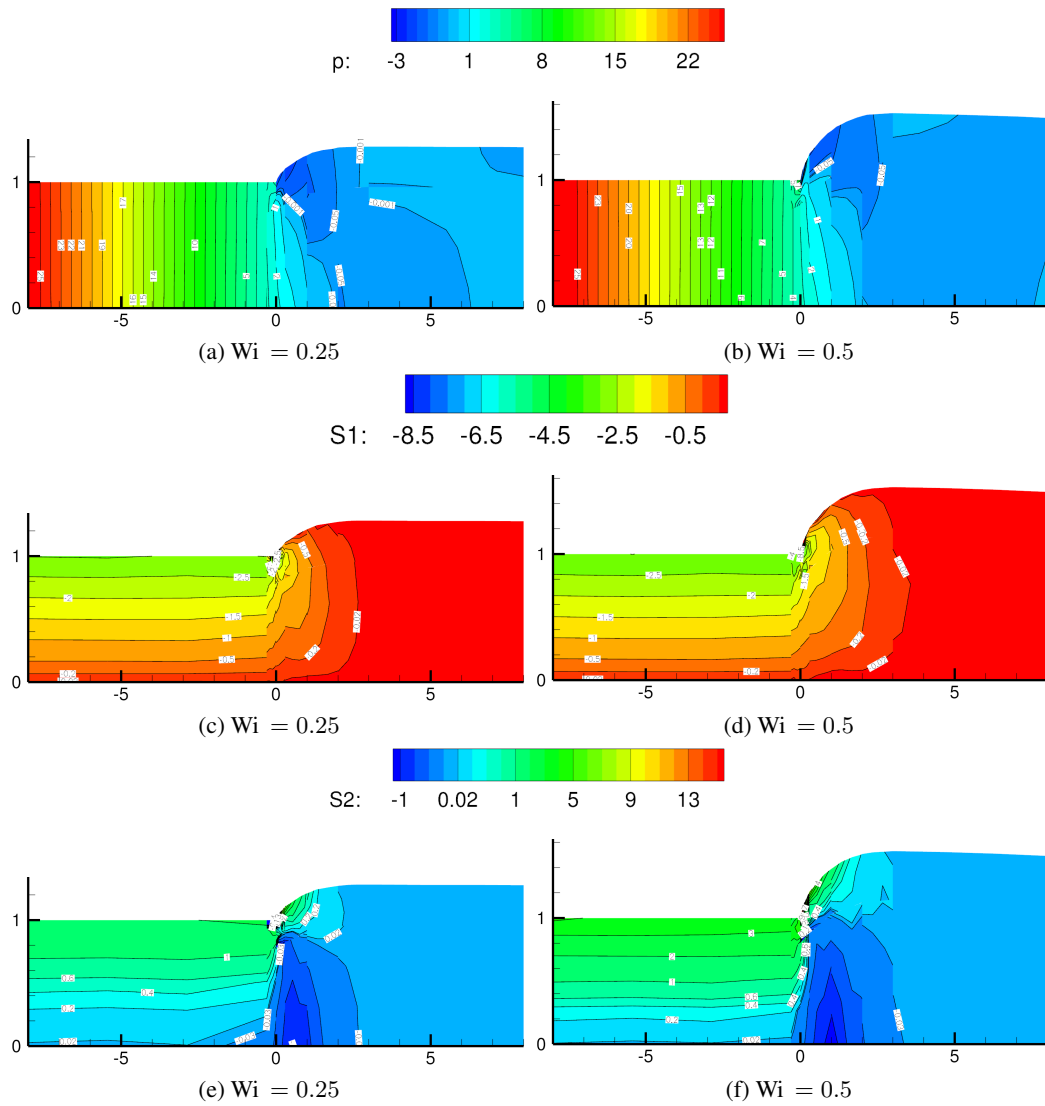


Figure 7.24.: Contour plots of pressure p (a)-(b) and flow dependent shear stress S_1 (c)-(d), normal stress S_2 (e)-(f) for Oldroyd-B model for $Wi = 0.25, 0.5$.

7.3.3. Mesh Refinement and Stress Components in the Vicinity of the Singularity

As discussed in the beginning of the Section, the jump from the no-slip or partial slip boundary condition to the free surface causes infinite stresses at the die exit. With mesh refinement, the increased resolution of the singularity yields a significant increase in the approximated stress values and the stress profiles steepen. With P -refinement of the mesh (i.e. increasing the polynomial order of the expansion basis) the closest quadrature point, where the weak forms are evaluated, is at a distance of approximately $\frac{h}{P^2}$ to the singularity, where h is the length of the element edge in the streamwise direction. This yields a significant increase in the magnitude of the approximated stress profiles with P -refinement. Figures 7.25 and 7.26 show the profiles of the pressure and polymeric stress components near the singularity for the no-slip and partial slip condition along the die wall for $Wi= 0.14$. We can clearly observe the steep increase of the profile values with increasing polynomial order. Note that the vertical lines in Figures 7.25 and 7.26 in the pressure and stress profiles at $x = -0.3, 0, 0.3$ are in fact discontinuities in the solution at element boundaries, which we allow in our discontinuous Galerkin method. For the no-slip boundary condition, the pressure jumps from a negative value to an increasingly high value with P -refinement at the die exit (Figure 7.25(a) at $x = 0$), while for the slip boundary condition it experiences a jump to a lower peak value (Figure 7.25(c) at $x = 0$). This minimum peak value increases much slower with increasing polynomial order than the maximum peak value in case of the no-slip condition. The polymeric stress τ_{xx} jumps from a steeply increasing high value to a low value at $x = 0$ before it experiences a second peak for the no-slip boundary condition (Figure 7.25(b)), while for the slip condition it undergoes a smoother symmetric peak that increases much slower with increasing P (Figure 7.25(d)). Figure 7.25(e) displays the increase in the peak values with increasing polynomial order in more detail and shows that the peak growth is much lower for the slip condition for $Wi= 0.1$. Figure 7.26 displays the comparison of slip and no-slip boundary condition with increasing polynomial order for the profiles of the stress components τ_{xy} and τ_{yy} . The stress component τ_{xy} undergoes a jump from a sharp high peak value, which increases significantly with increasing P , to a negative low value at $x = 0$ and then experiences a second peak, which also increases with P -refinement, for the no-slip boundary condition (Figure 7.26(a)). In contrast, for the slip boundary condition it undergoes a step change from a lower to a higher value and the growth of the peaks with increasing P is much lower (Figure 7.26(c)). The stress component τ_{yy} undergoes a sharp minimum at the die exit, which is more symmetric but sharper for the slip condition than for the no-slip condition (Figure 7.26(b), (d)). Figures 7.26(e) and 7.26(f) document the growth in the peak values for τ_{xy} and τ_{yy} . In addition, we clearly observe Gibbs-type oscillations in

the vicinity of the singularity for the polymeric stress components τ_{xy} and τ_{yy} . As these stress components interact with the velocity gradient tensor, these oscillations can cause oscillations in the velocity components. These oscillations of the velocity components impact the movement of the free surface boundary and oscillations appear on the free surface. Beyond a critical value, the oscillations of the free surface do not dampen and get amplified and transported downstream which causes a breakdown of the computation. Figure 7.27 shows two examples of the numerical breakdown of the scheme for critical Weissenberg numbers in case of the no-slip boundary condition. For no-slip along the die wall, a refinement of the mesh for $P = 6$ yields a breakdown at $Wi = 0.2$ with violent oscillations appearing at the free surface boundary (Figure 7.27(a)). For h -refinement and no-slip, we obtain a critical $Wi = 0.35$ and the free surface shows oscillations that travel downstream and eventually yield a breakdown (Figure 7.27(b)).

As shown in Figures 7.25 and 7.26 the increase in the peak values for the slip condition are much less severe than for the no-slip condition for increasing polynomial order. Indeed, in our computations, we observe that the introduction of the slip condition prevents the breakdown of the computation with mesh refinement for all tested polynomial orders. However, the critical Weissenberg number, which is now independent of the tested mesh refinements ($P = 3, 4, 6, 8$), is $Wi = 0.6$ and therefore lower than in the no-slip case for the coarsest mesh, where we obtain a critical $Wi = 0.9$. This breakdown at $Wi = 0.6$ for the slip condition is due to the growth of the stress values with increasing Wi as displayed in Figure 7.28 for the coarsest mesh (M1, $P = 3$). Roughly speaking, the increase of the peak values with increasing Wi is quasi-quadratic for the slip boundary condition, while it seems quasi-linear for the no-slip condition yielding to a lower critical Wi for the slip condition in the coarsest mesh.

Table 7.5 show the swelling ratios obtained for mesh refinement for the Oldroyd-B and the no-slip boundary condition. With increasing polynomial order the swelling ratio reduces. Table 7.6 lists the swelling ratios for the Oldroyd-B with slip along the wall, which also shows a reduction with mesh refinement.

Table 7.5.: Dependency of swelling ratio on mesh refinement for the Oldroyd-B model.

Wi	M1 ($P = 3$)	M2 ($P = 3$)	$P = 4$ (M1)	$P = 6$ (M1)
0.1	1.207	1.198	1.197	1.191
0.15	1.222	1.221	1.217	1.213

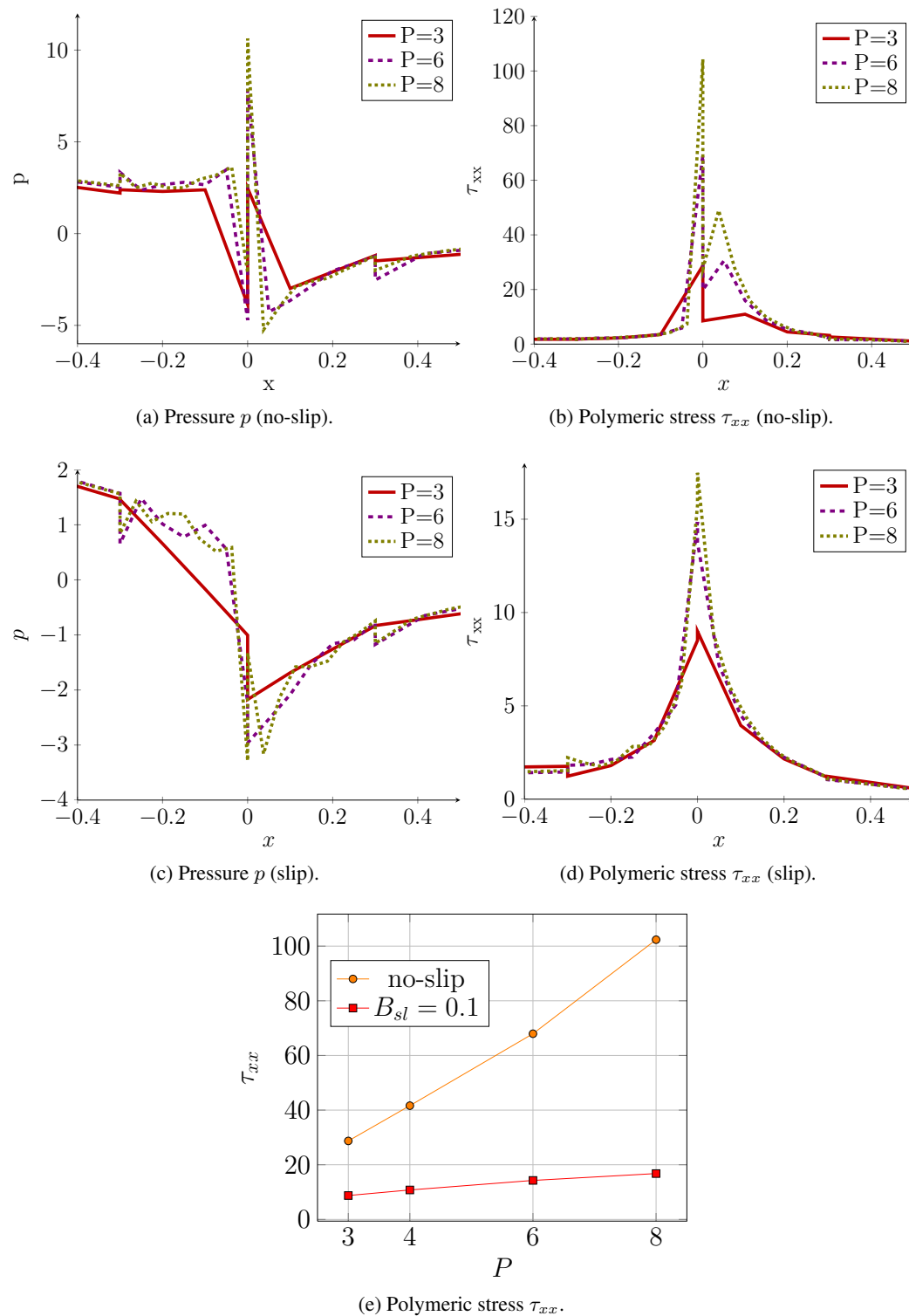


Figure 7.25.: Dependence of pressure ((a), (c)) and polymeric stress τ_{xx} ((b),(d)) in the vicinity of the singularity on the polynomial order for $Wi = 0.1$ for the no-slip and slip boundary condition and the increase in magnitude of τ_{xx} with polynomial order (e).

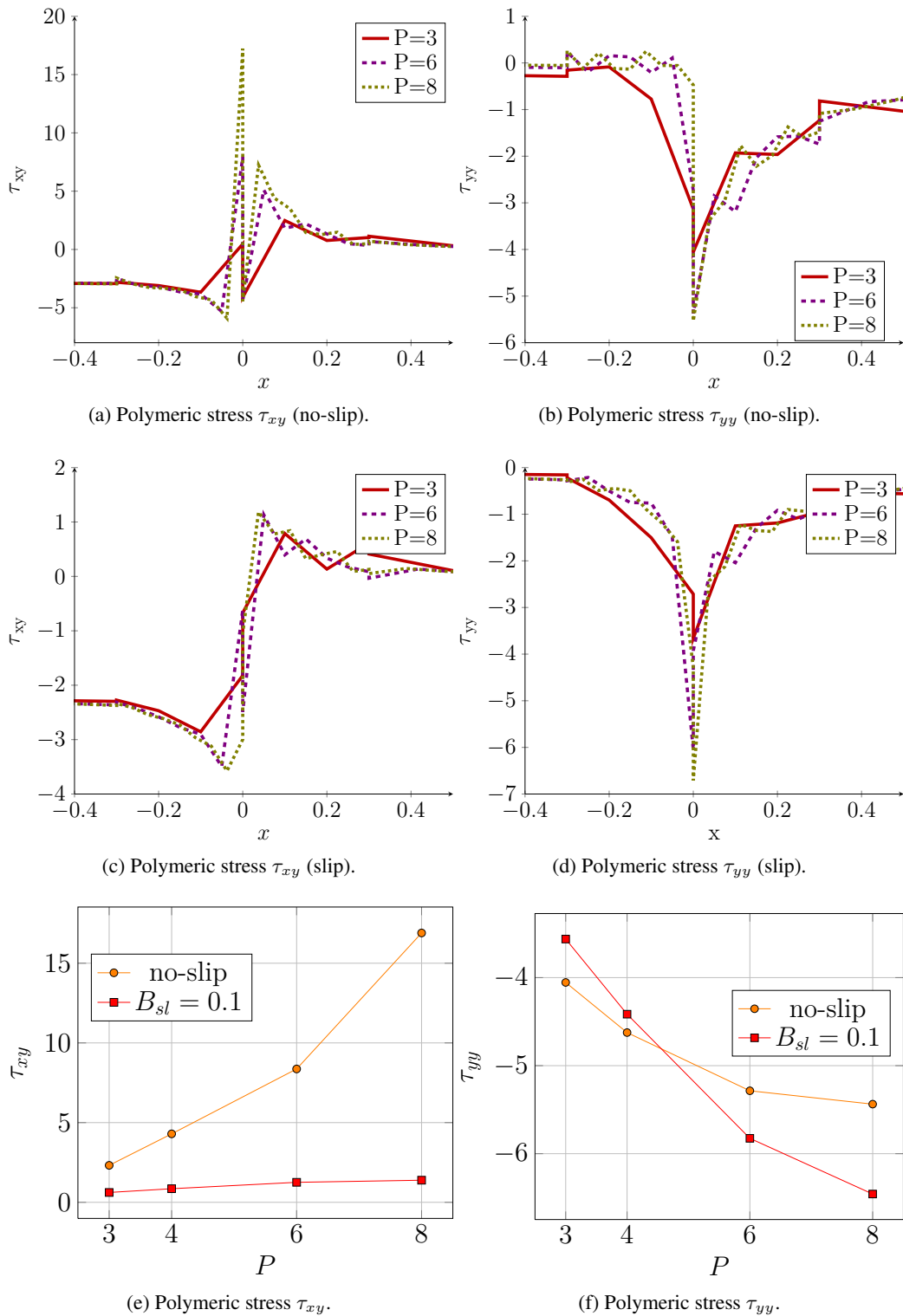


Figure 7.26.: Dependence of polymeric stress components τ_{xy} ((a), (c)) and τ_{yy} ((b),(d)) in the vicinity of the singularity on the polynomial order for $Wi = 0.1$ for the no-slip and slip boundary condition and their increase in magnitude with polynomial order (e),(f).

Table 7.6.: Dependency of swelling ratio on mesh refinement in mesh M1 for the Oldroyd-B model with slip along the wall $B_{sl} = 0.1$.

Wi	$P = 3$	$P = 6$	$P = 8$
0.1	1.12	1.112	1.113
0.2	1.135	1.122	1.118
0.5	1.303	1.253	1.244

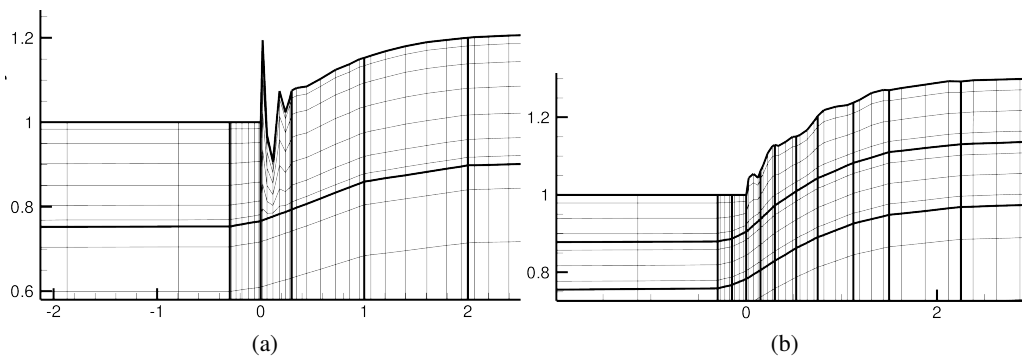


Figure 7.27.: Numerical breakdown for (a) Mesh M1 for $P = 6$ at $Wi = 0.2$ and (b) Mesh M2 for $P = 3$ at $Wi = 0.35$.

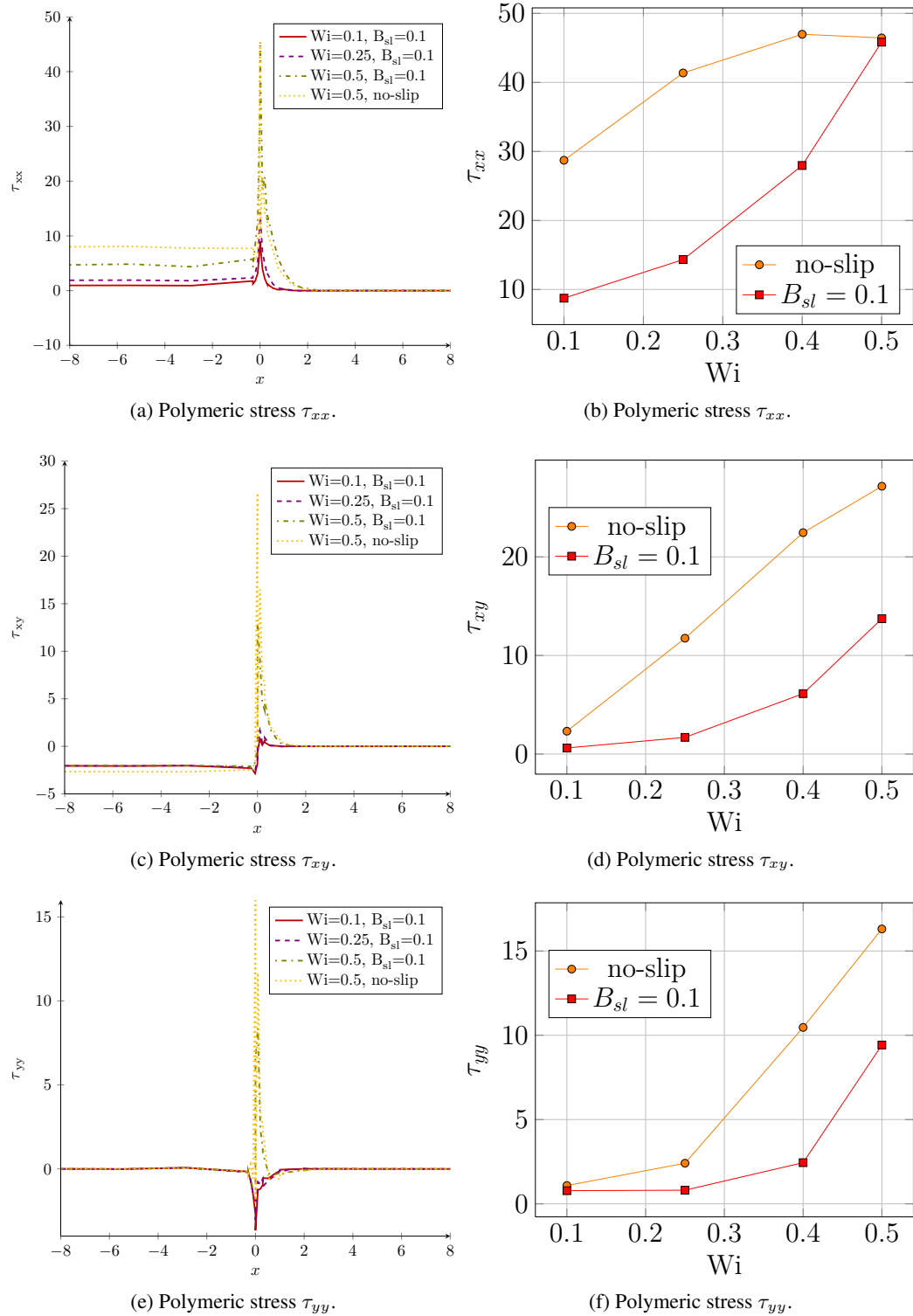


Figure 7.28.: Dependency of the profiles of velocity component u , pressure p and the polymeric stress components on the Weissenberg number with slip along the wall and the increase of magnitude with increasing Weissenberg number for the polymeric stress components for no-slip and partial slip along the die wall.

Chapter 8

Conclusions

One of the main bottlenecks in rheology is the extension of the identification and validation of mathematical models from simple flows to complex flows. Numerical methods can help tackle this issue, by providing the missing link between model and macroscopic prediction for complex flows. However, the numerical simulation of viscoelastic flows is very challenging. The formation of thin stress boundary layers near walls and solid structures and high stress concentrations near singularities has been commonly associated with the numerical breakdown of algorithms for solving the governing equations for viscoelastic fluids. In addition, resolving these stress layers and concentrations is of crucial importance in obtaining accurate results for parameters of interest such as the drag coefficient around solid structures. However, resolving these boundary layers and stress concentrations is usually prohibitively expensive for low order methods.

In this thesis, we have employed the spectral/hp element method, which uses high order polynomials and provides spectral accuracy in space at least for smooth functions. This method is capable of resolving thin layers at relatively low computational cost. To stabilise the computations, we have employed the discontinuous Galerkin method in combination with the DEVSS-G scheme. A continuous approximation space for the velocity and discontinuous approximation spaces for the pressure, velocity gradient projection tensor and the polymeric stress have been used. We have extended our scheme to describe free surface viscoelastic flows using an arbitrary Lagrangian Eulerian method to trace the free surface movement. Here, a cubic spline representation has been implemented to guarantee smoothness of normals and the curvature between spectral elements.

First, we have successfully applied the algorithm to unsteady Poiseuille flow of an Oldroyd-B fluid in a channel, for which an analytical solution exists, to demonstrate the stability and accuracy of the scheme. We have found that the DEVSS-G stabilisation yields small errors in the time dependent solution. However, the solution converges up to machine precision to the steady state solution. The DEVSS-G stabilisation significantly raises the

critical Weissenberg number from $Wi = 3.3$ without stabilisation to $Wi = 9.8$ for stabilisation with $\theta = (1 - \beta)$.

Secondly, we have investigated the flow around a cylinder for the Oldroyd-B model for $Re = \{0, 0.01, 0.1, 1\}$ and for the Giesekus model for $\alpha = \{0.001, 0.01, 0.1\}$. The results of this investigation have been published in essence in Claus and Phillips (2013a). Our drag coefficient values are in excellent agreement with the literature. For finer meshes, we have found a transient flow regime for $Wi > 0.6$ with a sinusoidal movement in the drag. We have interpreted these results by means of the theory of Dou and Phan-Thien (2007). In this theory the onset of the instability is explained in terms of a velocity inflection on top of the cylinder which leads to oscillations in the shear layer which are then transported downstream into the cylinder wake. We have demonstrated that the velocity and pressure profiles in the gap between the top of cylinder and the channel wall show a clear tendency for the formation of a velocity inflection with increasing Wi . The evidence that such a transient regime can be predicted by numerical simulations becomes more and more apparent with the enhancement of numerical algorithms and the use of high-resolution meshes. Oliveira and Miranda (2005) simulated the flow around a cylinder of a FENE-CR fluid and observed that the flow becomes unsteady for $De \approx 1.3$ for an extensibility parameter of $L^2 = 144$. Our scheme can predict this transient regime with very low computational cost and computations can even be performed on a desktop computer. For the Giesekus model, we have investigated the impact of the mobility parameter α on the flow configuration. We have demonstrated that for $\alpha = 0.001$ and $\alpha = 0.01$, the flow is dominated by normal stress effects while for $\alpha = 0.1$ the flow is dominated by the flow dependent shear stress and the flow patterns start to show shear thinning characteristics. In addition, we have shown that increasing the mobility parameter yields a decrease in the drag coefficient.

Finally, we extended the algorithm to incorporate the movement of a free surface boundary and investigated extrudate swell phenomena for Newtonian and viscoelastic flows. A journal article detailing our results for the Newtonian extrudate swell is in preparation (Claus and Phillips, 2013b). We have paid special attention to the behaviour of the pressure and the polymeric stress components at the singularity at the die exit, where a sudden change in the boundary condition yields infinite stress values. For Newtonian extrudate swell, we have demonstrated that the swelling ratio and the exit pressure loss are in excellent agreement with those in the literature. However, the comparable results by Mitsoulis et al. (2012) and Taliadorou et al. (2007), which were acquired using the finite element method, require a much larger number of degrees of freedom. We have shown agreement with the literature including the impact of inertia for a wide range of Reynolds numbers from 0 to 100. We have demonstrated that the solution is tainted by Gibbs oscillations

in the pressure, which stay local to the elements adjacent to the singularity. Therefore, these Gibbs oscillations impact accuracy but not the stability of the algorithm. Then, we have shown that the introduction of slip along the die wall changes the behaviour of the pressure at the singularity and the Gibbs oscillations disappear yielding improved mesh convergence rates in comparison to those including no-slip.

For viscoelastic flow and no-slip along the die wall, we could obtain swell ratios of up to 2.067 for $Wi = 0.85$ and $P = 3$ for the Oldroyd-B fluid and swell ratios up to 1.615 for $Wi = 1.5$ and $\alpha = 0.1$ for the Giesekus fluid. These results are in qualitative agreement with those in the literature. However, we have observed that mesh refinement yields numerical breakdown for $Wi \geq 0.2$ for the Oldroyd-B fluid. We have observed the behaviour of the pressure and polymeric stress values at the singularity and have demonstrated their almost exponential growth with p -refinement and the growth of the Gibbs oscillations with p -refinement. We have drawn the conclusion from our numerical observations including the appearance of oscillations in the free surface shape, that the Gibbs oscillations are transported downstream and grow downstream yielding numerical breakdown. For viscoelastic flows, this growth in error and the transport downstream can be associated with the constitutive equations and their hyperbolic nature (Renardy, 2000). We have investigated the impact of the slip condition on the viscoelastic die swell for the Oldroyd-B fluid. We have demonstrated that in this case, mesh p -refinement could be successfully applied for $P = 3, 4, 6, 8$. However, the computations breakdown for $Wi = 0.6$ for all tested meshes. We have demonstrated that this is possibly caused by the following behaviour. Although the introduction of the slip condition along the die wall has changed the behaviour of the stresses at the singularity and has improved the growth of the maximal values with p -refinement, the growth of maximum values in the polymeric stresses has become steeper with increasing Wi in comparison to the no-slip condition along the wall. In addition, the Gibbs oscillations in the polymeric stress components do not vanish for the slip condition. In summary, for the viscoelastic extrudate swell problem, Gibbs oscillations around the singularity in pressure and the polymeric stress components limit the applicability of spectral/hp element methods.

In future work, the limitations of the spectral/hp method in the die swell experiment, could be alleviated by introducing a method with variable polynomial order throughout the domain. Lower order elements around the singularity could be used to filter out the Gibbs oscillations and higher order elements further away from the singularity could provide high accuracy. Such variable order methods have been proven to be useful for re-entrant corner singularities as demonstrated in van Os and Gerritsma (2002) for a 4:1 contraction for an upper convected Maxwell fluid.

Furthermore, to use the full potential of geometric flexibility of the spectral/hp element

method, more viscoelastic flow examples should be tested including complex geometries discretised by triangles and the extension to three dimensional domains.

The ALE algorithm could be improved to include free surface flows with larger deformations of the free surface as the elliptic problem we have used to move the mesh in this thesis, can only be applied to mesh movements with small displacements. For larger mesh deformations, other elliptic problems to describe the mesh movement have to be solved, such as elliptic operators arising from Stokes or elasticity problems (see Deville et al. (2002)).

To gain more insights into the mechanism of the onset of the time dependent oscillations in the thin shear layer around the cylinder or the growth of the numerical error arising from the Gibbs oscillations at the die swell singularity, the implementation of the log conformation approach in the spectral/hp framework would be very useful. However, these extensions will not be straightforward. We have found in some preliminary investigations on channel flow that the use of the log conformation reformulation yields higher errors than the classical formulation. These errors destroy the spectral accuracy and could stem from the necessity of approximating zero stress values along the symmetry line of the flow. We are unaware of a successful implementation of the log conformation approach for spectral element methods in complex geometries. To the best of our knowledge, the thesis of Jafari (2011) includes the only application of the log conformation reformulation in the context of spectral elements in the literature. Jafari (2011) found that for spectral elements it did not behave in the same way as in the finite element context. No significant improvements over the classical formulation were found. However, if an accurate algorithm could be designed this could improve the simulation for higher Wi .

Appendix **A**

Jacobi Polynomials

Jacobi polynomials are the eigenfunctions, u_p , to countable infinite eigenvalues λ_p of the singular Sturm-Liouville problem, which, for a domain of $-1 < x < 1$ is written as

$$-\frac{d}{dx} \left((1+x)^{1+\alpha} (1-x)^{1+\beta} \frac{du_p(x)}{dx} \right) = \lambda w(x) u_p(x), \quad \alpha, \beta > -1 \quad (\text{A.1})$$

where

$$u_p(x) = P_p^{(\alpha, \beta)}(x), \quad w(x) = (1-x)^\alpha (1+x)^\beta, \quad \lambda_p = -p(\alpha + \beta + p + 1) \quad (\text{A.2})$$

According to the Sturm-Liouville theorem, the Jacobi polynomials form an orthogonal basis on $L_w^2(-1, 1)$ with

$$\int_{-1}^1 (1-x)^\alpha (1+x)^\beta P_p^{(\alpha, \beta)}(x) P_q^{(\alpha, \beta)}(x) dx = C \delta_{pq} \quad (\text{A.3})$$

with

$$C = \frac{2^{\alpha+\beta+1}}{2p + \alpha + \beta + 1} \frac{(p + \alpha)! (p + \beta)!}{p! (p + \alpha + \beta)!} \quad (\text{A.4})$$

This means that $P_p^{(\alpha, \beta)}(x)$ is orthogonal to all polynomials of order less than p with respect to the weight function $(1-x)^\alpha (1+x)^\beta$. When $\alpha = \beta = 0$, the polynomials $P_n^{(0,0)}(x)$ are the Legendre polynomials

$$\phi_n(x) = L_n(x) = P_n^{(0,0)}(x) \quad (\text{A.5})$$

and when $\alpha = \beta = -1/2$, $P_n^{(-1/2, -1/2)}(x)$ are the Chebyshev polynomials

$$\phi_n(x) = T^n(x) = \frac{2^{2n} (n!)^2}{(2n)!} P_n^{(-1/2, -1/2)}(x). \quad (\text{A.6})$$

The Jacobi polynomial $P_n^{(1,1)}(x)$ used in the spectral/hp element method have the following relations to the Legendre polynomials

$$L'_p(x) = 1/2(P+1)P_{p-1}^{(1,1)}(x), \quad (\text{A.7})$$

$$2p \int_{-1}^{\xi} L_p(s) ds = -(1-\xi)(1+\xi)P_{p-1}^{(1,1)}(\xi). \quad (\text{A.8})$$

Jacobi polynomials have several computationally useful properties. Firstly, they satisfy a three term recursion relation making them easy to evaluate. Secondly, for $p \geq 1$, $P_p^{(\alpha,\beta)}$ has p distinct real roots in $(-1, 1)$. Thirdly, Jacobi polynomials form a basis for $L_w^2(-1, 1)$, which means, we can represent any square integrable function f as an infinite series of Jacobi polynomials

$$f(x) = \sum_{k=0}^{\infty} \hat{f}_k P_k^{(\alpha,\beta)}(x) \quad (\text{A.9})$$

which has excellent approximation properties. The rate of convergence of a truncated series approximation formed from this series depends only on the rate of convergence of the coefficients \hat{f}_k . This can be seen in the following way. Splitting the series into a truncated part and the remainder

$$f(x) = \sum_{k=0}^N \hat{f}_k \phi_k(x) + \sum_{k=N+1}^{\infty} \hat{f}_k \phi_k(x) \quad (\text{A.10})$$

where the truncated sum can be expressed in terms of an orthogonal projection operator, P_N , defined as

$$P_N f(x) = \sum_{k=0}^N \hat{f}_k \phi_k(x) \quad (\text{A.11})$$

and the remainder can be evaluated using the norm of the truncation error defined by

$$\|\tau\|_{L_w^2}^2 = \sum_{k=N+1}^{\infty} |\hat{f}_k|^2 \|\phi_k(x)\|_{L_w^2}^2, \quad (\text{A.12})$$

we can see that the rate of convergence of the approximation $P_N f$ depends only on the rate of convergence of the coefficients \hat{f}_k , which are given by

$$\hat{f}_k = \frac{(f, P_k^{(\alpha,\beta)}(x))_w}{\|P_k^{(\alpha,\beta)}(x)\|_w} \quad (\text{A.13})$$

due to the orthogonality of the Jacobi polynomials. The rate of decay of the expansion coefficients depends only on the smoothness of the function being approximated. The

details for showing these facts are quite technical, and can be found, for example, in the book by Canuto et al. (2006). The Jacobi polynomial truncation converges spectrally fast as $N \rightarrow \infty$ but without the restrictions of periodic boundaries as required for Fourier series.

Appendix B

Free Surface Governing Equations in Components

B.1. Semi-Discretised Weak Formulation in Components

Conservation Equations

Momentum equation x-component:

$$\begin{aligned}
& \frac{\text{Re } \gamma_0}{\Delta t} \int_{\Omega(t)} u^{n+1} \phi_u d\Omega + \int_{\Omega(t)} \left[2 \left(\frac{\partial u}{\partial x} \right)^{n+1} \frac{\partial \phi_u}{\partial x} + \left(\frac{\partial u}{\partial y} \right)^{n+1} \frac{\partial \phi_u}{\partial y} \right] d\Omega \phi_u d\Omega \\
& + \text{Re} \int_{\Omega(t)} \left[\left(u^{(n)} - w_x^{(n)} \right) \left(\frac{\partial u}{\partial x} \right)^{n+1} + \left(v^{(n)} - w_y^{(n)} \right) \left(\frac{\partial u}{\partial y} \right)^{n+1} \right] \phi_u d\Omega \\
& + \int_{\Omega(t)} \left(\frac{\partial v}{\partial x} \right)^{(n+1)} \frac{\partial \phi_u}{\partial y} d\Omega - \int_{\Omega(t)} p^{n+1} \frac{\partial \phi_u}{\partial x} d\Omega \\
& - \int_{\Gamma_N(t)} \left[\left(2 \frac{\partial u}{\partial x} - p \right) n_x + \left(\frac{\partial u}{\partial y} + \frac{\partial v}{\partial x} \right) n_y \right]^{(n+1)} \phi_u d\Gamma \\
& - (1 - \beta) \int_{\Omega(t)} \left[2 G_{11} \frac{\partial \phi_u}{\partial x} + (G_{12} + G_{21}) \frac{\partial \phi_u}{\partial y} \right]^{(n+1)} d\Omega \\
& + (1 - \beta) \int_{\Gamma_N(t)} [2 G_{11} n_x + (G_{12} + G_{21}) n_y]^{(n+1)} \phi_u d\Gamma \\
& = \sum_{q=0}^J \beta_q \left[- \int_{\Omega(t)} \left[\tau_{xx} \frac{\partial \phi_u}{\partial x} + \tau_{xy} \frac{\partial \phi_u}{\partial y} \right] d\Omega + \int_{\Gamma_N(t)} [\tau_{xx} n_x + \tau_{xy} n_y] \phi_u d\Gamma \right]^{n-q} \\
& + \int_{\Gamma_f(t)} \sigma \kappa n_x \phi_u d\Gamma + \frac{\text{Re}}{\Delta t} \sum_{q=0}^J \alpha_q \int_{\Omega(t)} u^{n-q} \phi_u d\Omega. \tag{B.1}
\end{aligned}$$

Momentum equation y-component:

$$\begin{aligned}
& \frac{\text{Re } \gamma_0}{\Delta t} \int_{\Omega(t)} v^{n+1} \phi_v d\Omega + \int_{\Omega(t)} \left[\left(\frac{\partial v}{\partial x} \right)^{n+1} \frac{\partial \phi_v}{\partial x} + 2 \left(\frac{\partial v}{\partial y} \right)^{n+1} \frac{\partial \phi_v}{\partial y} \right] d\Omega \\
& + \text{Re} \int_{\Omega(t)} \left[\left(u^{(n)} - w_x^{(n)} \right) \left(\frac{\partial v}{\partial x} \right)^{n+1} + \left(v^{(n)} - w_y^{(n)} \right) \left(\frac{\partial v}{\partial y} \right)^{n+1} \right] \phi_v d\Omega \\
& + \int_{\Omega(t)} \left(\frac{\partial u}{\partial y} \right)^{(n+1)} \frac{\partial \phi_v}{\partial x} d\Omega - \int_{\Omega(t)} p^{n+1} \frac{\partial \phi_v}{\partial y} d\Omega \\
& - \int_{\Gamma_N(t)} \left[\left(\frac{\partial u}{\partial y} + \frac{\partial v}{\partial x} \right) n_x + \left(2 \frac{\partial v}{\partial y} - p \right) n_y \right]^{(n+1)} \phi_v d\Gamma \\
& - (1 - \beta) \int_{\Omega(t)} \left[(G_{21} + G_{12}) \frac{\partial \phi_v}{\partial x} + 2 G_{22} \frac{\partial \phi_v}{\partial y} \right]^{(n+1)} d\Omega \\
& + (1 - \beta) \int_{\Gamma_N(t)} [(G_{12} + G_{21}) n_x + 2 G_{22} n_y]^{(n+1)} \phi_v d\Gamma \tag{B.2}
\end{aligned}$$

$$\begin{aligned}
& = \sum_{q=0}^J \beta_q \left[- \int_{\Omega(t)} \left[\tau_{xy} \frac{\partial \phi_v}{\partial x} + \tau_{yy} \frac{\partial \phi_v}{\partial y} \right] d\Omega + \int_{\Gamma_N(t)} [\tau_{xy} n_x + \tau_{yy} n_y] \phi_v d\Gamma \right]^{n-q} \\
& + \int_{\Gamma_f(t)} \sigma \kappa n_y \phi_v d\Gamma + \frac{\text{Re}}{\Delta t} \sum_{q=0}^J \alpha_q \int_{\Omega(t)} v^{n-q} \phi_v d\Omega. \tag{B.3}
\end{aligned}$$

Mass conservation:

$$\left[\int_{\Omega(t)} \frac{\partial u}{\partial x} \psi d\Omega + \int_{\Omega(t)} \frac{\partial v}{\partial y} \psi d\Omega \right]^{n+1} = 0. \tag{B.4}$$

Constitutive Equations

Velocity gradient projection tensor:

$$\int_{\Omega(t)} G_{11} \phi_{G_{11}} d\Omega = \int_{\Omega(t)} \left(\frac{\partial u}{\partial x} \right)^{n+1} \phi_{G_{11}} d\Omega, \quad (\text{B.5})$$

$$\int_{\Omega(t)} G_{12} \phi_{G_{12}} d\Omega = \int_{\Omega(t)} \left(\frac{\partial u}{\partial y} \right)^{n+1} \phi_{G_{12}} d\Omega, \quad (\text{B.6})$$

$$\int_{\Omega(t)} G_{21} \phi_{G_{21}} d\Omega = \int_{\Omega(t)} \left(\frac{\partial v}{\partial x} \right)^{n+1} \phi_{G_{21}} d\Omega, \quad (\text{B.7})$$

$$\int_{\Omega(t)} G_{22} \phi_{G_{22}} d\Omega = \int_{\Omega(t)} \left(\frac{\partial v}{\partial y} \right)^{n+1} \phi_{G_{22}} d\Omega. \quad (\text{B.8})$$

Constitutive equation xx-component:

$$\begin{aligned} & \frac{\text{Wi} \gamma_0}{\Delta t} \int_{\Omega(t)} \tau_{xx}^{n+1} \phi_{\tau_{xx}} d\Omega + \int_{\Omega(t)} \tau_{xx}^{n+1} \phi_{\tau_{xx}} d\Omega \\ & - \text{Wi} \int_{\Omega(t)} \left[\left(u^{n+1} - w_x^n \right) \tau_{xx}^{n+1} \frac{\partial \phi_{\tau_{xx}}}{\partial x} + \left(v^{n+1} - w_y^n \right) \tau_{xx}^{n+1} \frac{\partial \phi_{\tau_{xx}}}{\partial y} \right] d\Omega \\ & - 2 \text{Wi} \int_{\Omega(t)} G_{11}^{n+1} \tau_{xx}^{n+1} \phi_{\tau_{xx}} d\Omega - 2 \text{Wi} \int_{\Omega(t)} G_{12}^{n+1} \tau_{xy}^{n+1} \phi_{\tau_{xx}} d\Omega \\ & = 2(1 - \beta) \int_{\Omega(t)} G_{11}^{n+1} \phi_{\tau_{xx}} d\Omega - \frac{\alpha \text{Wi}}{(1 - \beta)} \int_{\Omega(t)} \left(\tau_{xx}^2 + \tau_{xy}^2 \right)^{(it)} \phi_{\tau_{xx}} d\Omega \\ & - \text{Wi} \int_{\partial \Omega_e(t)} \left[\left(u^{n+1} - w_x^n \right) n_x + \left(v^{n+1} - w_y^n \right) n_y \right] \tilde{f} \left(\tau_{xx}^e, \tau_{xx}^i \right)^{(it)} \phi_{\tau_{xx}} d\Gamma \\ & + \frac{\text{Wi}}{\Delta t} \sum_{q=0}^J \alpha_q \int_{\Omega(t)} \tau_{xx}^{n-q} \phi_{\tau_{xx}} d\Omega. \end{aligned} \quad (\text{B.9})$$

Constitutive equation xy-component:

$$\begin{aligned}
& \frac{\text{Wi} \gamma_0}{\Delta t} \int_{\Omega(t)} \tau_{xy}^{n+1} \phi_{\tau_{xy}} d\Omega + \int_{\Omega(t)} \tau_{xy}^{n+1} \phi_{\tau_{xy}} d\Omega \\
& - \text{Wi} \int_{\Omega(t)} \left[(u^{n+1} - w_x^n) \tau_{xy}^{n+1} \frac{\partial \phi_{\tau_{xy}}}{\partial x} + (v^{n+1} - w_y^n) \tau_{xy}^{n+1} \frac{\partial \phi_{\tau_{xy}}}{\partial y} \right] d\Omega \\
& - \text{Wi} \int_{\Omega(t)} (G_{11}^{n+1} + G_{22}^{n+1}) \tau_{xy}^{n+1} \phi_{\tau_{xy}} d\Omega - \text{Wi} \int_{\Omega(t)} G_{21}^{n+1} \tau_{xx}^{n+1} \phi_{\tau_{xy}} d\Omega - \text{Wi} \int_{\Omega(t)} G_{12}^{n+1} \tau_{yy}^{n+1} \phi_{\tau_{xy}} d\Omega \\
& = (1 - \beta) \int_{\Omega(t)} (G_{12}^{n+1} + G_{21}^{n+1}) \phi_{\tau_{xy}} d\Omega - \frac{\alpha \text{Wi}}{(1 - \beta)} \int_{\Omega(t)} (\tau_{xx} \tau_{xy} + \tau_{yy} \tau_{xy})^{(it)} \phi_{\tau_{xy}} d\Omega \\
& - \text{Wi} \int_{\partial \Omega_e(t)} [(u^{n+1} - w_x^n) n_x + (v^{n+1} - w_y^n) n_y] \tilde{f}(\tau_{xy}^e, \tau_{xy}^i)^{(it)} \phi_{\tau_{xx}} d\Gamma \\
& + \frac{\text{Wi}}{\Delta t} \sum_{q=0}^J \alpha_q \int_{\Omega(t)} \tau_{xy}^{n-q} \phi_{\tau_{xy}} d\Omega. \tag{B.10}
\end{aligned}$$

Constitutive equation yy-component:

$$\begin{aligned}
& \frac{\text{Wi} \gamma_0}{\Delta t} \int_{\Omega(t)} \tau_{yy}^{n+1} \phi_{\tau_{yy}} d\Omega + \int_{\Omega(t)} \tau_{yy}^{n+1} \phi_{\tau_{yy}} d\Omega \\
& - \text{Wi} \int_{\Omega(t)} \left[(u^{n+1} - w_x^n) \tau_{yy}^{n+1} \frac{\partial \phi_{\tau_{yy}}}{\partial x} + (v^{n+1} - w_y^n) \tau_{yy}^{n+1} \frac{\partial \phi_{\tau_{yy}}}{\partial y} \right] d\Omega \\
& - 2 \text{Wi} \int_{\Omega(t)} G_{22}^{n+1} \tau_{yy}^{n+1} \phi_{\tau_{yy}} d\Omega - 2 \text{Wi} \int_{\Omega(t)} G_{21}^{n+1} \tau_{xy}^{n+1} \phi_{\tau_{yy}} d\Omega \\
& = 2(1 - \beta) \int_{\Omega(t)} G_{22}^{n+1} \phi_{\tau_{yy}} d\Omega - \frac{\alpha \text{Wi}}{(1 - \beta)} \int_{\Omega(t)} (\tau_{xy}^2 + \tau_{yy}^2)^{(it)} \phi_{\tau_{yy}} d\Omega \\
& - \text{Wi} \int_{\partial \Omega_e(t)} [(u^{n+1} - w_x^n) n_x + (v^{n+1} - w_y^n) n_y] \tilde{f}(\tau_{yy}^e, \tau_{yy}^i)^{(it)} \phi_{\tau_{yy}} d\Gamma \\
& + \frac{\text{Wi}}{\Delta t} \sum_{q=0}^J \alpha_q \int_{\Omega(t)} \tau_{yy}^{n-q} \phi_{\tau_{yy}} d\Omega. \tag{B.11}
\end{aligned}$$

Mesh Velocity

$$\int_{\Omega(t)} \left(\frac{\partial w_x}{\partial x} \frac{\partial \phi_{w_x}}{\partial x} + \frac{\partial w_x}{\partial y} \frac{\partial \phi_{w_x}}{\partial y} \right) d\Omega - \int_{\Gamma_N(t)} \left(\frac{\partial w_x}{\partial x} n_x + \frac{\partial w_x}{\partial y} n_y \right) \phi_{w_x} d\Gamma = 0, \quad (\text{B.12})$$

$$\int_{\Omega(t)} \left(\frac{\partial w_y}{\partial x} \frac{\partial \phi_{w_y}}{\partial x} + \frac{\partial w_y}{\partial y} \frac{\partial \phi_{w_y}}{\partial y} \right) d\Omega - \int_{\Gamma_N(t)} \left(\frac{\partial w_y}{\partial x} n_x + \frac{\partial w_y}{\partial y} n_y \right) \phi_{w_y} d\Gamma = 0. \quad (\text{B.13})$$

B.2. Matrix Notation in Components

The coupled system for velocity, pressure and velocity gradient projection tensor can be written as

$$\begin{aligned} \mathbf{H}_g(t_{n+1}) \hat{\mathbf{u}}_g^{n+1} - \mathbf{D}_g(t_{n+1})^T \hat{\mathbf{p}}_g^{n+1} + \mathbf{M}_{\mathbf{uG}}(t_{n+1}) \hat{\mathbf{G}}^{n+1} &= \mathbf{M}(t_{n+1}) \hat{\mathbf{u}}^n \\ &+ \mathbf{f}(t_{n+1}; \boldsymbol{\tau}^n) + \mathbf{b}(t_{n+1}), \\ \mathbf{D}_g(t_{n+1}) \hat{\mathbf{u}}_g^{n+1} &= 0, \\ \mathbf{M}_{\mathbf{Gu}}(t_{n+1}) \hat{\mathbf{u}}^{n+1} + \mathbf{M}_{\mathbf{GG}}(t_{n+1}) \hat{\mathbf{G}}^{n+1} &= 0, \end{aligned} \quad (\text{B.14})$$

where $\hat{\mathbf{u}}_g$ and $\hat{\mathbf{p}}_g$ are the vectors of unknown global coefficients, \mathbf{H}_g is the global modified Helmholtz matrix and $\mathbf{D}_g = (\mathbf{D}_x, \mathbf{D}_y)$ is the global discrete gradient operator. These global matrices are assembled from the elemental matrix contributions by

$$\mathbf{H}_g = \mathcal{A}^T \underline{\mathbf{H}}^e \mathcal{A}, \quad (\text{B.15})$$

as explained in Section 3.7.1 and Section 4.4.1. The discrete gradient operator is given by

$$\mathbf{D}_b^e = \begin{bmatrix} \mathbf{D}_x^e & \mathbf{D}_y^e \end{bmatrix}, \quad (\text{B.16})$$

$$\mathbf{D}_x^e[m, n] = \left(\frac{\partial \phi_u^m}{\partial x}, \psi^n \right)_{\Omega_e}^{\delta}, \quad (\text{B.17})$$

$$\mathbf{D}_y^e[m, n] = \left(\frac{\partial \phi_v^m}{\partial y}, \psi^n \right)_{\Omega_e}^{\delta} \quad (\text{B.18})$$

and the terms on the right hand side are given by

$$\begin{aligned} \mathbf{f}^e(\mathbf{u}, \boldsymbol{\tau}) = & \left(\frac{\text{Re}}{\Delta t} \sum_{q=0}^J \alpha_q \mathbf{u}^{n-q}, \phi_u \right)_{\Omega_e}^{\delta} + \sum_{q=0}^J \beta_q \left[(-\boldsymbol{\tau}, \nabla \phi_u)_{\Omega_e}^{\delta} + \langle \boldsymbol{\tau} \cdot \mathbf{n}, \phi_u \rangle_N \right]^{n-q} \\ & + \langle \sigma \kappa \mathbf{n}, \phi_u \rangle_f^{n+1}. \end{aligned} \quad (\text{B.19})$$

The components of the elemental modified Helmholtz matrix are given by

$$\mathbf{H}^e = \begin{bmatrix} \mathbf{H}_{uu}^e & \mathbf{H}_{uv}^e \\ \mathbf{H}_{vu}^e & \mathbf{H}_{vv}^e \end{bmatrix} \quad (\text{B.20})$$

with

$$\begin{aligned} \mathbf{H}_{uu}^e[i, j] = & \frac{\text{Re} \gamma_0}{\Delta t} (\phi_u^j, \phi_u^i)_{\Omega_e}^{\delta} + 2 \left(\frac{\partial \phi_u^j}{\partial x}, \frac{\partial \phi_u^i}{\partial x} \right)_{\Omega_e}^{\delta} + \left(\frac{\partial \phi_u^j}{\partial y}, \frac{\partial \phi_u^i}{\partial y} \right)_{\Omega_e}^{\delta} \\ & - \left\langle 2 \frac{\partial \phi_u^j}{\partial x} n_x + \frac{\partial \phi_u^j}{\partial y} n_y, \phi_u^i \right\rangle_{\Gamma_N}^{\delta} \\ & + \text{Re} \left((\mathbf{u}^n - \mathbf{w}^n) \cdot \nabla \phi_u^j, \phi_u^i \right)_{\Omega_e}^{\delta}, \end{aligned} \quad (\text{B.21})$$

$$\mathbf{H}_{uv}^e[i, j] = \left(\frac{\partial \phi_v^j}{\partial x}, \frac{\partial \phi_u^i}{\partial y} \right)_{\Omega_e}^{\delta} - \left\langle \frac{\partial \phi_v^j}{\partial x} n_y, \phi_u^i \right\rangle_{\Gamma_N}^{\delta}, \quad (\text{B.22})$$

$$\mathbf{H}_{vu}^e[i, j] = \left(\frac{\partial \phi_u^j}{\partial y}, \frac{\partial \phi_v^i}{\partial x} \right)_{\Omega_e}^{\delta} - \left\langle \frac{\partial \phi_u^j}{\partial y} n_x, \phi_v^i \right\rangle_{\Gamma_N}^{\delta}, \quad (\text{B.23})$$

$$\begin{aligned} \mathbf{H}_{vv}^e[i, j] = & \frac{\text{Re} \gamma_0}{\Delta t} (\phi_v^j, \phi_v^i)_{\Omega_e}^{\delta} + \left(\frac{\partial \phi_v^j}{\partial x}, \frac{\partial \phi_v^i}{\partial x} \right)_{\Omega_e}^{\delta} + 2 \left(\frac{\partial \phi_v^j}{\partial y}, \frac{\partial \phi_v^i}{\partial y} \right)_{\Omega_e}^{\delta} \\ & - \left\langle \frac{\partial \phi_v^j}{\partial x} n_x + 2 \frac{\partial \phi_v^j}{\partial y} n_y, \phi_v^i \right\rangle_{\Gamma_N}^{\delta} \\ & + \text{Re} \left((\mathbf{u}^n - \mathbf{w}^n) \cdot \nabla \phi_v^j, \phi_v^i \right)_{\Omega_e}^{\delta}. \end{aligned} \quad (\text{B.24})$$

To solve the system of equation (B.14), we compute in a first step

$$\tilde{\mathbf{H}}_{uu}^e = \mathbf{H}_{uu}^e - \left[\mathbf{M}_{uG_{11}} [\mathbf{M}_{G_{11}}]^{-1} \mathbf{M}_{G_{11}u} + \mathbf{M}_{uG_{12}} [\mathbf{M}_{G_{12}}]^{-1} \mathbf{M}_{G_{12}u} \right], \quad (\text{B.25})$$

$$\tilde{\mathbf{H}}_{uv}^e = \mathbf{H}_{uv}^e - \left[\mathbf{M}_{uG_{21}} [\mathbf{M}_{G_{21}}]^{-1} \mathbf{M}_{G_{21}v} \right], \quad (\text{B.26})$$

$$\tilde{\mathbf{H}}_{vu}^e = \mathbf{H}_{vu}^e - \left[\mathbf{M}_{vG_{12}} [\mathbf{M}_{G_{12}}]^{-1} \mathbf{M}_{G_{12}u} \right], \quad (\text{B.27})$$

$$\tilde{\mathbf{H}}_{vv}^e = \mathbf{H}_{vv}^e - \left[\mathbf{M}_{vG_{21}} [\mathbf{M}_{G_{21}}]^{-1} \mathbf{M}_{G_{21}v} + \mathbf{M}_{vG_{22}} [\mathbf{M}_{G_{22}}]^{-1} \mathbf{M}_{G_{22}v} \right], \quad (\text{B.28})$$

where

$$\begin{aligned} \mathbf{M}_{G11}[i, j] &= \left(\phi_{G11}^j, \phi_{G11}^i \right)_{\Omega_e}^\delta, & \mathbf{M}_{G12}[i, j] &= \left(\phi_{G12}^j, \phi_{G12}^i \right)_{\Omega_e}^\delta, \\ \mathbf{M}_{G21}[i, j] &= \left(\phi_{G21}^j, \phi_{G21}^i \right)_{\Omega_e}^\delta, & \mathbf{M}_{G22}[i, j] &= \left(\phi_{G22}^j, \phi_{G22}^i \right)_{\Omega_e}^\delta \end{aligned} \quad (\text{B.29})$$

$$\begin{aligned} \mathbf{M}_{G11u}[i, j] &= - \left(\frac{\partial \phi_u^j}{\partial x}, \phi_{G11}^i \right)_{\Omega_e}^\delta, & \mathbf{M}_{G12u}[i, j] &= - \left(\frac{\partial \phi_u^j}{\partial y}, \phi_{G12}^i \right)_{\Omega_e}^\delta, \\ \mathbf{M}_{G21v}[i, j] &= - \left(\frac{\partial \phi_v^j}{\partial x}, \phi_{G21}^i \right)_{\Omega_e}^\delta, & \mathbf{M}_{G22v}[i, j] &= - \left(\frac{\partial \phi_v^j}{\partial y}, \phi_{G22}^i \right)_{\Omega_e}^\delta, \end{aligned} \quad (\text{B.30})$$

$$\mathbf{M}_{uG11}[i, j] = -2\theta \left(\phi_{G11}^j, \frac{\partial \phi_u^j}{\partial x} \right)_{\Omega_e}^\delta + 2\theta \left\langle \phi_{G11}^j n_x, \phi_u^i \right\rangle_{\Gamma_N}^\delta, \quad (\text{B.31})$$

$$\mathbf{M}_{uG12}[i, j] = -\theta \left(\phi_{G12}^j, \frac{\partial \phi_u^j}{\partial y} \right)_{\Omega_e}^\delta + \theta \left\langle \phi_{G12}^j n_y, \phi_u^i \right\rangle_{\Gamma_N}^\delta, \quad (\text{B.32})$$

$$\mathbf{M}_{uG21}[i, j] = -\theta \left(\phi_{G21}^j, \frac{\partial \phi_u^j}{\partial y} \right)_{\Omega_e}^\delta + \theta \left\langle \phi_{G21}^j n_y, \phi_u^i \right\rangle_{\Gamma_N}^\delta, \quad (\text{B.33})$$

$$\mathbf{M}_{vG12}[i, j] = -\theta \left(\phi_{G12}^j, \frac{\partial \phi_v^j}{\partial x} \right)_{\Omega_e}^\delta + \theta \left\langle \phi_{G12}^j n_x, \phi_v^i \right\rangle_{\Gamma_N}^\delta, \quad (\text{B.34})$$

$$\mathbf{M}_{vG21}[i, j] = -\theta \left(\phi_{G21}^j, \frac{\partial \phi_v^j}{\partial x} \right)_{\Omega_e}^\delta + \theta \left\langle \phi_{G21}^j n_x, \phi_v^i \right\rangle_{\Gamma_N}^\delta, \quad (\text{B.35})$$

$$\mathbf{M}_{vG22}[i, j] = -2\theta \left(\phi_{G22}^j, \frac{\partial \phi_v^j}{\partial y} \right)_{\Omega_e}^\delta + 2\theta \left\langle \phi_{G22}^j n_y, \phi_v^i \right\rangle_{\Gamma_N}^\delta. \quad (\text{B.36})$$

The remainder of the algorithm is detailed in Section 6.6 and Section 6.7.

Bibliography

- D.J. Adrian. *Modeling of Three-Dimensional Viscoelastic Flows with Free Surfaces Using a Finite Element Method*. PhD thesis, Massachusetts Institute of Technology, Department of Chemical Engineering, 2010.
- M. Ainsworth and S. Sherwin. Domain decomposition preconditioners for p and hp finite element approximation of Stokes' equations. *Comput. Meth. Appl. Mech. Eng.*, 175(3-4):243–266, 1999.
- M. A. Alves, F. T. Pinho, and P. J. Oliveira. The flow of viscoelastic fluids past a cylinder: finite-volume high-resolution methods. *J. Non-Newtonian Fluid Mech.*, 97(2-3):207–232, 2001.
- F. Baaijens. Viscoelastic flow past a confined cylinder of a low density polyethylene melt. *J. Non-Newtonian Fluid Mech.*, 68(2-3):173–203, 1997.
- F.P.T. Baaijens. Mixed finite element methods for viscoelastic flow analysis: a review. *J. Non-Newtonian Fluid Mech.*, 79(2-3):361–385, 1998.
- J. Baranger and D. Sandri. A formulation of Stokes's problem and the linear elasticity equations suggested by the oldroyd model for viscoelastic flow. *Math. Modelling Numer. Anal.*, 26(2):331–345, 1992.
- A.N. Beris, R.C. Armstrong, and R.A. Brown. Finite element calculation of viscoelastic flow in a journal bearing: I. small eccentricities. *J. Non-Newtonian Fluid Mech.*, 16(1-2):141–172, 1984.
- R.B. Bird, C.F. Curtiss, R.C. Armstrong, and O. Hassager. *Dynamics of Polymeric Liquids*, volume 2. John Wiley and Sons, New York, 1987a.
- R.B. Bird, C.F. Curtiss, R.C. Armstrong, and O. Hassager. *Dynamics of Polymeric Liquids*, volume 1. John Wiley and Sons, New York, 1987b.
- H. Blum. The influence of reentrant corners in the numerical approximation of viscous flow problems. In *Numerical treatment of the Navier-Stokes equations: proceedings of the Fifth GAMM-Seminar, Kiel, January 20-22, 1989*, volume 30, pages 37–46. Vieweg, 1990.
- A.C.B Bogaerds, A.M. Grillet, G.W.M. Peters, and F.P.T. Baaijens. Stability analysis of polymer shear flows using the extended pom-pom constitutive equations. *J. Non-Newtonian Fluid Mech.*, 108(1-3):187–208, 2002.
- G. Böhme. *Strömungsmechanik nichtNewtonscher Fluide*. Teubner, Stuttgart, Leipzig, Wiesbaden, 2000.

- P. Bollada and T.N. Phillips. A physical decomposition of the stress tensor for complex flows. *Rheol. Acta*, 47:719–725, 2008.
- F. Brezzi. On the existence, uniqueness and approximation of saddle-point problems arising from Lagrangian multipliers. *RAIRO Anal. Numér.*, 8:129–151, 1974.
- A.N. Brooks and T.J.R. Hughes. Streamline upwind/Petrov-Galerkin formulations for convection dominated flows with particular emphasis on the incompressible Navier-Stokes equations. *Comput. Meth. Appl. Mech. Eng.*, 32(1):199–259, 1982.
- R.A. Brown, M.J. Szady, P.J. Northey, and R.C. Armstrong. On the numerical stability of mixed finite-element methods for viscoelastic flows governed by differential constitutive equations. *Theor. Comput. Fluid Dyn.*, 5(2):77–106, 1993.
- J.A. Byars. *Experimental characterization of viscoelastic flow instabilities*. PhD thesis, Massachusetts Institute of Technology, 1996.
- C. Canuto, MY Hussaini, A. Quarteroni, and TA Zang. *Spectral Methods: Fundamentals in Single Domains*. Springer-Verlag, Berlin, 2006.
- A.E. Caola, Y.L. Joo, R.C. Armstrong, and R.A. Brown. Highly parallel time integration of viscoelastic flows. *J. Non-Newtonian Fluid Mech.*, 100(1-3):191–216, 2001.
- E.O. Carew, P. Townsend, and M.F. Webster. Taylor-Galerkin algorithms for viscoelastic flow: Application to a model problem. *Numer. Meth. Partial Differential Equations*, 10: 171–190, 1994.
- Y.J. Choi and M.A. Hulsen. Simulation of extrudate swell using an extended finite element method. *Korea-Aust Rheol J*, 23(3):147–154, 2011.
- S. Claus. Numerical simulation of unsteady three-dimensional viscoelastic Oldroyd-B and Phan-Thien Tanner flows. Diplomarbeit, Institut für Numerische Simulation, Universität Bonn, 2008.
- S. Claus and T.N. Phillips. Viscoelastic flow around a confined cylinder using spectral/hp element methods. *J. Non-Newtonian Fluid Mech.*, 2013a. to appear.
- S. Claus and T.N. Phillips. Impact of slip and inertia on the flow singularity in plane Newtonian extrudate swell using spectral/hp element methods. *Comput. Fluids*, 2013b. in preparation for submission.
- B. Cockburn and A. Quarteroni. *Advanced numerical approximation of nonlinear hyperbolic equations: lectures given at the 2nd session of the Centro Internazionale Matematico Estivo (CIME) held in Cetraro, Italy, June 23-28, 1997*. Springer-Verlag, Berlin, 1998.
- M.J. Crochet and R. Keunings. Finite element analysis of die swell of a highly elastic fluid. *J. Non-Newtonian Fluid Mech.*, 10(3):339–356, 1982.
- M.J. Crochet, A.R. Davies, and K. Walters. *Numerical simulation of non-Newtonian flow*. Elsevier, Amsterdam, 1984.

- V. Delvaux and M. J. Crochet. Numerical simulation of delayed die swell. *Rheol. Acta*, 29:1–10, 1990.
- M.M. Denn. Extrusion instabilities and wall slip. *Annual Review of Fluid Mechanics*, 33(1):265–287, 2001.
- M.O. Deville and T.B. Gatski. *Mathematical modeling for complex fluids and flows*. Springer-Verlag, Berlin, 2012.
- M.O. Deville, P.F. Fischer, and E.H. Mund. *High-order methods for incompressible fluid flow*, volume 9. Cambridge Univ Pr, Cambridge, 2002.
- J. Donea, A. Huerta, J.P. Ponthot, and A. Rodríguez-Ferran. Arbitrary Lagrangian–Eulerian methods. *Encyclopedia of Comp. Mech.*, 2004.
- H.S. Dou and N. Phan-Thien. Viscoelastic flow past a confined cylinder: Instability and velocity inflection. *Chem. Eng. Sci.*, 62:3909 – 3929, 2007.
- H.S. Dou and N. Phan-Thien. An instability criterion for viscoelastic flow past a confined cylinder. *Korea-Aust. Rheol. J.*, 20(1):15–26, 2008.
- M. Dubiner. Spectral methods on triangles and other domains. *J. Sci. Comp.*, 6:345–390, 1991.
- J.D. Evans. Re-entrant corner flows of Oldroyd-B fluids. *Proc. R. Soc. A: Math., Phys. and Eng. Sci.*, 461(2060):2573–2603, 2005.
- J.D. Evans. Re-entrant corner behaviour of the Giesekus fluid with a solvent viscosity. *J. Non-Newtonian Fluid Mech.*, 165(9):538–543, 2010.
- Y. Fan, R.I. Tanner, and N. Phan-Thien. Galerkin/least-square finite-element methods for steady viscoelastic flows. *J. Non-Newtonian Fluid Mech.*, 84(2-3):233–256, 1999.
- Y. Fan, H. Yang, and R.I. Tanner. Stress boundary layers in the viscoelastic flow past a cylinder in a channel: limiting solutions. *Acta Mech. Sinica*, 21(4):311–321, 2005.
- C. Farhat, P. Geuzaine, and C. Grandmont. The discrete geometric conservation law and the nonlinear stability of ale schemes for the solution of flow problems on moving grids. *J. Comput. Phys.*, 174(2):669–694, 2001.
- R. Fattal and R. Kupferman. Constitutive laws for the matrix-logarithm of the conformation tensor. *J. Non-Newtonian Fluid Mech.*, 123(2-3):281–285, 2004.
- R. Fattal and R. Kupferman. Time-dependent simulation of viscoelastic flows at high Weissenberg number using the log-conformation representation. *J. Non-Newtonian Fluid Mech.*, 126(1):23–37, 2005.
- M.A. Fontelos and A. Friedman. The flow of a class of Oldroyd fluids around a re-entrant corner. *J. Non-Newtonian Fluid Mech.*, 95:185–198, 2000.

- C. Förster, W.A. Wall, and E. Ramm. On the geometric conservation law in transient flow calculations on deforming domains. *Int. J. Numer. Methods Fluids*, 50(12):1369–1379, 2006.
- M. Fortin. On the discrete EVSS method. *Comput. Meth. Appl. Mech. Eng.*, 189(1):121–139, 2000.
- M. Fortin and A. Fortin. A new approach for the FEM simulation of viscoelastic flows. *J. Non-Newtonian Fluid Mech.*, 32(3):295–310, 1989.
- M. Fortin and R. Pierre. On the convergence of the mixed method of Crochet and Marchal for viscoelastic flows. *Comp. Methods Appl. Mech. Eng.*, 7:1035–1052, 1987.
- V. Ganvir, A. Lele, R. Thaokar, and B.P. Gautham. Prediction of extrudate swell in polymer melt extrusion using an arbitrary Lagrangian Eulerian (ALE) based finite element method. *J. Non-Newtonian Fluid Mech.*, 156(1):21–28, 2009.
- G.C. Georgiou and A.G. Boudouvis. Converged solutions of the Newtonian extrudate-swell problem. *Int. J. Numer. Methods Fluids*, 29(3):363–371, 1999.
- G.C. Georgiou, L.G. Olson, W.W. Schultz, and S. Sagan. A singular finite element for Stokes flow: the stick-slip problem. *Int. J. Numer. Methods Fluids*, 9(11):1353–1367, 1989.
- M.I. Gerritsma. Time dependent numerical simulations of a viscoelastic fluid on a staggered grid. Proefschrift Rijksuniversiteit Groningen, Cip-Gegevens koninklijke bibliotheek, den Haag, 1996.
- M.I. Gerritsma and T.N. Phillips. Compatible spectral approximations for the velocity-pressure-stress formulation of the Stokes problem. *SIAM J. Sci. Comput.*, 20:1530–1550, 1999.
- M.I. Gerritsma and T.N. Phillips. On the use of characteristic variables in viscoelastic flow problems. *IMA J. Appl. Math.*, 66(2):127–147, 2001.
- H. Giesekus. Die Elastizität von Flüssigkeiten. *Rheol. Acta*, 5(1):29–35, 1966.
- W.J. Gordon and C.A. Hall. Transfinite element methods: blending-function interpolation over arbitrary curved element domains. *Numer. Math*, 21(2):109–129, 1973.
- D. Gottlieb and S.A. Orszag. *Numerical analysis of spectral methods: theory and applications*. SIAM, Philadelphia, 1977.
- R. Guénette and M. Fortin. A new mixed finite element method for computing viscoelastic flow. *J. Non-Newtonian Fluid Mech.*, 60(1):27–52, 1995.
- L.W. Ho and E.M. Rønquist. Spectral element solution of steady incompressible viscous free-surface flows. *Finite elements in analysis and design*, 16(3-4):207–227, 1994.
- M.A. Hulsen, R. Fattal, and R. Kupferman. Flow of viscoelastic fluids past a cylinder at high Weissenberg number: Stabilized simulations using matrix logarithms. *J. Non-Newtonian Fluid Mech.*, 127(1):27–39, 2005.

- A. Jafari. *Simulation of Time-Dependent Viscoelastic Fluid Flows by Spectral Elements*. PhD thesis, École Polytechnique Fédérale de Lausanne, 2011.
- G. E. Karniadakis and S. J. Sherwin. *Spectral/hp Element Methods for Computational Fluid Dynamics*. Oxford University Press, Oxford, 2005.
- R.A. Keiller. Numerical instability of time-dependent flows. *J. Non-Newtonian Fluid Mech.*, 43:229–246, 1992.
- R. Keunings. On the high weissenberg number problem. *J. Non-Newtonian Fluid Mech.*, 20:209–226, 1986.
- J.M. Kim, C. Kim, K.H. Ahn, and S.J. Lee. An efficient iterative solver and high-resolution computations of the Oldroyd-B fluid flow past a confined cylinder. *J. Non-Newtonian Fluid Mech.*, 123(2-3):161–173, 2004.
- J.M. Kim, C. Kim, J.H. Kim, C. Chung, K.H. Ahn, and S.J. Lee. High-resolution finite element simulation of 4: 1 planar contraction flow of viscoelastic fluid. *J. Non-Newtonian Fluid Mech.*, 129(1):23–37, 2005.
- D.A. Kopriva. *Implementing Spectral Methods for Partial Differential Equations: Algorithms for Scientists and Engineers*. Springer-Verlag, Berlin, 2009.
- Z. Kountouriotis, G.C. Georgiou, and E. Mitsoulis. On the combined effects of slip, compressibility, and inertia on the newtonian extrudate-swell flow problem. *Comput.Fluids*, 71:297 – 305, 2013.
- H.A. Kramers. The behavior of macromolecules in inhomogeneous flow. *J. Chem. Phys.*, 14:415–424, 1946.
- P. Lesaint and P.A. Raviart. *On a finite element method for solving the neutron transport equation*. Univ. Paris VI, Labo. Analyse Numérique, 1974.
- M. Lesoinne and C. Farhat. Geometric conservation laws for flow problems with moving boundaries and deformable meshes, and their impact on aeroelastic computations. *Comput. Meth. Appl. Mech. Eng.*, 134(1):71–90, 1996.
- A.W. Liu, D.E. Bornside, R.C. Armstrong, and R.A. Brown. Viscoelastic flow of polymer solutions around a periodic, linear array of cylinders: comparisons of predictions for microstructure and flow fields. *J. Non-Newtonian Fluid Mech.*, 77(3):153–190, 1998.
- AS Lodge. A network theory of flow birefringence and stress in concentrated polymer solutions. *Trans. Faraday Soc.*, 52:120–130, 1956.
- X. Ma, V. Symeonidis, and G.E. Karniadakis. A spectral vanishing viscosity method for stabilizing viscoelastic flows. *J. Non-Newtonian Fluid Mech.*, 115(2–3):125 – 155, 2003.
- C.W. MacMinn and G.H. McKinley. Tubeless siphon and die swell demonstration. <http://web.mit.edu/nnf/research/phenomena/Demos.pdf>, 2004.

- C.W. Macosko. *Rheology: Principles, Measurements, and Applications*. Wiley-VCH, New York, 1994.
- Y. Maday, A.T. Patera, and E.M. Rønquist. The $P_N \times P_{N-2}$ method for the approximation of the Stokes problem. *Laboratoire d'Analyse Numérique, Paris VI*, 11(4), 1992.
- J.M. Marchal and M.J. Crochet. A new mixed finite element for calculating viscoelastic flow. *J. Non-Newtonian Fluid Mech.*, 26(1):77–114, 1987.
- D.J. Mavriplis and Z. Yang. Construction of the discrete geometric conservation law for high-order time-accurate simulations on dynamic meshes. *J. Comput. Phys.*, 213(2): 557–573, 2006.
- G.H. McKinley. Non-Newtonian Fluid Dynamics Research Group, Massachusetts Institute of Technology. <http://web.mit.edu/nmf/>, 2008.
- G.H. McKinley, R.C. Armstrong, and R.A. Brown. The wake instability in viscoelastic flow past confined circular cylinders. *Phil. Trans. R. Soc. Lond. A*, 344:265–304, 1993.
- M.A. Mendelson, P.W. Yeh, R.A. Brown, and R.C. Armstrong. Approximation error in finite element calculation of viscoelastic fluid flows. *J. of Non-Newtonian Fluid Mech.*, 10(1-2):31–54, 1982.
- E. Mitsoulis. Extrudate swell of Boger fluids. *J. Non-Newtonian Fluid Mech.*, 165(13): 812–824, 2010.
- E. Mitsoulis and N.A. Malamataris. Free (open) boundary condition: some experiences with viscous flow simulations. *Int. J. Numer. Methods Fluids*, 68(10):1299–1323, 2011.
- E. Mitsoulis, G.C. Georgiou, and Z. Kountouriotis. A study of various factors affecting Newtonian extrudate swell. *Comput. Fluids*, 57(0):195 – 207, 2012.
- H.K. Moffatt. Viscous and resistive eddies near a sharp corner. *J. Fluid Mech*, 18(1):1–18, 1964.
- R.E. Nickell, R.I. Tanner, and B. Caswell. The solution of viscous incompressible jet and free-surface flows using finite-element methods. *J. Fluid Mech.*, 65(1):189, 1974.
- F. Nobile. *Numerical approximation of fluid-structure interaction problems with application to haemodynamics*. PhD thesis, Ecole Polytechnique Fédérale de Lausanne, Switzerland, 2001.
- P.J. Oliveira and A.I.P. Miranda. A numerical study of steady and unsteady viscoelastic flow past bounded cylinders. *J. Non-Newtonian Fluid Mech.*, 127(1):51–66, 2005.
- B.J. Omodei. Computer solutions of a plane Newtonian jet with surface tension. *Comput. Fluids*, 7:79–96, 1979.
- B.J. Omodei. On the die-swell of an axisymmetric Newtonian jet. *Comput. Fluids*, 8(3): 275–289, 1980.

- Y. Otsuki and T. Kajiwara. Numerical simulations of annular extrudate swell using various types of viscoelastic models. *Polymer Eng. & Sci.*, 39(10):1969–1981, 1999.
- R.G. Owens and T.N. Phillips. *Computational Rheology*. Imperial College Press, Singapore, 2005.
- R.G. Owens, C. Chauvière, and T.N. Phillips. A locally-upwinded spectral technique (LUST) for viscoelastic flows. *J. Non-Newtonian Fluid Mech.*, 108(1-3):49–71, 2002.
- A.T. Patera. A spectral element method for fluid dynamics: laminar flow in a channel expansion. *J. Comput. Phys.*, 54(3):468–488, 1984.
- G. Pena. *Spectral Element Approximation of the Incompressible Navier-Stokes Equations in a Moving Domain and Applications*. PhD thesis, École Polytechnique Fédérale de Lausanne, 2009.
- M.G.N. Perera and K. Walters. Long-range memory effects in flows involving abrupt changes in geometry:: Part I: flows associated with I-shaped and T-shaped geometries. *J. of Non-Newtonian Fluid Mech.*, 2(1):49–81, 1977.
- N. Phan-Thien. *Understanding Viscoelasticity: Basics of Rheology*. Springer-Verlag, New York, 2002.
- N. Phan-Thien and H.S. Dou. Viscoelastic flow past a cylinder: drag coefficient. *Comput. Meth. Appl. Mech. Eng.*, 180(3–4):243 – 266, 1999.
- Psidot. The Barus Effect. <http://www.youtube.com/watch?v=KcNWLIpv8gc>, 2007.
- D. Rajagopalan, R.C. Armstrong, and R.A. Brown. Finite element methods for calculation of steady, viscoelastic flow using constitutive equations with a Newtonian viscosity. *J. of Non-Newtonian Fluid Mech.*, 36:159–192, 1990.
- K.R. Reddy and R.I. Tanner. Finite element solution of viscous jet flows with surface tension. *Comput. Fluids*, 6(2):83–91, 1978.
- M. Renardy. Inflow boundary conditions for steady flows of viscoelastic fluids with differential constitutive laws. *Rocky Mt. J. Math.*, 18:445–453, 1988.
- M. Renardy. Re-entrant corner behavior of the PTT fluid. *J. Non-Newtonian Fluid Mech.*, 69:99–104, 1997.
- M. Renardy. *Mathematical Analysis of Viscoelastic Flows*. SIAM, Philadelphia, 2000.
- S. Richardson. The die swell phenomenon. *Rheol. Acta*, 9(2):193–199, 1970.
- I. Robertson, S.J. Sherwin, and J.M.R. Graham. Comparison of wall boundary conditions for numerical viscous free surface flow simulation. *J. Fluids Struct.*, 19(4):525–542, 2004.
- G. Russo. *Spectral Element Methods for Predicting the Die-Swell of Newtonian and Viscoelastic Fluids*. PhD thesis, School of Mathematics, Cardiff University, Wales (UK), 2009.

- G. Russo and T.N. Phillips. Numerical prediction of extrudate swell of branched polymer melts. *Rheol. Acta*, 49(6):657–676, 2010.
- G. Russo and T.N. Phillips. Spectral element predictions of die-swell for Oldroyd-B fluids. *Comput. Fluids*, 43(1):107–118, 2011.
- T.R. Salamon, D.E. Bornside, R.C. Armstrong, and R.A. Brown. The role of surface tension in the dominant balance in the die swell singularity. *Phys. Fluids*, 7(10):2328–2344, 1995.
- T.R. Salamon, D.E. Bornside, R.C. Armstrong, and R.A. Brown. Local similarity solutions in the presence of a slip boundary condition. *Phys. Fluids*, 9:1235, 1997.
- G. Scovazzi and T.J.R. Hughes. Lecture notes on continuum mechanics on arbitrary moving domains. Technical report, Technical report SAND-2007-6312P, Sandia National Laboratories, 2007.
- S.J. Sherwin and M. Ainsworth. Unsteady Navier-Stokes solvers using hybrid spectral/hp element methods. *Appl. Numer. Math.*, 33(1–4):357–363, 2000.
- W.J. Silliman and L.E. Scriven. Separating how near a static contact line: Slip at a wall and shape of a free surface. *J. Comput. Phys.*, 34(3):287–313, 1980.
- M.D. Smith, R.C. Armstrong, R.A. Brown, and R. Sureshkumar. Finite-element analysis of stability of two-dimensional viscoelastic flows to three-dimensional perturbations. *J. Non-Newtonian Fluid Mech.*, 93:203–244, 2000.
- J. Sun, N. Phan-Thien, and R.I. Tanner. An adaptive viscoelastic stress splitting scheme and its applications: AVSS/SI and AVSS/SUPG. *J. Non-Newtonian Fluid Mech.*, 65(1):75–91, 1996.
- J. Sun, M.D. Smith, R.C. Armstrong, and R.A. Brown. Finite element method for viscoelastic flows based on the discrete adaptive viscoelastic stress splitting and the discontinuous Galerkin method: DAVSS-G/DG. *J. Non-Newtonian Fluid Mech.*, 86(3):281–307, 1999.
- R. Sureshkumar, M.D. Smith, R.C. Armstrong, and R.A. Brown. Linear stability and dynamics of viscoelastic flows using time-dependent numerical simulation. *J. Non-Newtonian Fluid Mech.*, 82:57–104, 1999.
- E. Taliadorou, G.C. Georgiou, and E. Mitsoulis. Numerical simulation of the extrusion of strongly compressible Newtonian liquids. *Rheol. Acta*, 47(1):49–62, 2007.
- R.I. Tanner. Die-swell reconsidered: some numerical solutions using a finite element program. In *Appl. Polym. Symp*, volume 20, pages 201–208, 1973.
- R.I. Tanner. A new inelastic theory of extrudate swell. *J. Non-Newtonian Fluid Mech.*, 6(3):289–302, 1980.
- R.I. Tanner. *Engineering Rheology*. Oxford University Press, Oxford, 2002.

- R.I. Tanner, R.E. Nickell, and R.W. Bilger. Finite element methods for the solution of some incompressible non-Newtonian fluid mechanics problems with free surfaces. *Comput. Meth. Appl. Mech. Eng.*, 6(2):155–174, 1975.
- S. Tanoue, Y. Kuwano, T. Kajiwara, K. Funatsu, K. Terada, and M. Yamabe. Numerical simulation of blow molding—viscoelastic flow analysis of parison formation. *Polymer Eng. & Sci.*, 35(19):1546–1554, 1995.
- J.P.K. Tillett. On the laminar flow in a free jet of liquid at high reynolds numbers. *J. Fluid Mech.*, 32(2):273–292, 1968.
- M.F. Tomé, N. Mangiavacchi, J.A. Cuminato, A. Castelo, and S. McKee. A finite difference technique for simulating unsteady viscoelastic free surface flows. *J. Non-Newtonian Fluid Mech.*, 106(2):61–106, 2002.
- L.N. Trefethen. *Spectral methods in MATLAB*, volume 10. SIAM, Philadelphia, 2000.
- R.G.M. van Os and M.I. Gerritsma. A variable order spectral element scheme applied to the velocity–pressure–total-stress formulation of the upper convected Maxwell model. *J. Non-Newtonian Fluid Mech.*, 108(1–3):73 – 97, 2002.
- P.E.J. Vos. *From h to p Efficiently: Optimising the Implementation of Spectral/ hp Element Methods*. PhD thesis, Imperial College London, 2011.
- P. Wapperom and M. Renardy. Numerical prediction of the boundary layers in the flow around a cylinder using a fixed velocity field. *J. Non-Newtonian Fluid Mech.*, 125(1): 35–48, 2005.
- N.D. Waters and M.J. King. Unsteady flow of an elastico-viscous liquid. *Rheol. Acta*, 9: 345–355, 1970.
- K. Weissenberg et al. A continuum theory of rheological phenomena. *Nature*, 159(4035): 310–311, 1947.
- R.D. Wesson and T.C. Papanastasiou. Flow singularity and slip velocity in plane extrudate swell computations. *J. Non-Newtonian Fluid Mech.*, 26(3):277–295, 1988.
- H.C. Öttinger. *Stochastic Processes in Polymeric Fluids: Tools and Examples for Developing Simulation Algorithms*. Springer-Verlag, New York, 1996.